



TECHNISCHE UNIVERSITÄT MÜNCHEN

Fakultät für Chemie, Lehrstuhl für Technische Chemie II

**Developments into probing Ni catalyzed liquid phase
biomass conversion**

Stanislav Kasakov

Vollständiger Abdruck der von der Fakultät für Chemie der Technischen Universität
München zur Erlangung des akademischen Grades eines

Doktors der Naturwissenschaften (Dr. rer. nat.)

genehmigten Dissertation

Vorsitzender: Univ.-Prof. Dr. Dr. h.c. Bernhard Rieger

Prüfer der Dissertation:

1. Univ.-Prof. Dr. Johannes A. Lercher
2. Univ.-Prof. Dr. Reinhard Niessner

Die Dissertation wurde am 28.10.2015 bei der Technischen Universität München
eingereicht und durch die Fakultät für Chemie am 15.12.2015 angenommen.

Statutory Declaration

I declare that I have authored this thesis on my own, that I have not used other than the declared (re)sources, and I have explicitly marked all material which has been quoted either literally or by content from the used sources. At the end of each chapter all collaborators are listed and their contributions are explained. Published content of this thesis is clearly marked at the end of each chapter and the publishing agreement of the publisher is stated in the associated content of each chapter.

_____ , _____

“Der Mensch ist das Maß aller Dinge, der seienden, dass sie sind, der nichtseienden, dass sie nicht sind.“ nach Protagoras

Acknowledgments

This doctoral thesis has reached a successful completion with the help of many people during my scientific voyage.

First of all I want to thank Prof. Dr. Johannes A. Lercher for giving me the opportunity to work for such an inspiring topic. I really enjoyed our fruitful scientific discussions and your patient guidance and unconditional support.

Secondly I want to mention Prof. Dr. Chen Zhao, who guided me through my research career. You have supervised me from the very first steps of my scientific career and guided me through my research assistance, my Master's thesis and my PhD. I want to thank you for your outstanding guidance, your friendly and always constructive thinking and the time we have spent during endless scientific discussions.

I am also very thankful to Prof. Dr. Andreas Jentys for his scientific expertise and insightful discussions on the spectroscopy studies. It was always very interesting to listen to your delightful stories.

Next, I would like to thank my present supervisor, Dr. Eszter Baráth, who took care of me during the last period of my PhD.

Especially I would like to acknowledge the people at Pacific Northwest National Laboratory, i.e. Dr. Donald M. Camaioni, Dr. John Fulton, Dr. Hui Shi, Dr. Aleksei Vjunov and Zizwe Chase for fruitful scientific collaboration at Argonne, IL and PNNL, WA. The EXAFS measurements and its analyses were insightful and the further discussions and manuscript preparation were very helpful.

Further I acknowledge Xaver Hecht for being such a wonderful technician on the set ups, also thanks a lot for the nitrogen physisorption (BET) and H₂ chemisorption measurements. I always enjoyed our talks about fishing. Thanks to Martin Neukamm for the managing of chemicals, all the security instruction and safety regulations of chemicals, as well as the AAS and SEM measurements.

My thank goes to Bettina Federmann, Stefanie Maier, Ulrike Sanwald, Karen Schulz for administrative support, the interesting and inspiring discussions throughout all the years.

I am grateful to my colleagues who contributed to my thesis with the TEM measurements, namely Dr. Sonja Wyrzgol, Elisabeth Hanrieder and Sebastian Grundner, Marco Peroni and Andreas Ehrmaier.

I am very grateful for the whole TC 2 team, as the spirit and the positive atmosphere enabled to work in an pleasant environment with so many interesting people, namely Dr. Oliver Gutierrez, Dr. Erika Ember, Dr. Maricruz Sanchez-Sanchez, Dr. Jeongnam Kim, Dr.

Xianyong Sun, Dr. Baoxiang Peng, Bo Peng, Dr. John Ahn, Dr. Robin Kolvenbach, Dr. Maximilian Hahn, Dr. Christian Gärtner, Dr. Anastasia Pashigreva, Dr. Julia Martynova, Dr. Wenhao Luo and Dr. Elena Kondratieva. Within the biomass team, I want to thank Sebastian Foraita, Moritz Schreiber, Marco Peroni, Dr. Wenji Song, Dr. Jiayue He, Manuel Wagenhofer, Yuanshuai Liu, Martina Braun, Dr. Yuchun Zhi, Gouju Yang, Peter Hintermeier and Sebastian Eckstein for wonderful working atmosphere, discussions throughout the biomass meetings and for constructive advises and experience exchange in and outside the lab.

Further I acknowledge all my students who helped me with the hands-on lab work during the last three years, namely Elena Popp, Nikita Popov, Leonhard Schmalhorst, Elena Fritzler, Jonas Letica and Manuel Weber.

My thanks go to Dr. Franzisco Luiz-Penne for funny talks on-site and the exhausting but wonderful mountain bike tour through Garmischer alps off-site.

Further I would like to mention my fellow students, Sebastian Grundner, Tobias Berto, Elisabeth Hanrieder. It has been a wonderful time with you during the undergraduate studies and our daily life-time together in and outside the TC2 chair.

Great thanks go to Dr. Ricardo Bermejo-Deval for reading and revising this thesis.

I want to thank separately Sebastian Foraita, Moritz Schreiber, Marco Peroni, Dr. Ricardo Bermejo-Deval and Takaaki Ikuno for intense scientific, interesting and amusing non-scientific discussions, which I really enjoyed a lot. I have been travelling with you guys, spending with you most of my time in and outside of the university. I really enjoyed the time with you as we shared many marvelous moments. I hope our future will bring us together for further travelling and exploring into more adventures.

Finally I want to thank my family, my parents Valeria and Michael, my brother Vladimir and my sister in law, Tatjana, who always supported me during the studies, my PhD and always helped me during my whole life and made everything possible.

Thanks to all of you,
Stanislav

Table of Contents

Acknowledgments	i
Table of Contents	iii
Symbols and Abbreviations	ix
Abstract	x
Chapter I. Introduction	1
1. General background	1
2. Terrestrial wooden biomass	3
3. Lignocellulosic biomass valorization	5
4. Lignin deconstruction strategies	7
4.1 The base-catalyzed depolymerization of lignin	8
4.2 Oxidative depolymerization of lignin	9
4.3 Catalytic pyrolysis of lignin	9
5. Transition metal catalyzed lignin upgrading	10
5.1 Hydrodeoxygenation of liquid bio-oil	10
5.2 Ni catalyzed reactions of lignin model compounds in liquid phase	12
5.3 Heterogeneous catalyzed valorization of real lignin feeds	13
6. Dual-functional catalysts for liquid phase upgrading	14
6.1 Synthesis of Ni/zeolite bifunctional catalysts	15
6.2 Development of carbon supported Ni nanoparticles	16
7. Probing into liquid phase biomass conversion	18
7.1 Vibrational Spectroscopy Methods applied in Catalysis	18
7.2 Fundamentals of ATR spectroscopy	19
7.3 ATR-IR for In situ Investigations in Catalysis	21
7.3.1 Internal reflection spectroscopy for on-line reaction monitoring	22
7.3.2 Flow-Through ATR-IR Cell	23
8. Scope of thesis	26
9. References	29

Chapter II. Comparison of Ni/HZSM-5 and Ni/Al ₂ O ₃ -HZSM-5 catalysts for phenol hydrodeoxygenation	41
Abstract	41
1. Introduction	42
2. Experimental section	43
2.1 Chemicals	43
2.2 Catalyst preparation	43
2.3 Catalyst characterization	43
2.3.1 Atomic absorption spectroscopy (AAS)	43
2.3.2 Infrared (IR) spectroscopy of adsorbed pyridine	43
2.3.3 Transmission electron microscopy (TEM)	44
2.3.4 H ₂ chemisorption	44
2.4 Catalytic measurements	44
2.4.1 Kinetic study of phenol hydrodeoxygenation network	44
2.4.2 In situ IR spectroscopic studies of phenol hydrodeoxygenation	45
2.4.3 Hydrodeoxygenation of phenol and substituted phenol monomers	45
2.4.4 Catalyst leaching at the hydrothermal and acidic conditions	45
2.4.5 Catalyst recycle	46
3. Results and Discussion	47
3.1 Characterization of catalyst properties	47
3.2 Phenol hydrodeoxygenation network	48
3.3 Kinetic of four elementary reactions in phenol hydrodeoxygenation	48
3.3.1 Phenol hydrogenation	48
3.3.2 Cyclohexanone hydrogenation	50
3.3.3 Cyclohexanol dehydration	51
3.3.4 Cyclohexene dehydration	53
3.3.5 Summarized kinetic data for phenol hydrodeoxygenation reaction network	54
3.4 Kinetics of overall phenol hydrodeoxygenation over Ni catalyst	55
3.4.1 Time-resolved in situ IR spectroscopy study	55
3.4.2 Impact of reaction time	57
3.4.3 Impact of reaction temperature	58
3.5 Hydrodeoxygenation of substituted phenol monomers	59
3.6 Catalyst test in the recycling runs	60

3.6.1 Catalyst activity	60
3.6.2 Catalyst stability during the recycling runs	62
3.6.2.1 The Ni and zeolite leaching under acidic hydrothermal conditions	62
3.6.2.2 Metal site changes during the recycling runs	65
3.6.2.3 Acid site change during the recycling runs	66
4. Conclusion	69
5. References	70
6. Associated Content	71
Chapter III. Glucose and cellulose derived Ni/C-SO ₃ H catalysts for phenol hydrodeoxygenation	72
Abstract	72
1. Introduction	73
2. Experimental section	74
2.1 Catalyst preparation	74
2.1.1 Sulfonated carbon supports	74
2.1.2 Loading of Ni nanoparticles on C-SO ₃ H support	74
2.2 Catalyst characterization	75
2.2.1 Inductive coupled plasma-optical emission spectroscopy (ICP-OES)	75
2.2.2 Specific surface area and porosity	75
2.2.3 Boehm titration	75
2.2.4 X-ray diffraction (XRD)	76
2.2.5 Transmission electron microscopy (TEM)	76
2.2.6 Scanning electron microscopy (SEM) and energy dispersed X-ray (EDX)	76
2.2.7 Solid-state magic angle spinning nuclear magnetic resonance	76
2.2.8 Raman spectroscopy	76
2.2.9 Thermal gravimetric analysis (TGA)	76
2.2.10 X-ray absorption spectroscopy	77
2.2.11 In situ spectroscopy study of phenol hydrodeoxygenation	77
2.3 Catalytic measurements	78
2.3.1 Cyclohexanol dehydration	78
2.3.2 Phenol HDO	79
3. Results and Discussion	80
3.1 Synthesis, characterization, and activity tests of carbon catalysts	80

3.2 Textural property, and acidity of synthesized carbon materials	80
3.3 Morphology of the carbon and sulfonated carbon materials	82
3.4 Structure of carbon and sulfonated carbon materials	83
3.5 Carbon framework structures and surface $-\text{SO}_3\text{H}$ functional groups of HS carbons	85
3.6 Correlation of activities of cyclohexanol dehydration with structural properties of C- SO_3H materials	86
3.7 Characterization and activity evaluation of Ni/C- SO_3H catalyst	88
3.7.1 Ex situ analysis of Ni/C- SO_3H catalysts	88
3.7.2 In situ spectroscopic study of Ni state during aqueous phase phenol hydrodeoxygenation	90
3.8 Phenol reduction on Ni/C- SO_3H in aqueous phase	93
3.9 Evaluation of phenol hydrodeoxygenation catalyzed by Ni/C- SO_3H in the non-polar liquid phase (hexadecane)	94
3.10 <i>In situ</i> IR spectroscopy of phenol HDO catalyzed by Ni/C- SO_3H	95
3.11 Optimization of phenol HDO catalysis by Ni/C- SO_3H in liquid hexadecane	97
4. Conclusion	99
5. References	100
6. Associated Content	102
7. Appendix	103
Chapter IV. Reductive deconstruction of organosolv lignin catalyzed by zeolite supported nickel nanoparticles	105
Abstract	105
1. Introduction	106
2. Experimental section	107
2.1 Chemicals	107
2.2 Preparation of Ni-based catalysts	107
2.3 Catalyst characterization	108
2.3.1 Ni loadings	108
2.3.2 Sorption measurements	108
2.3.3 IR-spectra of adsorbed pyridine	108
2.3.4 Transmission electron microscopy (TEM)	108
2.3.5 X-ray diffraction (XRD)	108

2.3.6 H ₂ chemisorption	109
2.4 Organosolv Lignin characterization	109
2.4.1 Elemental Analysis	109
2.4.2 Gel permeation chromatography	109
2.4.3 MALDI-TOF MS	109
2.4.4 ATR-IR spectroscopy	110
2.4.5 Scanning electron microscopy – energy dispersed X-ray analysis	112
2.4.6 Solution state NMR spectroscopy	113
2.5 Catalytic measurements	113
2.6 Analysis of gas, solution and solid phases of reaction mixture	113
2.7 Recycle runs	114
3. Results and Discussion	115
3.1 Physicochemical properties of Ni catalysts	115
3.2 Analysis of organosolv lignin	118
3.3 Ni catalyzed lignin deconstruction and upgrading in the presence of H ₂	123
3.4 ATR-IR spectroscopy during reductive deconstruction of lignin on NiHBEA130	
3.5 A proposed mechanism for Ni-catalyzed reductive deconstruction of lignin	136
4. Conclusion	140
5. References	141
6. Associated Content	144
Chapter V. Monitoring catalysis by <i>in situ</i> IR spectroscopy	145
Abstract	145
1. Introduction	146
2. Experimental section	147
2.1 Chemicals	147
2.2 Catalyst preparation	147
2.3 <i>In situ</i> IR measurements	147
3. Results and Discussions	148
3.1 Proposed reaction pathways for palmitic acid conversion	148
3.2 Monitoring the conversion of palmitic acid over Ni/ZrO ₂ catalysts by <i>in situ</i> IR spectroscopy	149
4. Conclusion	153
5. References	154
6. Associated Content	155
7. Appendix	156

Chapter VI. Summary and Conclusions -----	158
Curriculum Vitae -----	160
List of publications -----	161

Symbols and Abbreviations

AAS	Atomic absorption spectroscopy
ATR	Attenuated total reflection
BAS	Brønsted acid site
BET	Brunauer-Emmett-Teller
DP	Deposition precipitation
GC	Gas chromatography
GPC	Gel permeation chromatography
HDO	Hydrodeoxygenation
HS	high surface
HSQC	Heteronuclear single quantum coherence spectroscopy
IR	Infrared
K	Kelvin
(k)J	(kilo)Joule
(M)Pa	(mega) Pascal
kV	Kilovolt
LCC	Lignin carbohydrate complex
LAS	Lewis acid site
LS	low surface
(m)L	(milli) Liter
MALDI-TOF	Matrix-assisted laser desorption/ionization - Time of Flight
MS	Mass spectrometry
min	Minute
nm	Nanometer
NMR	Nuclear magnetic resonance
TEM	Transmission electron microscopy
TOF	Turn over frequency
wt. %	weight percent
XRD	X-ray diffraction

Abstract

Ni nanoparticles supported on sulfonated carbon have been developed for phenol hydrodeoxygenation in liquid phase. Through combination of kinetic and spectroscopic studies the dehydration was elucidated to be the rate determining reaction. While the hydrodeoxygenation was determined by hydrogenation and elimination reactions, the successful deconstruction of lignin was mainly driven by hydrogenolysis of ether bonds in lignin polymer.

Kurzfassung

Ni Nanopartikel geträgert auf sulfoniertem Kohlenstoff wurden als Katalysatoren für die Hydrodeoxygenierung von Phenol in flüssiger Phase entwickelt. Durch Kombination kinetischer und spektroskopischer Messungen wurde die Dehydratisierung als die geschwindigkeitsbestimmende Reaktion ermittelt. Während die Hydrodeoxygenierung durch Hydrier- und Eliminierungsreaktionen bestimmt waren, war die erfolgreiche Dekonstruktion von Lignin vor allem eine Funktion der Hydrogenolyse der Etherbindungen im Lignin Polymer.

Chapter I.

Introduction

1. General background

Throughout history, biomass has been the primary energy source driving the development of human kind.^[1] However, the use of fossil fuels as energy carriers was prioritized during the era of industrialization, resulting in dwindling petroleum resources and increasing environmental concerns on anthropogenic carbon footprint.^[2, 3] Hence, substantial efforts to explore alternative resources, such as renewables, are crucial to satisfy both, the increasing energy demand and the reduction of greenhouse gas emissions.^[4, 5]

In the beginning of the 21th century, the global primary energy consumption has been diversified from fuels to petroleum (36 %), coal (18 %), natural gas (27 %), nuclear (8 %), and renewables including biofuels (9 %).^[6] In addition, renewables includes hydro, wind, solar energy as well as fuels from biomass and wastes. The International Energy Agency is forecasting a rise of primary energy consumption within the next 25 years, with an increase on non-hydro renewables.^[6] Nowadays, the political and social onus drives research and development of processes towards efficient conversion of biomass to produce liquid transportation fuels and/or chemicals. The European and American governments have established the goal to obtain 20% of liquid fuels from biomass by 2020 and 2030, respectively.^[7, 8] From the future perspective of energy generation and consumption, biomass should not be replaced for fossil resources, rather it must be (re)considered as a chemical and energy source, which can diversify the energy and power supply possibilities.

The main classes of biomass for fuel production are lignocellulose, starch (including polysaccharides) and oils (such as triglycerides). The itemized categorization of biogenic feedstock types is compiled in Table 1-1. Currently, to process the first generation feedstocks, integrated biomass related refineries conceptually comprise the following main sectors: feedstock harvest and storage, pretreatment, enzymatic hydrolysis, carbohydrates fermentation to ethanol and rapeseeds transesterification to fatty acid methyl esters (FAME), also known as biodiesel.^[9-11] These first generation biofuels experienced several drawbacks, such as limited availability (food versus fuel) and negative impact on agriculture.^[12, 13] Among the variety of biomass resources, plant and

wood related lignocellulosic matters are the most abundant nonedible biomass and are considered as potential feedstocks for production of second generation biofuels.^[14-17]

Table 1-1. Summary of feedstock generation types for the production of biofuels.^[18]

Feedstock type	Classification	Source
First generation	Food (energy) crops	Rapeseed, soybeans, sunflower, canola, camelina, palm fruits, wheat, corn, maize, seeds.
	Agricultural residues	Terrestrial materials such as straw, grass, leaves, willow, corn stover, rice husks.
Second generation	Forest residues	Lignocellulosic materials like wood chippings, branches, foliage, roots, straw etc.
	Animal and oil wastes	Animal manure, wastes of fish oils, vegetable oil, etc.
	Biowastes streams	Wastes of any kind, such as solid municipal, liquid industrial, packaging and wood wastes
Third generation	Microalgae	Botryococcus, Chlamydomonas, chlorella, spriulina, etc.
	Macroalgae (macrophytes or seaweeds)	Cladophora, Hydrodictyon, Caulerpa, Spirogyra, etc.

Additionally to the prospective goals mentioned above, the U.S. Energy Security and Independence Act of 2007 anticipates the development of 79 billion liters of second-generation biofuels on an annual basis to be reached by 2022.^[19] To achieve such ambitious aims, novel processes for the generation of high energy density biofuels from nonedible feeds have been initiated and are currently under investigation among various research groups worldwide. In this context, heterogeneous catalysis provides an opportunity to fulfil the promises of biofuels and improve the sustainability of current processes. In this thesis, dual-functional catalysts comprising metallic Ni and acidic supports, such as zeolites and sulfonated carbons, are synthesized and thoroughly

explored in the transformation of second generation biomass feedstocks, in particular, lignin and its model compounds. The strategical research approaches to convert woody biomass will be discussed later in this work, the following section deals with the nature and characteristics of terrestrial wooden biomass.

2. Terrestrial wooden biomass

Woody biomass is made of cellular and fibrous tissue present in the stock of trees.^[20] The cell walls of the terrestrial plants are constructed by the so called *lignin-carbohydrate complexes* (LCC).^[21] Figure 1-1 shows the LCC networks forming micro-fibrils of covalently cross-linked lignin and polysaccharides in wood.^[21] Cellulose (40 - 50 %) is bounded by a matrix of the hemicelluloses xylan and glucomannan (15 – 25 %), and lignin (15 - 25 %).^[22] The lignin is interconnecting the three polysaccharides to construct a rigid network. The three-dimensional lignin polymers consist of the three different phenylpropane also referred as monolignols, *para*-coumaryl alcohol, coniferyl alcohol, and sinapyl alcohol, substituted with zero, one, or two methoxy groups.^[23, 24] Through biological controlled condensation and radical polymerization reactions the monolignols are combined to the heterogeneous amorphous lignin polymers, where the primary structure is non-unified within the different types of wood.^[25] The lignin biosynthesis routes are described in literature in detail and are beyond the scope of this thesis.^[9, 21, 25]

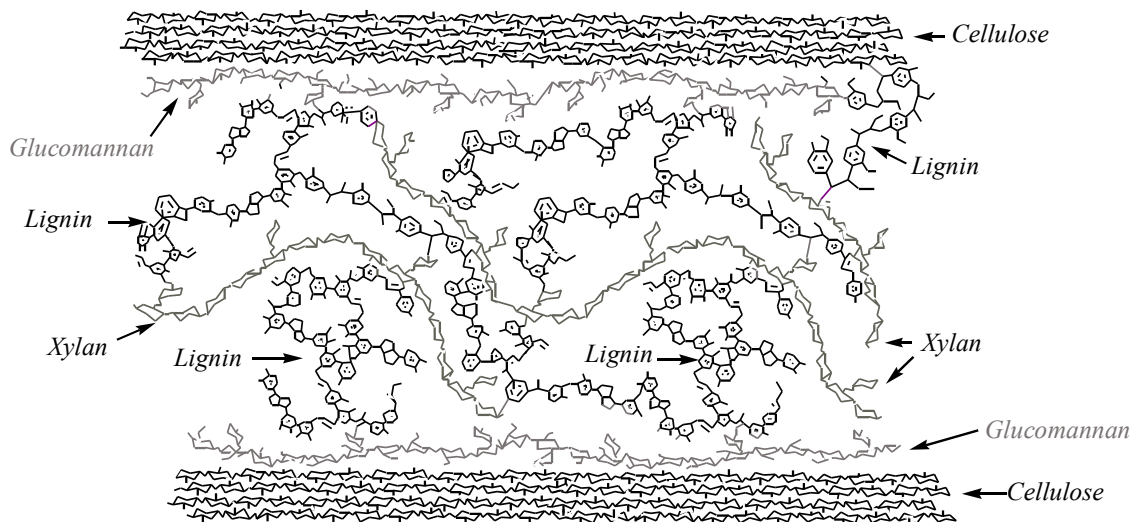


Figure 1-1. Lignin carbohydrate complex: Hypothetical arrangement of lignin and polysaccharides in wood.^[21]

Lignin, a random phenylpropane network of ethers and C-C bonds, exhibits distinct physiochemical properties within the LCC network. Lignin is amorphous because of its branched, racemic structure, with the importance of the biological function as a filling agent, encrusting the cellulosic micro-fibrils.^[26] Lignin has higher energy contents among the lignocellulose materials, due to the fact that the carbons in lignin are the most reduced

one compared to its accompanied polysaccharides. Beyond providing mechanical rigidity to a plant, lignin enables water transport due to its aromatic and relatively hydrophobic character, allowing vascular plants to grow into trees.^[27, 28] While lignocellulose is abundant, the major problem associated with its utilization is the complexity of its chemical structure, which is dependent on the lignin source, i.e. hardwood, softwood and its natural environment.^[29] A possible structure of lignin is represented in the Figure 1-2, where the interconnected C₉ monolignols are highlighted in color.^[29] Through the random insertion of the monolignols to the growing polymer chain, the lignin polymer is constructed by a variety of ether and C-C bonds linkages. The most common linkages are α -O-4, β -O-4, 4-O-5, β - β , 5-5', whose structures and occurrence in lignins are summarized in Table 1-2.

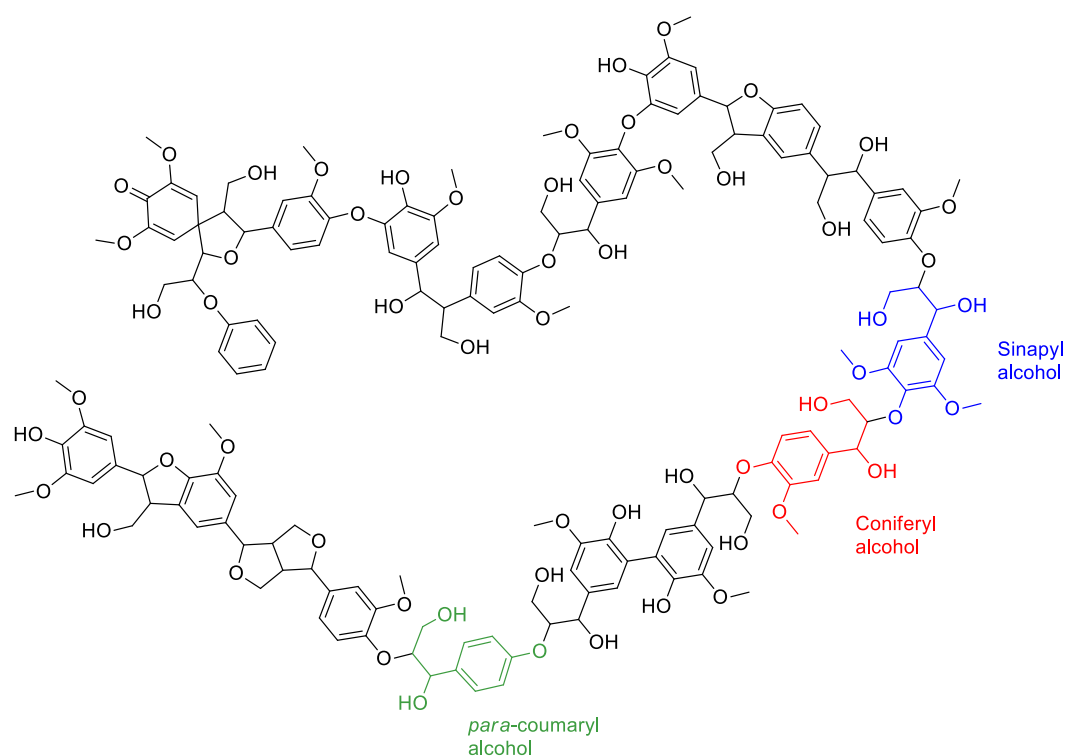
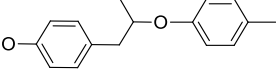
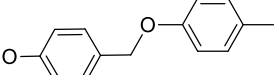
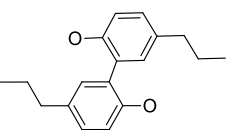
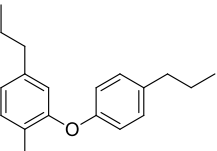
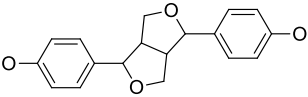
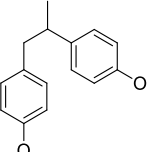
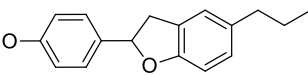


Figure 1-2. The theoretical structure of lignin is demonstrated schematically with the monomers, para-coumaryl, coniferyl and sinapyl alcohol highlighted in color.^[29]

While today lignin is predominantly burned for heat generation, its alternative applications comprehend the use as dispersant in cements^[30], thermoplastic elastomers^[31], polymeric foams and membranes^[9, 16]. The aromatic nature of lignin exhibits high potential as an important source for chemicals and fuels. Several strategies have been indorsed and developed for the lignin depolymerization and upgrading, including thermochemical treatments and homogeneous and heterogeneous catalysis. The perspective methods of carbon effective transformations of lignocellulose are discussed in the following section.

Table 1-2. Overview over most frequent bond types in lignins

Lignin linkage		Frequency (100 / C ₉ units) ^a		
Name	Structure	Nimz ^[32]	Sjöström ^[33]	Erickson and Miksche ^[34]
β-O-4		65	49 - 51	40 - 50
α-O-4				6 - 8
5-5		2	9	13
4-O-5		2	3	4
β-β		6	3	2
β-1		15	1-3	2
β-5		6	10-12	9-15

^a The sum of all the linkages does not add up to 100, as only the major representative model linkages were depicted.

3. Lignocellulosic biomass valorization

The valorization of lignocellulosic matter to chemicals and fuels can be divided into three conceptually different approaches (Figure 1-3).^[1] The first approach is the gasification of wood to produce syngas (CO + H₂), which then can be converted to Fischer-Tropsch synthetic fuels or *via* the Water-Gas Shift reaction to hydrogen. The second possibility to utilize woody biomass is its fast pyrolysis, where the feed is exposed to high temperatures (> 700 K) for a very short residence time (in the range of seconds). Under these conditions the lignocellulose matter converts to bio-oil containing an organic phase with hundreds of different organic compounds, such as phenols, ketones, aldehydes and furans, as well as an aqueous phase with up to 30 wt.% and inorganic residues of mineral ash.^[35] Through the pyrolysis step the energy density is increased by 10 to 12 times to 16-19 MJ/kg.^[36, 37]

The high reactivity, the corrosiveness and instability of the bio-oil requires further catalytic upgrading, for instance hydrotreating, cracking or hydrodeoxygenation.

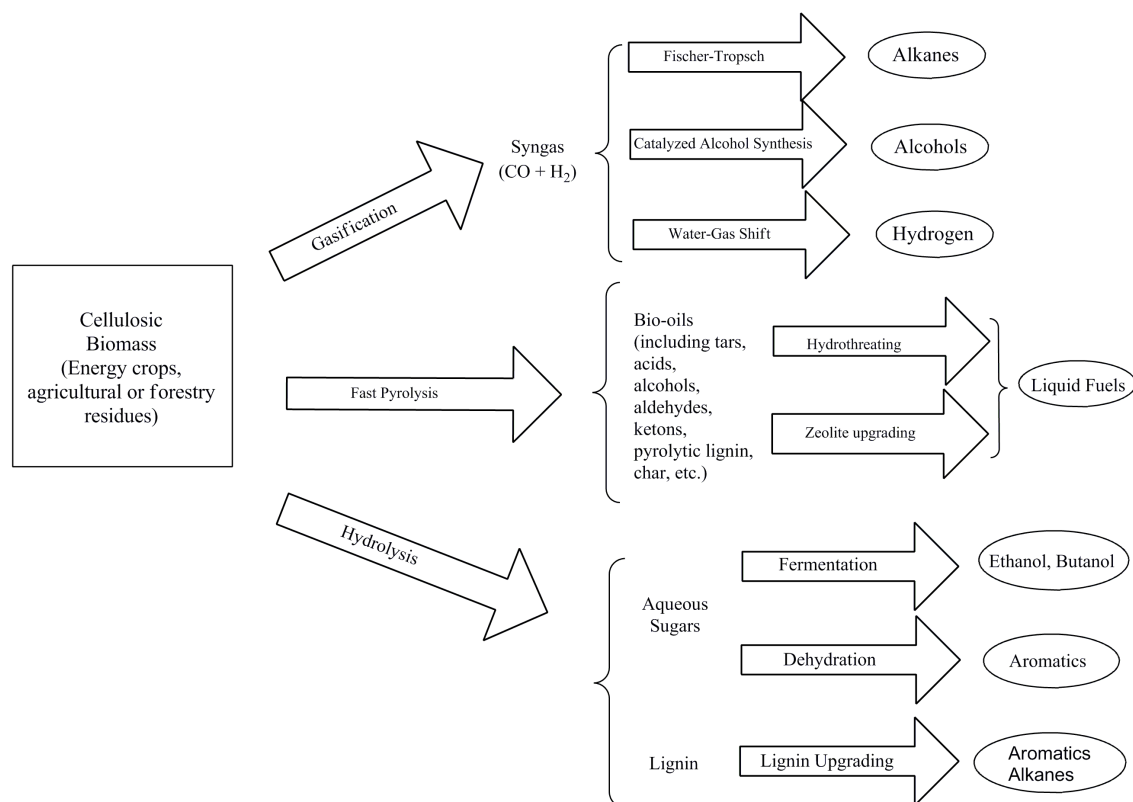


Figure 1-3. Overview of pathways for lignocellulosic biomass conversion to liquid fuels.^[1]

The third approach follows recovery of lignin from the cellulosic matrix prior its utilization, as the lignin is “locked” in the cellulose network. The paper pulping industry is mainly driven through Kraft and Sulfite processes, where the lignin is accumulated as a side product of cellulose production. However, the biggest disadvantage of both processes is that the recovered lignins contain a substantial amount of sulfur, which negatively influences its further valorization. In 1988, the Alcell™ process was established to isolate sulfur-free lignins by cooking the wood chips in an ethanol/water mixture (50/50 wt. %) at 473 K and 35 bars.^[38] When woody biomass is thermally treated in aqueous alcoholic solutions, (hemi)cellulose is subjected to deacetylation at 473 K resulting to *in situ* generated acetic acid, which then catalyzes the hydrolysis of covalent bonds within the lignocellulose matrix.^[39] Thus, the resulting dissolved Lignin can be separated from the cellulosic material and is precipitated to form a brownish powder. The so called Organsolv Lignin exhibits favorable properties, such as high functionality providing solubility for many organic solvents, with a less condensed structure than pulp lignins and low average molecular weights, which ideally suits its further utilization towards high-value chemicals and transportation fuels.^[40]

Based on these routes the concept of a biorefinery can be built on two different objectives to develop different product pools. The “sugar feed” can be used by chemical and biological processes, such as aqueous phase reforming, dehydration or fermentation to produce alcohols, chemicals and hydrogen. The “lignin feed” aims thermochemical conversions to intermediates such as pyrolyzed bio-oil and syngas, which can either substitute conventional commodities or further upgraded towards liquid transportation fuels. The two “platforms” based on thermochemical and biological conversion methods, differ in the scale of each unit. The biological processes, such as the fermentation of cellulose, are not profitable at small scale; thus this approach requires long residence times and need to be scaled extensively. Thermochemical processes involve reactions with short contact times with relatively small reactors, therefore the scaling is straightforward. Ergo, the thermochemical methods are advantageous at higher weight hourly space velocity for small-scale biomass processing. Further in this context, the strategies to process lignin are going to be discussed.

4. Lignin deconstruction strategies

Current established strategies and recent protocols take into account two main concerns for the intention of deconstructing lignins in the liquid phase; improving the activity and stability of catalysts under the selected reaction conditions and more critical, suppressing repolymerization and self-condensation reactions of reacted lignins, which results to a complicated pool of re-condensed aromatics.^[41, 42] Generally, there are three different deconstruction strategies for lignin utilization: (1) Base-catalyzed deconstruction, (2) oxidative degradation and (3) catalytic pyrolysis. Each representative product pool is summarized in Figure 1-4 and the involved catalytic processes are discussed in detail further in this section.

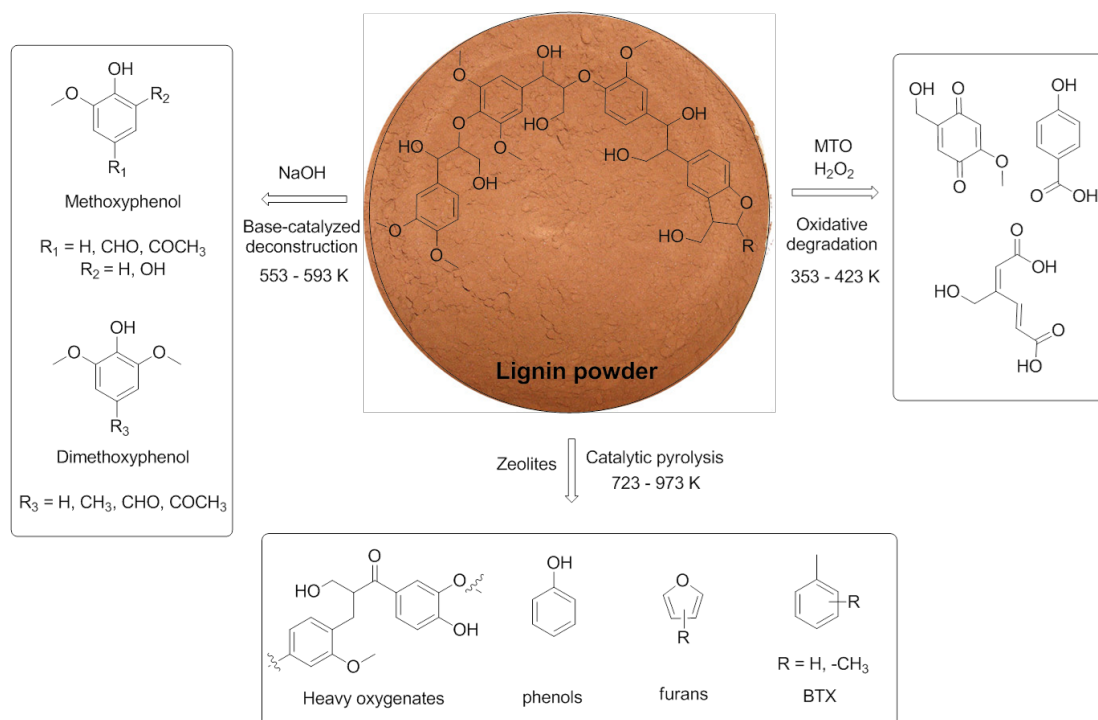


Figure 1-4. Overview on the lignin depolymerization strategies in the liquid phase.

4.1 The base-catalyzed depolymerization of lignin

The base-catalyzed depolymerization (BCD) of lignin involves a strong homogeneous base, such as sodium hydroxide, in aqueous phase at the temperatures of 513 – 613 K and pressures up to 25 MPa. At short residence times (within minutes) BCD achieves maximum yields of 20 -23 wt.% aromatic phenols, such as syringols, guaiacol, o-methoxy catechol and vanillin.^[43, 44] The proposed reaction mechanism of β -O-4 ether bond proceeds heterolytically *via* a six-membered transition state involving both the sodium cation and the hydroxide ion. The sodium cations form cation adducts with lignin and additionally polarize the ether bonds.^[45] Concurrent to heterolytic cleavage of the β -O-4 ether bond, dealkylation of the periphery and hydrolysis of methoxy groups attached to the lignols appear and prevail at higher severity. However, the obtained yields are limited due to recombination of the highly reactive lignin cleavage products. V.M. Roberts *et al.* added boric acid to the aqueous sodium hydroxide reaction mixture, resulting to increased yields for up to 42 wt. % phenolic products.^[45] The boric acid acted as a capping or coordinating agent for the generated phenols, preventing the repolymerization and self-condensation reactions.^[45] Due to the severe reaction conditions (> 600 K) and pressure requirements (> 20 MPa) of the BCD reaction, the formation of byproducts cannot be constrained, thus the resulting product mixture is difficult to purify.^[46]

4.2 Oxidative depolymerization of lignin

The catalytic oxidation is an inspiring possibility to degrade lignin due to its high oxy-functionality. The initiation for research on oxidative catalysts was stimulated by examples of efficient systems found in nature. Homogeneous catalysts, such as metalloporphyrin complexes, emerged from the desire to imitate the heme factor discovered as the active site of enzymes lignin peroxidase, which is located in white rot fungi.^[29, 47] The fungi are able to biodecompose (rotten) lignin into carbon dioxide and water, with high preference for the recalcitrant lignin above cellulose and other polysaccharides in wood.^[47] In early studies several investigators observed that iron porphyrin catalysts are capable to cleave the C α -C β bonds and oxidize lignin model compounds similar to the ligninase enzymes.^[48] Later on, several metal porphyrin catalysts were synthesized for lignin oxidation, especially the integration of a variety of ring substituents, axial ligands and other substituents, such as fluoro and sulfonato groups improved catalytic activity.^[49, 50] Regardless of the capability for lignin oxidation, the establishment of metalloporphyrins on an industrial scale is the biggest issue due to the costly complexes, particularly caused by catalyst degradation.^[29]

Another homogenous catalyst system based on methyl rhenium trioxide (MTO) was discovered to oxidize phenolic, monomeric and dimeric lignin model compounds from kraft pulp and sugar cane lignin.^[51] Herrmann and coworkers found that additional H₂O₂ enabled the methyl rhenium dioxide to cleave the C=C double bond.^[52]

The oxidative depolymerization approach is advantageous for the production of structurally-maintained oxophenols as well as acyclic organic acids. Regardless of the very recent reported articles^[53, 54], remarkable efforts need to be directed to further improve the product yields, the recombination and reasonable product separation.

4.3 Catalytic pyrolysis of lignin

Thermal pyrolysis of biomass, especially lignocellulose, was already mentioned in the previous section 1.3. As the pyrolysis facilitates the breaking of carbon-carbon bonds, it can be catalyzed by solid acids, e.g., zeolites, which are well known as catalysts in oil refineries for fluid catalytic cracking. Herein, the catalytic approach of thermal pyrolysis of lignins is introduced as developing process, converting lignin into solid, liquid and gaseous products. The reactions of lignin pyrolysis in the presence of H-ZSM-5 zeolite involve deoxygenation, decarboxylation, decarbonylation, alkylation, isomerization, oligomerization and aromatization *via* the carbenium-ion mechanism.^[55] Also, tar and coke are formed as undesired products. The presence of a catalyst results in a serious change in the bio-oil composition after such pyrolytic treatment. The pyrolytic (non-catalytic) bio-oil consist of an aqueous phase (up to 40 wt.%), the organic phase with phenols, carbonyls,

furans, acids (15 wt.%) and mostly heavy oxygenates (25 wt.%) and unidentified complex compounds (20 wt.%).^[56] When zeolite catalysts were applied to the lignin catalytic pyrolysis, the concentration of the phenols within the organic fraction doubles up to 30 wt.%, at the same time the fraction of heavy and unidentified compounds was tremendously reduced.^[57] Zeolite catalysts seem to be very active for this process since they crack the heavy compounds and yield oil with higher value.^[55, 57, 58]

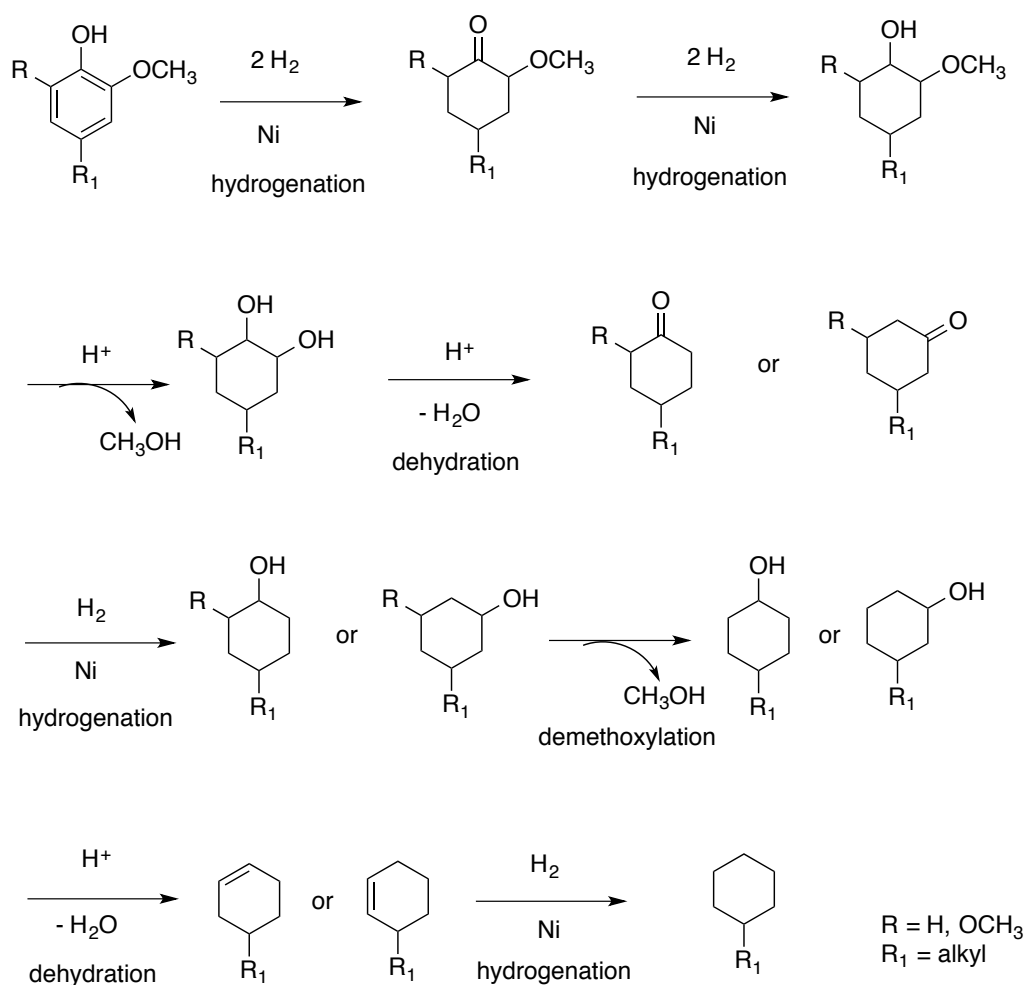
Current research aims at the one-stage conversion of lignins to produce either value-added chemicals or liquid transportation fuels. Recent studies performed on model compounds provided essential key findings to enable the catalytic conversion of the “lignin feeds”.^[41, 45, 59-63] Therefore, the following section is addressed to the catalytic upgrading of lignin on transition metal catalysts: (1) Hydrodeoxygenation of bio-oil containing monomeric lignin model compounds, (2) selective cleavage of dimeric model aryl alkyl ethers on Ni catalysts and (3) the ultimate approach to convert real lignin feeds on transition metals in the liquid phase.

5. Transition metal catalyzed lignin upgrading

5.1 Hydrodeoxygenation of liquid bio-oil

Hydrodeoxygenation (HDO) raised attention in the early 1980ies when tar-sand and oil shale liquids became additional feed stocks, which contained more oxygen than traditional petroleum feeds. Upon catalytic hydrotreatment of the mineral oils HDO take place concurrent with hydrodesulfurization (HDS) and hydrodenitrogenation (HDN) on Al_2O_3 supported CoMo and NiMo sulfides.^[64-66] However, the sulfided catalyst are not stable in the HDO as the high oxygen amount and the presence of water in the bio-oil cause rapid catalyst deactivation and the continuous supply of H_2S leads to sulfur contamination of the sulfur-free bio-derived feeds.^[67] Therefore, sulfur-free noble (Pt, Pd, Rh and Ru) and base (Ni, Co, Fe, W and Mo) transition metal catalysts have been explored for the hydrodeoxygenation processes in liquid phase.^[68-72] These catalysts can perform the HDO reaction in the presence of water exhibiting higher hydrogenation reactivity at less severe reaction conditions than sulfided catalysts.^[73, 74]

Research on HDO of lignin derived bio-oil was also performed also on lignin characteristic model compounds, such as guaiacol, anisole and syringol.^[68, 75-79] The reaction network of the methoxy substituted phenols is more complicated compared to phenol, which involves hydrogenolysis, transalkylation and hydrogenation. An overview on the individual steps of the guaiacol and syringol hydrodeoxygenation is shown in Scheme 1-1.



Scheme 1-1. Elementary steps of the guaiacol (R = H) respectively syringol (R = OCH₃) hydrodeoxygenation on dual-functional catalysts, such as Ni/HZSM-5, in aqueous phase.^[75]

Zhao, Lercher *et al.* investigated HDO of phenols using various transition metals (Pd, Pt, Rh, Ni) and acidic supports (Nafion, HZSM-5 and HBEA) at relatively mild conditions (473 – 523 K, 2 – 5 MPa H₂) in aqueous and non-polar phases.^[75, 79-83] The methodical approach to hydrodeoxygenate phenol was to use dual functional catalysts comprising a metal function for hydrogenation supported on an acidic support. The support plays a crucial role, as the proton catalyzed dehydration, hydrolysis and isomerization reactions on zeolitic supports are two orders of magnitude faster than catalyzed by a mineral acid, such as phosphoric or sulfuric acid.^[75, 80] The systematical design of bifunctional and bimetallic catalysts directed the research towards the possibility of efficient methods of lignin conversion in the liquid phase.^[84-86] Current and perspective strategies for lignin deconstruction in condensed phases will be reviewed in the following section.

5.2 Ni catalyzed reactions of lignin model compounds in liquid phase

The recent reports on the development of heterogeneous catalysts for hydrodeoxygenation subsequently continued to investigate the approach of lignin deconstruction on di- and oligomeric model linkages, such as presented in Table 1-2. For instance, the pioneering studies from Sergeev and Hartwig demonstrated a homogenous Ni catalysts, i.e. Ni(COD), to selectively catalyze the hydrogenolysis of alkyl aryl and diaryl ethers of dimeric model compounds.^[87] Later on, they improved the system by adding ^tBuONa to the Ni catalyst, which enhanced selective hydrogenolysis of aryl ether lignin linkages without further hydrogenating the arene ring in *m*-xylene as solvent.^[88]

With this background, the heterogeneous approach of metal-catalyzed hydrogenolytic C-O bond cleavage in aryl alkyl ethers of lignin model compounds in liquid phase have been addressed in the group of Lercher.^[79, 89, 90] Especially the base and relatively cheap Ni metal already showed its good catalytic activity for the selective cleavage of dimeric lignin model compounds at 373 K and 0.6 MPa H₂.^[89] The strategy to deconstruct lignin on Ni catalysts is shown in

Figure 1-5. In these studies, He *et al.* investigated the mechanism for catalytic cleavage of C-O bonds on the representative dimers of lignin molecule, namely α -O-4 (benzyl phenyl ether), β -O-4 (2-phenylethyl phenyl ether) and 4-O-5 linkage (biphenyl ether) over Ni and acid catalysts (H₂SO₄, H₃PO₄ and HZSM-5).^[91]

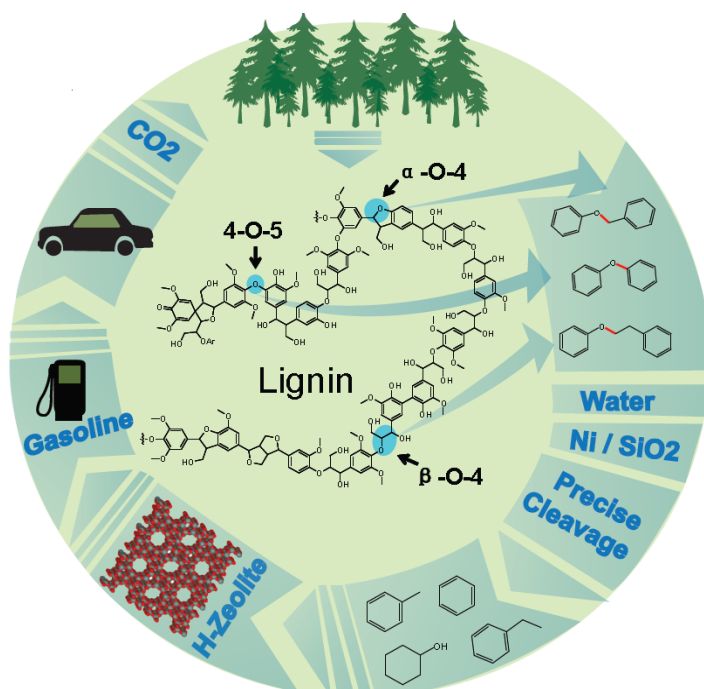


Figure 1-5. The strategy to convert lignin model compounds on Ni based catalysts.^[91]

It was found that hydrogenolysis on Ni is the main reaction pathway for the scission of alkyl aryl ethers, whereas the aryl aryl ethers are cleaved through concurrent

hydrogenolysis (major route) and hydrolysis (minor) pathways on Ni/SiO₂ catalysts in aqueous phase.^[90] Further the substitution (-H, -CH₃, -OH) of the dimeric compounds in the *para*-position significantly influences the rates of the reaction pathways of C-O cleavage over Ni catalysts.^[91] These findings are fundamentals towards heterogeneous catalyzed processes of real lignin feeds, which will be the topic in the section below.

5.3 Heterogeneous catalyzed valorization of real lignin feeds

Heterogeneously catalyzed lignin deconstruction has progressed as promising depolymerization strategy despite of the mass transfer limitations between the voluminous lignin polymer and the catalyst surface.^[29, 41] Many of the published studies with heterogeneous catalysts, such as supported metal transition catalysts, probe the hydrogenolytic cleavage of lignins on dimeric model compounds and lignin fragments through applying moderate to high pressure molecular hydrogen.

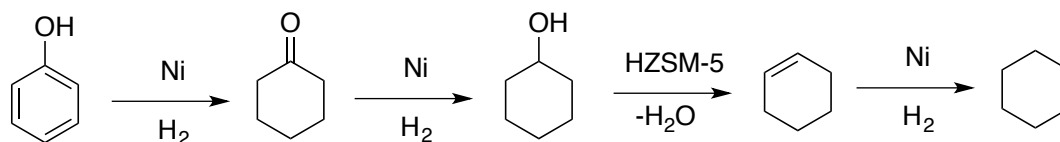
Harris and coworkers have reported catalytic reaction of hardwood lignin with hydrogen over copper-chromium oxide as early as 1938, where the rather severe hydrogenation conditions led to full reduction of the aromatics to obtain mainly monomeric substituted cyclohexanols and methanol.^[92] Pepper *et al.* studied the hydrotreatment of softwood lignin (e.g. spruce wood) with a series of catalysts, such as Raney Ni, Pd/C, Rh/C, Rh/Al₂O₃, Ru/C, Ru/Al₂O₃.^[93-96] The resulting product mixture was rich on monomeric products 4-propylguaiacol and dihydroconiferyl alcohol under moderate conditions (468 K, 3.4 MPa). The catalytic treatment of hardwood lignin (e.g. aspen wood), with Rh/C catalysts produced 40 wt. % of syringyl and guaiacyl compounds with a propyl or propanol side chain.^[94] Further research developed Ni-derived catalysts, NiMoP/γ-Al₂O₃ materials to break down lignin into monomeric units at high temperatures of 593 – 653 K and 4 – 7 MPa hydrogen pressure. The presented system yielded products in three separated phases. The aqueous phase comprised deoxygenation and dehydration products with little amount of phenols, the organic phase contained alkyl substituted aromatic compounds and gaseous compounds were carbon dioxide and carbon monoxide from lignin decarboxylation reactions.^[97] Another study showed that a Pd/C catalyst was able to perform hydrogenolysis of isolated lignin to yield monolignols (dihydroguaiacol, 4-propylguaiacol), dimers and oligomers (β-5, 5-5, 4-O-5, and β-1 types) at relatively mild reaction conditions (473 K, 3.5 MPa H₂).^[98] Recently, BASF has patented the application of transition-metal carbides catalysts, such as tungsten carbide, for the single stage hydrogenation of lignin under comparable conditions (403 – 464 K, 7 – 14 MPa H₂).^[99] This type of catalysts yielded mainly a mixture of low molecular weight oligomers, comprising dimers and trimers of coniferyl and coumaryl alcohols.^[99]

In the light of both, the deconstruction of real lignin feeds and hydrodeoxygenation of phenols for bio-oil upgrading, stable heterogeneous metal nanoparticles need to be addressed to enable efficient transformation of woody biomass towards value-added chemicals and liquid transportation fuels. The development and synthesis approaches of transition metals supported on acidic supports, such as zeolites and functionalized carbons for catalytic conversion of lignin (derived) feeds will be addressed in the following section.

6. Dual-functional catalysts for liquid phase upgrading

In the previous sections, we have shown that the strategy to utilize oxo-functionalized lignin-type biomass molecules involve multistep processes. Therefore the catalytic materials are required to perform cascade reactions without the need of intermediate separation and purification. This approach includes the use of tailor-made multifunctional catalysts by combining functions of distinct active sites.^[100] Developments of multifunctional catalyst for the selective conversion of biogenic platform molecules have been extensively researched.^[101-104] Inclusion of metal nanoparticles into solid acids facilitates the synthesis of catalysts that integrate the hydrogenation-dehydrogenation abilities of a metal and carbocation rearrangement activities of Brønsted or Lewis acid sites. Further recent studies also deal with a combination of bi- and trimetallic active sites, which are shown to be advantageous for catalytic efficiency in terms of activity, selectivity and stability^[85, 86], but this is beyond the scope of this thesis.

In previous studies, Zhao, Lercher *et al.* have developed a series of dual-functional (metal-acid) catalysts that are able to convert biogenic molecules, such as triglycerides and phenolic compounds, in one-pot processes. [62, 75, 79-81, 83, 89, 90, 105-107] This strategy aims at the selective oxygen removal through acid catalyzed reactions including dehydration, hydrolysis, in sequence with metal catalyzed reaction steps, such as hydrogenation, hydrogenolysis and decarbonylation. The dedicated studied reaction sequences of hydrogenation-dehydration-hydrogenation are elucidated through the aqueous hydrodeoxygenation of the simple model compound phenol over Ni/HZSM-5 catalyst.^[108] The hydrodeoxygenation reaction mechanism suggested by Zhao *et al.* is shown in Scheme 1-2 and is described as following steps: (1) the aromatic ring of phenol is saturated to yield cyclohexanone, (2) cyclohexanone is further hydrogenated to cyclohexanol, (3) the hydroxy group of cyclohexanol is eliminated through catalyzed dehydration reaction and (4) the C=C double bond is conclusively hydrogenated to cyclohexane.^[108]



Scheme 1-2. Reaction pathway for phenol hydrodeoxygenation over Ni/HZSM-5 catalyst in the aqueous phase.^[108]

6.1 Synthesis of Ni/zeolite bifunctional catalysts

The revival of supported nickel catalysts initiated through the rising importance to efficiently catalyze the upgrading of lignocellulosic feedstocks.^[88, 89, 109-111] The preparation of base transition Ni catalysts is more demanding comparable to the noble Pd- or Pt-catalysts, because nano-sized uniform particle sizes are essential to optimize their catalytic hydrogenation activity.^[112]

One possibility to incorporate Ni in-/onto zeolitic supports is the (incipient) wetness impregnation. In a typical synthesis, the solid support with defined pore volume is impregnated thoroughly with an aqueous or methanol solution of metal salts (e.g., nickel nitrate, nickel acetyl acetate), where the Ni(II) phase retained on the support surface, driven by the capillary adsorption. The catalyst precursor is then dried prior to its calcination in air, where the Ni(II) oxides are formed and subsequently reduced with H₂ at high temperatures. Through the calcination step the formed Nickel oxide ions are partially forming a 'surface spinel' species with the zeolitic lattice. A substantial fraction of the Ni remains as oxide phase. Subsequent reduction at high temperatures (one third of the Tamman temperature of Ni) in H₂, the metallic Ni is formed. Metal/support interaction is inter-crystallite and presumably not so strong. The Ni particle size cannot be controlled throughout the synthesis method and thus, the particle sizes are widely distributed.^[113, 114]

As the zeolites can contain a wide variety of cations, such as Na⁺, K⁺, Ca²⁺, and Mg²⁺, which are exchangeable with mobile metal ions from an additional salt solution, the ion exchange method is a different synthesis method for supported metal catalyst. In comparison with impregnation, the ion exchange method results in more uniform and relatively smaller metal particles due to the strong interactions of metal cations with partially negative charged oxygen of the supporting zeolites, which simulates the formation of a coordinative bond.^[115] The downside of this synthesis method is the low exchange capacity of the zeolite material, resulting to limited metal loading of a few weight percent.

With these limitations, Geus et al. have developed the method of deposition-precipitation (DP) to achieve high Ni dispersion accompanying relatively great loadings.^[116, 117] Upon the synthesis, the zeolite supports are suspended in an aqueous solution. Urea (CO(NH₂)₂) containing solution of nickel salts was added to the zeolite suspension to

initiate the precipitation of nickel ions through basification of the reaction mixture. The hydroxide ions are evenly generated through urea hydrolysis at elevated temperatures, such that local super-saturation upon precipitation of Ni hydroxide is avoided. The DP method benefits in the generation of high attainable Ni loadings, where the particles show a narrow and uniform nano-sized distribution (Figure 1-7). Although the synthetic approach of DP proceeds through same calcination and reduction steps, the resulting Ni nanoparticles show higher resistance to sintering than the above mentioned methods.^[118-120]

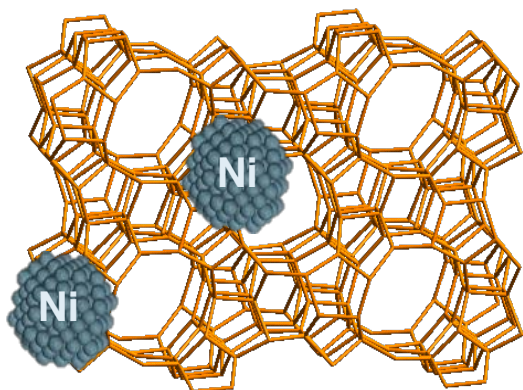


Figure 1-6. Schematic exemplification of Ni incorporated on and in zeolite support^[100]

6.2 Development of carbon supported Ni nanoparticles

Beyond the zeolitic supports, carbon materials play an important role as a catalyst or catalyst support for chemical transformation reactions, especially in the context of biomass conversion.^[121] Advantageously, carbon can be synthesized from residual biomass, with the possibility of pre- and post- chemical and physical treatments to tailor-designed material with high specific surface area, high porosity and various pore size distribution material.^[122] Additionally, the carbon can be functionalized chemically, where the oxygen bearing group is either an active site, such as $-\text{SO}_3\text{H}$, $-\text{COOH}$ groups, or the anchor for metal particles incorporation.^[123-125] Essential properties of carbon support in catalytic applications are: (1) resistance to acidic or basic reaction environment, (2) amphoteric nature due to functional oxygenated groups, which also enhance metal adsorption and catalyst dispersion, and (3) structural integrity at high temperatures ($> 700\text{ K}$, except in the presence of oxygen $> 500\text{ K}$).^[121]

Thermal carbonization of biogenic resources, such as carbohydrates, is performed at $473 - 573\text{ K}$, and further chemical functionalization of the resulting carbon proceeds through sulfuric acid refluxing to generate the active sulfonic functional groups, the so-called “sugar catalysts”.^[126-128] Carbon (supported) catalysts can promote diverse reactions for the catalytic conversion of biomass feedstocks into chemicals.^[123]

As already mentioned in the previous section, multifunctional catalysts are synthesized to catalyze more than one type of reactions. In this particular case, the strategy for highly efficient production of biofuels is to synthesize Ni/C-SO₃H catalysts (Figure 1-7) to perform dehydration reactions on acid groups of carbon support, and hydrogenation on metal nanoparticle being deposited on functionalized carbon material. The synthetic approach to achieve such dual function carbon supported Ni catalyst is not straightforward as the methods described for zeolite based catalysts include thermal treatments at high temperatures. The carbon materials cannot be calcined in air and the oxygen functionalities would decompose through the temperature programmed reduction in H₂. Therefore, the approach to synthesize metallic nanoparticles supported on SO₃H bearing carbon was performed in liquid phase. The Ni(II) precursor can be reduced in presence of strong reducing agents such as borohydride based chemicals in solution.^[129, 130] The method of fabricating nanoparticles aims at first the coordination of Nickel(II) acetyl acetonate in the presence of oleyl amine and oleic acid as surfactants that strongly bind to Ni, and second at reduction with a borane trialkylamine complex in solution.^[131]

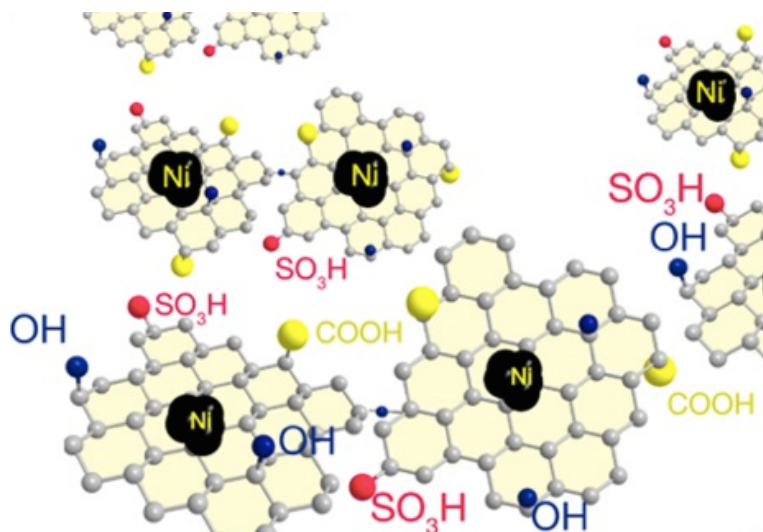


Figure 1-7. Schematic representation of sulfonated carbons supporting Ni NPs.

This synthetic approach to incorporate Ni NPs – referred to grafting – can also be applied on zeolitic supports with the limitation of lower Ni coverages compared to the deposition precipitation method.^[132, 133] With the uniform and well dispersed Ni catalysts the exploration of Ni NPs properties can be further investigated upon hydrodeoxygenation phenolic molecules in aqueous or generally liquid phase.

Throughout this thesis, the aqueous and liquid phase biomass conversion will be probed with dual-functional Ni based catalysts through kinetic and spectroscopic investigations. The kinetic studies are fundamental for the development of an analytical approach based on Internal Reflection Infrared Spectroscopy. In this context, the infrared (IR) spectroscopy

technique based on attenuated total reflection (ATR) will be applied to (1) elucidate the catalytic pathways of simple model compounds and (2) to track the deconstruction of real lignin feeds in condensed phases. The next section is dedicated to the IR spectroscopy and the methodical approach to explore the transformation of molecules as they react upon catalytic transformation spectroscopically.

7. Probing into liquid phase biomass conversion

7.1 Vibrational Spectroscopy Methods applied in Catalysis

Vibrational spectroscopy is by far the most popular technique to probe the interaction of reactants and intermediates with catalyst surfaces. In the 1950s Eischens and coworkers developed the characterization of heterogeneous catalysts by studying gas phase adsorption processes on supported metals *via* infrared (IR) spectroscopy^[134-136], outstanding developments have been accomplished on this field.^[137-139] State of art infrared spectroscopy (IRS) has been further advanced to four different modes for the interference of the IR beam with working catalysts, see Figure 1-8.^[140]

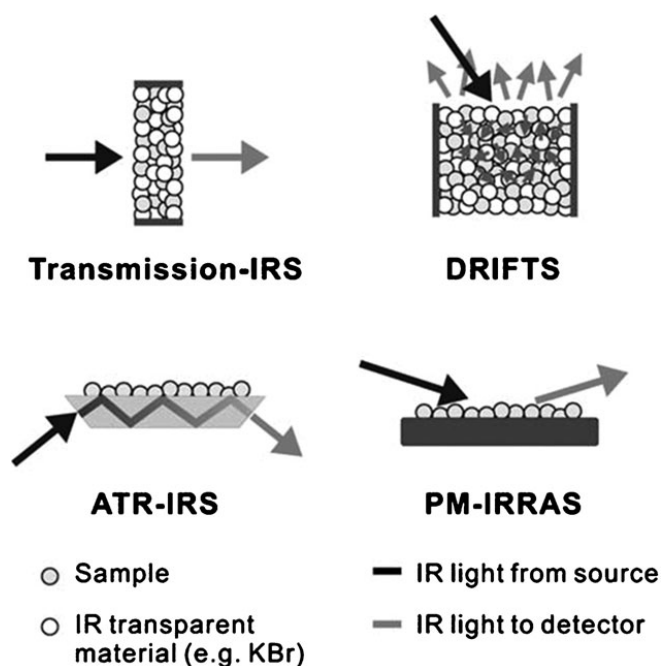


Figure 1-8. Graphic illustration of the four infrared spectroscopy (IRS) analysis modes: i) transmission-IRS, ii) diffuse reflectance infrared Fourier transformed spectroscopy (DRIFTS), iii) attenuated total reflection (ATR-IRS), and iv) polarization modulation infrared reflection absorption spectroscopy (PM-IRRAS), also referred as reflection-absorption RA-IRS.^[141]

The generated IR beam (with the intensity I_0) is penetrating the prepared sample (i.e. catalyst) and the transmitted beam (I_1), which is less energy intense for the individual vibration modes, is detected. The DRIFTS differentiates from transmission IRS through detection of the diffuse reflection of the IR light, which is generated through its interference

with the material. In the case of reflection-absorption IRS, the IR light is externally reflected on the surface of the sample under an effective incidence angle. Uniquely amongst these IRS methods, attenuated total reflection (ATR) relies on the phenomenon of internal reflection. The propagating IR beam undergoes multiple (total) reflexions within a transparent optical element, generating an evanescent wave at the interface to the rarer medium, i.e. the sample. After each reflection, the intensity of the IR wave gets attenuated upon the interaction of the evanescent field with the sample.

The investigation of heterogeneous catalysis occurring in liquid phase *via* infrared spectroscopy is a hurdle for monitoring the catalytic processes within the solid-liquid high-density phases.^[142] However, many chemical processes, such as the conversion of biomass, occur within heterogeneously catalyzed multi-phase systems, where transformation of compounds, such as lignins, fats and oils, and other intermediate products proceed on a solid-liquid-gas interface.^[109, 142, 143] Throughout the above described vibrational methods, the exclusive method capable of probing the solid-liquid reactions at high temperatures and pressures is the ATR-IRS.^[142, 144, 145] The basic principles of attenuated total reflection infrared spectroscopy are going to be introduced in the section below.

7.2 Fundamentals of ATR spectroscopy

The origin of internal reflection was already described by Newton^[146], but the fundamentals of ATR spectroscopy or internal reflection spectroscopy were established by Harrick and Fahrenfort in the early 1960s.^[147-149] The principle of ATR IRS is schematically shown in Figure 1-9, where a transparent optical element with a high refractive index n_c , also referred as internal reflection element (IRE), is in contact with an optically thinner medium, the sample, with refractive index n_s .^[145]

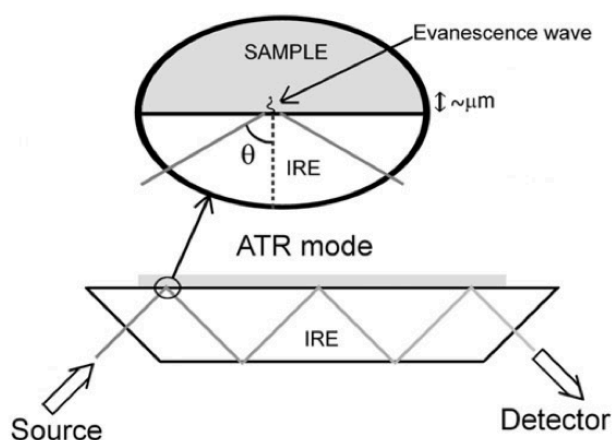


Figure 1-9. Principle of ATR-IR functioning at a solid-liquid interface with the IRE traversing the IR beam at the critical angle θ . The inset is describing the evanescent wave penetrating into the sample, which is the optically rarer medium.^[142]

When IR light traverses through the IRE at an angle of incidence (θ) larger than the critical angle (θ_c), given by equation 1, *total reflection* occurs at the interface.^[150]

$$\theta > \theta_{critical} = \sin^{-1}\left(\frac{n_s}{n_c}\right) = \sin^{-1}(n_{sc}) \quad (1)$$

Conclusively, under conditions of total internal reflection, an evanescent wave into the rarer medium (perpendicular to the crystal plane) is originated, which is an exponentially decaying field. (equation 2)^[150] This field in the rarer medium is named according the Latin origin, *evanescere*, meaning to disappear, vanish or fade away. Through the interaction of the evanescent wave and the sample, a fraction of the IR light is absorbed, thus the propagating IR beam becomes attenuated giving rise to a reflection spectrum, similar to an absorption spectrum.^[145]

$$E(z) = E_0 \exp\left(-\frac{z}{d_p}\right), \quad (2)$$

where E_0 and $E(z)$ are the electric field amplitudes at the frontier crystal-sample at a penetration distance z , where d_p is defined as penetration depth. The penetration depth is dependent on the specific wavelength λ , the angle of incidence θ , and the ratio of the refractive indices of sample and IRE (n_{sc}), designated by the equation 3.^[150]

$$d_p = \frac{\lambda}{2\pi (\sin^2(\theta) - n_{sc}^2)^{0.5}} \quad (3)$$

Harris correlated the penetration depth d_p to the effective thickness d_e , given by the equation 4, which is equivalent to the IR path yielding the same absorption as an ATR experiment compared to transmission or DRIFTS mode.^[140, 145]

$$d_e = \frac{n_{sc} E_0^2 d_p}{2 \cos \theta} \quad (4)$$

The equations 1 – 4 show that the penetrating evanescent wave is highly dependent on the refractive index of the sample medium and the specific wavenumber λ . For instance, if the sample is composed of diverse media, *e.g.*, deposited catalysts and solvent as well as adsorbed or dissolved molecules, the electric field does not decay evenly, and spectra acquired on a blank and on a catalyst-coated IRE will evidently diverge in intensity.^[151] To demonstrate the variation of the sample composition ($n_s = 1.5$ for toluene, $n_s = 1.7$ for γ - Al_2O_3 and n_s of 1.6 as a hypothetical value of its combination) on the measured intensity in an ATR experiment, the penetration depth, as well as the equivalent effective thickness were calculated for four individual wavelengths λ , shown in Table 1-3.

Table 1-3. ATR-IR penetration depth d_p and effective thickness d_e (μm) as a function of the wavelength λ and the refractive index of the sample n_s . For the angle of incidence and the refractive index of the IRE (Znse) values of 60° and 2.42 are defined, respectively. Critical angle θ_{critical} is calculated.

n_s	λ (cm^{-1})								θ_{critical}
	1000		2000		3000		4000		
	d_p	d_e	d_p	d_e	d_p	d_e	d_p	d_e	
1.5	1.11	1.53	0.55	0.77	0.37	0.52	0.28	0.38	38.7
1.6	1.2	1.91	0.6	0.96	0.4	0.64	0.3	0.48	41.8
1.7	1.33	2.46	0.67	1.23	0.44	0.82	0.33	0.61	45.1

The evanescent wave penetrating into the rarer medium, i.e. the sample, probes molecules which are located on the surface and surface near region (in the range of μm) of the IRE, i.e. the ZnSe crystal. This unique ATR mode enables to probe into catalytic materials interacting with a liquid film, such as solvents, reactants, intermediates, being in contact with the IRE. ATR IRS has gained rising importance, firstly in the field of electrochemistry^[152, 153] and later on in heterogeneous catalysis.^[154-158]

Throughout this thesis, ATR-IR spectroscopy is the approach to investigate catalytic biomass conversion at the solid/liquid and solid/liquid/gas interfaces. The advantage of the ATR-IR spectroscopy is the possibility of studying catalytic processes *in situ*, which describes the possibility to “look inside” into the chemical environment as the catalytic reaction takes place. The section below gives an overview on established *in situ* ATR-IRS techniques to study heterogeneously catalyzed reaction in liquid phase.

7.3 ATR-IR for In situ Investigations in Catalysis

Heterogeneous catalyzed reaction in liquid phase are usually performed in batch or slurry reactors, where the catalyst particles (mainly 10 – 100 μm) are either dispersed in liquid through either mechanical stirring or gas bubbling through the slurry.^[144] Also the fixed or/and trickle bed reactor are relevant for the catalytic biomass conversion in liquid phase, where the packed catalyst with bigger catalyst particle sizes (> 300 μm) are contacted to the reactants dissolved in liquid phase within the catalytic bed. Thus, probing into process analytics can be established through the appropriate cell design of the ATR-IR spectroscopy technique. Various cell designs for internal reflection or attenuated total reflection spectroscopy have been studied, emphasizing the versatility of this technology.^[145, 151] Based on the two different reactor types, the cell design of the ATR-IR

will be considered as probing technique for the batch (section below) and plug flow reactor (section 7.3.2).

7.3.1 Internal reflection spectroscopy for on-line reaction monitoring

For the application of process control, a batch chemical reactor is equipped with an internal reflection probe/element, referred as IRE. The evanescent wave is penetrating into the liquid phase, where the catalyst is dispersed among the reactants and reactant-intermediates (Figure 1-10). The objective of this on-line process analysis is the monitoring of reactant and reactant-intermediates or product concentrations to yield real-time knowledge about the conversion. As compared with off-line analysis, such as gas-chromatography, high-pressure liquid chromatography, mass spectrometry, and NMR spectroscopy, the ATR-IR spectroscopy is significantly faster as spectra are acquired during the reaction.^[143] Further, a sample/aliquot extraction^[143] from the reaction mixture is not required, which enables monitoring of labile compounds or detection of unstable intermediates, when reaction mixture is quenched.^[145]

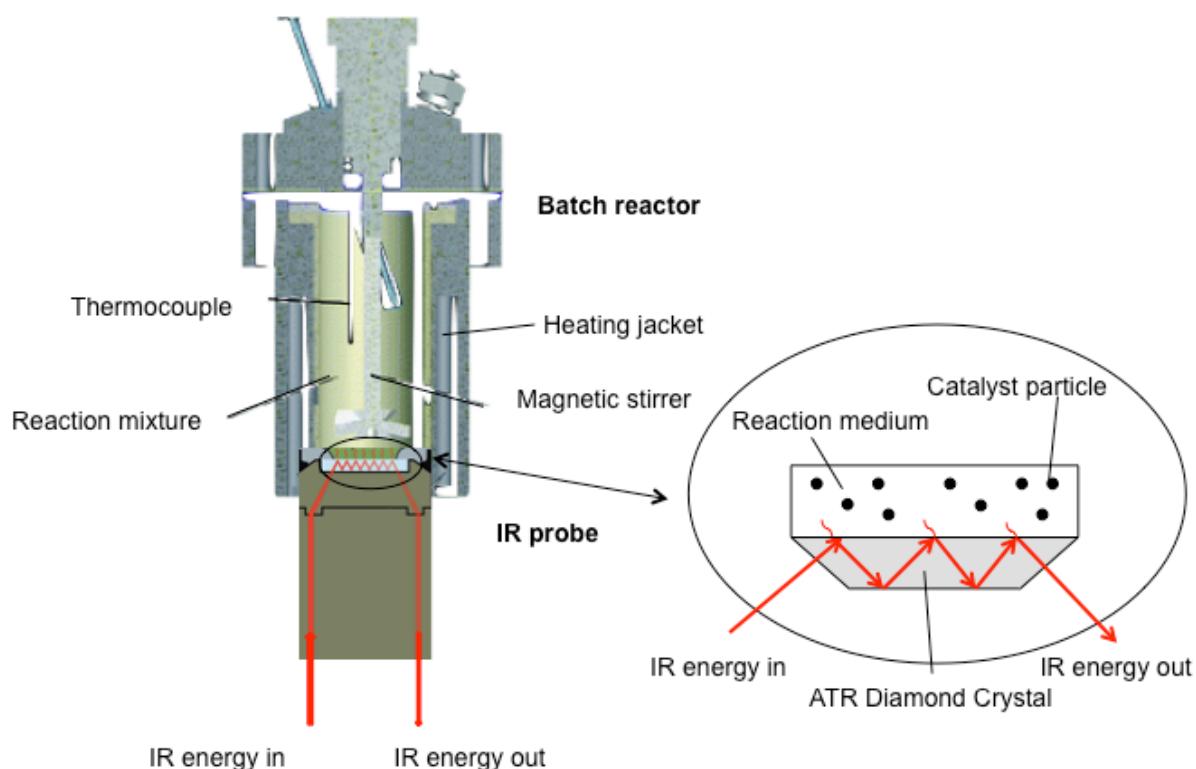


Figure 1-10. Schematic illustration of batch reactor equipped with ATR-IR probe for on-line monitoring of catalytic reactions in liquid phase.

Several reports aim the study of kinetics of chemical reactions as reflected by the changes in liquid-phase concentrations. For instance, the implementation of heterogeneous catalytic reactions has been investigated for hydrogenation of α,β -unsaturated ketones on Pd/C catalysts.^[159, 160] Mul *et al.* studied the esterification of caproic acid with octanol

catalyzed by solid acid Nafion supported on silica, performed at 447 K, atmospheric pressure in the presence of non-polar n-decane solvent.^[161] Due to distinguishable IR spectra of reactants (acid and alcohol) and product (ester), the individual concentration profiles could have been tracked and verified through *ex situ* GC analysis.^[161] Both C = O stretching vibrations at 1720 and 1745 cm⁻¹ are identified with the relatively large transition dipole moments, resulting in strong absorption signals, facilitating a steady analysis. In the same study, the researchers observed a strong band at 1100 cm⁻¹, which originated from the catalyst itself (Si-O-R groups) being located within the volume probed by evanescent field. It seems plausible that if the catalyst dispersed in reaction mixture is in contact with the ATR element, the evanescent wave will be additionally absorbed by the framework or functionalities active IR modes. This examples demonstrates that the study of heterogeneous catalyzed reactions in liquid phase is not straightforward, because each studied system has its own drawbacks depending on many configurational set-ups, such as the insertion of the IR probe into the stirred tank reactor (i.e. from the bottom/the side/top).

The detection limits depend based on design of the optical apparatus, comprising IR spectrometer, energy throughput, source, detector, number of internal reflections and scans. Pintar and co-workers stated a detection limit of 0.8 mmol L⁻¹ for α,β -unsaturated ketones for six internal reflections.^[162] The detection limit of ATR-IR was approximated with an assumption of 0.01% absorbance units characteristic for the C = O stretching vibration and a 5% sensitivity for 0.4 molar concentration of the dissolved reactants and products to be 0.0008 mol L⁻¹ = (0.4 mol L⁻¹ x 0.01%) : 5%.^[145, 162]

The modus operandi depicted in Figure 1-10 is subjected in this thesis to investigate catalytic biomass conversion on Ni catalysts in liquid phase in the context of (1) phenol hydrodeoxygenation (HDO) in both aqueous and non-polar phase and (2) stearic acid HDO in non-polar solvent. Furthermore, the plug flow configuration of ATR-IR spectroscopy is the alternate mode into probing the continuous catalytic conversion of biomass, which is introduced in the section below.

7.3.2 Flow-Through ATR-IR Cell

Particular catalysts possess the ability to stick to the IRE, thus, enabling the deposition of catalytic powdered material close to the evanescent wave. The technology described in the preceding section is therefore also applicable to continuous reactors, where the ATR crystal is used as one wall of the reactor, contemporary bearing the coated catalyst as a film (Figure 1-11). For particular materials, stable films can be prepared by drop coating a suspension of the solid powdered catalyst onto the IRE and followed by evaporation of the solvent.^[145, 163] The stability of the powdered catalysts deposited as film on the IRE highly

depends on the catalyst and also the crystal material.^[145] Influenced by interfacial properties, some catalyst powder films are not stable in flowing solvent. For instance, materials comprised of SiO₂ were reported to adhesive badly to the IRE under liquid flow.^[164] Under these circumstances, the addition of little amount of a binder, such as polyethylene, fixates the catalyst particles to the IRE, prior its exposition to the flowing solvent. For research performed on powdered catalyst, ZnSe crystals are advantageous due their small refraction index (RF = 2.4), enabling the evanescent wave to penetrate to a greater depth (d_p , equation 3) into the measured sample, i.e. catalytic material, compared to other crystals materials, such as Ge or diamond (RF = 4).

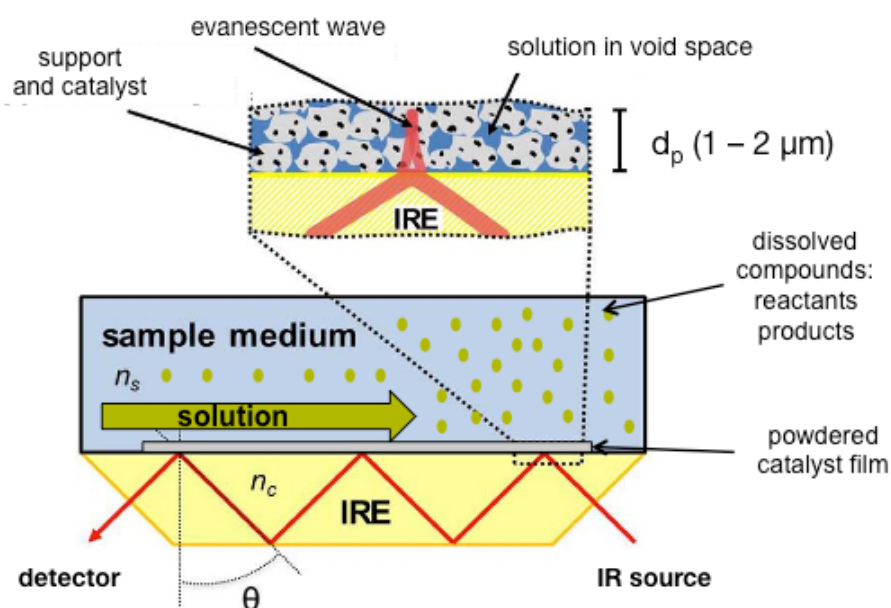


Figure 1-11. Schematic drawing of an *in situ* flow through ATR-IR setup^[151]

The immobilized catalyst on the ATR crystal does not represent a homogenous layer in perfect contact with the IRE, and consequently the evanescent field is not exactly originated as described by theory (equation 3). The evanescent wave (upper insert of Figure 1-11) is probing the catalyst being in contact with dissolved molecules as well as the void space between the particles. The refractive index of the heterogeneous catalytic layer in contact with the continuous flow can be approximated by equation 5:^[144]

$$n_{eff} = \sqrt{(1 - \phi)n_c^2 + n_s^2} \quad (5)$$

where ϕ is the volume of the interparticle pores, and n_c and n_s are the refractive indices of the continuous and dispersed (deposited) phases, respectively.^[144, 151] The void spaces specify the fraction of the bulk fluid which will be probed by the evanescent field, which can be experimentally evaluated.^[144, 145] Moreover, if the catalyst particle size is smaller than the penetration depth, the IR radiation probes an “effective medium”, which has been

expressed in theories, such as Maxwell-Garnett^[165], and Bruggemann^[166], to calculate the optical constraints of a heterogeneous composite layer.

With this background, the flow-through ATR-IR apparatus can track the response to reactant concentration and its transformation considering its interaction with the catalyst layer, and such ATR-IR configuration has been approved to be an impressive tool for mechanistic studies.^[159-163] Due to the geometry of the flow-through ATR method, diffusion of dissolved molecules from the bulk solution phase to and within the catalyst has been studied extensively.^[140, 142-145, 150, 151, 161] Moreover, the great advantage of the method is that it also provides insight into the species adsorbed on the catalyst during reaction, such as reaction intermediates.^[159, 160] The group of Baiker and Hungerbühler developed a double chamber ATR-IR flow cell to distinguish signals from adsorbed species by measuring simultaneously the reactants at the catalyst coated region and at the liquid solution at the empty region of the ATR crystal.^[145, 151] To achieve time-resolved (semi)quantitative information on the surface intermediate species, mass transport limitations at the solid-liquid interface in the ATR cell need to be addressed. For the liquid phase hydrogenation on supported metal catalysts external mass transfer limitations are mainly studied by alteration of stirrer speed and intraparticle mass transfer limitations by modification of particle size.^[145]

The flow-through ATR-IR spectroscopy has been developed into a dispensable analysis technique, allowing investigations of liquid phase catalysis, such as catalytic upgrading of biomass-derived oxygenates. In the rapidly growing field of catalytic biomass conversion, the ATR-IR spectroscopy can provide insights into the reaction mechanism of such catalytic processes in solution, as those still lack fundamental insights in liquid phase in terms of mechanism.^[41, 63, 109, 143, 161, 167] In light of this, scope of this thesis is going to be outlined in the concluding section.

8. Scope of thesis

The scope of this doctoral thesis is to study the conversion of woody biomass with supported Ni catalysts in liquid phase, i.e. aqueous and non-polar phase. Chapter 2 deals with the fundamental insights into the kinetics and reaction mechanism by investigating hydrodeoxygenation of phenol as model compound on Ni/HZSM-5 catalysts. Specifically, the kinetics and reaction mechanism of developed Ni/HZSM-5 were examined upon upgrading phenolic molecules in aqueous phase. In particular, the application of batch IR method described in section 0 is going to be applied to *in situ* follow the reaction mechanism of phenol hydrodeoxygenation in aqueous phase. These findings, directly correlated to *ex situ* kinetic studies, gained novel insights towards understanding elementary catalyzed steps in cascade reactions, such as depicted in Scheme 1-2.

Consequently, based on the studies with zeolite supported Ni catalysts, Chapter 3 deals with the synthesis of Ni/C-SO₃H catalysts for phenol hydrodeoxygenation in aqueous and non-polar phases. The synthesis of sugar and cellulose derived carbon supports, as well as the post-chemical modification for the functionalization of the support is going to be explored in detail. Further, the incorporation of Ni particles on such sulfonated carbon is going to play major role to develop highly efficient Ni nanoparticles (NPs) supported on various C-SO₃H supports. The interplay of the acid site with the Ni NPs is going to be evaluated through physical mixtures of sulfonated carbon support and the dual-functional Ni/C-SO₃H catalyst. Moreover in this study, the batch IR set-up has been successfully applied to determine the bottle-neck of the subsequently catalyzed elementary steps in Ni/C-SO₃H catalysts, to be the acid-catalyzed dehydration of intermediated cycloalkanols. Finally, an in-depth *in-situ* EXAFS analysis on the Ni edge during catalytic aqueous phase hydrogenation revealed the nature and oxidation state of Ni nanoparticles deposited on sulfonated carbons.

Through the evaluation of Ni catalysis in respect to liquid phase upgrading of biomass-related model compounds, the fundamentals to approach real lignin valorization has been settled. In Chapter 4 lignin, specifically Organosolv lignin has been studied for the heterogeneous supported Ni catalyzed deconstruction and upgrading in one-stage process. The single batch experiments achieved remarkable yields of cyclic hydrocarbons at relative mild reaction conditions (i.e. temperature 523 – 593 K and 2 MPa H₂). The comprehensive analysis of Organosolv Lignin (solution state 2D HSQC NMR, MALDI-TOF MS) as well as the analysis of products in gas (GC TCD), liquid (GC-MS FDI) and remaining solid phase (TGA, solid state NMR) provided information on the start and end point of the lignin catalyzed reactions. To close this understanding gap, lab built ATR-IR

apparatus has been applied into probing *in situ* Ni catalyzed lignin deconstruction, as depicted in Figure 1-12.

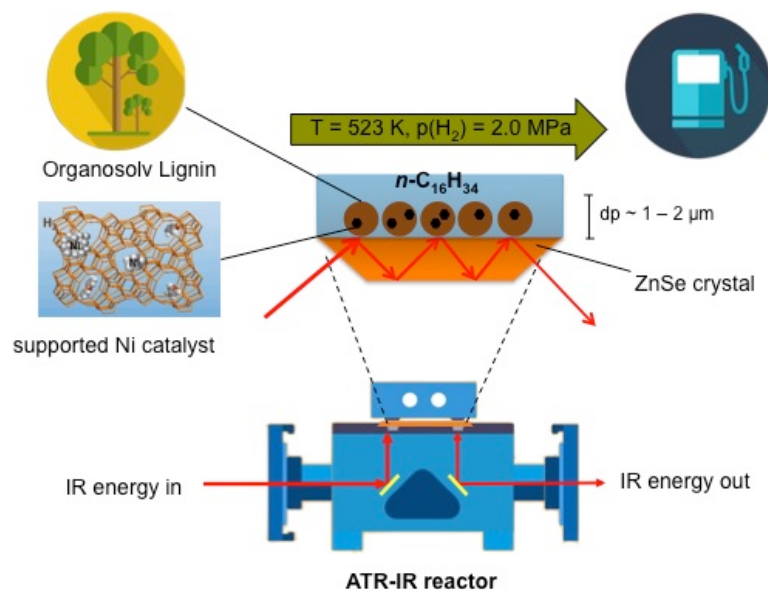


Figure 1-12. Schematic illustration of time-resolved lignin deconstruction study on supported Ni catalysts in the lab-built reactor at 523 K, 2 MPa H_2 .

The obtained *in situ* IR spectra provided the hitherto unexplored insights on reaction pathways of lignin deconstruction on Ni catalysts. The lab developed ATR-IR apparatus provides the general methodical approach to shed light into the biomass conversion catalyzed in liquid phase.

The hydrodeoxygenation of micro algae oil is considered as the third generation biofuel, comprising the production of green diesel and/or jet-fuel. Although the motivational and chemical background on the catalytic conversion of microalgae oil are beyond the scope of this thesis, the Chapter 5 is dealing with probing Batch IR technique (see Figure 1-10 in section 0) to reveal the reaction mechanism of stearic acid hydrodeoxygenation on Ni based catalysts. The proposed reaction mechanism of stearic acid conversion on Ni catalysts can proceed through a series of reactions, including hydrogenation, hydrodeoxygenation, decarboxylation and decarbonylation, ketonization and hydrogenolysis in non-polar solvents. Through the Batch IR study, a surface bonded species, the ketene of the H abstracted octadecanal, was identified spectroscopically. Thus we were able to shed light into the mechanism of subsequent reaction steps within liquid phase stearic acid hydrodeoxygenation. This outstanding study reflects the possibilities towards understanding complex biomass processes through applying Batch ATR-IR spectroscopy in liquid phase.

The final chapter concludes the general discoveries of this thesis which includes both, the synthesis and optimization of dual-functional Ni catalysts and the establishment of process analysis techniques, such as ATR-IR in batch and flow mode.

9. References

1. Crocker, M. and R. Andrews, *Chapter 1 The Rationale for Biofuels*, in *Thermochemical Conversion of Biomass to Liquid Fuels and Chemicals*. 2010, The Royal Society of Chemistry. p. 1-25.
2. Vernon, C., E. Thompson, and S. Cornell, *Carbon dioxide emission scenarios: limitations of the fossil fuel resource*. *Procedia Environmental Sciences*, 2011. 6: p. 206-215.
3. Raupach, M.R., et al., *Global and regional drivers of accelerating CO₂ emissions*. *Proceedings of the National Academy of Sciences*, 2007. 104(24): p. 10288-10293.
4. Panwar, N., S. Kaushik, and S. Kothari, *Role of renewable energy sources in environmental protection: a review*. *Renewable and Sustainable Energy Reviews*, 2011. 15(3): p. 1513-1524.
5. Everett, R., et al., *Energy systems and sustainability: power for a sustainable future*. 2012: Oxford University Press.
6. *Key World Energy Statistics 2014*, International Energy Agency: Paris, France.
7. Lauber, V. and L. Mez, *Three Decades of Renewable Electricity Policies in Germany*. *Energy & Environment*, 2004. 15(4): p. 599-623.
8. Hoekman, S.K., *Biofuels in the U.S. – Challenges and Opportunities*. *Renewable Energy*, 2009. 34(1): p. 14-22.
9. Ragauskas, A.J., et al., *Lignin valorization: improving lignin processing in the biorefinery*. *Science*, 2014. 344(6185): p. 1246843.
10. Dale, B.E. and R.G. Ong, *Energy, wealth, and human development: why and how biomass pretreatment research must improve*. *Biotechnology progress*, 2012. 28(4): p. 893-898.
11. Naqvi, M.R. and J. Yan, *First-Generation Biofuels*. 2015.
12. Damartzis, T. and A. Zabaniotou, *Thermochemical conversion of biomass to second generation biofuels through integrated process design—A review*. *Renewable and Sustainable Energy Reviews*, 2011. 15(1): p. 366-378.
13. Naik, S., et al., *Production of first and second generation biofuels: a comprehensive review*. *Renewable and Sustainable Energy Reviews*, 2010. 14(2): p. 578-597.
14. Sims, R.E.H., et al., *An overview of second generation biofuel technologies*. *Bioresource Technology*, 2010. 101(6): p. 1570-1580.
15. Zinoviev, S., et al., *Next-generation biofuels: survey of emerging technologies and sustainability issues*. *ChemSusChem*, 2010. 3(10): p. 1106-1133.

16. Ragauskas, A.J., et al., *The path forward for biofuels and biomaterials*. science, 2006. 311(5760): p. 484-489.
17. Pu, Y., et al., *The new forestry biofuels sector*. Biofuels, Bioproducts and Biorefining, 2008. 2(1): p. 58-73.
18. Alakangas, E., J. Valtanen, and J.-E. Levlín, *CEN technical specification for solid biofuels—Fuel specification and classes*. Biomass and Bioenergy, 2006. 30(11): p. 908-914.
19. Sissine, F. *Energy Independence and Security Act of 2007: a summary of major provisions*. 2007. DTIC Document.
20. Gellerstedt, G. and G. Henriksson, *Lignins: major sources, structure and properties*. 2008: Amsterdam, the Netherlands: Elsevier.
21. Henriksson, G., et al., *Chapter 9 Lignin Utilization*, in *Thermochemical Conversion of Biomass to Liquid Fuels and Chemicals*. 2010, The Royal Society of Chemistry. p. 222-262.
22. McKendry, P., *Energy production from biomass (part 1): overview of biomass*. Bioresource Technology, 2002. 83(1): p. 37-46.
23. Forss, K. and K.E. Fremer, *The Nature of Lignin: A Different View*, in *Lignin: Historical, Biological, and Materials Perspectives*. 1999, American Chemical Society. p. 100-116.
24. McCarthy Joseph, L. and A. Islam, *Lignin Chemistry, Technology, and Utilization: A Brief History*, in *Lignin: Historical, Biological, and Materials Perspectives*. 1999, American Chemical Society. p. 2-99.
25. Boerjan, W., J. Ralph, and M. Baucher, *Lignin biosynthesis*. Annual review of plant biology, 2003. 54(1): p. 519-546.
26. Hatakeyama, H. and T. Hatakeyama, *Lignin structure, properties, and applications*, in *Biopolymers*. 2010, Springer. p. 1-63.
27. Westoby, M. and B. Rice, *Evolution of the Seed Plants and Inclusive Fitness of Plant Tissues*. Evolution, 1982. 36(4): p. 713-724.
28. Kenrick, P. and P.R. Crane, *The origin and early evolution of plants on land*. Nature, 1997. 389(6646): p. 33-39.
29. Zakzeski, J., et al., *The Catalytic Valorization of Lignin for the Production of Renewable Chemicals*. Chemical Reviews, 2010. 110(6): p. 3552-3599.
30. Aso, T., et al., *Preparation of novel lignin-based cement dispersants from isolated lignins*. Journal of Wood Chemistry and Technology, 2013. 33(4): p. 286-298.
31. Saito, T., et al., *Turning renewable resources into value-added polymer: development of lignin-based thermoplastic*. Green Chemistry, 2012. 14(12): p. 3295-3303.

32. Nimz, H., *Beech Lignin—Proposal of a Constitutional Scheme*. Angewandte Chemie International Edition in English, 1974. 13(5): p. 313-321.
33. Sjostrom, E., *Wood chemistry: fundamentals and applications*. 2013: Elsevier.
34. Erickson, M. and G. Miksche, *On the occurrence of lignin or polyphenols in some mosses and liverworts*. Phytochemistry, 1974. 13(10): p. 2295-2299.
35. Czernik, S. and A. Bridgwater, *Overview of applications of biomass fast pyrolysis oil*. Energy & Fuels, 2004. 18(2): p. 590-598.
36. Dahmen, N., et al., *State of the art of the bioliq® process for synthetic biofuels production*. Environmental Progress & Sustainable Energy, 2012. 31(2): p. 176-181.
37. Raveendran, K. and A. Ganesh, *Heating value of biomass and biomass pyrolysis products*. Fuel, 1996. 75(15): p. 1715-1720.
38. Karl, W., *Repap's Alcell process: is it all it's cracked up to be*. Pulp & Paper J, 1988. 41(7): p. 17-21.
39. Glasser, W.G. and S. Sarkanen, *Lignin, properties and materials*. 1989, Washington, DC (USA); American Chemical Society.
40. El Mansouri, N.-E. and J. Salvadó, *Structural characterization of technical lignins for the production of adhesives: Application to lignosulfonate, kraft, soda-anthraquinone, organosolv and ethanol process lignins*. Industrial Crops and Products, 2006. 24(1): p. 8-16.
41. Xu, C., et al., *Lignin depolymerisation strategies: towards valuable chemicals and fuels*. Chemical Society Reviews, 2014. 43(22): p. 7485-7500.
42. Pandey, M.P. and C.S. Kim, *Lignin Depolymerization and Conversion: A Review of Thermochemical Methods*. Chemical Engineering & Technology, 2011. 34(1): p. 29-41.
43. Saisu, M., et al., *Conversion of lignin with supercritical water-phenol mixtures*. Energy & Fuels, 2003. 17(4): p. 922-928.
44. Thring, R.W. and J. Breau, *Hydrocracking of solvolysis lignin in a batch reactor*. Fuel, 1996. 75(7): p. 795-800.
45. Roberts, V.M., et al., *Towards Quantitative Catalytic Lignin Depolymerization*. Chemistry – A European Journal, 2011. 17(21): p. 5939-5948.
46. Vigneault, A., D.K. Johnson, and E. Chornet, *Base-Catalyzed Depolymerization of Lignin: Separation of Monomers*. The Canadian Journal of Chemical Engineering, 2007. 85(6): p. 906-916.
47. Tien, M. and T.K. Kirk, *Lignin-Degrading Enzyme from the Hymenomycete Phanerochaete chrysosporium Burds*. Science, 1983. 221(4611): p. 661-663.
48. Shimada, M., et al., *The C C bond cleavage of a lignin model compound, 1, 2-diarylpropane-1, 3-diol, with a heme-enzyme model catalyst*

- tetraphenylporphyrinatoiron (III) chloride in the presence of tert-butylhydroperoxide*. Biochemical and biophysical research communications, 1984. 122(3): p. 1247-1252.
49. Crestini, C., et al., *Biomimetic degradation of lignin and lignin model compounds by synthetic anionic and cationic water soluble manganese and iron porphyrins*. Bioorganic & medicinal chemistry, 1999. 7(9): p. 1897-1905.
 50. Cui, F. and D. Dolphin, *Metallophthalocyanines as possible lignin peroxidase models*. Bioorganic & medicinal chemistry, 1995. 3(5): p. 471-477.
 51. Crestini, C., et al., *Methyltrioxorhenium: a new catalyst for the activation of hydrogen peroxide to the oxidation of lignin and lignin model compounds*. Bioorganic & medicinal chemistry, 2005. 13(7): p. 2569-2578.
 52. Harms, R.G., et al., *Cleavage of C-O Bonds in Lignin Model Compounds Catalyzed by Methyltrioxorhenium in Homogeneous Phase*. ChemSusChem, 2014. 7(2): p. 429-434.
 53. Rahimi, A., et al., *Formic-acid-induced depolymerization of oxidized lignin to aromatics*. Nature, 2014. 515(7526): p. 249-252.
 54. Rahimi, A., et al., *Chemoselective Metal-Free Aerobic Alcohol Oxidation in Lignin*. Journal of the American Chemical Society, 2013. 135(17): p. 6415-6418.
 55. Li, X., et al., *Catalytic fast pyrolysis of Kraft lignin with HZSM-5 zeolite for producing aromatic hydrocarbons*. Frontiers of Environmental Science & Engineering, 2012. 6(3): p. 295-303.
 56. Mullen, C.A. and A.A. Boateng, *Chemical composition of bio-oils produced by fast pyrolysis of two energy crops†*. Energy & Fuels, 2008. 22(3): p. 2104-2109.
 57. Ben, H. and A.J. Ragauskas, *Influence of Si/Al ratio of ZSM-5 zeolite on the properties of lignin pyrolysis products*. ACS Sustainable Chemistry & Engineering, 2013. 1(3): p. 316-324.
 58. Dickerson, T. and J. Soria, *Catalytic fast pyrolysis: a review*. Energies, 2013. 6(1): p. 514-538.
 59. Dabral, S., et al., *Base-catalysed cleavage of lignin [small beta]-O-4 model compounds in dimethyl carbonate*. Green Chemistry, 2015.
 60. Deepa, A.K. and P.L. Dhepe, *Lignin Depolymerization into Aromatic Monomers over Solid Acid Catalysts*. ACS Catalysis, 2015. 5(1): p. 365-379.
 61. Parsell, T., et al., *A synergistic biorefinery based on catalytic conversion of lignin prior to cellulose starting from lignocellulosic biomass*. Green Chemistry, 2015. 17(3): p. 1492-1499.
 62. Song, W., et al., *Synergistic effects of Ni and acid sites for hydrogenation and C-O bond cleavage of substituted phenols*. Green Chemistry, 2015. 17(2): p. 1204-1218.

63. Zaheer, M. and R. Kempe, *Catalytic Hydrogenolysis of Aryl Ethers: A Key Step in Lignin Valorization to Valuable Chemicals*. ACS Catalysis, 2015. 5(3): p. 1675-1684.
64. Lee, C.-L. and D.F. Ollis, *Catalytic hydrodeoxygenation of benzofuran and o-ethylphenol*. Journal of Catalysis, 1984. 87(2): p. 325-331.
65. Nagai, M., T. Masunaga, and N. Hana-oka, *Selectivity of molybdenum catalyst in hydrodenitrogenation, hydrodesulfurization and hydrodeoxygenation: Effects of sulfur and oxygen compounds on acridine hydrodenitrogenation*. Journal of Catalysis, 1986. 101(2): p. 284-292.
66. Elliott, D.C. and E. Baker, *Upgrading biomass liquefaction products through hydrodeoxygenation*. 1984, Pacific Northwest Lab., Richland, WA (USA).
67. Kubička, D. and J. Horáček, *Deactivation of HDS catalysts in deoxygenation of vegetable oils*. Applied Catalysis A: General, 2011. 394(1): p. 9-17.
68. A. Gutierrez, R.K.K.M.L.H., R. Slioor, A.O.I. Krause, *Hydrodeoxygenation of guaiacol on noble metal catalysts*. Catalysis Today, 2009. 147: p. 239 - 246.
69. Yakovlev, V.A., et al., *Development of new catalytic systems for upgraded bio-fuels production from bio-crude-oil and biodiesel*. Catalysis Today, 2009. 144(3-4): p. 362-366.
70. Bridgwater, A. and D. Boocock, *Science in thermal and chemical biomass conversion*. 2006: CPL Press.
71. Elliott, D.C. and T.R. Hart, *Catalytic Hydroprocessing of Chemical Models for Bio-oil*. Energy & Fuels, 2009. 23(2): p. 631-637.
72. Centeno, A., R. Maggi, and B. Delmon, *Use of noble metals in hydrodeoxygenation reactions*. Studies in surface science and catalysis, 1999. 127: p. 77-84.
73. Choudhary, T. and C. Phillips, *Renewable fuels via catalytic hydrodeoxygenation*. Applied Catalysis A: General, 2011. 397(1): p. 1-12.
74. Wildschut, J., et al., *Hydrotreatment of fast pyrolysis oil using heterogeneous noble-metal catalysts*. Industrial & engineering chemistry research, 2009. 48(23): p. 10324-10334.
75. Zhao, C., et al., *Highly Selective Catalytic Conversion of Phenolic Bio-Oil to Alkanes*. Angewandte Chemie International Edition, 2009. 48(22): p. 3987-3990.
76. Liu, H., et al., *Selective Phenol Hydrogenation to Cyclohexanone Over a Dual Supported Pd-Lewis Acid Catalyst*. Science, 2009. 326(5957): p. 1250-1252.
77. Li, K., R. Wang, and J. Chen, *Hydrodeoxygenation of Anisole over Silica-Supported Ni₂P, MoP, and NiMoP Catalysts*. Energy & Fuels, 2011. 25(3): p. 854-863.

78. Nimmanwudipong, T., et al., *Catalytic Conversion of Guaiacol Catalyzed by Platinum Supported on Alumina: Reaction Network Including Hydrodeoxygenation Reactions*. Energy & Fuels, 2011. 25(8): p. 3417-3427.
79. Zhao, C., et al., *Aqueous-phase hydrodeoxygenation of bio-derived phenols to cycloalkanes*. Journal of Catalysis, 2011. 280(1): p. 8-16.
80. Zhao, C. and J.A. Lercher, *Selective Hydrodeoxygenation of Lignin-Derived Phenolic Monomers and Dimers to Cycloalkanes on Pd/C and HZSM-5 Catalysts*. ChemCatChem, 2012. 4(1): p. 64-68.
81. Zhao, C., et al., *Hydrodeoxygenation of bio-derived phenols to hydrocarbons using RANEY[registered sign] Ni and Nafion/SiO₂ catalysts*. Chemical Communications, 2010. 46(3): p. 412-414.
82. Zhao, C., D.M. Camaioni, and J.A. Lercher, *Selective catalytic hydroalkylation and deoxygenation of substituted phenols to bicycloalkanes*. Journal of Catalysis, 2012. 288(0): p. 92-103.
83. Zhao, C. and J.A. Lercher, *Chapter 9 - Catalytic Depolymerization and Deoxygenation of Lignin*, in *The Role of Catalysis for the Sustainable Production of Bio-fuels and Bio-chemicals*, Stöcker, Editor. 2013, Elsevier: Amsterdam. p. 289-320.
84. V.A. Yakovlev, S.A.K., O.V. Sherstyuk, V.O. Dundich, D.Yu. Ermakov, V.M. Novopashina, M.Yu. Lebedev, O. Bulavchenko, V.N. Parmon, *Development of new catalytic systems for upgraded bio-fuels production from bio-crude-oil and biodiesel*. Catalysis Today, 2009. 144: p. 362 - 366.
85. Alonso, D.M., S.G. Wettstein, and J.A. Dumesic, *Bimetallic catalysts for upgrading of biomass to fuels and chemicals*. Chemical Society Reviews, 2012. 41(24): p. 8075-8098.
86. Zhang, J., et al., *Highly efficient, NiAu-catalyzed hydrogenolysis of lignin into phenolic chemicals*. Green Chemistry, 2014. 16(5): p. 2432-2437.
87. Sergeev, A.G. and J.F. Hartwig, *Selective, nickel-catalyzed hydrogenolysis of aryl ethers*. Science, 2011. 332(6028): p. 439-443.
88. Sergeev, A.G., J.D. Webb, and J.F. Hartwig, *A heterogeneous nickel catalyst for the hydrogenolysis of aryl ethers without arene hydrogenation*. Journal of the American Chemical Society, 2012. 134(50): p. 20226-20229.
89. He, J., C. Zhao, and J.A. Lercher, *Ni-Catalyzed Cleavage of Aryl Ethers in the Aqueous Phase*. Journal of the American Chemical Society, 2012. 134(51): p. 20768-20775.
90. He, J., et al., *Mechanisms of catalytic cleavage of benzyl phenyl ether in aqueous and apolar phases*. Journal of Catalysis, 2014. 311(0): p. 41-51.

91. He, J., *Selective Cleavage of C-O Bonds and Hydrodeoxygenation of Lignin Fragment Molecules*, in *Chair of Technical Chemistry II*. 2014, Technische Universität München.
92. Harris, E.E., J. D'Ianni, and H. Adkins, *Reaction of hardwood lignin with hydrogen*. *Journal of the American Chemical Society*, 1938. 60(6): p. 1467-1470.
93. Pepper, J. and W. Steck, *The effect of time and temperature on the hydrogenation of aspen lignin*. *Canadian Journal of Chemistry*, 1963. 41(11): p. 2867-2875.
94. Pepper, J.M. and R.W. Fleming, *Lignin and related compounds. V. The hydrogenolysis of aspen wood lignin using rhodium-on-charcoal as catalyst*. *Canadian Journal of Chemistry*, 1978. 56(7): p. 896-898.
95. Pepper, J. and Y. Lee, *Lignin and related compounds. I. A comparative study of catalysts for lignin hydrogenolysis*. *Canadian Journal of Chemistry*, 1969. 47(5): p. 723-727.
96. Pepper, J.M. and H. Hibbert, *Studies on Lignin and Related Compounds. LXXXVII. High Pressure Hydrogenation of Maple Wood¹*. *Journal of the American Chemical Society*, 1948. 70(1): p. 67-71.
97. Horáček, J., et al., *Lignin to liquids over sulfided catalysts*. *Catalysis Today*, 2012. 179(1): p. 191-198.
98. Torr, K.M., et al., *Mild hydrogenolysis of in-situ and isolated Pinus radiata lignins*. *Bioresource technology*, 2011. 102(16): p. 7608-7611.
99. S. Kortel, M.E., A. Benohr, *World Organization for Intellectual Property*, in *WO 2009 / 037281 A2*. 2009.
100. Song, W., *Bifunctional Ni/Zeolite Catalysts for Hydrodeoxygenation of Microalgae Oil and Lignin*, in *Chair of Technical Chemistry II*. 2015, Technische Universität München: Garching.
101. Geilen, F., et al., *Selective and flexible transformation of biomass-derived platform chemicals by a multifunctional catalytic system*. *Angewandte Chemie*, 2010. 122(32): p. 5642-5646.
102. Thomas, J.M., *Design, synthesis, and in situ characterization of new solid catalysts*. *Angewandte Chemie International Edition*, 1999. 38(24): p. 3588-3628.
103. Vennestrøm, P.N., et al., *Next-Generation Catalysis for Renewables: Combining Enzymatic with Inorganic Heterogeneous Catalysis for Bulk Chemical Production*. *ChemCatChem*, 2010. 2(3): p. 249-258.
104. Alamillo, R., et al., *The selective hydrogenation of biomass-derived 5-hydroxymethylfurfural using heterogeneous catalysts*. *Green Chemistry*, 2012. 14(5): p. 1413-1419.

105. Peng, B., et al., *Towards Quantitative Conversion of Microalgae Oil to Diesel-Range Alkanes with Bifunctional Catalysts*. *Angewandte Chemie*, 2012. 124(9): p. 2114-2117.
106. Peng, B., et al., *Stabilizing catalytic pathways via redundancy: selective reduction of microalgae oil to alkanes*. *Journal of the American Chemical Society*, 2012. 134(22): p. 9400-9405.
107. Song, W., C. Zhao, and J.A. Lercher, *Importance of size and distribution of Ni nanoparticles for the hydrodeoxygenation of microalgae oil*. *Chemistry-A European Journal*, 2013. 19(30): p. 9833-9842.
108. Zhao, C. and J.A. Lercher, *Upgrading Pyrolysis Oil over Ni/HZSM-5 by Cascade Reactions*. *Angewandte Chemie*, 2012. 124(24): p. 6037-6042.
109. Lin, Y.-C. and G.W. Huber, *The critical role of heterogeneous catalysis in lignocellulosic biomass conversion*. *Energy & Environmental Science*, 2009. 2(1): p. 68-80.
110. Stöcker, M., *Biofuels and biomass-to-liquid fuels in the biorefinery: Catalytic conversion of lignocellulosic biomass using porous materials*. *Angewandte Chemie International Edition*, 2008. 47(48): p. 9200-9211.
111. Kobayashi, H., H. Ohta, and A. Fukuoka, *Conversion of lignocellulose into renewable chemicals by heterogeneous catalysis*. *Catalysis Science & Technology*, 2012. 2(5): p. 869-883.
112. Cushing, B.L., V.L. Kolesnichenko, and C.J. O'Connor, *Recent advances in the liquid-phase syntheses of inorganic nanoparticles*. *Chemical reviews*, 2004. 104(9): p. 3893-3946.
113. Zanjanchi, M. and A. Ebrahimian, *Studies on the solid-state ion exchange of nickel ions into zeolites using DRS technique*. *Journal of molecular structure*, 2004. 693(1): p. 211-216.
114. Nares, R., et al., *Ni/H β -zeolite catalysts prepared by deposition-precipitation*. *The Journal of Physical Chemistry B*, 2002. 106(51): p. 13287-13293.
115. Townsend, R.P. and E.N. Coker, *Ion exchange in zeolites*. *Studies in surface science and catalysis*, 2001. 137: p. 467-524.
116. Geus, J.W., *Dutch Pat. Appl.*, 6705, Editor. 1967: Netherlands.
117. Hermans, L. and J. Geus, *Interaction of nickel ions with silica supports during deposition-precipitation*. *Studies in Surface Science and Catalysis*, 1979. 3: p. 113-130.

118. Delmon, B., *Dynamic processes in active phase-support interactions*. Journal of Molecular Catalysis, 1990. 59(2): p. 179-206.
119. Burattin, P., M. Che, and C. Louis, *Molecular approach to the mechanism of deposition-precipitation of the Ni (II) phase on silica*. The Journal of Physical Chemistry B, 1998. 102(15): p. 2722-2732.
120. Burattin, P., M. Che, and C. Louis, *Characterization of the Ni (II) phase formed on silica upon deposition-precipitation*. The Journal of Physical Chemistry B, 1997. 101(36): p. 7060-7074.
121. Lam, E. and J.H.T. Luong, *Carbon Materials as Catalyst Supports and Catalysts in the Transformation of Biomass to Fuels and Chemicals*. ACS Catalysis, 2014. 4(10): p. 3393-3410.
122. Rodríguez-Reinoso, F., *The role of carbon materials in heterogeneous catalysis*. Carbon, 1998. 36(3): p. 159-175.
123. Hara, M., *Biomass conversion by a solid acid catalyst*. Energy & Environmental Science, 2010. 3(5): p. 601-607.
124. Elliott, D.C. and T.R. Hart, *Catalytic hydroprocessing of chemical models for bio-oil*. Energy & Fuels, 2008. 23(2): p. 631-637.
125. Machek, V., et al., *Relation between the distribution of platinum, its dispersion, and activity of catalysts prepared by impregnation of activated carbon with chloroplatinic acid solutions*. Collection of Czechoslovak Chemical Communications, 1981. 46(13): p. 3270-3277.
126. Hara, M., et al., *A carbon material as a strong protonic acid*. Angewandte Chemie International Edition, 2004. 43(22): p. 2955-2958.
127. Toda, M., et al., *Green chemistry: biodiesel made with sugar catalyst*. Nature, 2005. 438(7065): p. 178-178.
128. Okamura, M., et al., *Acid-catalyzed reactions on flexible polycyclic aromatic carbon in amorphous carbon*. Chemistry of Materials, 2006. 18(13): p. 3039-3045.
129. Boudjahem, A.-G., et al., *Study of support effects on the reduction of Ni²⁺ ions in aqueous hydrazine*. Langmuir, 2004. 20(1): p. 208-213.
130. Li, Z., C. Han, and J. Shen, *Reduction of Ni²⁺ by hydrazine in solution for the preparation of nickel nano-particles*. Journal of materials science, 2006. 41(11): p. 3473-3480.
131. Metin, O., et al., *Monodisperse nickel nanoparticles and their catalysis in hydrolytic dehydrogenation of ammonia borane*. Journal of the American Chemical Society, 2010. 132(5): p. 1468-1469.

132. Bönnemann, H., W. Brijoux, and T. Jousen, *The preparation of finely divided metal and alloy powders*. Angewandte Chemie International Edition in English, 1990. 29(3): p. 273-275.
133. Han, M., et al., *Controllable synthesis and magnetic properties of cubic and hexagonal phase nickel nanocrystals*. Advanced Materials, 2007. 19(8): p. 1096-1100.
134. Eischens, R. and W. Pliskin, *The infrared spectra of adsorbed molecules*. Adv. Catal, 1958. 10(1).
135. Mapes, J. and R. Eischens, *The infrared spectra of ammonia chemisorbed on cracking catalysts*. The Journal of Physical Chemistry, 1954. 58(12): p. 1059-1062.
136. Eischens, R. and W. Pliskin, *Infrared Study of the Catalyzed Oxidation of CO*. Advances in Catalysis, 1957. 9: p. 662-668.
137. Lercher, J., A. Jentys, and A. Brait, *Catalytic Test Reactions for Probing the Acidity and Basicity of Zeolites, Acidity and Basicity*. 2008, Springer Berlin / Heidelberg. p. 153-212.
138. Peri, J., *Infrared spectroscopy in catalytic research*, in *Catalysis*. 1984, Springer. p. 171-220.
139. Ryczkowski, J., *IR spectroscopy in catalysis*. Catalysis Today, 2001. 68(4): p. 263-381.
140. Newton, M.A. and W. van Beek, *Combining synchrotron-based X-ray techniques with vibrational spectroscopies for the in situ study of heterogeneous catalysts: a view from a bridge*. Chemical Society Reviews, 2010. 39(12): p. 4845-4863.
141. Roedel, E., et al., *On the local sensitivity of different IR techniques: Ba species relevant in NO_x storage-reduction*. Physical Chemistry Chemical Physics, 2008. 10(40): p. 6190-6198.
142. Andanson, J.-M. and A. Baiker, *Exploring catalytic solid/liquid interfaces by in situ attenuated total reflection infrared spectroscopy*. Chemical Society Reviews, 2010. 39(12): p. 4571-4584.
143. Shi, H., J.A. Lercher, and X.-Y. Yu, *Sailing into uncharted waters: recent advances in the in situ monitoring of catalytic processes in aqueous environments*. Catalysis Science & Technology, 2015. 5(6): p. 3035-3060.
144. Mojet, B.L., S.D. Ebbesen, and L. Lefferts, *Light at the interface: the potential of attenuated total reflection infrared spectroscopy for understanding heterogeneous catalysis in water*. Chemical Society Reviews, 2010. 39(12): p. 4643-4655.
145. Bürgi, T. and A. Baiker, *Attenuated Total Reflection Infrared Spectroscopy of Solid Catalysts Functioning in the Presence of Liquid-Phase Reactants*, in *Advances in Catalysis*, C.G. Bruce and K. Helmut, Editors. 2006, Academic Press. p. 227-283.

146. Newton, I., *Optics*. 2nd Edition. Vol. Book III. 1717.
147. Harrick, N., *Enhanced Sensitivity for Internal Reflection Spectroscopy*, in *Modern Aspects of Reflectance Spectroscopy*. 1968, Springer. p. 207-215.
148. Fahrenfort, J., *Attenuated total reflection: A new principle for the production of useful infra-red reflection spectra of organic compounds*. *Spectrochimica Acta*, 1961. 17(7): p. 698-709.
149. Harrick, N., *Surface chemistry from spectral analysis of totally internally reflected radiation**. *The Journal of Physical Chemistry*, 1960. 64(9): p. 1110-1114.
150. Mirabella, F.M., *Internal reflection spectroscopy: Theory and applications*. Vol. 15. 1992: CRC Press.
151. Meemken, F., et al., *Simultaneous probing of bulk liquid phase and catalytic gas-liquid-solid interface under working conditions using attenuated total reflection infrared spectroscopy*. *Review of Scientific Instruments*, 2014. 85(8): p. 084101.
152. Mark Jr, H. and B.-S. Pons, *An in situ Spectrophotometric Method for Observing the Infrared Spectra of Species at the Electrode Surface During Electrolysis*. *Analytical Chemistry*, 1966. 38(1): p. 119-121.
153. Hansen, W.N., T. Kuwana, and R.A. Osteryoung, *Observation of electrode-solution interface by means of internal reflection spectrometry*. *Analytical Chemistry*, 1966. 38(13): p. 1810-1821.
154. Ferri, D., T. Bürgi, and A. Baiker, *Pt and Pt/Al₂O₃ thin films for investigation of catalytic solid-liquid interfaces by ATR-IR spectroscopy: CO adsorption, H₂-induced reconstruction and surface-enhanced absorption*. *The Journal of Physical Chemistry B*, 2001. 105(16): p. 3187-3195.
155. Ferri, D. and T. Bürgi, *An in situ attenuated total reflection infrared study of a chiral catalytic solid-liquid interface: Cinchonidine adsorption on Pt*. *Journal of the American Chemical Society*, 2001. 123(48): p. 12074-12084.
156. Ortiz-Hernandez, I. and C.T. Williams, *In situ investigation of solid-liquid catalytic interfaces by attenuated total reflection infrared spectroscopy*. *Langmuir*, 2003. 19(7): p. 2956-2962.
157. Hamminga, G.M., G. Mul, and J.A. Moulijn, *Real-time in situ ATR-FTIR analysis of the liquid phase hydrogenation of γ -butyrolactone over Cu-ZnO catalysts: A mechanistic study by varying lactone ring size*. *Chemical engineering science*, 2004. 59(22): p. 5479-5485.
158. Ebbesen, S.D., B.L. Mojet, and L. Lefferts, *CO adsorption and oxidation at the catalyst-water interface: An investigation by attenuated total reflection infrared spectroscopy*. *Langmuir*, 2006. 22(3): p. 1079-1085.

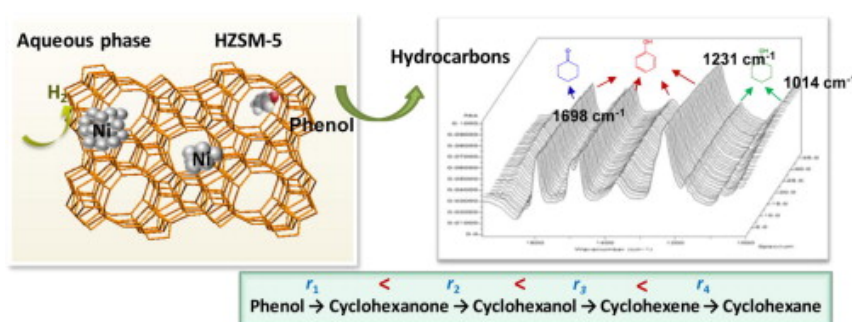
159. Meemken, F., et al., *Platinum-Catalyzed Asymmetric Hydrogenation: Spectroscopic Evidence for an O-H-O Hydrogen-Bond Interaction between Substrate and Modifier*. *Angewandte Chemie International Edition*, 2012. 51(33): p. 8212-8216.
160. Meemken, F., K. Hungerbühler, and A. Baiker, *Monitoring Surface Processes During Heterogeneous Asymmetric Hydrogenation of Ketones on a Chirally Modified Platinum Catalyst by Operando Spectroscopy*. *Angewandte Chemie International Edition*, 2014. 53(33): p. 8640-8644.
161. Mul, G., G.M. Hamminga, and J.A. Moulijn, *Operando ATR-FTIR analysis of liquid-phase catalytic reactions: can heterogeneous catalysts be observed?* *Vibrational spectroscopy*, 2004. 34(1): p. 109-121.
162. Pintar, A., et al., *In situ monitoring of catalytic three-phase enantioselective hydrogenation using FTIR/ATR spectroscopy*. *Applied Catalysis A: General*, 2004. 264(1): p. 1-12.
163. Wawrzetz, A., et al., *Towards understanding the bifunctional hydrodeoxygenation and aqueous phase reforming of glycerol*. *Journal of Catalysis*, 2010. 269(2): p. 411-420.
164. Wirz, R., et al., *Absolute configuration modulation attenuated total reflection IR spectroscopy: an in situ method for probing chiral recognition in liquid chromatography*. *Analytical chemistry*, 2004. 76(18): p. 5319-5330.
165. Garnett, J.M., *Colours in Metal Glasses and in Metallic Films.[Abstract]*. *Proceedings of the Royal Society of London*, 1904: p. 443-445.
166. Bruggeman, V.D., *Berechnung verschiedener physikalischer Konstanten von heterogenen Substanzen. I. Dielektrizitätskonstanten und Leitfähigkeiten der Mischkörper aus isotropen Substanzen*. *Annalen der physik*, 1935. 416(8): p. 665-679.
167. Triantafyllidis, K., A. Lappas, and M. Stöcker, *The Role of Catalysis for the Sustainable Production of Bio-fuels and Bio-chemicals*. 2013: Newnes.

Chapter II.

Comparison of Ni/HZSM-5 and Ni/Al₂O₃-HZSM-5 catalysts for phenol hydrodeoxygenation

Abstract

We have investigated the detailed kinetics of phenol hydrodeoxygenation in aqueous medium over Ni supported on HZSM-5 or HZSM-5 with 19.3 wt.% γ -Al₂O₃ binder. The



individual reaction steps on two Ni catalysts followed the rate order r_1 (phenol hydrogenation) < r_2 (cyclohexanone hydrogenation) < r_3 (cyclohexanol dehydration) \ll r_4 (cyclohexene hydrogenation), so that phenol hydrogenation was the rate determining step. As Ni/Al₂O₃-HZSM-5 showed up to five times higher catalytic activity for phenol hydrogenation than Ni/HZSM-5, it also delivered higher rates for overall phenol hydrodeoxygenation, verified by both the kinetic study monitored by GC and in situ IR spectroscopy to trace the product concentrations. Under the present conditions, Ni leaching was almost negligible from Ni/Al₂O₃-HZSM-5 after 90 h. The HZSM-5 support was stable, but the Al₂O₃-HZSM-5 support lost 7 wt.%. The catalytic activity gradually decreased when catalyst was recovered and reused, mainly due to Ni particle sintering tracked by transmission electron microscopy. The change of acid sites on the fresh and used catalysts monitored by IR of adsorbed pyridine demonstrated that Brønsted acid sites of HZSM-5 could be irreversibly transformed to Lewis acid sites during calcination.

1. Introduction

Awareness of global warming and diminishing crude oil reserves promotes focus on alternative sustainable fuel supplies. Biomass to liquid (BtL) process is a promising route to produce high-energy density fuels. ^[1] Usually, two methods are applied for bio-oil production, (i) fast pyrolysis or liquefaction of biomass at fixed condition (temperature > 700 K) ^[2]; (ii) catalytic depolymerization of biomass at relatively milder conditions. ^[3] The depolymerized moieties, however, are prone to repolymerize to form tars via radical reactions even at ambient temperature. Recently, we developed a novel method using boric acid as protecting agent to hydrolyze lignin in alkaline aqueous solution, achieving a phenolic monomer yield up to 85 wt.%. ^[4] In the step following hydrolysis, selective hydro-processing, for example, the hydrodeoxygenation (HDO) technique for removing the high oxygen content (up to 50 wt.%) in biomass ^[1,5], is required for hydrocarbon production. The traditional hydrotreating catalysts such as sulfided CoMo and NiMo, however, leach sulfur and are rapidly deactivated by oxygenates and ubiquitous water. ^[6]

Sulfur-free bifunctional catalysts with metal and acid sites have been developed for hydrodeoxygenation via consecutive hydrogenation and dehydration steps at mild conditions (473 – 523 K, 4 MPa H₂). Our first generation catalysts combined Pd/C (noble metal) and H₃PO_{4(aq)} ^[7,8], progressing to the second generation comprising bulk Raney Ni (base metal) together with Nafion/SiO₂ (solid acid). ^[9] Recently, we developed the third-generation Pd/HZSM-5 and Ni/HZSM-5 catalysts ^[10-12], which were effective, scalable, and stable for the target hydrodeoxygenation process.

To enhance the hydrodeoxygenation activity, we have incorporated Ni particles into the HZSM-5 support with a 19.3 wt.% fraction of γ -Al₂O₃ binder. Herein, we compared the detailed kinetics of elementary steps involved in phenol hydrodeoxygenation. The hydrodeoxygenation was also tested on lignin-derived substituted phenols such as guaiacols. The tendency to leach Ni and weight loss was measured at the reaction hydrothermal conditions in the autoclave reactor or with acetic acid in the Soxhlet apparatus. In addition, the catalyst stability was evaluated by recovering catalyst and then starting new batch runs. Associated changed metal sites were diagnosed by TEM, and changed acid sites were measured by IR of adsorbed pyridine.

2. Experimental section

2.1 Chemicals

All chemicals were purchased from commercial suppliers: phenol (Sigma-Aldrich, 99.5%), cyclohexanone (Sigma-Aldrich, 99%), cyclohexanol (Sigma-Aldrich, 99%), cyclohexene (Sigma-Aldrich, 99%), 4-n-propylguaiacol (SAFC, >99%), Ni(NO₃)₂·6H₂O (Sigma-Aldrich, 99%), HZSM-5 (Süd Chemie AG München, powder, 0.5 μm), and bound HZSM-5 (γ-Al₂O₃-HZSM-5, Süd Chemie AG München, cylindrical pellet 5 mm * 5 mm * 3cm). The Si/Al ratio in the HZSM-5 was 45. The binder was γ-Al₂O₃ comprising 21.2 wt.% of the pellets. Gases in this study included air (Air Liquide, 20.5 vol.% O₂ and 79.5% vol.% N₂), N₂ (Air Liquide, >99.999%), He (Air Liquide, >99.999%), and H₂ (Air Liquide, > 99.999%).

2.2 Catalyst preparation

A 9.2 wt.% Ni/HZSM-5 (BET surface area: 383 m² g⁻¹), 7.0 wt.% Ni/Al₂O₃-HZSM-5 (BET surface area: 360 m² g⁻¹), and 9.3% Ni/Al₂O₃-HZSM-5 (BET surface area: 351 m² g⁻¹) catalysts were prepared by the wetness impregnation method. Ni(NO₃)₂·6H₂O (20 g) was dissolved in water (20 ml), and the aqueous solution was slowly dropped into HZSM-5 or Al₂O₃-HZSM-5 with stirring. After the metal incorporation for 2 h, the catalyst was dried at 373 K for 12 h, air-calcined (flow rate: 100 ml min⁻¹) at 673 K for 4 h, and reduced under a H₂ flow (flow rate: 100 ml min⁻¹) at 733 K with a heating rate of 2 K min⁻¹.

2.3 Catalyst characterization

2.3.1 Atomic absorption spectroscopy (AAS)

Atom absorption spectroscopy with a UNICAM 939 AA-Spectrometer determined the Ni content of the catalysts and Ni concentrations in water for the leaching experiments.

2.3.2 Infrared (IR) spectroscopy of adsorbed pyridine

IR spectra of adsorbed pyridine were measured on a Perkin-Elmer 2000 spectrometer operated at a resolution of 4 cm⁻¹. The catalyst samples were activated in vacuum (p = 10⁻⁶ mbar) at 673 K for 1 h before the IR investigation. The activated catalyst samples were then exposed to pyridine (p_{Py} = 10⁻¹ mbar) at 423 K for 0.5 h. The spectra were recorded at 423 K after evacuation for 1 h, continuing sweeps until equilibrium was achieved. The concentrations of Brønsted acid sites (BAS) and Lewis acid sites (LAS) are determined from the integrated intensities of peaks at ca. 1540 cm⁻¹ and 1450 cm⁻¹,

respectively. The molar extinction coefficients published by Emeis were used for quantification.^[13]

2.3.3 Transmission electron microscopy (TEM)

For TEM measurements, an ultra-sonicated methanol suspension of the solid samples was dropped onto a carbon-coated Cu grid. The TEM images were recorded on a JEM-2010 Jeol transmission microscope operated at 120 kV. 300 particles were counted for size calculation.

2.3.4 H₂ chemisorption

Before the H₂ chemisorption, the reduced Ni catalysts were activated in vacuum at 588 K for 1 h and then cooled to ambient temperature. Subsequently, the H₂ adsorption isotherm was measured between 1 and 40 kPa. The sample was then outgassed at ambient temperature for 1 h, and a second isotherm measured physisorbed hydrogen. The hydrogen chemisorbed on Ni was the difference between intercepts of the isotherms extrapolated to zero H₂ pressure. Ni dispersions were estimated assuming chemisorption stoichiometry of H/Ni_{surf} = 1.

2.4 Catalytic measurements

2.4.1 Kinetic study of phenol hydrodeoxygenation network

Based on the reaction network of aqueous-phase hydrodeoxygenation of phenol to cyclohexane over Ni/HZSM-5^[7-10], the kinetic study was separated into four steps: (i) phenol hydrogenation, (ii) cyclohexanone hydrogenation, (iii) cyclohexanol dehydration, and (iv) cyclohexene hydrogenation. For reaction measurements quantities of reactants, catalysts in 80 ml H₂O were as follows: (a) phenol (5.0 g), Ni/Al₂O₃-HZSM-5 (0.1 g); (b) cyclohexanone (10.0 g), Ni/Al₂O₃-HZSM-5 (0.050 g); (c) cyclohexanol (12.5 g), Ni/Al₂O₃-HZSM-5 (0.050 g); and (d) cyclohexene (35.0 g), Ni/Al₂O₃-HZSM-5 (0.050 g).

A typical reaction was carried out in an autoclave batch reactor (Parr, Series 4843, 300 ml). After loading the reactant, catalyst, and water, the reactor was flushed three times with N₂. At reaction temperature, H₂ was charged to 5 MPa and the reaction time initiated. Each of the hydrodeoxygenation intermediates was reacted individually for 20, 40, 60, 80, 100 and 120 min at a stirring speed of 700 rpm. For calculation of apparent activation energies, the reactions were measured at 433, 453, 473 to 493 K and reaction times of 100 min.

After the reactor was cooled to room temperature, the H₂ pressure was released and the organic phase was extracted with ethyl acetate (3 x 20 ml). The organic phase and the

carbon balance in the aqueous phase were analyzed by gas chromatography (GC, Shimadzu 2010) with a HP-5 capillary column (30 m x 250 μm) and flame ionization detector (FID). In addition, a gas chromatograph-mass spectrometer (GC-MS, Shimadzu QP 2010S) was used to identify the organic compounds. Since it is a biphasic reaction, these kinetic data were collected after separate batch runs with different duration times and temperatures. The gas phase was determined by GC (HP 6890) equipped with a plot Q capillary column (30 m x 250 μm) with thermal conductivity detector (TCD).

2.4.2 In situ IR spectroscopic studies of phenol hydrodeoxygenation

The in situ IR spectroscopic study used the React IR device (Mettler Toledo, React IR 1000) coupled to a Parr reactor (100 ml). A diamond placed in the bottom of the autoclave was used as a probe to collect the in situ IR spectra in the liquid phase. First, a background spectrum was collected at reaction conditions (473 K, 4 MPa H_2) with 0.5 g catalyst dispersed in 50 ml water. Then, the autoclave reactor was loaded with the reactant phenol (5.0 g), and H_2 (4 MPa) was charged into the system after reaction temperature (473 K) had reached. The spectra were collected at every 10 min for 360 min. To normalize the IR absorbance value, for example, the phenol adsorption intensities at 1231 cm^{-1} are recorded as $A_1, A_2, A_3, A_4 \dots$, and the normalized values are $1, A_2/A_1, \dots, A_n/A_1$. For normalizing cyclohexanone (B_1, B_2, B_3, B_4) adsorption intensities at 1698 cm^{-1} , the normalized values are $0, (B_2-B_1)/B_1, \dots, (B_n-B_1)/B_1$. Cyclohexanol intensity normalization is similar to the treatment on cyclohexanone.

2.4.3 Hydrodeoxygenation of phenol and substituted phenol monomers

In the typical experiment for hydrodeoxygenation of phenol and substituted phenol monomers, first a mixture of reactant (0.01 mol), H_2O (80 ml), and Ni/HZSM-5 or Ni/ Al_2O_3 -HZSM-5 (0.5 g) was charged into the reactor. After flushing the reactor with H_2 three times, reaction started at 473 or 523 K in 4 MPa H_2 and continued for 0.5 h. After reaction, the workup was as described in section 0.

2.4.4 Catalyst leaching at the hydrothermal and acidic hydrothermal conditions

The leaching of Ni/HZSM-5 and Ni/ Al_2O_3 -HZSM5 catalysts was tested in a Soxhlet apparatus equipped with a Whatman extraction thimble (33 x 130 mm, thickness 1.5 mm) loaded with 2.0 g catalyst, and water (350 ml) or an acetic acid aqueous solution (15 wt.%, 350 ml) in the two-necked round bottom flask (500 ml). After the system began to reflux a 3 ml aliquot was collected at every 12 hours for 120 h.

Ni leaching was also evaluated in the autoclave loaded with 2.0 g catalysts in 80 ml water at 473 K under H_2 (4 MPa) and stirred at 700 rpm, for 72 h. AAS was used to analyze the

Ni concentration in the aqueous phase and in remaining Ni catalysts, and the weight losses of the Ni catalysts before and after hydrothermal treatment were also measured.

2.4.5 Catalyst recycle

Catalyst recycling procedure for phenol hydrodeoxygenation was as follows: a mixture of phenol (8.0 g), catalyst (2.0 g), and water (80 ml) was loaded into the autoclave and then reacted at 473 K in presence of 5 MPa H₂ at a stirring speed of 700 rpm for 30 min. After the first reaction run, the organic phase was extracted by ethyl acetate and analyzed by GC and GC-MS. The catalyst was separated from the aqueous phase by centrifugation, and ~ 0.1 g of the used catalyst was sampled to characterize the catalyst state by TEM and IR spectroscopy of adsorbed pyridine. The catalyst was then washed by acetone and water, dried at 383 K overnight, and activated in H₂ before its reuse in the next run. Four recycling runs were conducted in the present work for phenol hydrodeoxygenation with Ni/HZSM-5 and Ni/Al₂O₃-HZSM-5 catalysts.

3. Results and Discussion

3.1 Characterization of catalyst properties

Physical characteristics of the two Ni catalysts are summarized in . The Ni contents were 9.2 and 9.3 wt.% for Ni/HZSM-5 and Ni/Al₂O₃-HZSM-5 catalysts, respectively, with HZSM-5 framework Si/Al ratios of 90. The Al₂O₃-HZSM-5 support contained 21.2 wt.% Al₂O₃ binder, which was decreased to 19.3 wt.% after metal incorporation.

Table 2-1. Physical characteristics of supported Ni catalysts.

Catalyst	Composition (wt.%)			Acidity ($\mu\text{mol}\cdot\text{g}^{-1}$) ^a		d_{Ni} (nm) ^b	D_{Ni} (%) ^c
	Ni	Al ₂ O ₃ binder	Si/Al ratio in framework	BAS	LAS		
Ni/HZSM-5	9.2	-	90	70	21	35 ± 13	2.5
Ni/Al ₂ O ₃ -HZSM-5	9.3	19.3	90	45	46	8.8 ± 1.6	8.0

^a Determined by IR spectra of adsorbed pyridine, BAS: Brønsted acid site, LAS: Lewis acid site.

^b Determined by TEM images (300 particles are counted for size calculation).

^c Determined by H₂ chemisorption.

The Brønsted (BAS) and Lewis acid sites (LAS) were distinguished and quantified by IR spectra of adsorbed pyridine (Py-IR). The BAS concentration of Ni/Al₂O₃-HZSM-5 (45 $\mu\text{mol}\cdot\text{g}^{-1}$) was 65% of that of Ni/HZSM-5 (70 $\mu\text{mol}\cdot\text{g}^{-1}$). Conversely the LAS concentration of Ni/Al₂O₃-HZSM-5 (46 $\mu\text{mol}\cdot\text{g}^{-1}$) was more than double that of Ni/HZSM-5 catalyst (21 $\mu\text{mol}\cdot\text{g}^{-1}$) due to the added Al₂O₃-binder.

Determined by TEM images, the Ni⁰ particle size of Ni/Al₂O₃-HZSM-5 was 8.8 nm with a narrow standard deviation of 1.6 nm. By comparison, the mean Ni cluster size of Ni/HZSM-5 catalysts was 35 nm with a much broader standard deviation of 13 nm. The metal dispersion (determined by H₂ chemisorption) in Ni/Al₂O₃-HZSM-5 (8.0%) was three times higher than in Ni/HZSM-5 (2.5%), agreeing quite well with TEM results.

A more detailed comparative characterization on the supported Ni catalysts including the chemical composition (AAS), BET surface areas (N₂ sorption), morphology (SEM), crystalline (XRD), accessible Ni sites (H₂ chemisorption and IR of adsorbed CO), Ni environmental chemistry and geochemistry (EXAFS and XANES), acid sites (TPD of NH₃ and IR of adsorbed pyridine), metal-support interaction (TPR-H₂), and adsorption capacities towards reactant and intermediates (IR of adsorbed species) has been reported in the previous publication of our group. ^[14]

3.2 Phenol hydrodeoxygenation network

Phenol hydrodeoxygenation involves the sequential reactions shown in Scheme 1-2, phenol hydrogenation (Step 1), cyclohexanone hydrogenation (Step 2), cyclohexanol dehydration (Step 3), and final cyclohexene hydrogenation (Step 4). We studied such sequence previously over the dual or bi- functional catalysts combining metals Pd, Pt, Ru, Rh, and Ni together with mineral acids H_3PO_4 and CH_3COOH or solid acid Nafion[®] [8-12], in aqueous solution at 473-523 K in presence of H_2 . In the overall reaction, the metal sites catalyze the hydrogenations of phenol, cyclohexanone, and cyclohexene, and the acid sites dehydrate the intermediate cyclohexanol to cyclohexene. In the gas phase, hydrogenolysis of phenol and cyclohexanol forming benzene and cyclohexane, respectively, were common side-reactions over the supported Pt or Ni. [15,16] The hydrogenolysis and hydrogenation reactions were parallel, leading to a consequent complex reaction network. But hydrogenolysis was negligible in the aqueous phase over the present Ni catalysts.

3.3 Kinetic of four elementary reactions in phenol hydrodeoxygenation

3.3.1 Phenol hydrogenation

The rate of phenol hydrogenation was measured with a batch reactor at 473 K in presence of 5 MPa H_2 . To avoid the conversion during heating from ambient temperature, the hydrogen was introduced into the reactor after the required temperature was achieved and the reaction time was recorded from that time. After required time the reaction was quenched by ice to ambient temperature in less than 2 min. Since these are always two-phase reactions, the rate data were collected at separate batch duration times, but not by in situ sampling. The reaction rates and turnover frequencies (TOFs) reported correspond to initial conversions.

The rate data and E_a calculation for phenol hydrogenation over two Ni catalysts are plotted in Figure 2-1, where conversion describes declining phenol concentration in the aqueous phase. The products included cyclohexanone, cyclohexanol, and cyclohexanes on the bifunctional Ni/ Al_2O_3 -HZSM-5 catalysts, but no benzene. Also no ring-opening products including C_1 - C_6 alkanes were found in the gas phase. Thus with the present catalysts, hydrogenation but not hydrogenolysis was the exclusive route for phenol conversion. Figure 2-1 shows that the conversion increased linearly during 20 to 120 min on both catalysts. Determined from the slopes in Figure 2-1, the initial rates of phenol hydrogenation over Ni/HZSM-5 and Ni/ Al_2O_3 -HZSM-5 were 14 and 61 $\text{mmol}\cdot\text{g}^{-1}\cdot\text{h}^{-1}$, respectively. If the rates are normalized to per mole of surface Ni atoms, TOFs of individual reactions were respectively 398 and 553 $\text{mol}\cdot\text{mol}_{\text{Surf. Ni}}^{-1}\cdot\text{h}^{-1}$. In our previous test

with Pd/C [9], Pd showed a much higher TOF of 4200 h^{-1} than Ni in Ni/HZSM-5 (398 h^{-1}) at comparable conditions for phenol hydrogenation. The apparent activation energies for the reaction steps were calculated from the TOFs at 423, 453, 473, and 493 K. The activation energies for phenol hydrogenation were 48 and $56 \text{ kJ}\cdot\text{mol}^{-1}$ on Ni/HZSM-5 and Ni/Al₂O₃-HZSM-5, respectively.

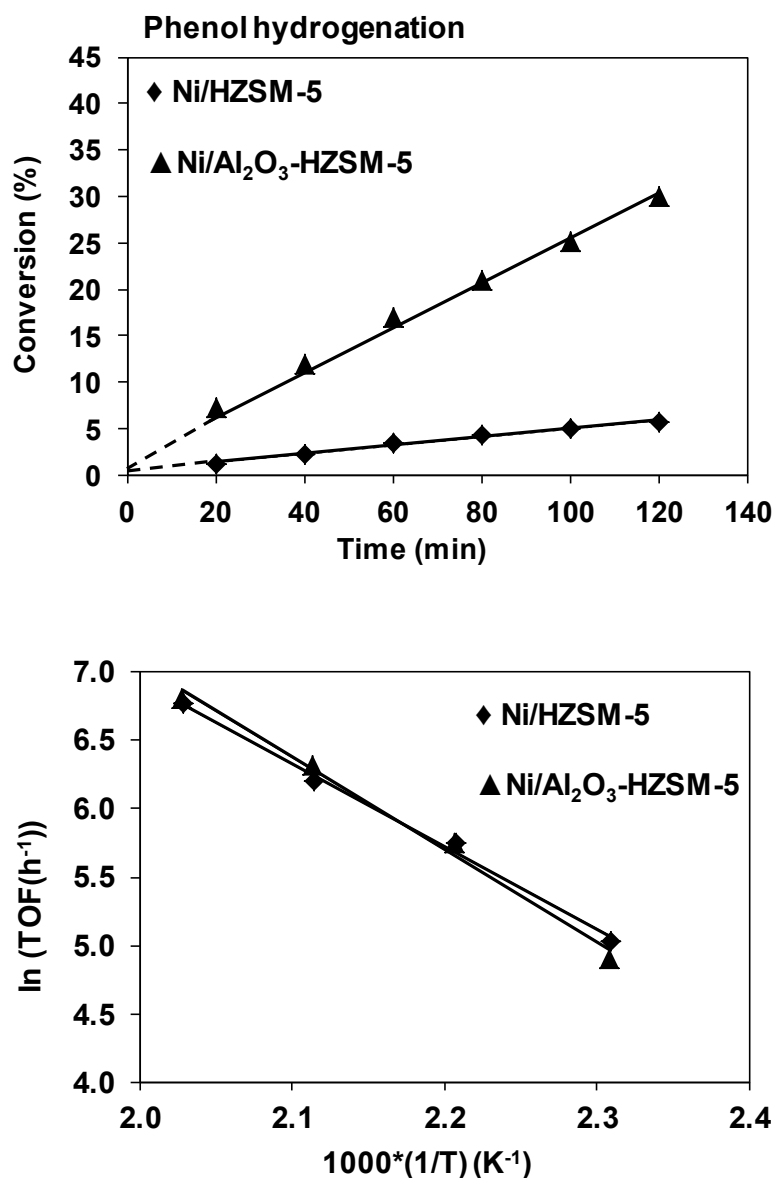
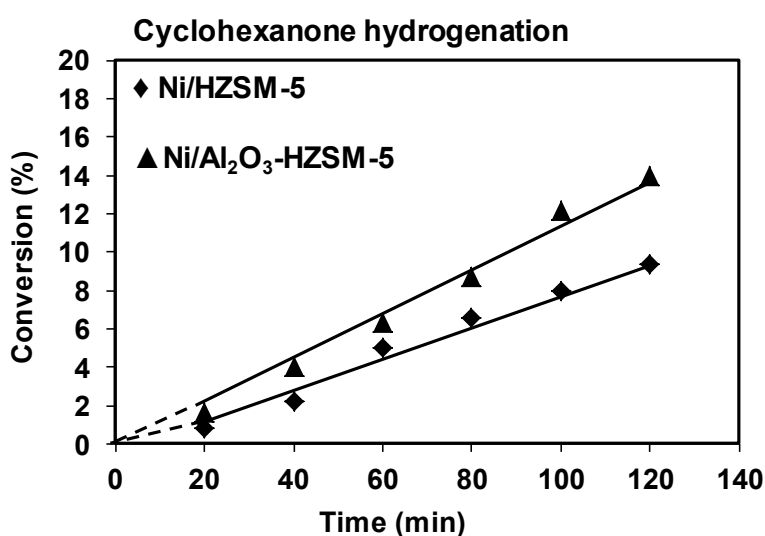


Figure 2-1. Phenol hydrodeoxygenation over Ni/HZSM-5 and Ni/Al₂O₃-HZSM-5 at 473 K as a function of time, and E_a calculation at 100 min and 423, 453, 473, 493 K. Reaction conditions: phenol (5.0 g), Ni/HZSM-5 (9.2 wt.%, 0.1 g) or Ni/Al₂O₃-HZSM-5 (9.3 wt.%, 0.1 g), 5 MPa H₂, stirred at 700 rpm.

3.3.2 Cyclohexanone hydrogenation

The rates of hydrogenation of cyclohexanone were measured at the same conditions (473 K, 5 MPa H₂). The conversions graphed in Figure 2-2 had linear increase against reaction time. Ni/Al₂O₃-HZSM-5 yielded a much higher hydrogenation rate (159 mmol·g⁻¹·h⁻¹) compared to Ni/HZSM-5 (108 mmol·g⁻¹·h⁻¹) for cyclohexanone hydrogenation, which follows the same hydrogenation trend in phenol. But the rates for cyclohexanone hydrogenation were much higher than those for phenol hydrogenation. If calculated from the exposed Ni atoms, the TOF on Ni/Al₂O₃-HZSM-5 (1233 mol·mol_{Surf. Ni}⁻¹·h⁻¹) was much lower than that on Ni/HZSM-5 (2443 mol·mol_{Surf. Ni}⁻¹·h⁻¹). In the case of Pd/C catalyzed hydrogenation^[9], the rate on cyclohexanone hydrogenation (21000 mol·mol_{Surf. Pd}⁻¹·h⁻¹) was also much higher than that of phenol hydrogenation (4200 mol·mol_{Surf. Pd}⁻¹·h⁻¹).

If considering that Ni/Al₂O₃-HZSM-5 showed five times higher phenol hydrogenation rates compared to Ni/HZSM-5, it is also indicated that the cyclohexanone hydrogenation on Ni/Al₂O₃-HZSM-5 was dramatically suppressed in which only shows a rate ratio of 1.5 times to Ni/HZSM-5. It has been reported that that Lewis acid such as AlCl₃ favor stabilizing the cyclohexanone^[17], which would suppress the keto-enol isomeric equilibrium shift towards cyclohexanol formation. IR spectroscopy^[17] showed that the absorption band of the C=O stretching vibration shifted from 1714 cm⁻¹ in the absence of AlCl₃ to 1624 cm⁻¹ in the presence of AlCl₃, which is attributed to the coordination of the Lewis basic C=O group to the Lewis acid. Thus, the cyclohexanone hydrogenation rate is concluded to be kinetically hindered in the presence of a high fraction of Al₂O₃ binder (Lewis acid sites) over Ni/Al₂O₃-HZSM-5. In addition, the apparent activation energies for cyclohexanone hydrogenation were 142 and 129 kJ·mol⁻¹ on Ni/Al₂O₃-HZSM-5 and Ni/HZSM-5 (see Figure 2-2), respectively.



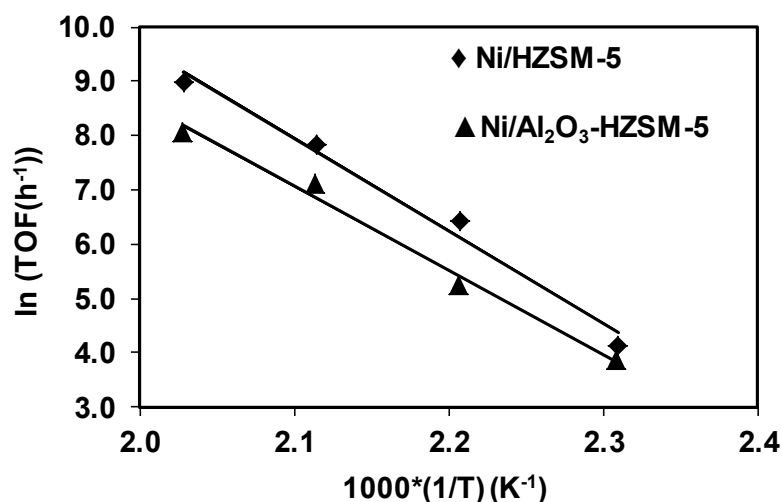


Figure 2-2. Cyclohexanone hydrodeoxygenation over Ni/HZSM-5 and Ni/ Al₂O₃-HZSM-5 at 473 K as a function of time, and E_a calculation at 100 min and 423, 453, 473, 493 K. Reaction conditions: cyclohexanone (10 g), Ni/HZSM-5 (9.2 wt.%, 0.05 g), Ni/Al₂O₃-HZSM-5 (9.3 wt.%, 0.05 g), 5 MPa H₂ (reaction temperature), stirred at 700 rpm.

3.3.3 Cyclohexanol dehydration

The conversion versus time and the Arrhenius graphs for cyclohexanol dehydration over Ni/Al₂O₃-HZSM-5 and Ni/HZSM-5 catalysts are shown in Figure 2-3. The dehydration rate on Ni/HZSM-5 (528 mmol·g⁻¹·h⁻¹) was much higher than on Ni/Al₂O₃-HZSM-5 (354 mmol·g⁻¹·h⁻¹). In our previous work, we compared the cyclohexanol dehydration rates over γ -Al₂O₃, amorphous silica alumina (ASA), Nafion, Amberlyst in water at 200 °C, and the results showed that Brønsted acid sites (BAS) were active sites for dehydration in hot water and Lewis acid sites (LAS) on γ -Al₂O₃ was almost inactive for such reaction in aqueous phase [11]. Thus, the higher dehydration rate on Ni/HZSM-5 is attributed to its higher concentrations of BAS (0.070 mmol·g⁻¹) than with Ni/Al₂O₃-HZSM-5 (0.045 mmol·g⁻¹) (Table 2-1) and these BAS were in closer proximity to the metal sites in the catalyst Ni/HZSM-5 without the binder. If normalized to the concentration of BAS, the respective dehydration TOFs were 7428 and 8333 mol·mol_{BAS}⁻¹·h⁻¹ on Ni/HZSM-5 and Ni/Al₂O₃-HZSM-5, respectively. In previous study with Pd/C and H₃PO₄ bifunctional catalysts [9], it was shown that the dehydration step was rate determining for overall phenol hydrodeoxygenation with a low dehydration TOF of 15 mol·mol_{H+}⁻¹·h⁻¹ over H₃PO₄. But in this case with HZSM-5 based catalysts, the dehydration rates (TOF) are 500 times higher compared to H₃PO₄. Without Ni, on the pure HZSM-5 the dehydration rate was 1600 mol·mol_{BAS}⁻¹·h⁻¹ [11], which was much slower than Ni incorporated Ni/HZSM-5 (7428 mol·mol_{BAS}⁻¹·h⁻¹). This indicates that the dehydration-hydration occurs in an equilibrium in an aqueous solution, and the additional Ni consumes the dehydrated cyclohexene and

accelerates so the dehydration rate to some extent. The dehydration activation energies on two present catalysts were indistinguishable at 112 and 114 kJ·mol⁻¹.

Dehydration of an alcohol might be inhibited in liquid water. But here the dehydration rate is greatly enhanced with porous material zeolite compared to other solid acids such as Amberlyst, Nafion, H₂SO₄/ZrO₂, and heteropoly acid^[11], which is mainly attributed to the fact that either the cyclohexanol adsorption was highly enhanced on HZSM-5 active sites other than Brønsted solid acids^[11,12] or the narrow pore of HZSM-5 prevent the formation of alcohol oligomer, and hence by promote the equilibrium shift towards alcohol monomer formation and accelerate so the dehydration rates.^[18]

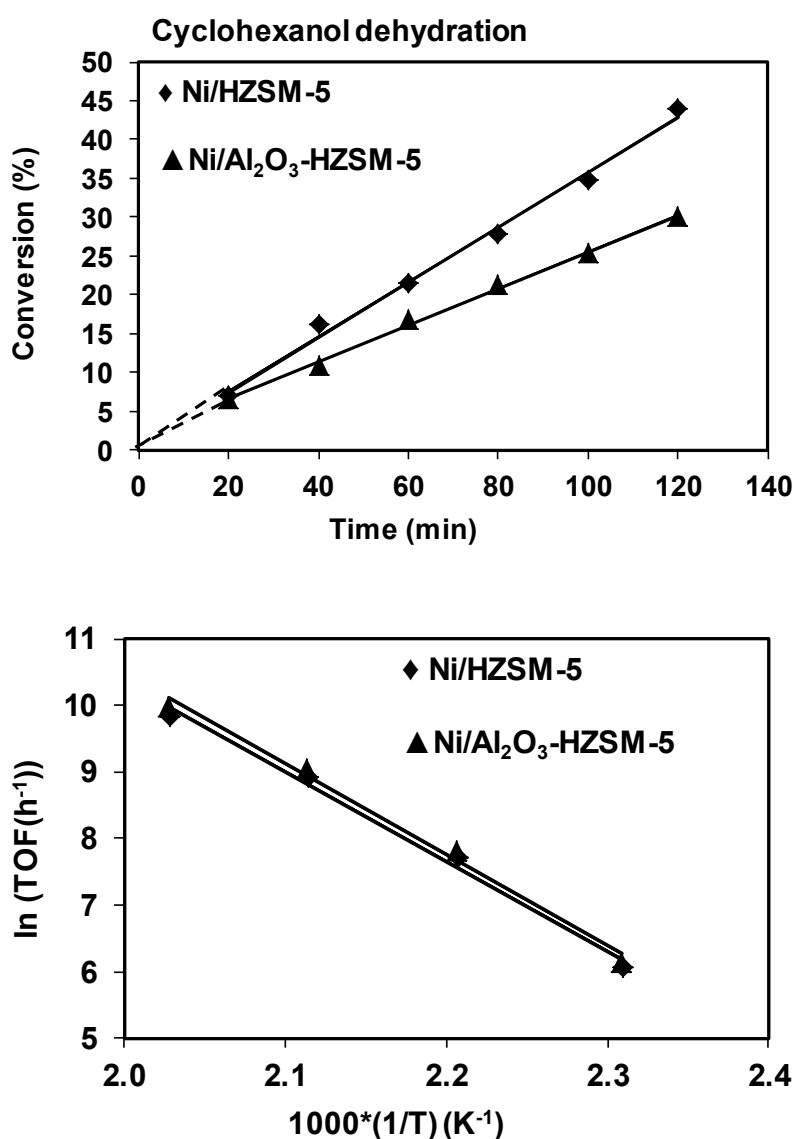


Figure 2-3. Cyclohexanol dehydration over Ni/HZSM-5 and Ni/ Al₂O₃-HZSM-5 at 473 K as a function of time, and E_a calculation at 100 min and 423, 453, 473, 493 K. Reaction conditions: cyclohexanol (12.5 g), Ni/HZSM-5 (9.2 wt.%, 0.05 g), Ni/Al₂O₃-HZSM-5 (9.3 wt.%, 0.05 g), 5 MPa H₂ (reaction temperature), stirred at 700 rpm.

3.3.4 Cyclohexene dehydration

The fourth step involves the hydrogenation of C=C double bonds of cyclohexene in water over Ni metal sites. The conversions are plotted in Figure 2-4, in which the hydrogenation rate on Ni/Al₂O₃-HZSM-5 (2156 mmol·g⁻¹·h⁻¹) was slightly faster than that on Ni/HZSM-5 (1813 mmol·g⁻¹·h⁻¹). This result agrees with the reaction on hydrogenation of phenol and cyclohexanone where Ni/Al₂O₃-HZSM-5 was more active. The conversion (even up to 60%) was linear against reaction time, indicating zero reaction order for cyclohexene hydrogenation over both catalysts. The TOFs on Ni/Al₂O₃-HZSM-5 and Ni/HZSM-5 were 20287 and 55136 mol·mol_{Surf.}⁻¹·h⁻¹, which is approximately one tenth of the rate of Pd catalyzed cyclohexene hydrogenation with a TOF of 200000 h⁻¹.^[9] The obtained E_a were comparable at 35 and 25 kJ·mol⁻¹, respectively.

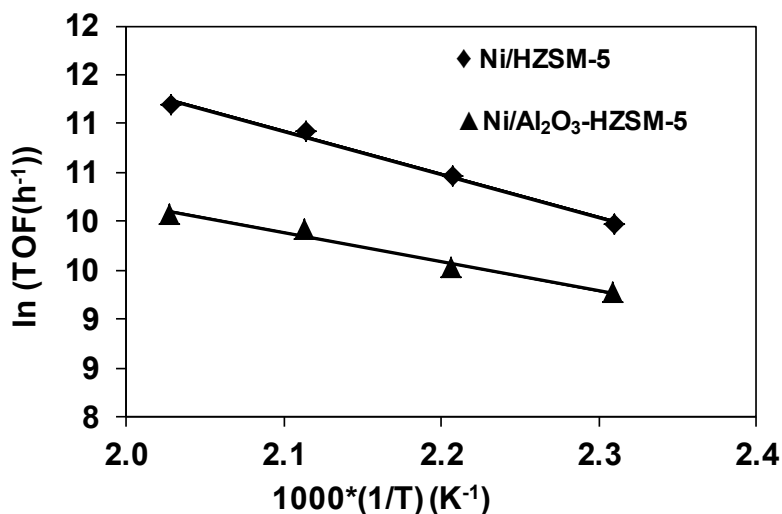
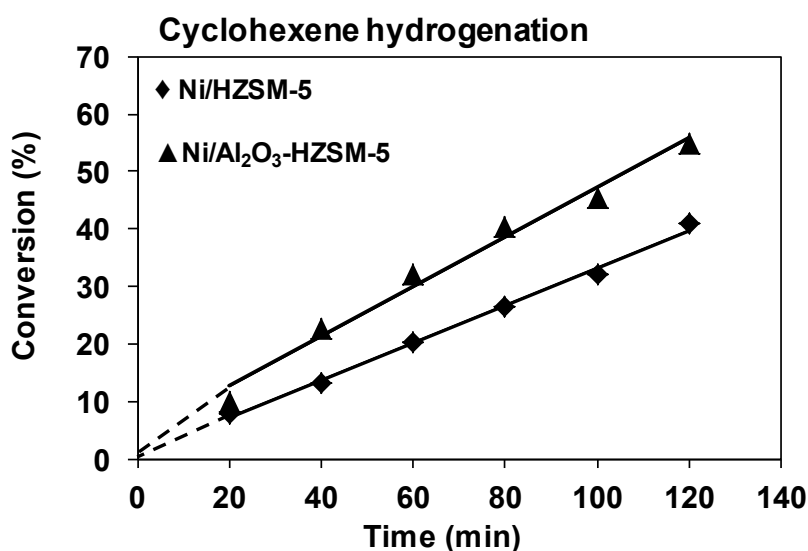


Figure 2-4. Cyclohexene hydrogenation over Ni/HZSM-5 and Ni/Al₂O₃-HZSM-5 at 473 K as a function of time, and E_a calculation at 100 min and 423, 453, 473, 493 K. Reaction conditions: cyclohexene (35 g), Ni/HZSM-5 (9.2 wt.%, 0.050 g), Ni/Al₂O₃-HZSM-5 (9.3 wt.%, 0.050 g), 5 MPa H₂ (reaction temperature), stirred at 700 rpm.

3.3.5 Summarized kinetic data for phenol hydrodeoxygenation reaction network

The rate data for the four steps over the Ni catalysts were summarized in Table 2-2. The four reactions in aqueous phase were either: (i) hydrogenations of phenol, cyclohexanone, and cyclohexene, without hydrogenolysis, or (ii) dehydration of cyclohexanol. The active hydrogenation sites were on the exposed Ni nanoclusters, while the dehydration was catalyzed by the BAS sites that were associated with the HZSM-5. In three hydrogenation reactions, Ni/Al₂O₃-HZSM-5 was consistently more active compared to Ni/HZSM-5. This is assigned to two factors. First the Ni/Al₂O₃-HZSM-5 catalyst had three times more accessible Ni sites than Ni/HZSM-5 verified by H₂ chemisorption and the IR spectroscopy of adsorbed CO.^[14] The second is related to the fact that Ni/Al₂O₃-HZSM-5 had higher adsorption capability for phenol, cyclohexanone, and cyclohexanol than Ni/HZSM-5.^[14] The phenol or ketone hydrogenation reactions usually showed positive reaction orders in organic and H₂ concentrations in the previous literature^[19], suggesting that the hydrogenation rates on phenol would be much higher. But the Lewis acid Al₂O₃ binder may have stabilized the ketone and inhibited its hydrogenation (Figure 2-2). In addition the cyclohexene hydrogenation had zero reaction order, and thus, cyclohexene hydrogenation rates on the two Ni catalysts were similar (Figure 2-4).

The dehydration reaction rate on Ni/HZSM-5 was slightly faster due to higher BAS density than on Ni/Al₂O₃-HZSM-5, but the apparent E_a on the catalysts were almost identical (112 and 114 kJ·mol⁻¹). It should be emphasized that the four elementary steps all showed comparable E_as on two Ni catalysts, and this is related to the fact that the adsorption heat of both reactant and product that could influence the apparent activation energy should be principally comparable, as the active sites and their surroundings are quite similar. The rates of phenol hydrodeoxygenation elementary steps on two Ni supported catalysts increased in the order as phenol hydrogenation < cyclohexanone hydrogenation < cyclohexanol dehydration, << cyclohexene hydrogenation. The phenol hydrogenation controlled the overall rate and hence the more active and accessible Ni nanoclusters on Ni/Al₂O₃-HZSM-5 yielded the more active catalyst. In addition, it should also be noted that the reaction rates gradually increase in the sequence of $r_1 < r_2 < r_3 < r_4$. This indicates that once the hydrogenation (r_1) starts, the produced cyclohexanone will be quickly converted through the increasingly faster subsequent hydrogenation and dehydration steps (r_2 , r_3 , and r_4). Thus it can be predicted that very small concentrations of intermediates were

present during the conversion. In contrast, the combination of Pd/C with H₃PO₄ [8,9] gave much greater hydrogenation rates than the dehydration, and thus cyclohexanol was accumulated. Note that the balance of metal and acid sites is crucial for optimized performance.

Table 2-2. TOF and E_a data for aqueous phase phenol hydrodeoxygenation reaction network at 473 K on Ni catalysts.

Reaction	Ni/HZSM-5	Ni/Al ₂ O ₃ -HZSM-5
Step 1: Phenol hydrogenation		
r_1 (mmol·g ⁻¹ ·h ⁻¹)	14	61
TOF ₁ (mol·mol _{Surf. Ni} ⁻¹ ·h ⁻¹)	398	553
E _{a1} (kJ·mol ⁻¹)	48	56
Step 2: Cyclohexanone hydrogenation		
r_2 (mmol·g ⁻¹ ·h ⁻¹)	108	159
TOF ₂ (mol·mol _{Surf. Ni} ⁻¹ ·h ⁻¹)	2443	1233
E _{a2} (kJ·mol ⁻¹)	142	129
Step 3: Cyclohexanol dehydration		
r_3 (mmol·g ⁻¹ ·h ⁻¹)	528	354
TOF ₃ (mol·mol _{BAS} ⁻¹ ·h ⁻¹)	7428	8333
E _{a3} (kJ·mol ⁻¹)	112	114
Step 4: Cyclohexene hydrogenation		
r_4 (mmol·g ⁻¹ ·h ⁻¹)	1813	2156
TOF ₄ (mol·mol _{Surf. Ni} ⁻¹ ·h ⁻¹)	55136	20287
E _{a4} (kJ·mol ⁻¹)	35	25

3.4 Kinetics of overall phenol hydrodeoxygenation over Ni catalyst

3.4.1 Time-resolved *in situ* IR spectroscopy study

Phenol hydrodeoxygenation was also monitored with time-resolved *in situ* IR spectroscopy. A catalyst charge of 0.5 g and 1.2 MPa H₂ (equipment limit) was employed in the *in situ* IR measurement. The time-resolved IR spectra measured during phenol hydrodeoxygenation over Ni/HZSM-5 and Ni/Al₂O₃-HZSM-5 catalysts are shown in Figure 2-5a and b, respectively.

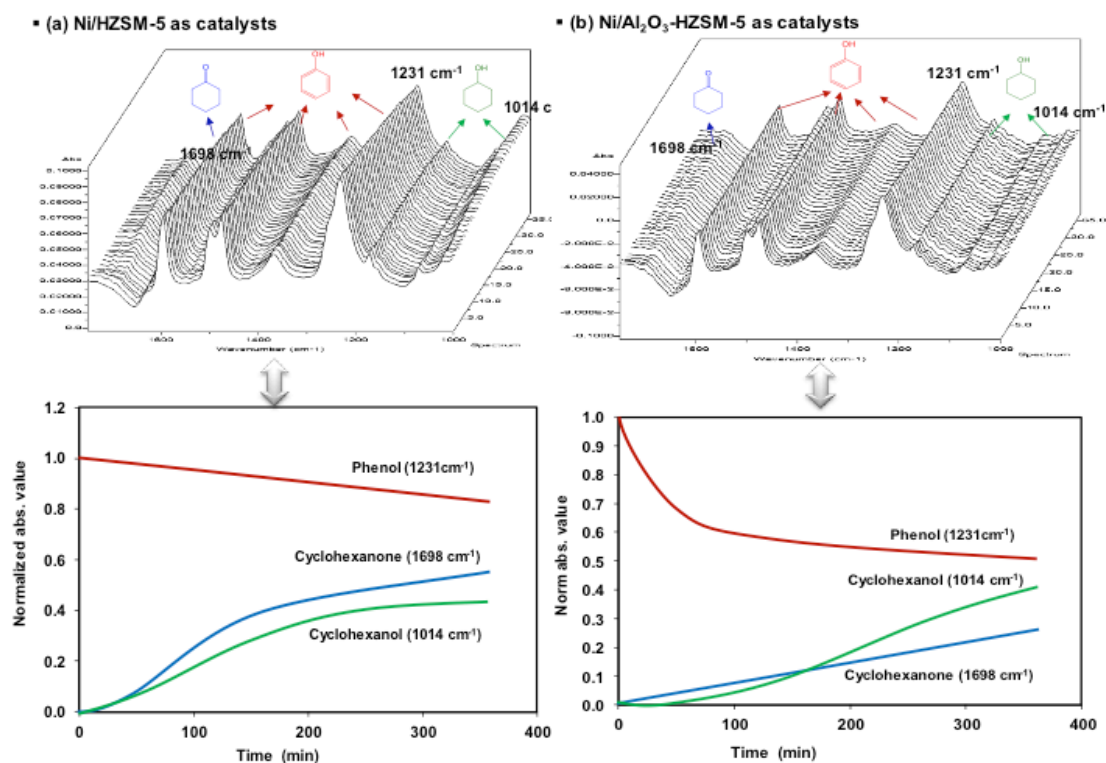


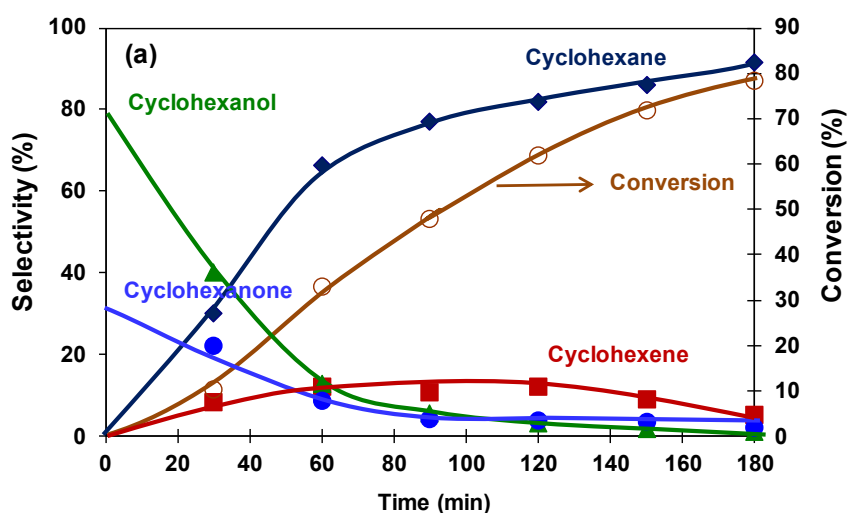
Figure 2-5. *In situ* IR spectra during aqueous phase phenol hydrodeoxygenation over (a) Ni/HZSM-5 and (b) Ni/Al₂O₃-HZSM-5. Reaction conditions: phenol (5.0 g), H₂O (50 ml), Ni/HZSM-5 (9.2 wt.%, 0.5 g), Ni/Al₂O₃-HZSM-5 (9.3 wt.%, 0.5 g), 473 K, 1.2 MPa H₂, stirred at 700 rpm.

The specific peaks for phenol (1231 cm⁻¹, aromatic OH bond stretch), cyclohexanone (1698 cm⁻¹, C=O stretch), and cyclohexanol (1014 cm⁻¹, alicyclic OH stretch) were monitored to flow concentrations of respective reactants. With increasing reaction time, the intensity of the IR peaks at 1698 cm⁻¹ (cyclohexanone) and 1014 cm⁻¹ (cyclohexanol) both increased and the intensity at 1231 cm⁻¹ (phenol) declined. The detected concentrations of intermediates remained low. Cyclohexene and cyclohexane were not detected because the diamond probe was in the aqueous phase, but those species segregated to the upper organic phase.

In the separate preliminary experiment, we have demonstrated that the substance (phenol, cyclohexanone, and cyclohexanol) concentration was proportional to the IR light absorbance, thus the normalized absorption value was plotted with the reaction time to reflect a changing concentration profile (see Figure 2-5). Seen from Figure 2-5, it can be obviously observed that the slope of decreasing phenol concentration was much slower with Ni/Al₂O₃-HZSM-5 than that with Ni/HZSM-5, in which the former phenol conversion rate (31.9 mmol·g⁻¹·h⁻¹) was 8.3 times higher than the latter one (3.8 mmol·g⁻¹·h⁻¹).

3.4.2 Impact of reaction time

For the reaction carried out in the batch autoclave, it was quenched after various reaction times to measure directly the concentrations of intermediates and products (Figure 2-6). At $t = 0$, the primary products were hydrogenated cyclohexanone (ca. 65% selectivity) and cyclohexanol (ca. 35% selectivity) from both Ni based catalysts. In agreement with the *in situ* IR study, Ni/Al₂O₃-HZSM-5 delivered higher initial phenol conversion rate (117 mmol·g⁻¹·h⁻¹) than Ni/HZSM-5 (21 mmol·g⁻¹·h⁻¹). After 3 h, reaction was complete over Ni/Al₂O₃-HZSM-5, while Ni/HZSM-5 only attained 72% yield. Note that these obtained rates for phenol hydrogenation monitored by GC were much higher than the data from reactions monitored by *in situ* IR spectroscopy, attributing to the applied higher hydrogen pressure (5 vs 1.2 MPa) in the former case. Cyclohexene intermediate was observed with selectivity lower than 10%, and by comparison cyclohexene was not detected at all with Pd catalyzed phenol hydrodeoxygenation ^[8,9], which is related to the one tenth activity for cyclohexene hydrogenation on Ni/HZSM-5 (2×10⁴ h⁻¹) compared to that on Pd/C (2×10⁵ h⁻¹). It has been found that cyclohexane quickly dominated the product distribution (70-80%) at 30-80% conversions, and the primary products of cyclohexanone and cyclohexanol decreased to quite low selectivity (5-10%) in a short time. This also fits for the comparison of elementary step rates in experimental kinetics monitored by GC and *in situ* IR spectroscopy that the increasingly faster r_1 to r_4 would lead to the final cyclohexane to be highly selective during phenol conversion.



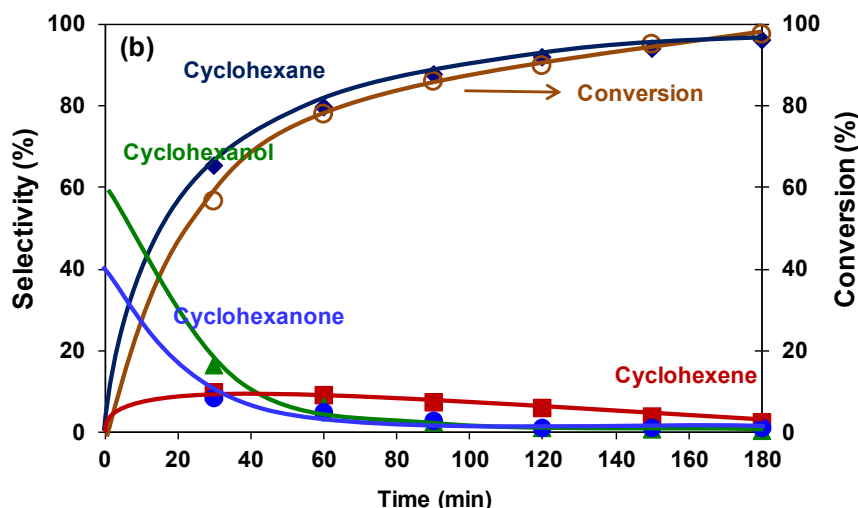


Figure 2-6. Hydrodeoxygenation of phenol over (a) Ni/HZSM-5 and (b) Ni/Al₂O₃-HZSM-5 at 473 K as a function of time. Reaction conditions: phenol (5 g), Ni/HZSM-5 (9.2 wt.%, 0.5 g), Ni/Al₂O₃-HZSM-5 (9.3 wt.%, 0.5 g), 5 MPa H₂, stirring at 700 rpm.

3.4.3 Impact of reaction temperature

The product distributions from the two catalysts at 433, 453, 473, and 493 K and 100 min were measured directly (Figure 2-7). At 433 K, Ni/HZSM-5 led to 2% conversion with a high selectivity of 90% cyclohexanone. The hydrogenation activity of Ni/Al₂O₃-HZSM-5 attained 2.5 times higher conversion (5%) than Ni/HZSM-5 under the same conditions. At the higher temperatures the cyclohexanone concentration at the end of 100 min decreased relative to the increase of cyclohexene and cyclohexane. Generally, Ni/Al₂O₃-HZSM-5 showed much higher temperature dependence towards hydrogenation (conversion from 10% to 35%) at temperatures from 433 to 493 K, while Ni/HZSM-5 led to only the slight increase from 5% to 10% at identical conditions. This is characteristic of a higher activation energy occurs on Ni/Al₂O₃-HZSM-5 (56 kJ·mol⁻¹) compared to Ni/HZSM-5 (48 kJ·mol⁻¹).

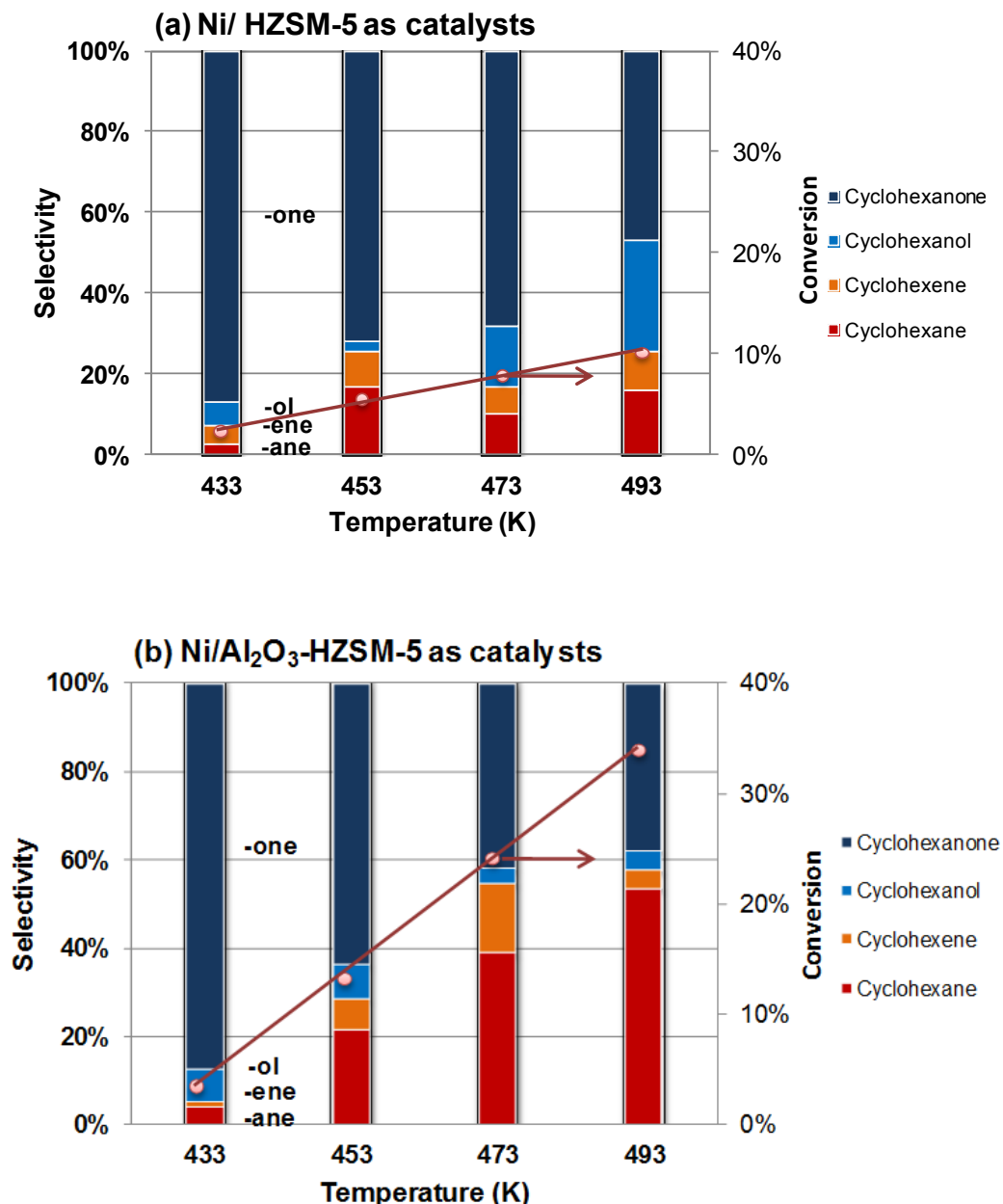


Figure 2-7. Hydrodeoxygenation of phenol over Ni/HZSM-5 (a) and Ni/Al₂O₃-HZSM-5 (b) as a function of temperature. Reaction conditions: phenol (5 g), Ni/HZSM-5 (9.2 wt.%, 0.1 g), Ni/ Al₂O₃-HZSM-5 (9.3 wt.%, 0.1 g), 433, 453, 473, 493 K, 5 MPa H₂, 100 min, stirred at 700 rpm.

3.5 Hydrodeoxygenation of substituted phenol monomers

Besides phenol, we are also interested in the performance of these catalysts for hydrodeoxygenation of more complex substituted phenols in aqueous medium. Depolymerized lignin products include alkyl- and methoxy- substituted phenols and here 4-*n*-propylphenol and 4-*n*-propylguaiacol were selected as model compounds to evaluate the two Ni catalysts (Table 2-3). The alkyl phenol reacted as fast as phenol. The Ni/Al₂O₃-HZSM-5 and Ni/HZSM-5 delivered C₉ hydrocarbon yields of 100% and 43%, respectively, after 0.5 h at 473 K. Even employed with only 7 wt.% Ni, the Al₂O₃-HZSM-5 support

delivered a 49% C₉ hydrocarbons yield in 0.5 h at 473 K, still higher than 9 wt.% Ni/HZSM-5 at the same conditions.

The 4-*n*-propylguaiacol, with both alkyl and methoxy groups on the phenol ring, reacted more slowly than phenol on the Ni catalysts. Conversions in 0.5 h at 473 K decreased to 15% with a selectivity of 3.7% C₉ hydrocarbons on Ni/HZSM-5 catalysts, and Ni/Al₂O₃-HZSM-5 led to a conversion of 26% with a selectivity of 15% C₉ hydrocarbons. This dramatically decreased activity is attributed to the increased stability of aromatic-ring with the added methoxy group, agreeing with our former results on hydrodeoxygenation of phenolic compounds over Pd catalysts that methoxy substituted phenol are more stable and requires higher temperature for further conversion.^[9] At 523 K, the conversions were increased to 21 and 55% with 100% selectivity to C₉ hydrocarbons. When the reaction was extended to 2 h, the conversion increased to 43% on Ni/HZSM-5 and to 62% on Ni/Al₂O₃-HZSM-5 with 100% alkane selectivity. The conversion to alkanes was increased to 100% in 2 h when the Ni loading was increased to 20 wt.% on HZSM-5 at identical conditions.^[13]

Table 2-3. Hydrodeoxygenation of lignin-derived substituted phenols on Ni catalysts.^a

Reactant	T (K)	Catalyst	Ni loading (wt.%)	Conv. (%)	Select. (C%)
					C ₉ hydrocarbon
4- <i>n</i> -propylphenol	473	Sample 1	7.0	49	100
4- <i>n</i> -propylphenol	473	Sample 2	9.3	43	100
4- <i>n</i> -propylphenol	473	Sample 1	9.2	100	100
4- <i>n</i> -propylguaiacol	473	Sample 2	9.3	15	3.7
4- <i>n</i> -propylguaiacol	473	Sample 1	9.2	26	10.8
4- <i>n</i> -propylguaiacol	523	Sample 2	9.3	21	100
4- <i>n</i> -propylguaiacol	523	Sample 1	9.2	55	100
4- <i>n</i> -propylguaiacol ^c	523	Sample 2	9.3	43	100
4- <i>n</i> -propylguaiacol ^c	523	Sample 1	9.2	62	100

^a Reaction conditions: reactant (0.010 mol), Ni/HZSM-5 (2.0 g) or Ni/ Al₂O₃-HZSM-5 (2.0 g), H₂O (80 ml), 473 K, 5 MPa H₂, 0.5 h, stirred 700 rpm.

^b Sample 1: Ni/Al₂O₃-HZSM-5, Sample 2: Ni/HZSM-5.

^c Reaction time: 2 h.

3.6 Catalyst test in the recycling runs

3.6.1 Catalyst activity

For testing the activity in the recycling runs, the catalysts were separated by centrifugation, washed with acetone and then deionized water to remove organics, and

dried in ambient air at 383 K overnight. It has been observed after reaction at 473 K for 0.5 h in water that the used catalysts had become grey due to the surface oxidation of Ni during hydrothermal treatment. Before use in the next run, the Ni catalysts were calcined in air at 673 K and activated again in H₂ carrier gas at 733 K, and subsequently they turned to be black again. In subsequent runs at 473 K, the Ni/Al₂O₃-HZSM-5 and Ni/HZSM-5 catalysts attained ca. 70% and 45% alkane formation, respectively (Figure 2-8a). The alkane yields gradually decreased from 70% to 25% in four consecutive recycle runs on Ni/Al₂O₃-HZSM-5, while such yields decreased from 30% to 10% on Ni/HZSM-5 during sequential four catalytic recycle runs at the same conditions. If we compare the reaction rate variation during the catalyst recycling (see Figure 2-8b), the activity of Ni/Al₂O₃-HZSM-5 decreased from 270 mol·mol_{Ni}⁻¹·h⁻¹ to 70 mol·mol_{Ni}⁻¹·h⁻¹ after four catalytic runs, while the other activity of fresh Ni/HZSM-5 started from 70 mol·mol_{Ni}⁻¹·h⁻¹, and decreased to 50, 30, 20 mol·mol_{Ni}⁻¹·h⁻¹ after the sequential hydrothermal runs. In the following we examine changes of catalyst weight, metal sites, and acid sites between the fresh and used catalysts.

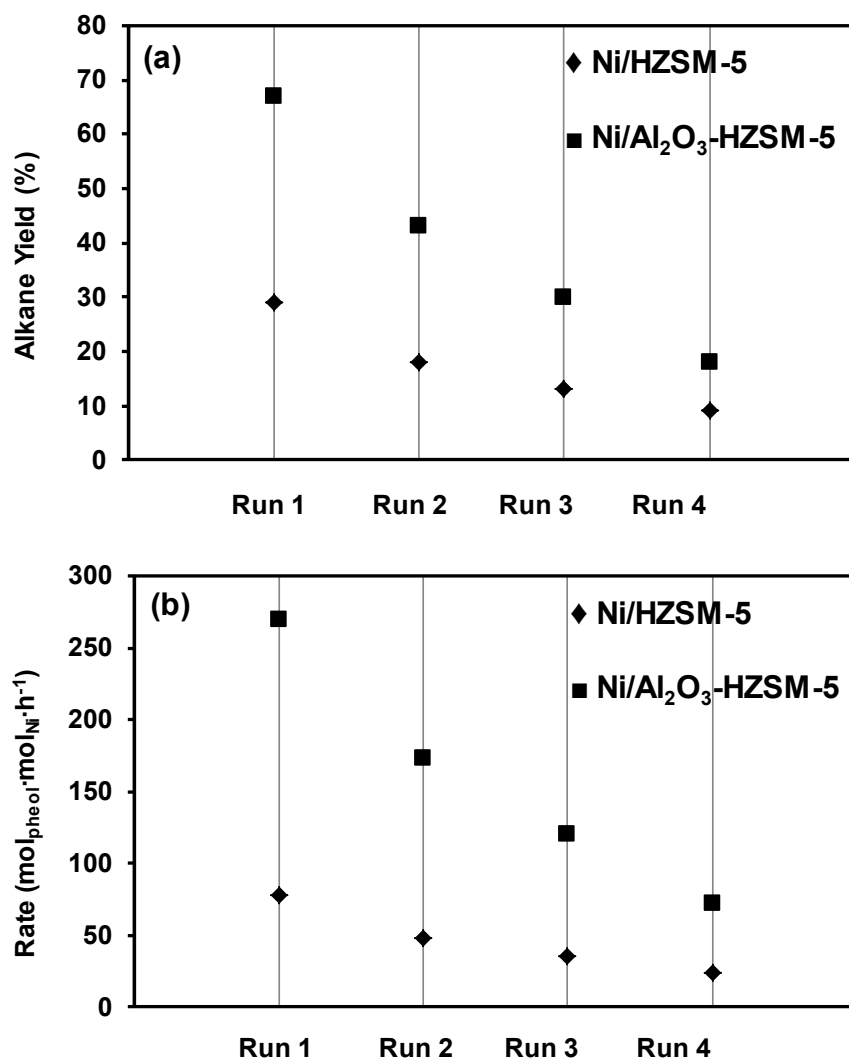


Figure 2-8. Catalysts recycle for hydrodeoxygenation of phenol with (a) alkane yield and (b) reaction rate in each reaction run. Reaction conditions: phenol (12.0 g) and Ni/Al₂O₃-HZSM-5 (2.0 g); phenol (8.0 g) and Ni/HZSM-5 (2.0 g); H₂O (80 ml), 473 K, 5 MPa H₂, 0.5 h, stirred at 700 rpm.

3.6.2 Catalyst stability during the recycling runs

To understand deactivation during the four recycling runs, we investigated catalyst physical changes including metal and support losses by leaching at hydrothermal conditions and acid site loss between the fresh and used catalysts.

3.6.2.1 The Ni and zeolite leaching under acidic hydrothermal conditions

These Ni catalysts were developed for hydrothermal operation in liquid aqueous phase, so Ni and Al leaching were firstly investigated. Catalysts (2.0 g) were loaded with 350 ml deionized water into the Soxhlet apparatus, and the Ni concentrations in the aqueous phase extracted by reflux were measured by AAS (Figure 2-9). The Ni leaching from Ni/Al₂O₃-HZSM-5 was much slower than from Ni/HZSM-5, leaving 1.5 or 5 ppm respectively in solution after 90 h. Compared to the original loading of 9.2-9.3 wt.% Ni, Ni/Al₂O₃-HZSM-5 retained 9.0 wt.% Ni but Ni/HZSM-5 only 8.2 wt.% Ni. The total catalyst weight losses were also compared (Table 2-4). The weight loss from Ni/HZSM-5 was less than 2% after 90 h reflux in water, consistent with our recent results on the stability comparison of zeolites HZSM-5 and HY in hydrothermal conditions.^[20] In contrast Ni/Al₂O₃-HZSM-5 lost 7 wt.%, attributed to extra-framework dealumination during the hydrothermal treatment. When the two catalysts were treated in the autoclave at 473 K for 72 h, Ni/HZSM-5 was quite stable with the catalyst loss lower than 0.1 wt.%, while Ni/Al₂O₃-HZSM-5 lost a much higher fraction of 7.4 wt.%. The remaining Ni contents were 7.7 and 8.7 wt.% on Ni/HZSM-5 and Ni/Al₂O₃-HZSM-5, respectively, indicating that the Ni particles on Al₂O₃-HZSM-5 are more stable at hydrothermal conditions than those on HZSM-5.

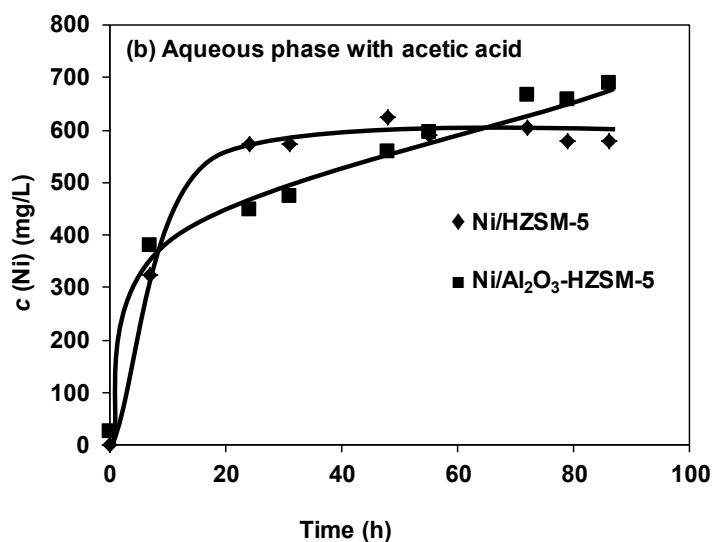
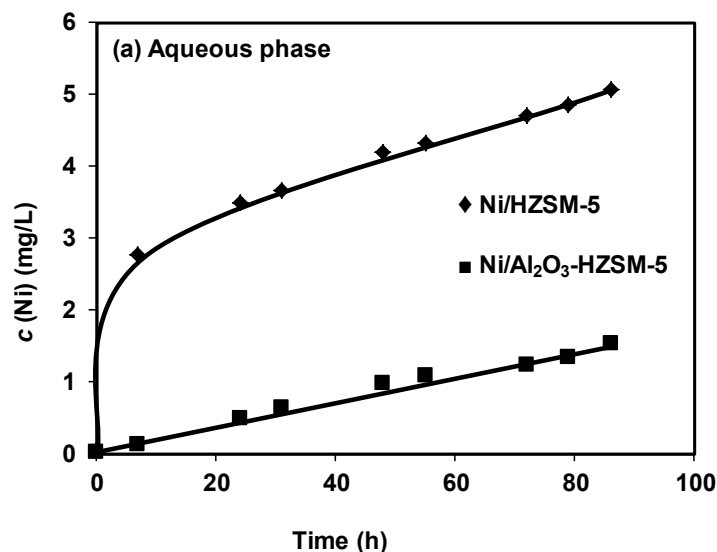


Figure 2-9. Ni leaching in the Soxhlet apparatus with refluxing in (a) water, and (b) aqueous 15% acetic acid solution. Conditions: catalyst (2.0 g), water solution (350 ml) or acetic acid water solution (15 wt.%, 350 ml), and 3.5 ml aliquots were drawn for measuring the Ni concentrations by AAS.

Summarizing these results allows us to conclude that (i) the Ni metal sites are much more stable to aqueous leaching on Al₂O₃-HZSM-5, and (ii) HZSM-5 was stable in hot water but the Al₂O₃ binder partly dissolved under these conditions. The stability of Ni ions in hot water was mainly related to the interaction of Ni metal and HZSM-5 support. In the former contribution^[14], the EXAFS, XANES, and TPR results demonstrated that Ni/Al₂O₃-HZSM-5 had a stronger interaction between metal and support and the Ni oxide on Al₂O₃-HZSM-5 was more difficult to reduce. The strong interaction to Al₂O₃ evidently stabilized the Ni on Al₂O₃-HZSM-5 against leaching by water at 473 K.

Table 2-4. Catalyst changes under hydrothermal conditions in Soxhlet apparatus and autoclave reactor.

	at 408 K ^a	With acetic acid at 408 K ^a	at 473 K ^b
Ni/HZSM-5 (9.2 wt.%)			
Catalyst loss (wt.%)	< 2.0	13	< 0.1
Remaining Ni content (wt.%)	8.2	6.9	7.7
Ni concentration in water (ppm)	6.0	580	-
Ni/Al₂O₃-HZSM-5 (9.3 wt.%)			
Catalyst loss (wt.%)	< 7.0	18	7.4
Remaining Ni content (wt.%)	9.0	6.5	8.7
Ni concentration in water (ppm)	2.0	690	-

^a Soxhlet apparatus, catalyst (2.0 g), water (350 ml), 408 K, 90 h.

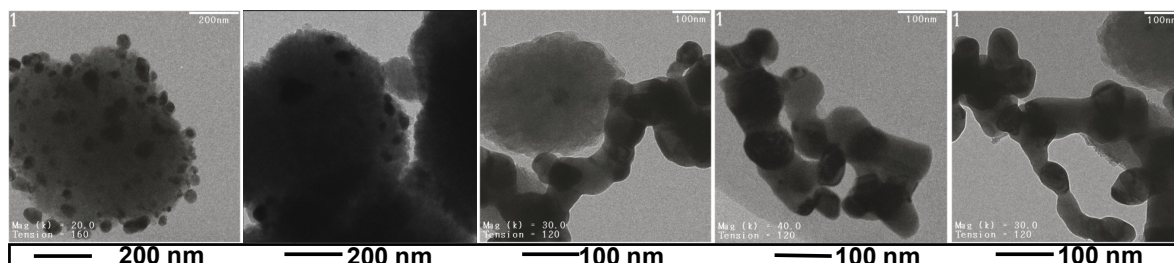
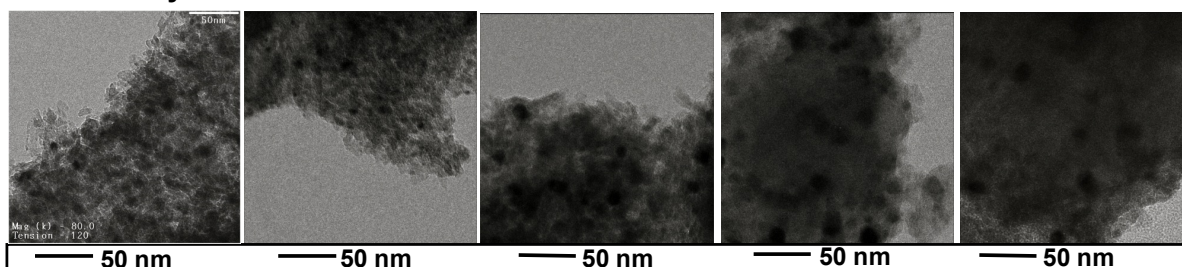
^b Carried out at autoclave reactor, catalyst (2.0 g), water (80 ml), 473 K, 5.0 MPa H₂, 72 h.

As the crude bio-oil contains acetic acid, the stability of Ni catalysts has also been tested by dilute aqueous 15 wt.% acetic acid solution at 373 K in the Soxhlet apparatus. The results are plotted at Figure 2-9. The dilute acid leached more Ni than the deionized water and only 6.9 and 6.5 wt.% Ni remained on Ni/HZSM-5 and Ni/Al₂O₃-HZSM-5 after 90 h, respectively. The 690 ppm Ni leaching was detected by AAS in the aqueous solution after the continuous treatment for Ni/Al₂O₃-HZSM-5 with acetic acid, whereas Ni/HZSM-5 showed a smaller amount of nickel leaching (580 ppm). The original color of Ni catalysts turned from black to almost white after acetic acid reflux. The total catalyst weight loss reached 13 wt.% from Ni/HZSM-5 and 18 wt.% from Ni/Al₂O₃-HZSM-5 after 90 h of acid reflux. Ni losses were 2.3 wt.% and 2.7 wt.%, and the losses of the Al-Si oxide support were so determined to be 10.7 wt.% and 15.3 wt.% for Ni/HZSM-5 and Ni/Al₂O₃-HZSM-5 catalysts during such treatment, respectively. In principle, carboxylic acids chelate 3d metal cations and thereby promote both dissolution and oxidation of Ni based zeolite catalysts. We conclude that these catalysts are not stable enough for one-pot hydrodeoxygenation of lignin-derived phenolic residues that carry a high concentration of carboxylic acids.

3.6.2.2 Metal site changes during the recycling runs

The evolution of Ni metal sites during successive runs was indicated in the TEM images (Figure 2-10a). Fresh Ni/Al₂O₃-HZSM-5 showed a mean size Ni particle size of 8.8 nm, and Ni/HZSM-5 mean size of 35 nm. During the four catalyst recycling runs, the Ni particle size on Ni/Al₂O₃-HZSM-5 increased by 2 nm per run and the distribution broadened from 1.3 to 3.6 nm (Figure 2-10b). The Ni particles on Ni/HZSM-5 grew by 18 nm per run and the distribution broadened from 13 nm to 33 nm after four runs (Figure 2-10b). Under water or acid reflux the growth of Ni particles on Ni/Al₂O₃-HZSM-5 was slower than on Ni/HZSM-5, so Ni/Al₂O₃-HZSM-5 is more resistant to sintering compared to Ni/HZSM-5 during catalyst recycling.

(a)

Ni/HZSM-5**Fresh catalyst****After Run 1****After Run 2****After Run 3****After Run 4****41 ± 13 nm****59 ± 24 nm****80 ± 28 nm****86 ± 30 nm****94 ± 33 nm****Ni/Al₂O₃-HZSM-5****Fresh catalyst****After Run 1****After Run 2****After Run 3****After Run 4****8.8 ± 1.3 nm****11 ± 2.5 nm****13 ± 2.9 nm****15 ± 3.1 nm****17 ± 3.6 nm**

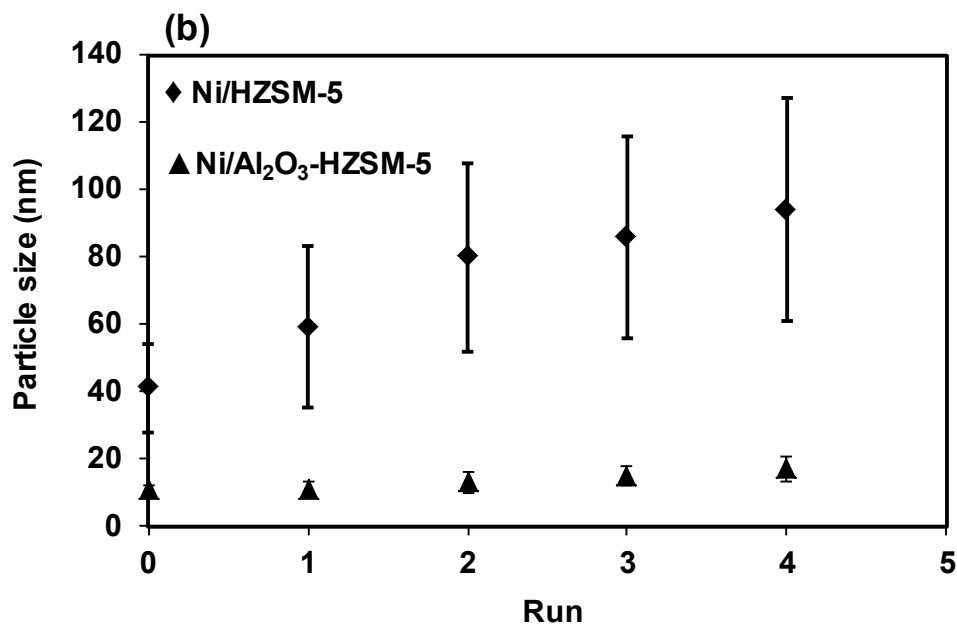
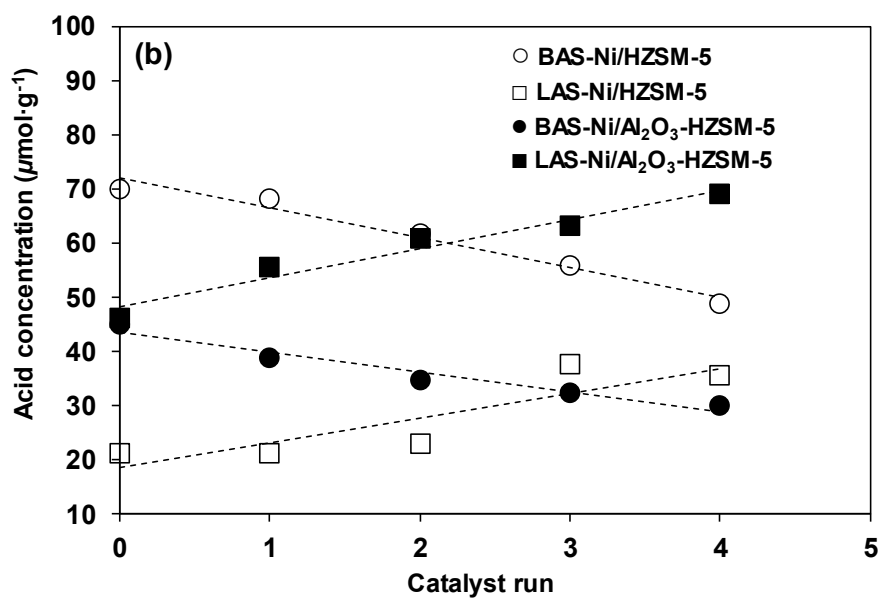
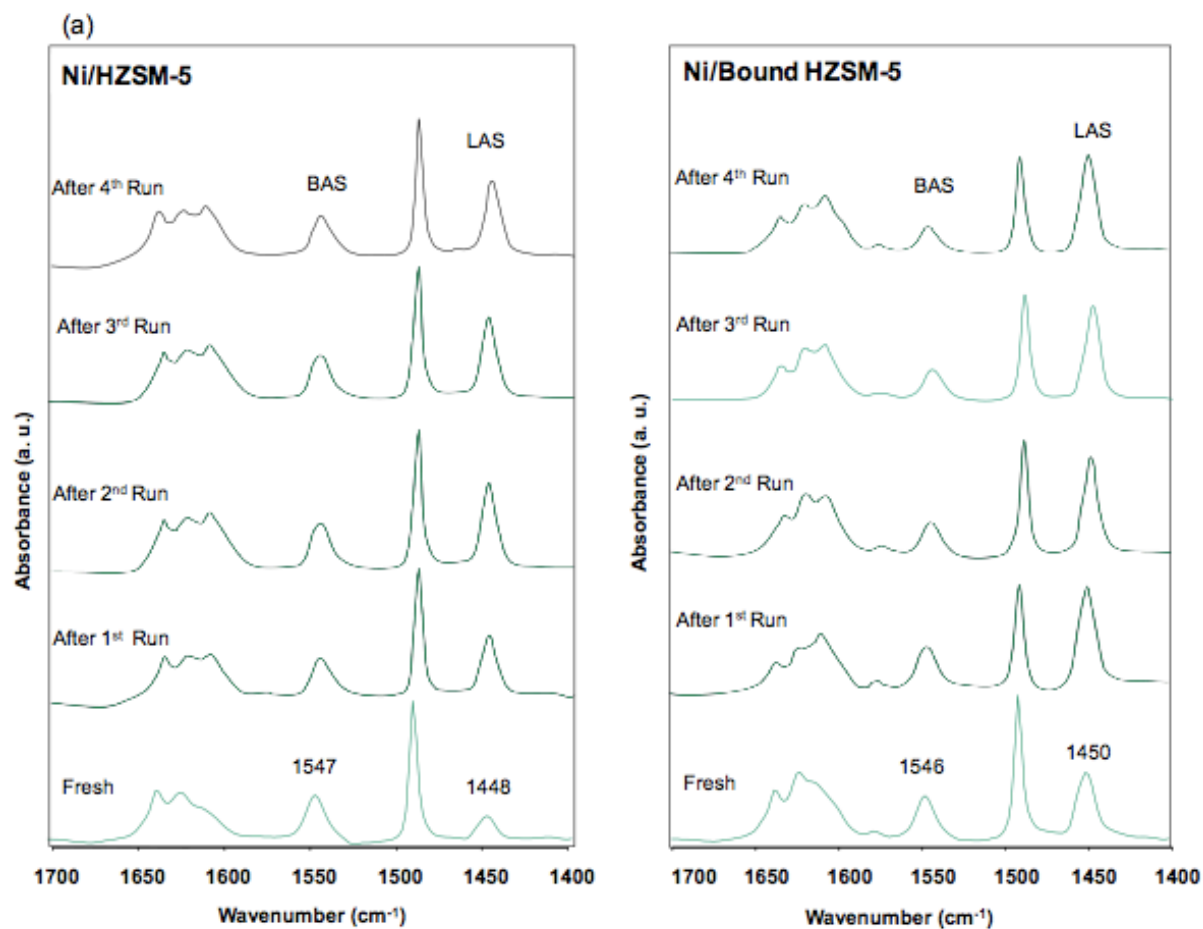


Figure 2-10. Metal particle size evolution: (a) TEM images (300 particle are counted for size calculation), and (b) Ni particle size distributions in the catalyst recycling.

3.6.2.3 Acid site change during the recycling runs

The IR spectroscopy of adsorbed pyridine was applied to evaluate changes in acid sites during the recycling runs. IR spectra of adsorbed pyridine were measured at 413 K in presence of 0.1 mbar pyridine (Figure 2-11a) for assessing Brønsted and Lewis acid sites as described above. The calculated results reflected the kinetic change of acid sites (see Table 2-5). The ratios of BAS/LAS were decreased on both catalysts after four catalyst recycle runs. The acid site concentrations on both catalysts changed in the same fashion: (i) the LAS increased and the BAS decreased, (ii) the magnitudes of BAS and LAS changes ($4 \mu\text{mol}\cdot\text{g}^{-1}\cdot\text{run}^{-1}$) during catalyst runs were the same catalysts. Thus the sums of BAS and LAS (ca. $90 \mu\text{mol/g}$) were nearly unchanged (Figure 2-11b).

There are structural changes to HZSM-5 during calcination in flow air. Above 723 K, the dehydration formed Lewis acid sites at the expense of losing Brønsted acid sites (Figure 2-11c). BAS and LAS are inter-convertible if the water adsorbed onto Brønsted acid sites leading to hydroxyl group formation ^[21,22] during the catalyst regeneration process, but the LAS created here by calcinations did not revert to the original Al-OH-Si structure (BAS) in presence of water. In fact, the change on the acid site hardly affected hydrodeoxygenation rates, because the dehydration catalyzed by BAS was much faster than other hydrogenation steps in the conversion of phenol to cyclohexane. Thus, in principle catalyst deactivation majorly resulted from Ni sintering during the recycling runs.



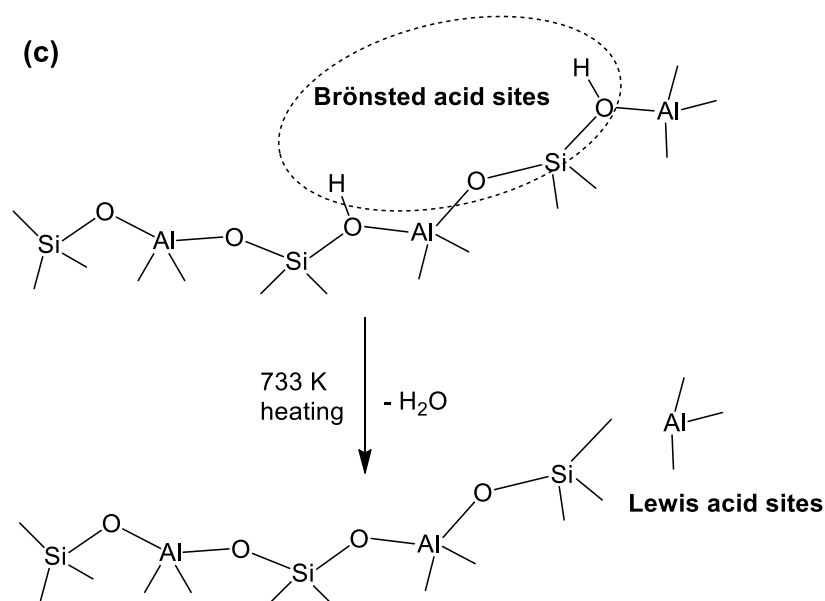


Figure 2-11. Measurement of acid sites changes through (a) IR spectra of adsorbed pyridine, (b) BAS and LAS changes, (c) transformation between Brønsted and Lewis acid sites in HZSM-5 during the catalyst recycling.

Table 2-5. Acid site concentrations (unit: $\mu\text{mol}\cdot\text{g}^{-1}$) in the fresh and reused catalysts from IR of adsorbed pyridine.

Ni/HZSM-5	LAS	BAS	Total acid sites	B/L
Fresh	21	70	91	3.33
After 1 st run	21	68	89	3.22
After 2 nd run	23	62	84	2.71
After 3 rd run	37	56	93	1.49
After 4 th run	36	49	84	1.37
Ni/Al ₂ O ₃ -HZSM-5				
Fresh	46	45	91	0.98
After 1 st run	56	39	94	0.70
After 2 nd run	61	35	95	0.57
After 3 rd run	63	32	95	0.51
After 4 th run	69	30	99	0.43

4. Conclusion

The rates of the four sequential reactions of phenol hydrodeoxygenation were compared over two Ni catalysts. In three hydrogenation reactions of phenol, cyclohexanone, and cyclohexene, Ni/Al₂O₃-HZSM-5 was more active than Ni/HZSM-5 due to higher Ni dispersion on Ni/Al₂O₃-HZSM-5. The Al₂O₃ binder introduced Lewis acidity that stabilized a ketone intermediate and inhibited its hydrogenation. The cyclohexanol dehydration reaction rate on Ni/HZSM-5 was slightly higher due to higher BAS concentration, and such dehydration was highly enhanced by close proximity between acid sites and metal sites where cyclohexene is irreversibly hydrogenated.

The reaction rates increased in the sequence of r_1 (phenol hydrogenation) < r_2 (cyclohexanone hydrogenation) < r_3 (cyclohexanol dehydration) << r_4 (cyclohexene hydrogenation). Phenol hydrogenation was rate determining in the overall reaction sequence, so the relatively higher Ni dispersion on Ni/Al₂O₃-HZSM-5 would deliver higher overall phenol hydrodeoxygenation rate. Low concentrations of intermediates cyclohexanone, cyclohexanol, and cyclohexene were present due to the increasingly faster subsequent hydrogenation (r_2 and r_4) and dehydration (r_3) steps than r_1 .

The catalysts both deactivated due to Ni sintering during the hydrothermal and recycling process. Ni leaching into water at 473 K was negligible from Ni/Al₂O₃-HZSM-5 but more rapid from Ni/HZSM-5 at identical conditions. Ni and Al-Si oxide components were extracted from both catalysts by 15 wt.% aqueous acetic acid above 373 K. During the recycling process, the Brønsted acid sites comprising protonated oxide bridges as Al-OH-Si were dehydrated by calcination to coordinately unsaturated Al atom Lewis acid sites.

5. References

- [1] D.C. Elliott, *Energy Fuels*, 21 (2007) 1792.
- [2] A.A. Boateng, C.A. Mullen, N. Goldberg, K.B. Hicks, H.G. Jung, J.F.S. Lamb, *Ind. Eng. Chem. Res.* 47 (2008) 4115.
- [3] T.D. Matson, K. Barta, A.V. Iretskii, P.C. Ford, *J. Am. Chem. Soc.* 133 (2011) 14090.
- [4] V.M. Roberts, V. Stein, T. Reiner, X. Li, A.A. Lemonidou, X. Li, J.A. Lercher, *Eur. J. Chem.* 17 (2011) 5939.
- [5] D. C. Elliott, *Energy Fuels* 21 (2007) 1792.
- [6] E. Laurent, B. Delmon, *J. Catal.* 146 (1994) 281.
- [7] E. Furimsky, F.E. Massoth, *Catal. Today* 52 (1999) 381.
- [8] C. Zhao, Y. Kou, A.A. Lemonidou, X. Li, J.A. Lercher, *Angew. Chem. Int. Ed.* 48 (2009) 3987.
- [9] C. Zhao, J. He, A.A. Lemonidou, X. Li, J.A. Lercher, *J. Catal.* 280 (2011) 8.
- [10] C. Zhao, Y. Kou, A.A. Lemonidou, X. Li, J.A. Lercher, *Chem. Commun.* 46 (2010) 412.
- [11] C. Zhao, J.A. Lercher, *ChemCatChem* 4 (2012) 64.
- [12] C. Zhao, D.M. Camaioni, J.A. Lercher, *J. Catal.* 288 (2012) 92.
- [13] C. Zhao, J.A. Lercher, *Angew. Chem. Int. Ed.* 51 (2012) 5935.
- [14] C. Zhao, Y. Yu, A. Jentys, J.A. Lercher, *Appl. Catal. B.* 132-133, 282-292 (2013).
- [15] M.J. Girgis, B.C. Gates, *Ind. Eng. Chem. Res.* 30 (1991) 2021.
- [16] E. Furimsky, *Appl. Catal. A* 199 (2000) 147.
- [17] H. Liu, T. Jiang, B. Han, S. Liang, Y. Zhou, *Science* 326 (2009) 1250.
- [18] J. Macht, M.J. Janik, M. Neurock, E. Iglesia, *Angew. Chem. Int. Ed.* 46 (2007) 7864.
- [19] N. Mahata, V. Vishwanathan, *Catal. Today* 49 (1999) 65.
- [20] R.M. Ravenelle, F. Schussler, A. D'Amico, N. Danilina, J.A. van Bokhoven, J.A. Lercher, C.W. Jones, C. Sievers, *J. Phys. Chem. C* 114 (2010) 19582.
- [21] D. Coster, J. J. Fripiat, M. Muscas, A. Auroux, *Langmuir* 11 (1995) 2615.
- [22] M. Trueba, S. P. Trasatti, *Eur. J. Inorg. Chem.* 17 (2005) 3393

6. Associated Content

Peer-Reviewed Publication

This chapter is based on the following article: Chen Zhao, Stanislav Kasakov, Jiayue He and Johannes A. Lercher, Comparison of kinetics, activity and stability of Ni/HZSM-5 and Ni/Al₂O₃-HZSM-5 for phenol hydrogenation, *Journal of Catalysis*, 2012, Vol. 296, 12-23

Contributions

Chen Zhao supervised the topic of phenol hydrodeoxygenation on Ni/HZSM-5 catalysts to compare the catalytic activities and stabilities with alumina-bound HZSM-5 supported Ni catalyst. Stanislav Kasakov contributed with design of experiments and data analysis. Jiayue He performed preliminary experiments of phenol HDO on Ni/HZSM-5 catalysts. Chen Zhao, Stanislav Kasakov and Johannes A. Lercher were responsible for data analysis and manuscript preparation. Johannes A. Lercher is the principal investigator of this work.

Acknowledgment

This work was financially supported by the Technische Universität München in the framework of the European Graduate School for Sustainable Energy.

Clearance by the Publisher

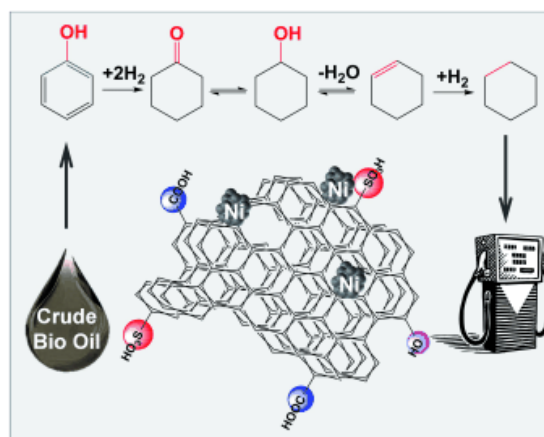
Elsevier gave approval to non-commercially reproduce the accepted article both in print and online.

Chapter III

Glucose and cellulose derived Ni/C-SO₃H catalysts for phenol hydrodeoxygenation

Abstract

Sulfonated carbons were explored as functionalized supports for Ni nanoparticles to hydrodeoxygenate (HDO) phenol. Both hexadecane and water were used as solvents. The dual-functional Ni catalysts supported on sulfonated carbon (Ni/C-SO₃H) showed high rates for phenol hydrodeoxygenation in liquid hexadecane, but not in water. Glucose and cellulose were precursors to the carbon supports. Changes in the carbons resulting



from sulfonation of the carbons resulted in variations of carbon sheet structures, morphologies and the surface concentrations of acid sites. While the C-SO₃H supports were active for cyclohexanol dehydration in hexadecane and water, Ni/C-SO₃H only catalyzed the reduction of phenol to cyclohexanol in water. The state of 3 – 5 nm grafted Ni particles was analyzed by *in situ* X-ray absorption spectroscopy. The results show that the metallic Ni was rapidly formed *in situ* without detectable leaching to the aqueous phase, suggesting that just the acid functions on Ni/C-SO₃H are inhibited in presence of water. Using *in situ* IR spectroscopy, it was shown that even in hexadecane, phenol HDO is limited by the dehydration step. Thus, phenol HDO catalysis was further improved by physically admixing C-SO₃H with the Ni/C-SO₃H catalyst to balance the two catalytic functions. The minimum addition of 7 wt.% C-SO₃H to the most active of the Ni/C-SO₃H catalysts enabled nearly quantitative conversion of phenol and the highest selectivity (90%) towards cyclohexane in 6 h, at temperatures as low as 473 K, suggesting that the proximity to Ni limits the acid properties of the support.

1. Introduction

Effective utilization of biomass as a renewable source of energy and feedstock for conversion to useful chemicals hinges upon designing highly active and stable catalysts.^[1,2] A one-step efficient conversion of lignin-derived phenolic oil, such as lignin waste from industrial paper production,^[3-5] has yet to be developed. This approach requires multifunctional catalysts that have sufficient contact with reactants and high stability of the active sites under process conditions.

To achieve this, we have prepared and studied a series of dual-functional catalysts that are able to hydrodeoxygenate phenols.^[6-13] These catalysts include physical mixtures of noble metals and mineral acids (Pd supported on active carbons (Pd/C) and aqueous phosphoric acid),^[6,7] base metals and solid acids (Raney Ni and Nafion[®]),^[8] as well as those integrating metal-acid bi-functionality in one catalyst particle (Pd/HZSM-5, Pd/HBEA and Ni/HZSM-5).^[9-14] Base metal catalysts such as Ni, Co, and Fe supported on carbon are less frequently investigated,^[15,16] because it is challenging to incorporate nano-sized particles of these metals onto the carbon supports.^[17-19] Suitable carbon materials can be produced via pyrolysis of biogenic sources. The chemical composition, morphology, specific surface area, functional group density of such carbon materials is influenced by the carbon precursor, the synthesis procedure including physical or chemical activation as well as post-synthetic treatments.^[20-24] Such subsequent treatments on carbon materials derived from carbohydrates result, e.g., in acid sites on the outer surface of carbon sheets (e.g., C-SO₃H or C-COOH, etc.), which are known to be catalytically active for several acid catalyzed reactions.^[25-28] Cellulose and glucose were chosen as carbon precursors in this work, because both are the main components of woody biomass minimizing so the carbon footprint of the catalyst.

The synthetic anchoring of Ni particles onto sulfonated carbon is challenging, because of the thermal instability of carbon supports and especially of C-SO₃H groups in air and N₂ at high temperatures, making conventional calcination and reduction treatments of Ni salts unfeasible. Therefore, grafting of metallic Ni nanoparticles, produced via reduction of Ni salt precursors by borane triethylamine, was used.^[28] This technique does not require high temperature treatment, and leads to well-permitted dispersed Ni nanoparticles with accessible surface acid sites on the carbon supports.

In this contribution, we report a novel dual-functional Ni/C-SO₃H catalyst that exhibits remarkably high activity towards phenol hydrodeoxygenation (HDO) in liquid hexadecane at mild reaction conditions (473 K, 4 MPa H₂). An in-depth *ex situ* and *in situ* characterization of sulfonated carbon supports, and Ni incorporated carbon catalysts permitted correlating catalyst properties and catalytic activity. Mutual influences of metal

and acid sites anchored either on one (Ni/C-SO₃H) or physically mixed (C-SO₃H + Ni/C-SO₃H) carbon sheets have been investigated with respect to the model reaction of phenol HDO.

2. Experimental section

2.1 Catalyst preparation

2.1.1 Sulfonated carbon supports

Carbon supports bearing SO₃H groups Carbon blacks were produced by pyrolysis of D-glucose or α -cellulose in N₂ flow (flow rate: 100 ml min⁻¹) at 748 K with a heating rate of 5 K min⁻¹ for 15 h. The HS carbons were synthesized by impregnating the raw materials with an aqueous hydrochloric solution with enriched ZnCl₂ (75 wt.% of the raw material). After two hours of stirring the acidic aqueous phase was removed by rotation evaporation, whereas the cellulosic suspension was filtered under vacuum. Before pyrolysis both ZnCl₂ impregnated raw materials were dried at 120 °C. LS and HS carbons were then washed with ultra-pure water (363 K) and dried at 383 K for 24 h. In a Schlenk line, the resultant carbon material (5 g) was sulfonated with concentrated sulfuric acid (96 wt.%, 150 ml) at 423 K for 15 h. After reaction, the black solid was filtered, and then washed with ultra-pure water (363 K) until the pH of the filtrate became neutral. Finally, it was dried in convection oven at 383 K overnight.

2.1.2 Loading of Ni nanoparticles on C-SO₃H support

The carbon-supported Ni catalysts were synthesized by three methods:

a) Impregnation and thermal reduction with H₂: Ni(NO₃)₂·6H₂O was dissolved in methanol (30 ml), and the solution was slowly dropped onto C-SO₃H support with stirring. After 1 h of stirring, the catalyst was dried at 373 K for 8 h, flushed with N₂ (flow rate) for 1 h and reduced under a H₂ flow (flow rate: 100 ml min⁻¹) at 623 K for 3 h with a heating rate of 1 K min⁻¹.

b) Chemical reduction with ethylene glycol.^[38] Ni(acac)₂ precursor and C-SO₃H support were dispersed in ethylene glycol in a three-neck flask under vigorous stirring. The solution was heated up to 513 K for 2 h with continuous stirring and refluxing. After that, the solution was cooled to ambient temperature and washed with absolute ethanol, and then sequentially filtered and dried under N₂ flow (flow rate: 100 ml min⁻¹) for 8 h at ambient temperature.

c) Grafting as-synthesized Ni nanoparticles reduced by borane triethylamine: a mixture of Ni(acac)₂ (2.57 g), oleylamine (150 ml) and oleic acid (3.2 ml) was loaded into a 250 ml two-neck schlenk flask under N₂ flow and the mixture was stirred for 1 h at 383 K to remove oxygen and humidity. The blue Ni(II) solution was cooled down to 363 K and the

reducing agent triethylamine borane (2.5 ml) was quickly added. The resulting black mixture was stirred for one hour and then cooled down to ambient temperature. In a sequence, the black nanoparticles were washed with ethanol (300 ml), separated from the ethanol *via* centrifugation at 4000 rpm and re-dispersed in hexane (300 ml). Finally the Ni particles were grafted onto carbon support (2.5 g) by stirring the mixture for 3 days at ambient temperature and the solvent hexane was removed by rotary evaporation under vacuum.

2.2 Catalyst characterization

2.2.1 Inductive coupled plasma-optical emission spectroscopy (ICP-OES)

The Ni contents on carbon supports were analyzed by ICP-OES with a SpectroFlame Spectro Analytica Instrument FTMOA81A. Before measurement, a calibration series of 0, 25, 50, 75, and 100 ppm Ni was prepared by diluting analytical standard 1000 ppm Ni (Fluka) in 0.5 M aqueous HNO₃ solution.

2.2.2 Specific surface area and porosity

Nitrogen sorption analysis was carried out at 77 K using a PMI automated sorptometer. BET surface areas and pore volumes were acquired from N₂ adsorption-desorption isotherms over a pressure range from 0.01 to 0.1 p/p₀.

2.2.3 Boehm titration

Boehm titration was carried out to determine the concentration of -SO₃H, -COOH, -OH groups on carbon materials. C-SO₃H (0.5 g) was agitated with 50 ml of 0.05 M NaOH, NaHCO₃ and Na₂CO₃ solutions in separate batches with continuous stirring for 24 h. Then, the solution was filtered and degassed with N₂ for 2 h. A 10 ml aliquot was taken from the NaOH and NaHCO₃ solution and acidified by 20 ml of 0.05 M HCl, whereas the aliquot of Na₂CO₃ was acidified by 30 ml of 0.05 M HCl to ensure complete neutralization. The solutions were then back-titrated with 0.05 M NaOH to a potentiometric point of pH = 7.0. For the back titration method, the following equation is used to calculate the overall surface site concentration.^[39,40]

$$n_{\text{surface}} = \frac{n_{\text{HCl}}}{n_{\text{B}}} [B] V_{\text{B}} - ([\text{HCl}] V_{\text{HCl}} - [\text{NaOH}] V_{\text{NaOH}}) \frac{V_{\text{B}}}{V_{\text{a}}}$$

where [B] and V_B are the concentration and volume of the base mixed with the carbon, V_a is the volume of aliquot taken from the V_B and [HCl] and V_{HCl} are the concentration and volume of the acid added to the aliquot.

2.2.4 X-ray diffraction (XRD)

X-ray powder diffraction (XRD) was performed on Philips X'Pert Pro System equipped with a Cu K_α radiation source (40 kV, 45 mA) with 1.08 ° min⁻¹ in the 2 θ range of 5–70 °.

2.2.5 Transmission electron microscopy (TEM)

The TEM images were recorded on a JEM-2010 JEOL transmission microscope operated at 120 kV, and over 300 particles were counted for size calculation. Before TEM measurement, an ultra-sonicated methanol suspension of the solid samples was dropped onto a Cu grid.

2.2.6 Scanning electron microscopy (SEM) and energy dispersed X-ray (EDX)

SEM was performed on a JEOL JSM 7500F, high-resolution scanning electron microscope with cold emission electron gun, operated at 1 kV. Sample preparation followed the same procedure as TEM. EDX was performed during SEM measurements with a JEOL JED-2300F energy dispersive X-ray analyzer with dry SD detector.

2.2.7 Solid-state magic angle spinning nuclear magnetic resonance (MAS NMR)

The ¹³C solid state MAS NMR spectra were obtained on a Bruker AV500 spectrometer (B₀ = 11.7 T) at 125.76 MHz with a spinning rate of 10 kHz. For ¹³C MAS NMR measurements the sample were fully hydrated before packing them into a 4 mm ZrO₂ rotor. 35000 scans were recorded by a recycle time of 4 ms. The excitation pulse had a length of 5 ms, with a relaxation delay between transients of 0.5 s. The chemical shifts are reported relative to an external standard of adamantane (δ = 29.472 ppm).

2.2.8 Raman spectroscopy

Raman spectra were collected with a Renishaw Raman spectrometer 1000 equipped with a CCD detector using a 514 nm diode laser for excitation and Si(111) wafer as an external standard.

2.2.9 Thermal gravimetric analysis (TGA)

The thermal gravimetric analysis was performed on a Setaram TG-DSC 111 thermo analyzer connected to a high vacuum system. About 30 mg of the carbon sample was placed in a quartz sample holder and the measurement started at 273 K under vacuum (p < 10⁻⁴ mbar) with an incremental heating rate of 1 K min⁻¹ to reach 1000 K. The SO₂ release from the sample was measured in a Pfeiffer Vacuum PrismaPlus mass spectrometer.

2.2.10 X-ray absorption spectroscopy

The near-edge structure (XANES) and extended X-ray absorption fine-structure (EXAFS) measurements were performed at the Pacific Northwest Consortium/X-ray Science Division (PNC/XSD) bending-magnet beamline at Sector 20 of the Advanced Photon Source (APS) at Argonne National Laboratory (ANL). The experiments were performed in transmission mode with a focused beam (0.7 × 0.6 mm) sending 10¹⁰ photons through the sample with a harmonic rejection of 5.6 mrad and 8100 eV to decrease the effects of harmonics. A Ni foil was placed downstream of the sample cell, as a reference to calibrate the photon energy of each spectrum. A continuous series of Ni-K edge spectra were acquired throughout the entire reaction sequence using either 4 min ($k = 12 \text{ \AA}^{-1}$) or 12 min ($k = 18 \text{ \AA}^{-1}$) acquisition times. The quantitative analysis allowed to evaluate bond distances and Debye-Waller factors (structural disorder) (σ^2) up to 6 Å from the core Ni atom. The data were processed with the ATHENA program^[41,42] and subsequently analyzed with the ARTEMIS program.^[43] The Fourier transform of the k -space EXAFS data (both real and imaginary parts of $\tilde{\chi}(R)$) were fitted to the FEFF9 theoretical model.^[44] Reference standards used in the analysis included bulk (fcc) NiO, bulk (hcp) α -Ni(OH)₂, and bulk (fcc) Ni. Their lattice parameters were obtained from the literature.^[45,46]

In situ measurements were performed using the microreactor cell and procedures described by Chase et al.^[35] with a few modifications. HiP[®] medium pressure Hastelloy[®] tees with an internal volume of 2 ml were used as reactor cells. Glassy-carbon discs, 0.75 mm thick by 3 mm in diameter, were used as windows. The discs were affixed to through-bore plugs which had been machined such that the distance between the windows was approximately 1 mm. Samples containing approximately 30 mg catalyst were pressed into a pellet, 0.4 mm thick by 3.5 mm in diameter, and held between the windows by a polyether ether ketone (PEEK) mesh (35 μm^2). Typically, the reactor was charged with 0.9 mL of 0.56 M phenol solution and then purged with H₂ at room temperature using five fill/purge cycles, then filled to pressure of ~4.9 MPa. (In some experiments water or no liquid at all was used.) A spectrum was recorded and then cell was heated to 473 K while repeatedly recording spectra. The reaction conditions ($T = 473 \text{ K}$, $p_{\text{total}} \sim 5 \text{ MPa}$) were maintained for periods of up to 12 h during acquisition of the X-ray spectra. The liquid contents of the cell were removed after reaction and analyzed by capillary gas chromatography (Agilent 7890A GC equipped with HP-5MS 25-m 0.25- μm i.d. column, coupled with Agilent 5975C MS).

2.2.11 In situ spectroscopy study of phenol HDO

In situ IR spectra were recorded on the ReactIR 45m device (Mettler Toledo) connected to the sentinel probe through the conduit K4. The sentinel probe is coupled to a Parr reactor (150 ml), where a diamond probe is used to collect the in situ IR spectra in the liquid

phase (Figure 3-1). Before measurement, a background was collected at reaction conditions (473 K, 3 MPa H₂) with 1.0 g catalyst (Ni/C₆₁-Zn-SO₃H) dispersed in 50 ml hexadecane. Then the autoclave was loaded with the reactant phenol (5.0 g) and H₂ (3 MPa) was charged at ambient temperature. The reactor was heated up and the stirring started once the temperature reached 463 K. The spectra were collected at every 1 min for a total duration of 180 min, with 8 cm⁻¹ spectral resolution and 256 scans per spectrum.

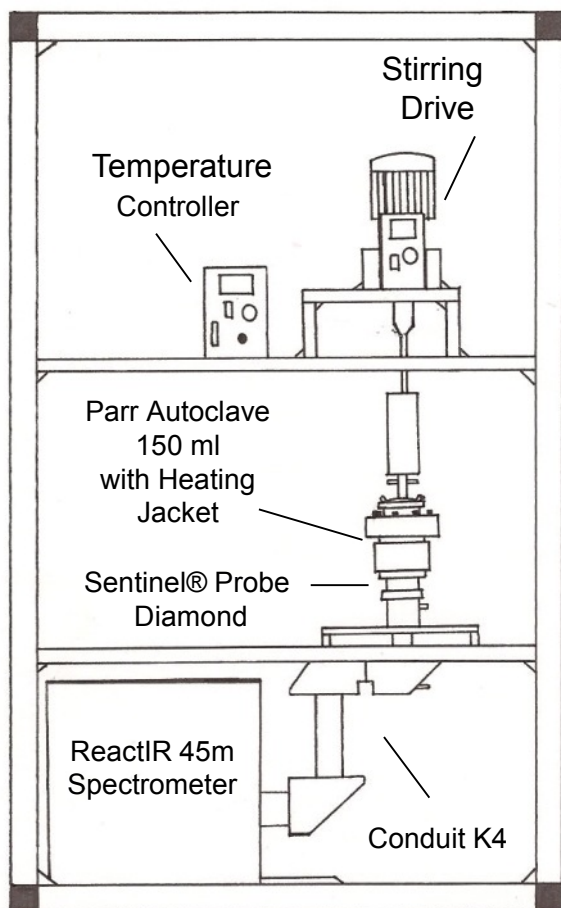


Figure 3-1. Schematic view of the *in situ* IR setup

2.3 Catalytic measurements

2.3.1 Cyclohexanol dehydration

In a typical experiment for cyclohexanol dehydration, a mixture of cyclohexanol (0.10 mol), hexadecane (60 ml), and C-SO₃H (0.5 g) was first charged into the reactor (Parr, Series 4843, 300 ml). After flushing the reactor with H₂ three times, it was heated to 473 K at 5 MPa H₂ while stirring at 700 rpm and continued for one hour at reaction temperature. After the reactor was cooled to room temperature, the H₂ pressure was released and an aliquot of 2 ml was analyzed by gas chromatography (GC, Shimadzu 2010) with a HP-5 capillary column (30 m × 250 μm) and flame ionization detector (FID). Additionally, a gas chromatograph-

mass spectrometer (GC-MS, Shimadzu QP 20105) was used to identify the organic compounds. The gas phase was determined by GC (HP 6890) equipped with a plot Q capillary column (30 m × 250 μm) with thermal conductivity detector (TCD).

2.3.2 Phenol HDO

Phenol HDO was studied on Ni/C-SO₃H catalysts to evaluate the kinetic data in separated batches: a) phenol (6.4 mmol), hexadecane (60 ml), Ni/C-SO₃H (0.12 g), 473 K, 4 MPa H₂, and b) same conditions with physically admixed C-SO₃H (12, 25 and 60 mg). A typical reaction was performed in an autoclave batch reactor (Parr, Series 4843, 300 ml). After loading the reactant, catalyst, and hexadecane, the reactor was flushed three times with H₂. At reaction temperature, H₂ was charged to a total pressure of 4.0 MPa and the from which time the mixture was allowed to react for times of 60, 120, 180, 240, 300 and 360 min while stirring at 700 rpm. After reaction, the work up procedure was similar to that described in section above.

3. Results and Discussion

3.1 Synthesis, characterization, and activity tests of carbon catalysts

Glucose and cellulose were selected for the synthesis of carbons. Both were pyrolyzed in N₂ atmosphere at 673 K for 15 h yielding carbon black, labeled as C_{GI} and C_{Ce}, respectively. Carbonization of ZnCl₂/HCl-impregnated glucose or cellulose precursors in N₂ resulted in the formation of HS carbons, identified as C_{Zn-GI} and C_{Zn-Ce}, respectively. These four carbon materials were subsequently functionalized with sulfonic acid sites (-SO₃H) *via* treatment with concentrated sulfuric acid (96 wt.%) at 423 K in flowing N₂.

3.2 Textural property, and acidity of synthesized carbon materials

The physiochemical properties of carbon materials, i.e., specific surface areas, pore volumes, and acid site distributions are compiled in Table 3-1. The N₂ sorption analysis shows that the specific BET surface areas of the carbon black materials C_{GI} and C_{Ce} were quite small (< 25 m² g⁻¹).

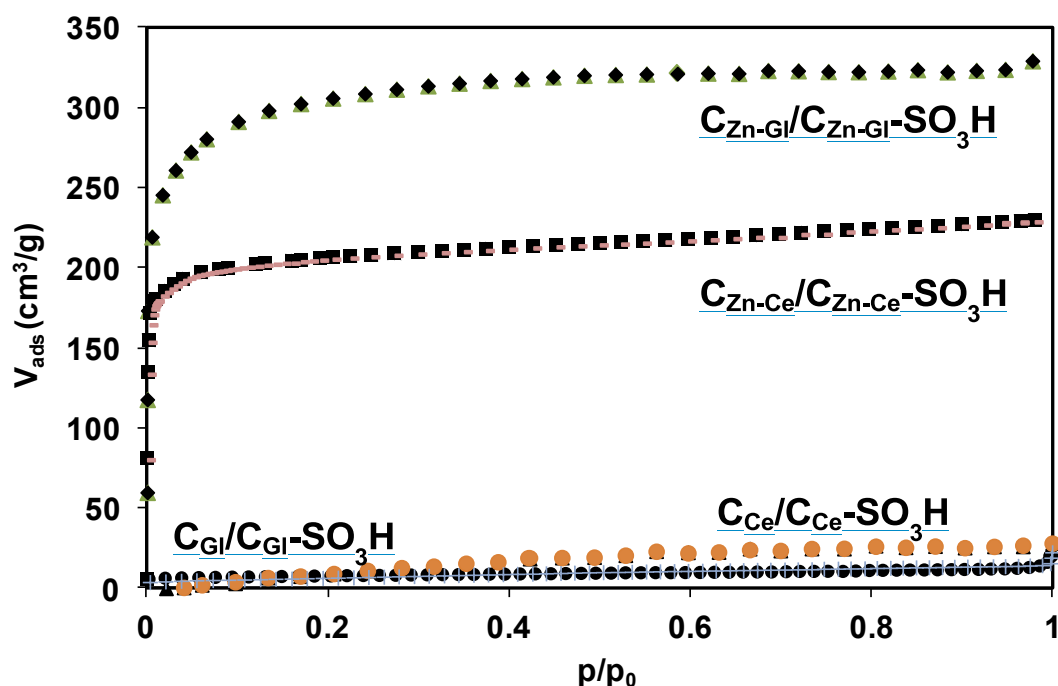


Figure 3-2. N₂ sorption isotherms of pyrolyzed carbons (C_{GI}, C_{Ce}), high surface carbon (C_{Zn-GI}, C_{Zn-Ce}) and its subsequent sulfonated form (C_{GI}-SO₃H, C_{Ce}-SO₃H, C_{Zn-GI}-SO₃H, C_{Zn-Ce}-SO₃H)

However, in presence of ZnCl₂ the specific surface areas increased 70 and 30 fold (1388 and 793 m² g⁻¹) for C_{Zn-GI} and C_{Zn-Ce} respectively. The N₂ sorption data indicate that parent C_{GI} and C_{Ce}, with pore volumes of 0.07 and 0.08 cm³ g⁻¹ respectively, were nonporous materials (isotherm and hysteresis shown in Figure 3-2). The HS carbons had two to three

times higher pore volumes than carbon black, i.e., 0.14 and 0.22 cm³ g⁻¹ from glucose and cellulose precursors, respectively. Zinc chloride is a moderate Lewis acid, which disrupts structural features of the precursor leading to carbon materials with higher specific surface areas and pore volumes.^[30] Due to their non-porous textures, the impact of the sulfuric acid treatment on the specific surface areas of carbon blacks was minimal, whereas the surface areas of the HS carbons C_{Zn-Gl} and C_{Zn-Ce} decreased by 20% to 1189 and 622 m² g⁻¹, respectively. Remarkably, sulfonation increased the pore volumes of the four carbon materials by 2–4 fold, to 0.14–0.19 and 0.39–0.50 cm³ g⁻¹ for the sulfonated carbon black and HS carbons, respectively. It is speculated that sulfonation minimizes the carbon structure leading to smaller surface areas, the strong acidic environment breaking down the carbon sheets, which results in larger micropore volumes in the carbon structures.

Table 3-1. Physicochemical properties of low surface and high surface carbons as well as their sulfonated counterparts.

Sample	S _{BET} (m ² g ⁻¹)	V _{micropore} (cm ³ g ⁻¹)	Acidity (mmol g ⁻¹) ^[a]		
			-SO ₃ H	-COOH	-OH
C _{Gl}	< 20	0.07	-	-	-
C _{Zn-Gl}	1388	0.14	-	-	-
C _{Ce}	25	0.08	-	-	-
C _{Zn-Ce}	793	0.22	-	-	-
C _{Gl} -SO ₃ H	< 20	0.14	0.85	0.35	0.11
C _{Zn-Gl} -SO ₃ H	1189	0.50	0.90	0.55	0.40
C _{Ce} -SO ₃ H	24	0.19	1.00	0.25	0.20
C _{Zn-Ce} -SO ₃ H	622	0.39	1.10	0.40	0.35

[a] Analyzed by Boehm titration

The treatment with sulfuric acid in N₂ atmosphere produces acid functional groups, i.e., -SO₃H, -COOH, and aromatic -OH groups on the external surface of the layered or stacked carbon sheets. Boehm titration was applied to determine the concentration surface acid sites in the final carbon materials. For all, the concentration of surface acidic groups increased in the sequence -SO₃H > -COOH > aromatic-OH (Table 3-1). Additional treatment with ZnCl₂/HCl increased the total concentration of acid sites of -SO₃H, -COOH, and aromatic -OH by 0.05–0.10, 0.15–0.20, and 0.15–0.19 mmol g⁻¹, respectively. However, it was also observed that the differences in surface area between the glucose and cellulose precursors as well as carbon black and HS carbons did not lead to considerable differences in the concentration of sulfonic groups. Thus, very similar -SO₃H acid site concentrations (0.85–1.10 mmol g⁻¹) were determined for the four sulfonated carbon samples.

3.3 Morphology of the carbon and sulfonated carbon materials

The incorporation of ZnCl₂/HCl into glucose and cellulose precursors led to enhancement of surface areas and pore volumes of carbon materials (Table 3-1). The variations in their morphologies are evident in the SEM images (Figure 3-4 and Figure 3-3). The C_{Zn-Gl} material retained the rigid triangular shape with an average particle size of ~100 μm (Figure 3-3), whereas the sulfonated material were highly disordered foam-like structures with increased concentrations of defects as well as with a reduction of rigid structures (Figure 3-3b). These observations are in accordance with the significant increase of pore volume of C_{Zn-Gl} from 0.14 to 0.50 cm³ g⁻¹ after ZnCl₂/HCl treatment (Table 3-1). In comparison, the C_{Zn-Ce} and C_{Zn-Ce-SO₃H} materials were similar, the SEM images of both exhibiting soft graphene-like sheets in a fibrous network (Figure 3-3c and Figure 3-3d).

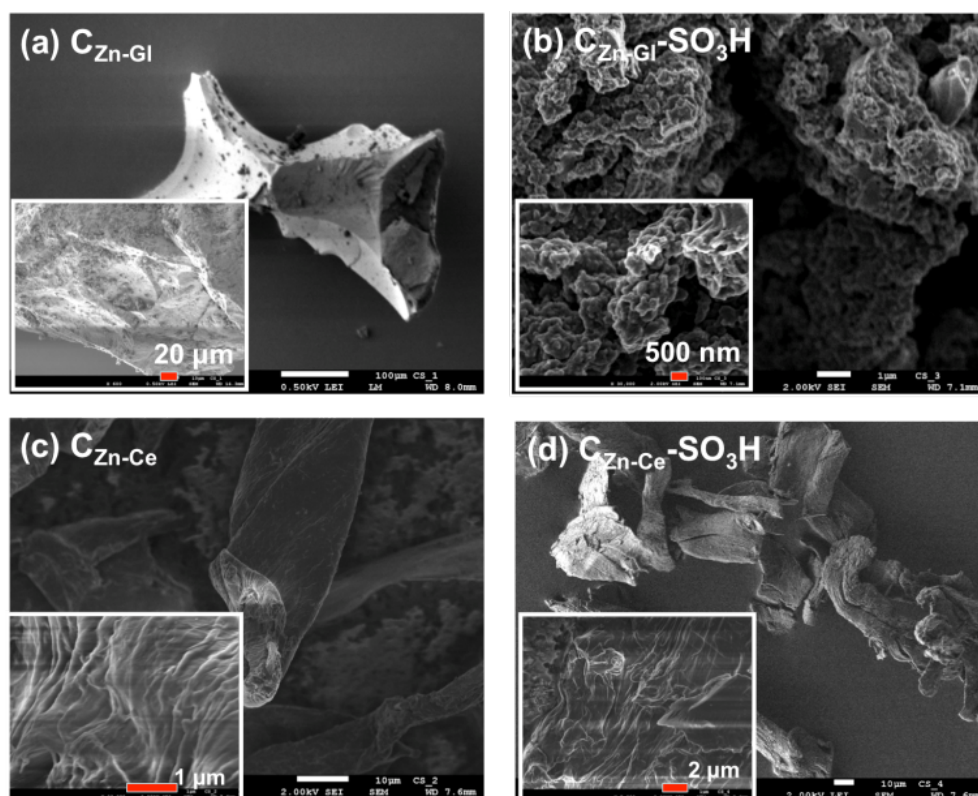


Figure 3-3. SEM images of HS carbons and corresponding sulfonated counterparts. (a) HS carbon from pyrolyzed glucose with ZnCl₂ and (b) sulfonated as-synthesized HS carbon from glucose, (c) HS carbon from pyrolyzed cellulose, and (d) sulfonated HS carbon from cellulose with ZnCl₂.

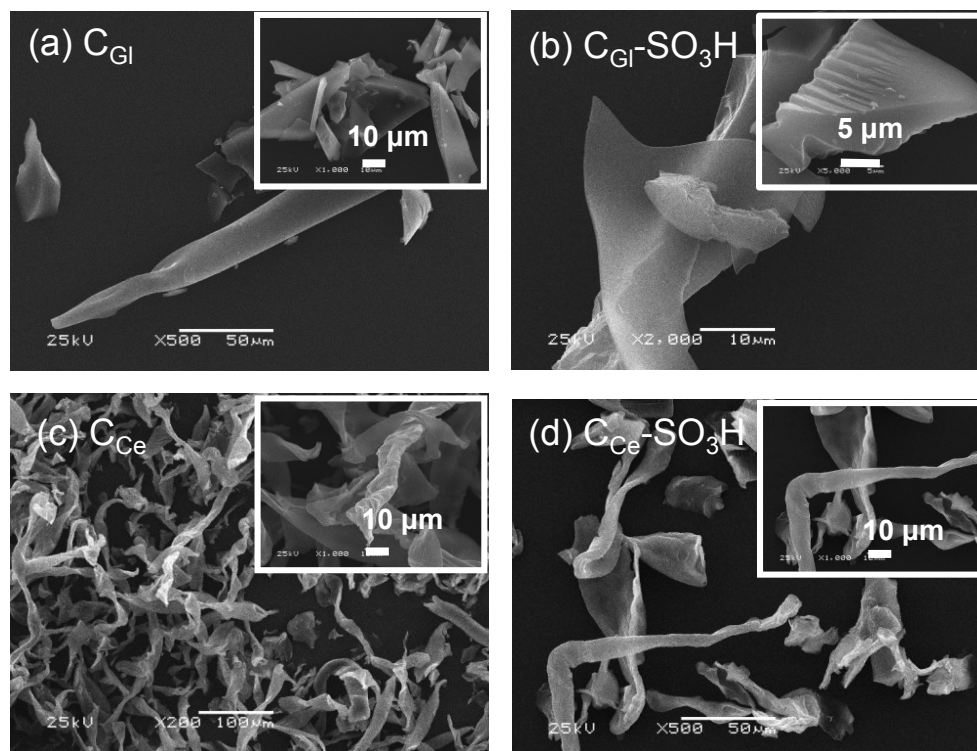


Figure 3-4. SEM images of carbon and sulfonated carbon materials: (a) carbon black from pyrolyzed glucose and (b) sulfonated carbon black from glucose, (c) carbon black from pyrolyzed cellulose, and (d) sulfonated carbon black from cellulose.

SEM images of glucose-derived C_{Gl} and cellulose-derived C_{Ce} carbons and their sulfonated counterparts are displayed in Figure 3-4. The C_{Gl} carbon black showed a rigid flake-shape texture (Figure 3-4), whereas the C_{Ce} carbon black appeared as a fibrous strip without a distinct structure (Figure 3-4c). Upon sulfonation, the morphology of C_{Gl-SO_3H} was almost unchanged (Figure 3-4b), while C_{Ce-SO_3H} showed more pronounced fibrous carbon strips with a smoothing of the surface (Figure 3-4d), demonstrating a highly disordered amorphous structure.

3.4 Structure of carbon and sulfonated carbon materials

Figure 3-5 displays the X-ray diffraction (XRD) patterns of the synthesized LS and HS carbons, as well as the sulfonated carbon derivatives. The major peaks at 2θ of 15–30° and 40–50° are assigned to [002] and [100] diffractions, originating from an amorphous carbon composed of aromatic carbon sheets randomly oriented and an axis of the graphitic plane, respectively.^[30] By comparison, HS carbon samples showed much more symmetric [002] and [100] diffraction peaks, implying better-defined domain sizes. In addition, sulfonated $C_{Zn-Gl-SO_3H}$ and $C_{Zn-Ce-SO_3H}$ had more symmetric and much narrower [002] diffraction peaks, indicating a higher order because of the stacking of carbon sheets. Thus, we conclude that the HS carbon samples were in a disordered state, and the sulfuric acid treatment rearranged the carbon sheets into better ordered domains. While

the presence of ZnCl₂ activation orders carbon domains, the subsequent sulfonic acid modification disrupts such order and generates more defects in graphene carbon sheets and amorphous carbons. These results together with the SEM images (Figures 3-3 and 3-4) show that the carbon blacks only undergo moderate changes in structure during sulfonation, but the HS carbons rearrange substantially during the same treatment.

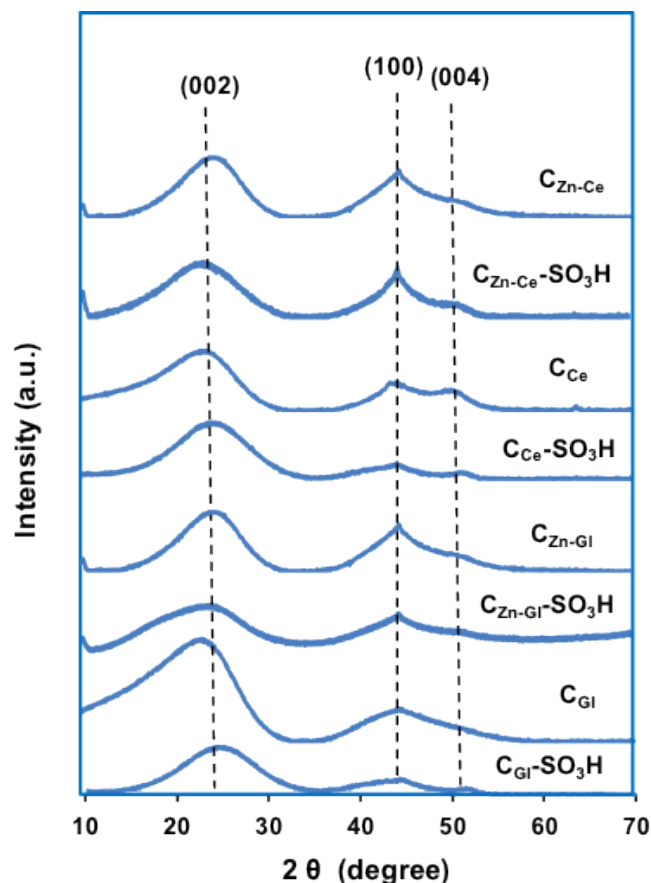


Figure 3-5. XRD patterns of low surface, high surface and sulfonated carbon materials.

The Raman spectra of the (a) cellulose- and (b) glucose-derived carbon materials are quite different (Figure 3-6). The G-band at 1580 cm⁻¹ is assigned to the Raman active E_{2g2} mode of graphite and sp² C=C vibration mode, while the D-band at 1350 cm⁻¹ is attributed to alternating ring stretch vibration in benzene or condensed benzene rings.^[10] Cellulose-derived carbons showed a pronounced D-band at 1350 cm⁻¹ (Figure 3-6a), highlighting the dominant defect sites of irregular shaped amorphous carbon. Knight and White suggested that the intensity ratio of the D-band to the G-band (I_D/I_G) is correlated with the graphitic domain size.^[11] The I_D/I_G ratios (1.5 to 1.8) of the present cellulose derived carbon materials suggest that the graphene sheet are smaller than 1 nm in width. Thus, carbonization of the cellulose precursor produces highly disordered amorphous structures. In comparison, glucose-derived carbons displayed a noticeable G-band at 1580 cm⁻¹ (Figure 3-6b), suggesting a prevalent graphene-layer structure in these carbon materials.

Based on the I_D/I_G ratio LS (C_{GI}) as well as HS carbon (C_{Zn-GI}) had a graphene sheet size of 1.4 and 1.7 nm, respectively. The higher graphene sheet size in the HS carbon is tentatively attributed to crosslinking of the carbon sheets during the activation process. The graphene sheet sizes of sulfonated LS and HS carbon were estimated to have a diameter of 1.5 and 1.6 nm, respectively, indicating that little changes were induced in the structures of the carbon sheets upon the sulfuric acid treatment.

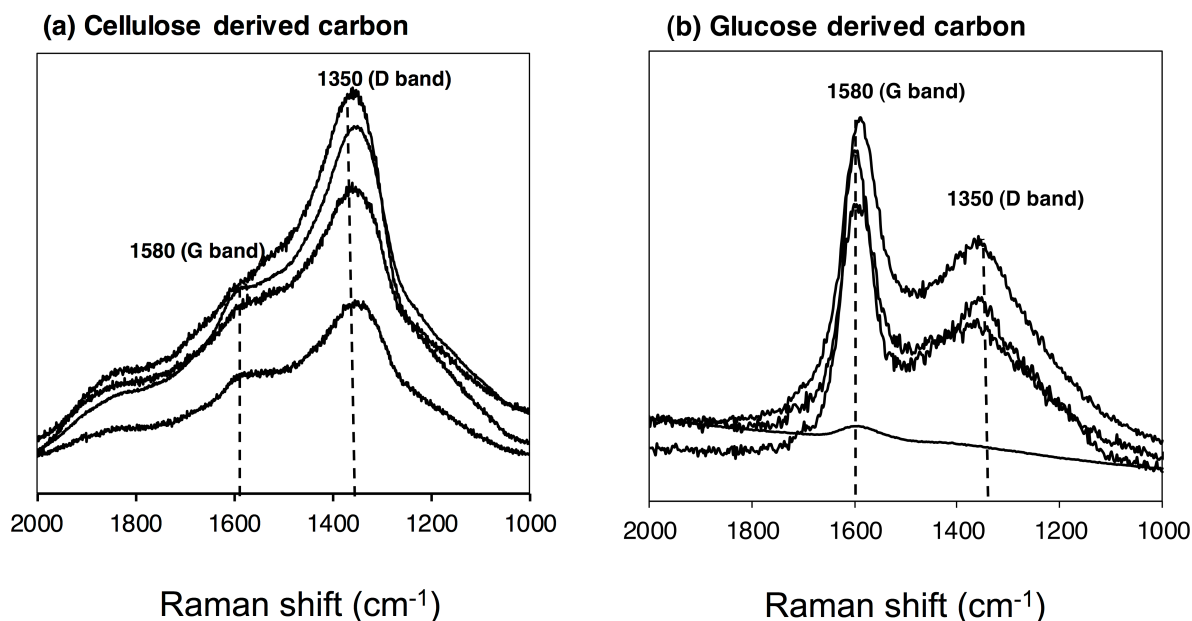


Figure 3-6. Raman spectra of (a) cellulose (bottom to top: C_{Ce}, C_{Ce}-SO₃H, C_{Zn-Ce}, C_{Zn-Ce}-SO₃H) and (b) glucose derived LS and HS carbon (bottom to top: C_{GI}, C_{GI}-SO₃H, C_{Zn-GI}, C_{Zn-GI}-SO₃H).

3.5 Carbon framework structures and surface –SO₃H functional groups

The major carbon species in the sulfonated HS carbon were speciated by ¹³C MAS solid NMR spectroscopy (Figure 3-7a). The chemical shifts at 130, 150 and 180 ppm in the NMR spectrum are assigned to polycyclic aromatic carbon atoms, phenolic hydroxyl, and carboxylic groups, respectively.^[32] While aromatic carbons attached to –SO₃H groups would appear at 140 ppm, this shift region is overlapped by broad bands assigned to aromatic carbon atoms at 130 ppm and aromatic carbons attached to hydroxyl groups at 150 ppm. Based on ¹³C solid state NMR data, the carbon framework components of HS carbon from glucose and cellulose (before and after sulfonation) are very similar. The ZnCl₂/HCl aided carbonization of cellulose and glucose (HS carbons) resulted primarily in polycyclic aromatic groups with the framework structures of graphene sheets. The introduction of sulfonic acid groups converted these surface sheets partly to amorphous *sp*³ hybridized carbon.

The concentrations of surface SO₃H groups attached to the carbon materials were measured by energy dispersive X-ray analysis (EDX) (Figure 3-7b). The results show that the concentration of surface–SO₃H groups were 0.80 mmol·g⁻¹ for C_{Zn-GI}-SO₃H and 1.05 mmol g⁻¹ for C_{Zn-Ce}-SO₃H, agreeing well with the Boehm titration results, i.e., 0.90 and 1.10 mmol g⁻¹,

respectively (Table 3-1). TGA-MS measurements (SO₂ fragment, m/e = 64, Figure 3-7c) show that the C-SO₃H group started to decompose at 620 K for cellulose-derived C_{Zn-Ce}-SO₃H catalyst, while it occurred at 710 K for glucose-derived C_{Zn-Gl}-SO₃H.

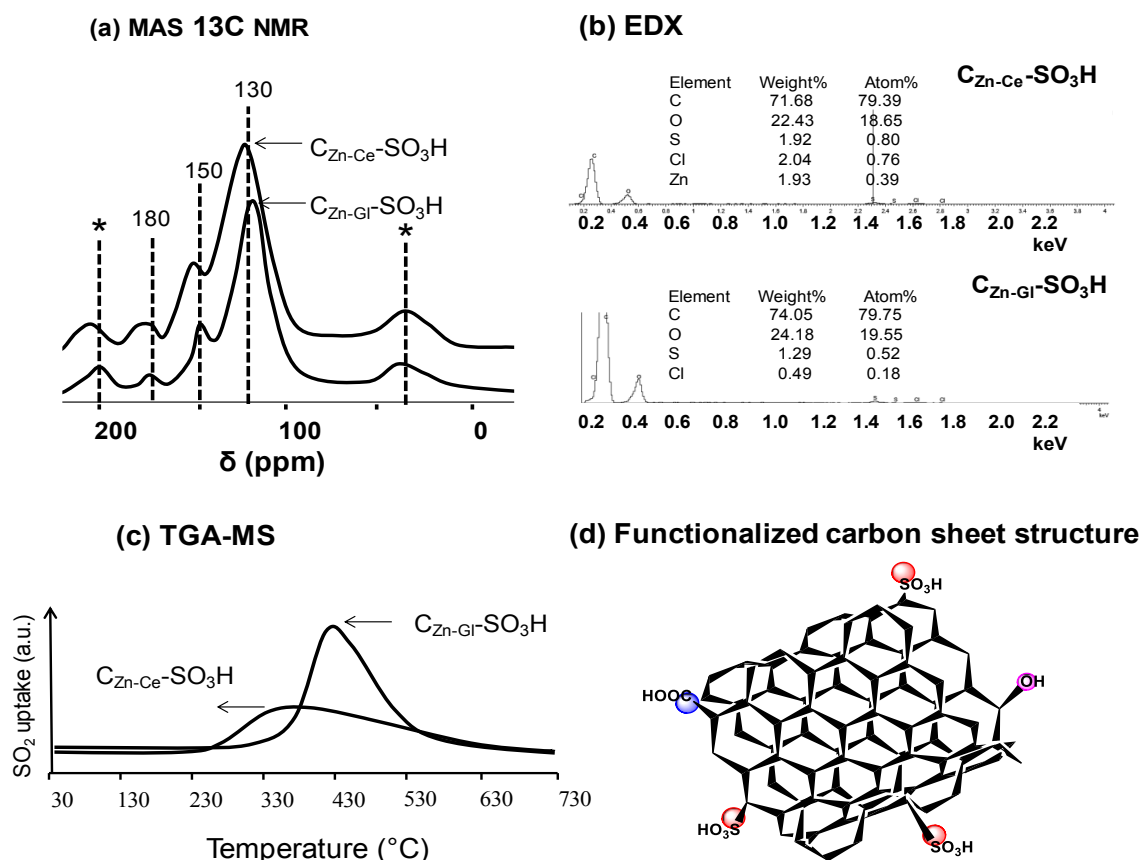


Figure 3-7. (a) ¹³C MAS Solid NMR, (b) EDX spectra, (c) TGA-MS of two sulfonated HS carbons and (d) proposed structure of the functionalized carbon sheet of glucose-derived HS carbon (C_{Zn-Gl}-SO₃H)

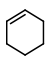
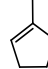
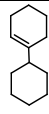
This implies that glucose-derived carbons have a higher thermal stability of C-SO₃H bonds attached to the carbon sheet surface. The proposed structure of the functionalized carbon sheets of HS carbon is depicted in Figure 3-7d. The acid functional groups of –SO₃H, –COOH, and –OH are concluded to be anchored on the edges of carbon sheets with a graphene domain size of 1.6 nm.

3.6 Correlation of activities of cyclohexanol dehydration with structural properties of C-SO₃H materials

The acidic properties of the sulfonated carbons were evaluated with respect to the dehydration of cyclohexanol (a key step in phenol HDO) in hexadecane (Table 3-2). The selected materials encompass the four sulfonated carbons described in this work, as well as three commercial carbons after sulfonation. Cyclohexene was the major product, with selectivities above 96% in all cases. Other olefinic products were isomerized 1-methylcyclopentene and condensed 1-cyclohexyl-cyclohexene. Parent carbons did not convert

cyclohexanol showing that the active sites are related to the surface sulfonate groups. [25,26] Acidic sites (–COOH and –OH) of lower strength are less abundant (Table 3-2) and are concluded to be less active than sulfonate groups. The initial turnover frequencies (TOFs) for dehydration were 120 - 498 mol mol_[SO₃H]⁻¹ h⁻¹ over C-SO₃H (Table 3-2, entries 1–3).

Table 3-2. Dehydration of cyclohexanol using sulfonated carbon catalysts.

Entry	Catalyst	Conv. [%]	Selectivity (C%)			Rate ^[b] (mmol g ⁻¹ h ⁻¹)	TOF ^[b] (mol mol _[SO₃H] ⁻¹ h ⁻¹)
							
1	C-SO ₃ H ^[c]	58	96	2.0	1.5	120	341
2	C-SO ₃ H ^[d]	29	97	2.0	0.2	30	120
3	C-SO ₃ H ^[e]	68	98	1.5	0.2	150	498
4	C _{GI} -SO ₃ H	59	96	1.0	1.0	130	153
5	C _{Zn-GI} -SO ₃ H	100	98	1.0	1.0	260	289
6	C _{Ce} -SO ₃ H	48	97	2.0	0.2	80	80
7	C _{Zn-Ce} -SO ₃ H	100	98	1.7	1.0	170	153

[a] Reaction conditions: cyclohexanol (10 g), catalyst (0.5 g), hexadecane (80 ml), 4.0 MPa H₂ (ambient temperature), 473 K, 1 h, stirring at 700 rpm.

[b] The initial rates and TOFs were determined at reaction conditions: cyclohexanol (20 g), catalyst (0.1 g), hexadecane (80 ml), 4.0 MPa H₂ (ambient temperature), 473 K, 1 h, stirring at 700 rpm, see supporting information Table S2.

[c] Carbon source: active carbon Darco[®], acid-washed lignite carbon, granular.

[d] Carbon source: active charcoal Norit[®] W35, from peat, steam activated.

[e] Carbon source: active charcoal DARCO[®]KB-G.

Interestingly, commercial carbon materials which were treated with acid during the carbonization procedure (Entries 1 and 3) showed low surface sulfonate concentration but a much higher concentration of carboxylic acid sites (see Table 3-3). The sulfonated commercial carbon materials show apparently high activities per surface sulfonate group. This however lead to overall a slightly lower activity per mass of the catalyst (30 - 150 mmol·g⁻¹·h⁻¹) than the home made carbon samples prepared in this work (Table 3-2). In addition, these commercial active carbons are usually produced *via* pyrolysis at high temperature, above 1023 K, which leads to sp² cross-linking of the polycyclic aromatic carbon sheets that may have limited access of the reactant molecules. [33,34]

Table 3-3. Surface areas, micropore volumes and concentrations of acidic functional group of sulfonated commercial carbon catalysts

Sample	S _{BET} (m ² g ⁻¹)	V _{micropore} (cm ³ g ⁻¹)	Acidity (mmol g ⁻¹) ^[a]		
			-SO ₃ H	-COOH	-OH
C-SO ₃ H ^[b]	1400	0.39	0.35	0.55	0.40
C-SO ₃ H ^[c]	845	0.29	0.25	0.80	0.20
C-SO ₃ H ^[d]	1700	0.59	0.30	0.65	0.35

[a] Determined by Boehm titration

[b] Carbon source: activate carbon Darco®, acid-washed lignite carbon, granular.

[c] Carbon source: activate charcoal Norit® W35, from peat, steam activated.

[d] Carbon source: activate charcoal Darco® KB-G.

Reactions with glucose and cellulose derived C_{GI}-SO₃H and C_{Ce}-SO₃H yielded 59% and 48% olefins from cyclohexanol, with dehydration rates of 130 and 80 mmol g⁻¹ h⁻¹, respectively (Table 3-2). Normalized to the surface -SO₃H concentrations, the corresponding TOFs were 153 and 80 mol mol_[-SO₃H]⁻¹ h⁻¹. Reactions with the sulfonated HS carbons led to quantitative cyclohexanol dehydration under identical conditions, reaching rates as high as 289 and 153 mmol g⁻¹ h⁻¹, respectively. Since the -SO₃H concentrations are almost identical between the sulfonated LS and HS samples (see Table 3-1), the higher TOFs (289 and 153 mol mol_[-SO₃H]⁻¹ h⁻¹ for HS glucose and cellulose derived carbon) are attributed to increased accessibility of the acid sites.

3.7 Characterization and activity evaluation of Ni/C-SO₃H catalyst

3.7.1 Ex situ analysis of Ni/C-SO₃H catalysts

Table 3-4. Physicochemical properties and Ni particles sizes of Ni/C-SO₃H catalysts

Catalyst	Ni content (wt.%) ^[a]	Total acidity in mmol g ⁻¹ ^[b]	S _{BET} (m ² g ⁻¹)	V _{volume} (cm ³ g ⁻¹)	d _{TEM} (nm) ^[c]
Ni/C _{GI} -SO ₃ H	9.2	1.55	<20	0.06	5.3 ± 2.3
Ni/C _{Zn-GI} -SO ₃ H	9.4	1.79	613	0.54	3.8 ± 1.1
Ni/C _{Ce} -SO ₃ H	9.7	1.68	<20	0.01	4.2 ± 1.2
Ni/C _{Zn-Ce} -SO ₃ H	9.9	1.85	68.0	0.08	3.5 ± 0.8

[a] determined by ICP-OES

[b] determined by Boehm titration

[c] determined by TEM images (300 Ni particles were counted for estimating particle sizes)

The physicochemical properties of four sulfonated carbon supports are compiled in Table 3-4 incorporated with Ni nanoparticles, prepared by liquid-phase Ni(acac)₂ reduction with Et₃N-BH₃ protected by oleylamine and oleic acid surfactants. The Ni contents were determined by ICP-OES to be 9.2, 9.4, 9.7, and 9.9 wt.% for Ni/C_{GI}-SO₃H, Ni/C_{Zn-GI}-SO₃H,

Ni/C_{Ce}-SO₃H, and Ni/C_{Zn-Ce}-SO₃H catalysts, respectively. The total acidities of the four catalysts were measured by the Boehm titration method giving overall Brønsted acidity, which varies between 1.55 and 1.85 mmol·g⁻¹. Note that the amount of the accessible -SO₃H sites has been actually decreased by ca. 10 % after the Ni incorporation, as one Ni atom with the oxidation state 2+ consumes 2 OH⁻ and therefore increases the consumption of HCl as titrant. All catalysts show lower specific surface areas and pore volumes after Ni incorporation (Tables 3-1 and 3-4). The Ni catalysts supported on sulfonated LS carbon (C_{GI}-SO₃H and C_{Ce}-SO₃H) had two orders of magnitude lower surface areas than those supported on HS carbons. With respect to the HS carbons, the BET surface area of the Ni/C_{Zn-Ce}-SO₃H decreased by one order of magnitude (622 vs. 68 m² g⁻¹), while the surface area of C_{Zn-GI}-SO₃H decreased by half upon Ni incorporation (1189 vs. 613 m² g⁻¹). After Ni incorporation, the porous volumes of sulfonated carbon black were almost filled up by the newly formed Ni nanoparticles, i.e., decreased to non-measurable values for Ni/C_{GI}-SO₃H and Ni/C_{Ce}-SO₃H (vs. 0.14 and 0.19 cm³ g⁻¹ for C_{GI}-SO₃H and C_{Ce}-SO₃H, respectively). For the HS carbons, the pore volume of C_{Zn-Ce}-SO₃H decreased from 0.39 to 0.08 cm³ g⁻¹ after Ni loading, whereas the pore volume of Ni/C_{Zn-GI}-SO₃H was almost unchanged (0.54 vs. 0.50 cm³ g⁻¹), probably due to the special pore structure and rigid morphology of the HS samples as discussed on detail in previous section.

The representative TEM images of the Ni particles grafted on the four sulfonated carbon supports are shown in Figure 3-8, along with the particle size distributions obtained from statistical analysis of at least 300 Ni particles from the TEM images. Ni nanoparticles on cellulose-derived carbon black (Ni/C_{Ce}-SO₃H) exhibited an average size of 4.3 ± 1.3 nm. Larger and less uniform particles (5.3 ± 2.3 nm) were observed for Ni/C_{GI}-SO₃H. When deposited on the sulfonated HS carbon (Ni/C_{Zn-Ce}-SO₃H and Ni/C_{Zn-GI}-SO₃H), the Ni nanoparticles decreased in average size (3.8 and 3.5 nm) with a slight smaller deviation (1.1 and 0.8 nm). These results suggest that surface structure and morphology of the carbon support influence the size and distribution of supported Ni particles after adding the common batch of pre-synthesized Ni particles.

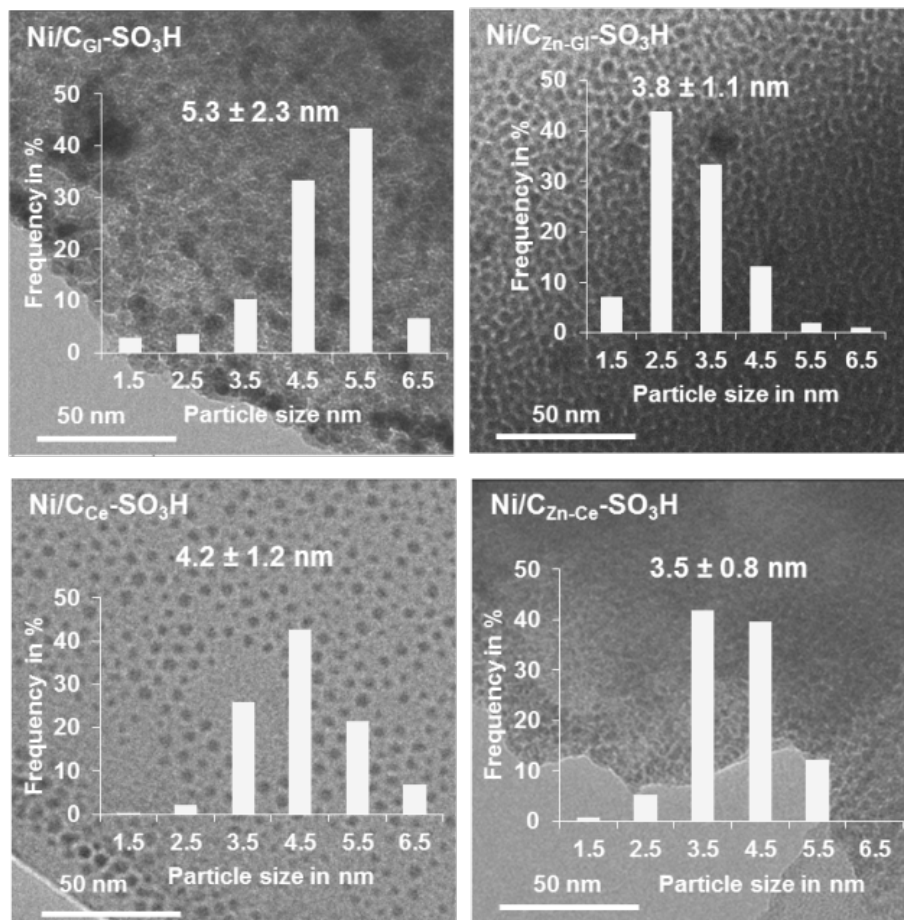


Figure 3-8. TEM images and particle size distribution diagrams of Ni nanoparticles grafted on the four sulfonated carbon supports.

3.7.2 *In situ* spectroscopic study of Ni state during aqueous phase phenol hydrodeoxygenation

The impact of the condensed phase (H₂O, hexadecane) on the reducibility of the metal as well as the catalyst stability under reaction conditions was explored by *in situ* X-ray absorption spectroscopy (XAS). The state of Ni and its particle size in the Ni/C_{Zn-GI}-SO₃H catalyst were investigated by XAS during phenol HDO. Figure 3-9 contains the near-edge (XANES) portion of the spectra of the 10 wt. % Ni/C_{Zn-GI}-SO₃H during HDO of 0.56 M phenol/water solution at 473 K and a total pressure of 5 MPa. To determine the concentration of both the Ni(0) and Ni(II) phase as a function of time, we simulated the XANES spectra as linear combinations of Ni foil (473 K), NiO and α-Ni(OH)₂ standards.

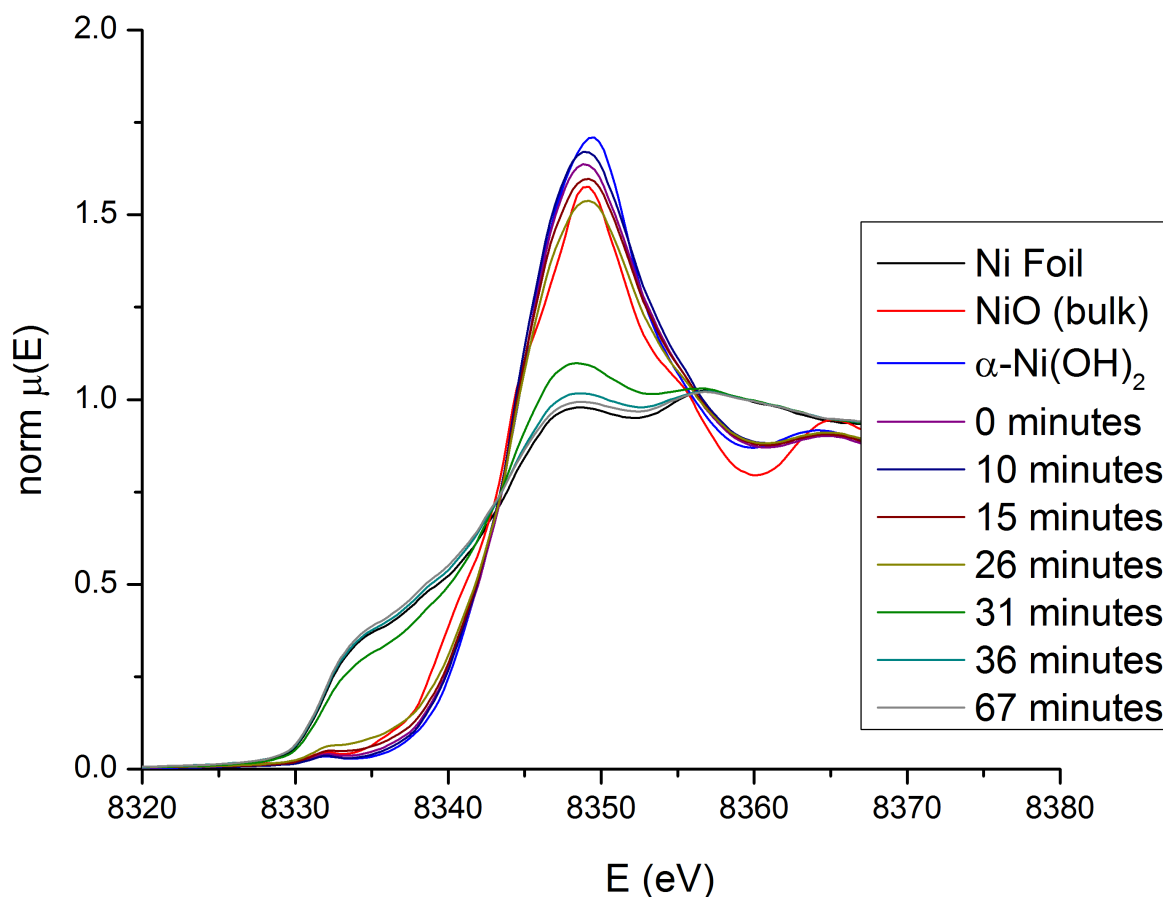


Figure 3-9. Changes in the oxidation state of Ni in 10 wt% Ni/C_{Zn-Gl}-SO₃H monitored by the white line intensity in XANES at different time intervals during phenol hydrogenation (0.56 M aqueous solution) at 473 K and a total pressure (mainly H₂ and water vapor) of ~5 MPa. The black curve represents the Ni foil standard, the red curve represents the nanoparticle NiO standard, and the blue curve represents the nanoparticle α -Ni(OH)₂ standard.

Figure 3-10 shows the fractions of the Ni(0) and Ni(II) species in the catalysts as a function of time during the aqueous phase HDO of phenol. Initially, the Ni particles were 100 % in the Ni(II) state, or specifically, a 20:80 mixture of NiO and Ni(OH)₂. The reduction to Ni(0) started after 12 min, i.e., when the temperature of 473 K was reached, and proceeded to completion within 50 min. The metallic state of Ni dominated after 30 min following the start of the reaction. During the experiment, a phenol conversion of 33% was attained in 67 min, corresponding to a TOF of 180 mol_{phenol}·mol_{Ni}⁻¹·h⁻¹. This value represents a lower boundary condition as the concentration of Ni(0) increased during the kinetic measurements. The spectra of Ni K-edge for 10 wt. % Ni/C_{Zn-Gl}-SO₃H measured prior to (ex situ) and at the end of reduction in H₂ are shown in the Appendix. Table 3-5 provides values for the first shell coordination numbers for the Ni nanoparticles. The Ni coordination numbers upon complete reduction were above 10, corresponding to an average particle size greater than 4.5 nm.^[36] The structural disorder and 1st shell Ni–Ni bond distance after 70 min of reaction match that of the Ni metal standard. Also the

amplitude of the sample at 67 min (Figure 3-9) closely matches that of bulk Ni, suggesting that Ni particles have a bulk-like structure.

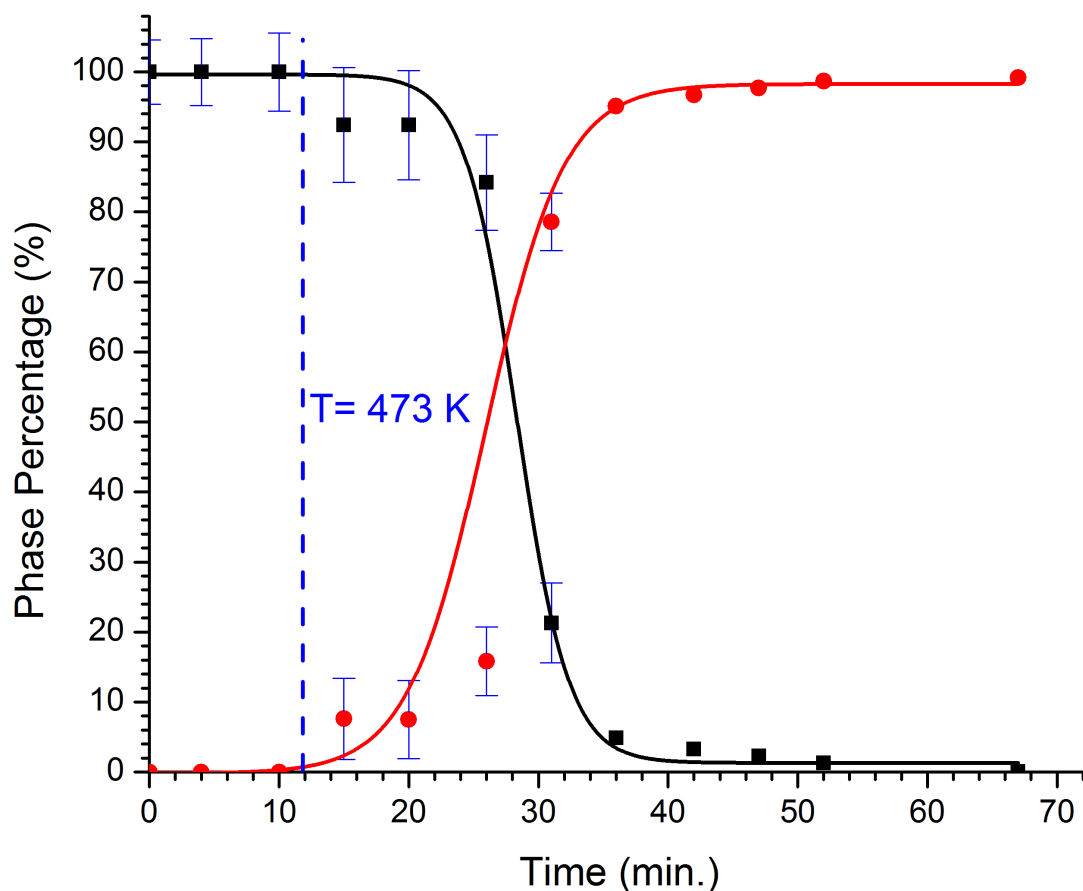


Figure 3-10. Changes in the composition of the Ni nanoparticles (10 wt% Ni/C_{Zn-GI}-SO₃H) during phenol hydrogenation (0.56 M aqueous solution) at 473 K and a total pressure (mainly H₂ and water vapor) of ~5 MPa. The black curve shows the percentage of the Ni(II) phases during reaction. The red curve represents the percentage of the metallic Ni phase. The reactor reached 473 K in 12 min (blue dashed line) and right after the reaction temperature was reached the phase change began to occur.

Table 3-5. The 1st shell Ni–O and 2nd shell Ni–Ni nearest-neighbour geometries of the Ni nanoparticles at the start and the end of the HDO reaction with 10 wt% Ni/C_{Zn-GI}-SO₃H after 67 min. (k-weight of 2)

State	Distance(Å)		CN		Debye-Waller factor, $\sigma^2 \times 10^{-3} (\text{Å}^2)$	
	Ni-O	Ni-Ni	NiO	Ni-Ni	Ni-O	Ni-Ni
Ni(II) (ex situ)	2.071 (12)	2.989 (7)	6	12	7.9 (11)	9.1 (13)
Ni(0) (473 K, 67 min)	N/A	2.498 (4)	N/A	10.4 (3)	N/A	9.8 (1)
NiO bulk (298 K)	2.076 (16)	2.956 (11)	6	12	7.0 (15)	6.3 (5)
Ni Foil (473 K)	N/A	2.499 (4)	N/A	12	N/A	9.4 (1)

Errors shown in the parentheses refer to the error to the last significant digit

3.8 Phenol reduction on Ni/C-SO₃H in aqueous phase

All catalysts were active in hydrogenation of phenol with high selectivities (95–97%) to cyclohexanol (Table 3-6). Nickel supported on C_{Zn-GI}-SO₃H was the most active. However, cyclohexene or cyclohexane were not observed. As is shown by EXAFS, water does not negatively impact the state of Ni(0); Ni was rapidly reduced under the reaction conditions and stayed in the catalyst without leaching.

The absence of alkenes and alkanes in the products clearly indicates that the acid sites in the Ni/C-SO₃H catalysts are not able to catalyze alcohol dehydration. Since the Ni was nearly 100% in the metallic state after the induction period, the acid exchange sites should be free from Ni²⁺. At this point, we speculate that the acid sites have been rendered inactive, neutralized by adventitious poisons (e.g., residual bases from the incorporation of Ni) or exchanged by Ni²⁺ such that protons are hardly present. Importantly, by switching to a non-polar solvent, hexadecane, the acid site is able to catalyze the dehydration of cyclohexanol (Table 3-2) and the cascade reactions of phenol HDO.

Table 3-6. Hydrodeoxygenation of phenol with Ni/C-SO₃H catalysts in aqueous phase.^[a]

Entry	Catalyst	Conv. (%)	Selectivity (C%)			
			-one	-ol	-ene	-ane
1	Ni/C _{GI} -SO ₃ H	79	4	96	0	0
2	Ni/C _{Zn-GI} -SO ₃ H	85	5	95	0	0
3	Ni/C _{Ce} -SO ₃ H	68	4	96	0	0
4	Ni/C _{Zn-Ce} -SO ₃ H	73	3	97	0	0

[a] Reaction conditions: phenol (0.60 g), Ni/C-SO₃H (0.12 g), H₂O (100 ml), 473 K, 4 MPa H₂, stirring at 700 rpm, 2 h.

3.9 Evaluation of phenol HDO catalyzed by Ni/C-SO₃H in the non-polar liquid phase (hexadecane)

The four Ni/C-SO₃H catalysts were tested for phenol HDO in hexadecane solvent at 473 K and 4 MPa H₂ (Table 3-7). Scheme 1-2 shows the sequential reactions for phenol HDO in the liquid phase over dual functional metal/acid sites.^[6-11] The steps involve sequential hydrogenation of phenol to cyclohexanol over Ni sites, dehydration of cyclohexanol over the acidic C-SO₃H sites, and cyclohexene hydrogenation over the Ni sites to cyclohexane. The catalysts based on glucose-derived carbon materials showed higher HDO activity than those based on cellulose-derived carbons (entries 1–4). The C_{Ce}-SO₃H and C_{Zn-Ce}-SO₃H supported Ni catalysts delivered 75–80% conversion, while phenol conversion reached 95–100% on C_{Gl}-SO₃H and C_{Zn-Gl}-SO₃H supported catalysts. As the Ni particle sizes of these catalysts were similar, the higher HDO activity seems to be related to the carbon morphologies and pore structures, which permit greater interaction of phenol with Ni. In addition, it is also observed that the use of HS carbon slightly enhanced HDO activity for Ni/C-SO₃H (Table 3-7). This modest increase, however, does not seem directly proportional to the differences in surface areas and pore volumes of the carbon materials (Table 3-1).

Table 3-7. Hydrodeoxygenation of phenol with Ni/C-SO₃H catalysts.^[a]

Entry	Catalyst	Conv. (%)	Selectivity (C%)			
			-one	-ol	-ene	-ane
1	Ni/C _{Gl} -SO ₃ H	95	4	55	18	20
2	Ni/C _{Zn-Gl} -SO ₃ H	100	5	50	15	25
3	Ni/C _{Ce} -SO ₃ H	75	4	65	9	20
4	Ni/C _{Zn-Ce} -SO ₃ H	82	2	59	13	23
Physically mixed						
5	C _{Zn-Gl} -SO ₃ H + Ni/C _{Zn-Gl} -SO ₃ H (0.1 g/g)	98	1	18	25	55
6	C _{Zn-Gl} -SO ₃ H + Ni/C _{Zn-Gl} -SO ₃ H (0.2 g/g)	64	4	50	12	29
7	C _{Zn-Gl} -SO ₃ H + Ni/C _{Zn-Gl} -SO ₃ H (0.5 g/g)	38	9	69	5	12

[a] Reaction conditions: phenol (0.60 g), Ni/C-SO₃H (0.12 g), C-SO₃H (0.06, 0.024, 0.012 g), hexadecane (60 ml), 473 K, 4 MPa H₂, stirring at 700 rpm, 2 h.

All four products (2–5) in Scheme 1-2 were detected. Cyclohexanol was the major product (50–60% selectivity), while cyclohexanone was formed only in trace amounts (< 5% selectivity). This is consistent with observations that Ni catalyzes the hydrogenation of cyclohexanone at much higher rates than of phenol.^[12] The presence of a substantial concentrations of cyclohexene (9–18%) suggests that the Ni-catalyzed cyclohexene hydrogenation rate was in significantly lower than noble metals such as Pd or Pt.^[6,7]

The selectivity to HDO products (alkane and alkene) was lower than 50 % on all Ni/C-SO₃H catalysts at 473 K. As the formation of these products depends on cyclohexanol dehydration, the temperature was raised from 453 to 523 K in hope that increasing the rate of cyclohexanol dehydration would increase the yield. These results are depicted in Figure A-3 in the Appendix. It shows that raising the temperature from 453 to 523 K increased the conversion of phenol from 80% to 100% under otherwise identical conditions, but the selectivity to alkane/alkene products remained at ca. 30%. Cyclohexanol was still the major product with ~60% selectivity, while cyclohexanone was produced with a selectivity lower than 5%. This means that phenol HDO in hexadecane on the Ni/C-SO₃H catalysts is limited by the dehydration of cyclohexanol over a significant temperature range. To testify this hypothesis, *in situ* IR experiments were performed and discussed further.

3.10 *In situ* IR spectroscopy of the reaction pathway of phenol HDO catalyzed by Ni/C-SO₃H

As shown in Figure 3-11, the compounds can be identified by their characteristic vibration modes, i.e., the aromatic C–O stretch vibration in the case of phenol the aliphatic C–O stretch vibration for cyclohexanol as intermediate. The C–H stretching vibrations are associated with cyclohexanone, cyclohexanol, cyclohexene, as well as cyclohexane. The carbonyl group in cyclohexanone, which has an IR band at 1700 cm⁻¹ was not detected, due to its relatively low concentration (3–5% selectivity).

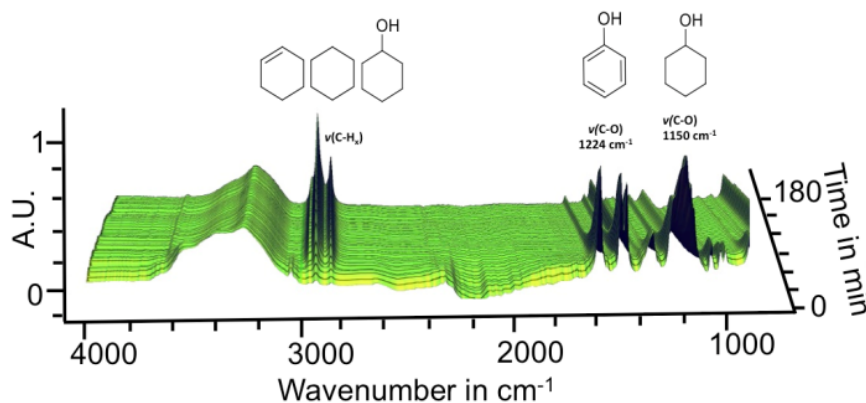


Figure 3-11. Time resolved in situ IR spectroscopy study during phenol HDO over Ni/C_{Zn-GI}-SO₃H in hexadecane as solvent at 473 K and 3 MPa H₂

Although the extinction coefficients for the IR bands are not known, the time-resolved IR spectra (Figure 3-12) provide semi-quantitative information on the kinetics. With increasing reaction time, the intensity of IR peaks of phenol (1224 cm⁻¹ aromatic CO stretch) declined, while cyclohexanol (1067 cm⁻¹ alicyclic CO stretch) increased first and then slowly dropped to a low value, indicating that cyclohexanol was still present after 180 minutes of reaction. The sharp increase of the C-H_x stretching vibration peaks (2928 cm⁻¹ representing the CH_x peaks) demonstrates the high hydrogenation rates on the nano-sized Ni particles. Thus, the rate-determining step is concluded shown to be the dehydration of cyclohexanol.

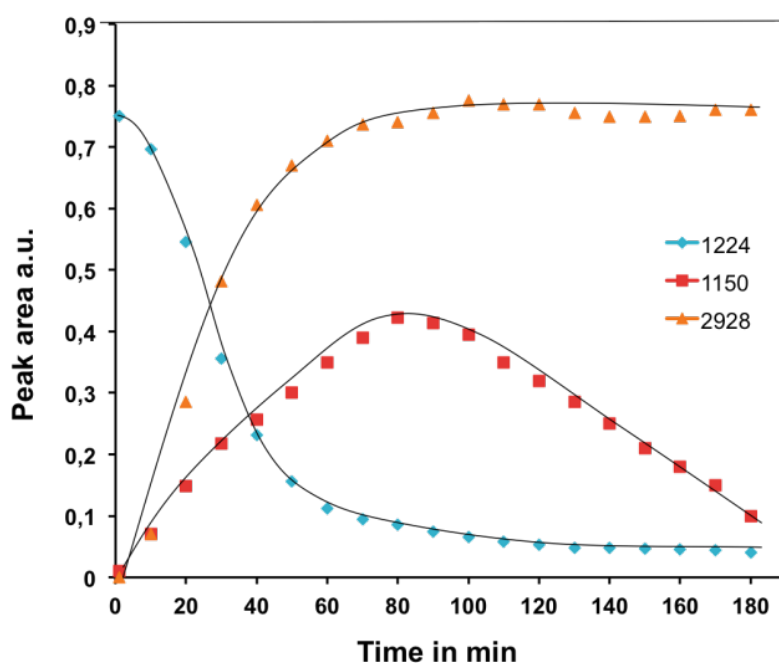


Figure 3-12. Relative trend of the phenol hydrogenation (1224 cm⁻¹) to cyclohexanol (1067 cm⁻¹) as intermediate and the cumulative CH_x (2928 cm⁻¹) formation.

3.11 Optimization of phenol HDO catalysis by Ni/C-SO₃H in liquid hexadecane

Based on the insight from *in situ* IR studies, we attempted to accelerate the rates of cyclohexanol dehydration, the limiting step in phenol HDO in hexadecane, by adding sulfonated carbon (C_{Zn-GI}-SO₃H) with the supported Ni/C_{Zn-GI}-SO₃H catalyst (Table 3-7, entries 5–7). Interestingly, the additional amounts of sulfonated carbon influenced not only the dehydration of cyclohexanol but also the hydrogenation of phenol. A mixture of 0.012 g C_{Zn-GI}-SO₃H and 0.12 g Ni/C_{Zn-GI}-SO₃H catalyst produced an almost quantitative conversion of phenol (98%) with a high selectivity to cyclohexene and cyclohexane (combined 80 %). Mixtures with higher ratios (0.2–0.5 g g⁻¹) of the C_{Zn-GI}-SO₃H showed only lower rates of phenol conversion. A 0.07 g g⁻¹ or 1:15 ratio by weight was determined to be optimum. The results suggest that the sulfonic acid groups interact with Ni directly or indirectly, reducing its availability for hydrogenation.

Figure 3-13 compares the HDO of phenol in hexadecane at 473 K in the presence of 4 MPa H₂ over the Ni/C_{Zn-GI}-SO₃H catalyst and over the optimum 1:15 (wt:wt) mixture of C_{Zn-GI}-SO₃H and Ni/C_{Zn-GI}-SO₃H. The initial products on Ni/C_{Zn-GI}-SO₃H were cyclohexanol (92% selectivity) and cyclohexanone (8% selectivity). Subsequently, dehydration of cyclohexanol produced cyclohexene. Cyclohexene was further hydrogenated to cyclohexane, becoming the major product at longer times (70% yield at 6 h). For the optimized mixture of C_{Zn-GI}-SO₃H and Ni/C_{Zn-GI}-SO₃H, hydrogenation of phenol and cyclohexene were found to be relatively unaffected by the added C_{Zn-GI}-SO₃H material, but the dehydration rates increased, as indicated by the faster conversion of cyclohexanol. Whereas Ni/C_{Zn-GI}-SO₃H produced 75% cyclohexane/ene after 6 h, the optimum mixture achieved 95% cyclohexane/ene formation in 6 h under the same conditions. The conversion was maintained above 90% on Ni/C_{Zn-GI}-SO₃H after three runs, showing high stability of both Ni and acid sites attached to the carbon sheets during phenol HDO in hexadecane.

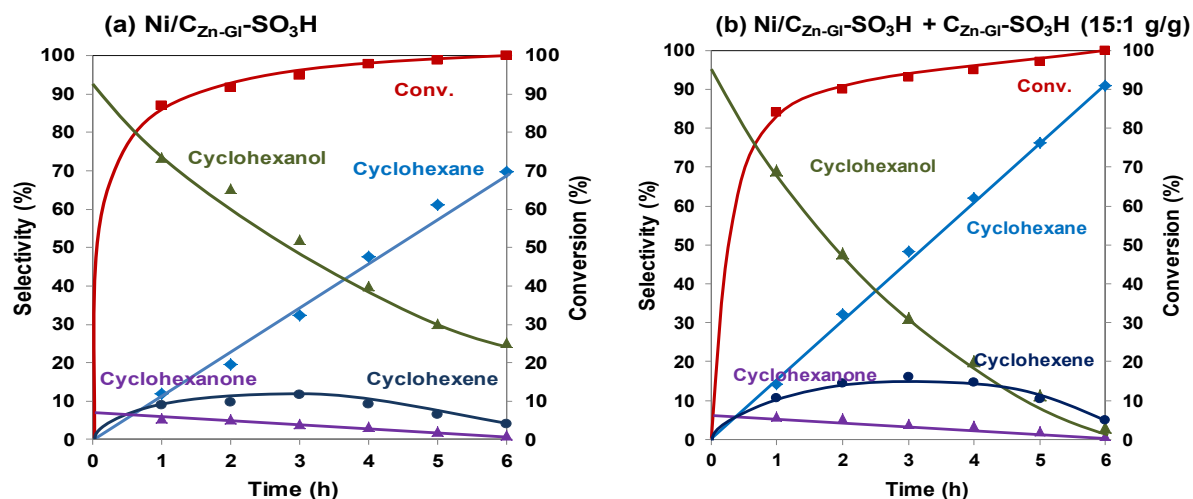


Figure 3-13. Product distributions on hydrodeoxygenation of phenol over (a) Ni/C_{Zn-GI}-SO₃H, and (b) physically mixed Ni/C_{Zn-GI}-SO₃H and C_{Zn-GI}-SO₃H catalysts as a function of time. Conditions: phenol (1.0 g), hexadecane (60 ml), 473 K, 4 MPa H₂, stirring at 700 rpm, (a) Ni/C_{Zn-GI}-SO₃H (10 wt.%, 0.15 g), and (b) Ni/C_{Zn-GI}-SO₃H (10 wt.%, 0.15 g), C_{Zn-GI}-SO₃H (0.01 g).

4. Conclusion

Bifunctional, highly active, and stable catalysts have been developed that combine metallic Ni nanoparticles (3–5 nm) with acidic sulfonated HS carbons derived from glucose and cellulose. Grafting of colloidal Ni nanoparticles proves to be the best preparation method. These catalysts quantitatively convert phenol and, upon optimization, afford 90% selectivity to the saturated hydrocarbon, cyclohexane, in hexadecane solvent under mild reaction conditions (473 K, 4 MPa H₂).

Physicochemical characterization shows that the glucose- and cellulose-derived carbons exhibit drastically different textural properties, morphologies, and physicochemical properties. However, after sulfonation these carbon materials show similar activities in four cyclohexanol dehydration. This is attributed to the similar concentrations of acidic functional groups (most importantly, -SO₃H).

In contrast to be an efficient HDO catalyst in hexadecane, the current bifunctional formulations catalyze only ring hydrogenation of phenol without deoxygenation in the presence of water. *In situ* XAFS measurements demonstrate that the active metallic Ni phase in the Ni/C-SO₃H catalysts is stable in the aqueous phase under HDO conditions. Therefore, acid functions in the bifunctional Ni/C-SO₃H catalysts seem to be inhibited in the aqueous environments, in contrast to the metal-free carbon supports, which are able to dehydrate alcohols in both water and hexadecane.

In situ IR measurements used to follow the evolution of intermediate products over time show that the HDO of phenol on the Ni/C-SO₃H catalysts in hexadecane proceeds via a cascade of steps (ring hydrogenation, dehydration and hydrogenation) similar to those reported previously on noble metals. The rate-determining step is shown to be the acid-catalyzed dehydration of cyclohexanol. Thus, the catalysis of HDO could be optimized by mixing additional C-SO₃H with the Ni/C-SO₃H catalyst to provide the subtle balance required for the two synergistic catalytic functions.

5. References

- [1] T. P. Vispute, H. Zhang, A. Sanna, R. Xiao, G. W. Huber, *Science* 2010, 330, 1222 – 1227.
- [2] J. M. Thomas, *Angew. Chem. Int. Ed.* 1999, 38, 3588 – 3628 ; *Angew. Chem.* 1999, 111, 3800–3843.
- [3] C. O. Tuck, E. PØrez, I. T. Horvuth, R. A. Sheldon, M. Poliakoff, *Science* 2012, 337, 695–699.
- [4] H. R. Bungay, *Science* 1982, 218, 643 – 646.
- [5] J. He, C. Zhao, J. A. Lercher, *J. Am. Chem. Soc.* 2012, 134, 20768 – 20775.
- [6] C. Zhao, J. He, A. A. Lemonidou, X. Li, J. A. Lercher, *J. Catal.* 2011, 280, 8–16.
- [7] C. Zhao, Y. Kou, A. A. Lemonidou, X. Li, J. A. Lercher, *Angew. Chem. Int. Ed.* 2009, 48, 3987–3990; *Angew. Chem.* 2009, 121, 4047–4050.
- [8] C. Zhao, Y. Kou, A. A. Lemonidou, X. Li, J. A. Lercher, *Chem. Commun.* 2010, 46, 412–414.
- [9] C. Zhao, J. A. Lercher, *Angew. Chem. Int. Ed.* 2012, 51, 5935–5940; *Angew. Chem.* 2012, 124, 6037–6042.
- [10] C. Zhao, S. Kasakov, J. He, J. A. Lercher, *J. Catal.* 2012, 296, 12 – 23.
- [11] C. Zhao, J. A. Lercher, *ChemCatChem* 2012, 4, 64 – 68.
- [12] C. Zhao, D. M. Camaioni, J. A. Lercher, *J. Catal.* 2012, 288, 92 – 103.
- [13] C. Zhao, Y. Yu, A. Jentys, J.A. Lercher, *Appl. Catal. B* 2013, 132–133, 282 – 292.
- [14] A. Gutierrez, R. K. Kaila, M. L. Honkela, R. Slioor, A. O. I. Krause, *Catal. Today* 2009, 147, 239–246.
- [15] J. Jiao, S. Seraphin, X. Wang, J. C. Withers, *J. Appl. Phys.* 1996, 80, 103 – 108.
- [16] P. Gorria, M. P. Fernandez-Garcia, M. Sevilla, J. A. Blanco, A. B. Fuertes, *Phys. Status Solidi RRL* 2009, 3, 4–6.
- [17] P. Gorria, M. Sevilla, J. A. Blanco, A. B. Fuertes, *Carbon* 2006, 44, 1954 – 1957.
- [18] A. B. Fuertes, P. Tartaj, *Chem. Mater.* 2006, 18, 1675.
- [19] A. B. Fuertes, P. Tartaj, *Small* 2007, 3, 275 – 279.
- [20] S. J. Tauster, S. C. Fung, R. T. K. Baker, J. A. Horsley, *Science* 1981, 211, 1121 – 1125.
- [21] M. Sevilla, A. B. Fuertes, *Carbon* 2009, 47, 2281 – 2289.
- [22] K. Nakajima, M. Okamura, J.N. Kondo, K. Domen, T. Tatsumi, S. Hayashi, M. Hara, *Chem. Mat.* 2008, 21, 186 – 193.
- [23] C. Falco, N. Baccile, M.-M. Titirici, *Green Chem.* 2011, 13, 3273 – 3281.
- [24] M. Kitano, K. Arai, A. Kodama, T. Kousaka, K. Nakajima, S. Hayashi, M.Hara, *Catal. Lett.* 2009, 131, 242 – 249.

- [25] K. Fukuhara, K. Nakajima, M. Kitano, H. Kato, S. Hayashi, M. Hara, *Chem-SusChem* 2011, 4, 778–784.
- [26] M. Toda, A. Takagaki, M. Okamura, J. N. Kondo, S. Hayashi, K. Domen, M. Hara, *Nature* 2005, 438, 178.
- [27] X. Mo, E. Lotero, C. Lu, Y. Lin, J. G. Goodwin, *Catal. Lett.* 2008, 123, 1 – 6.
- [28] H. Yano, M. Kataoka, H. Yamashita, H. Uchida, M. Watanabe, *Langmuir* 2007, 23, 6438–6445.
- [29] Ö. Metin, V. Mazumder, S. Özkar, S. Sun, *J. Am. Chem. Soc.* 2010, 132, 1468 – 1469.
- [30] M. Smisek, S. Cerny, *Active Carbon: Manufacture, Properties and Applications*, Elsevier, Amsterdam, 1970.
- [31] N. Baccile, G. Laurent, F. Babonneau, F. Fayon, M.-M. Titirici, M. Antonietti, *J. Phys. Chem. C* 2009, 113, 9644–9654.
- [32] D. S. Knight, W. B. White, *J. Mater. Res.* 1989, 4, 385 – 393.
- [33] K. Nakajima, M. Hara, *ACS Catal.* 2012, 2, 1296–1304.
- [34] K. Nakajima, M. Hara, S. Hayashi, *J. Am. Ceram. Soc.* 2007, 90, 3725–3734.
- [35] Z. A. Chase, J. L. Fulton, D. M. Camaioni, D. Mei, M. Balasubramanian, V. Pham, C. Zhao, R. Weber, Y. Wang, J. A. Lercher, *J. Phys. Chem. C* 2013, 117, 17603–17612.
- [36] A. I. Frenkel, C. W. Hills, R. G. Nuzzo, *J. Phys. Chem. B* 2001, 105, 12689 –12703.
- [37] W. Song, C. Zhao, J. A. Lercher, *Chem. Eur. J.* 2013, 19, 9833 – 9842.
- [38] J. W. Han, H. Lee, *Catal. Commun.* 2012, 19, 115 – 118.
- [39] S. L. Goertzen, K. D. Thøriault, A. M. Oickle, A. C. Tarasuk, H. A. Andreas, *Carbon* 2010, 48, 1252–1261.
- [40] A. M. Oickle, S. L. Goertzen, K. R. Hopper, Y. O. Abdalla, H. A. Andreas, *Carbon* 2010, 48, 3313–3322.
- [41] B. Ravel, M. Newville, *J. Synchrotron Radiat.* 2005, 12, 537–541.
- [42] M. Newville, *J. Synchrotron Radiat.* 2001, 8, 322.
- [43] E. Bayram, J. C. Linehan, J. L. Fulton, J. A. S. Roberts, N. K. Szymczak, T. D. Smurthwaite, S. Ozkar, M. Balasubramanian, R. G. Finke, *J. Am. Chem. Soc.* 2011, 133, 18889–18902.
- [44] J. J. Rehr, J. J. Kas, F. D. Vila, M. P. Prange, K. Jorissen, *Phys. Chem. Chem. Phys.* 2010, 12, 5503–5513.
- [45] N. Smith, *J. Am. Chem. Soc.* 1936, 58, 173–179.
- [46] H. Bode, K. Dehmelt, J. Witte, *Electrochim. Acta* 1966, 11, 1079–1087.

6. Associated Content

Peer-Reviewed Publication

This chapter is based on the following article: Stanislav Kasakov, Chen Zhao, Eszter Barath, Zizwe A. Chase, Hui Shi, Donald M. Camaioni, Aleksei Vjunov, John Fulton and Johannes A. Lercher, Glucose and Cellulose derived Ni/C-SO₃H catalysts for liquid phase phenol hydrodeoxygenation, *Chemistry – A European Journal*, 2015, Vol 21, p. 1567 – 1577

Contributions

Stanislav Kasakov synthesized the catalysts, performed the experiments and contributed to the design of experiments. Chen Zhao and Eszter Barath were supervising the work and contributed with data analysis and data treatment. Zizwe A. Chase, Donald M. Camaioni, Aleksei Vjunov and John Fulton were responsible for EXAFS measurements, contributed with design of experiments, data treatment and interpretation. Stanislav Kasakov, Chen Zhao, Zizwe A. Chase, Hui Shi, Donald M. Camaioni, John Fulton and Johannes A. Lercher were responsible for data analysis and manuscript preparation. Johannes A. Lercher is the principal investigator of this work.

Acknowledgments

This work was supported by the US Department of Energy (DOE), Office of Basic Energy Sciences (BES), Division of Chemical Sciences, Geosciences and Biosciences. Pacific Northwest National Laboratory is a multiprogram national laboratory operated for DOE by Battelle through Contract DE-AC05-76L01830. PNC/XSD facilities at the Advanced Photon Source, and research at these facilities, are supported by DOE/BES, the Canadian Light Source and its funding partners, the University of Washington, and the Advanced Photon Source. Use of the Advanced Photon Source, an Office of Science User Facility operated for the DOE Office of Science by Argonne National Laboratory, was supported by the DOE under Contract No. DE-AC02-06CH11357.

Clearance by the Publisher

Wiley VCH gave approval to non-commercially reproduce the accepted article both in print and online.

7. Appendix

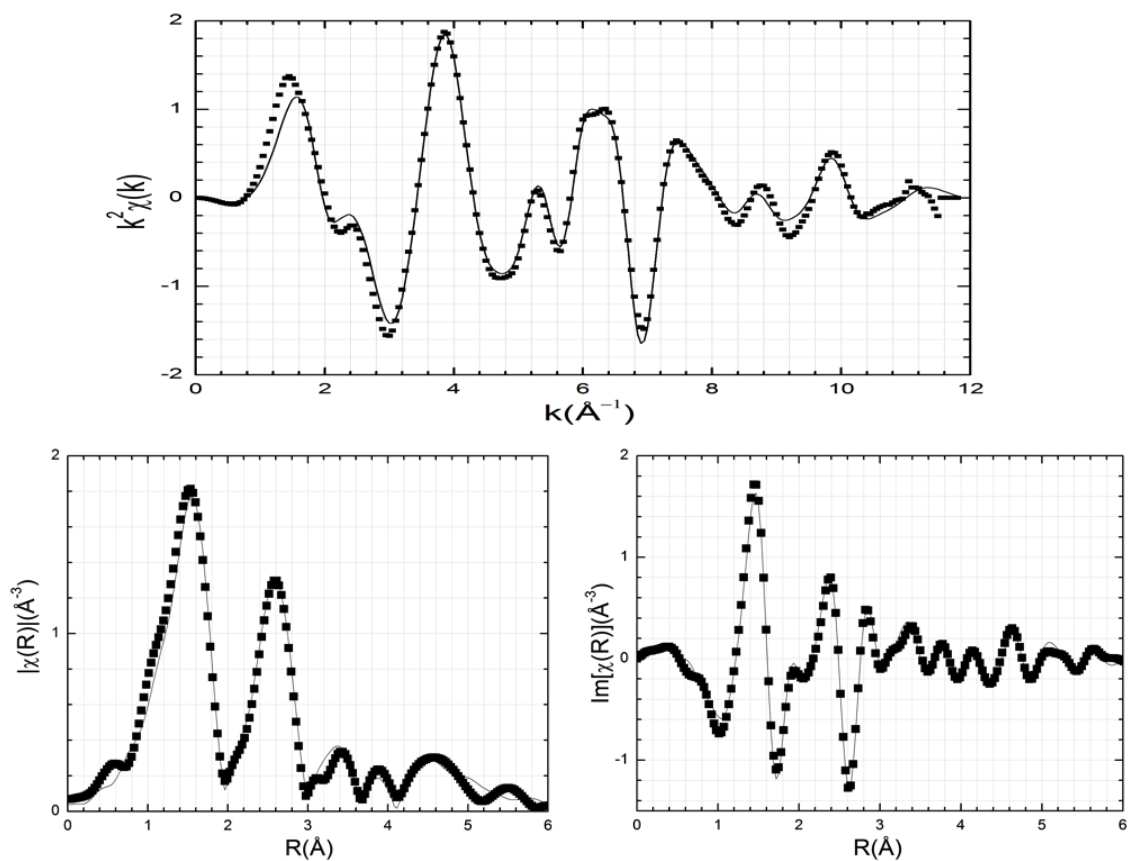


Figure A-1. Ni K-edge spectra recorded at 298 K and 5 MPa PH₂ on 10 wt.% Ni/C_zn-GI-SO₃H in 0.56 M phenol/water solution: (top) k^2 -weighted $\chi(k)$, (bottom left) $\chi(R)$ magnitude, and (bottom right) $\chi(R)$ imaginary plots. The black dots are recorded before the start of the reaction and the lines are the regression fits to data.

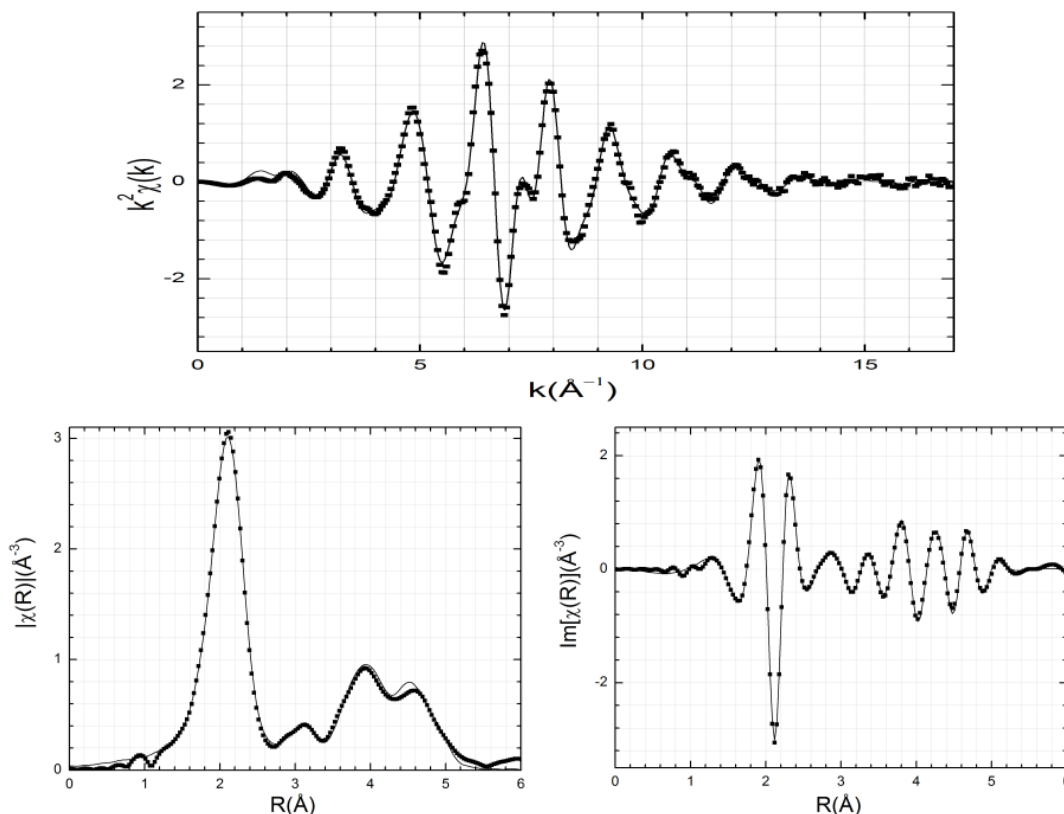


Figure A-2. Ni K-edge spectra recorded at 473 K and 5 MPa P_{H_2} during HDO of phenol catalyzed by 10 wt.% Ni/CZn-GI-SO₃H in 0.56 M phenol/water solution: (top) k^2 -weighted $\chi(k)$, (bottom left) $\chi(R)$ magnitude, and (bottom right) $\chi(R)$ imaginary plots. The black dots are recorded 67 min (reduction of Ni is complete) after the start of the reaction, and the lines are the regression fits to data.

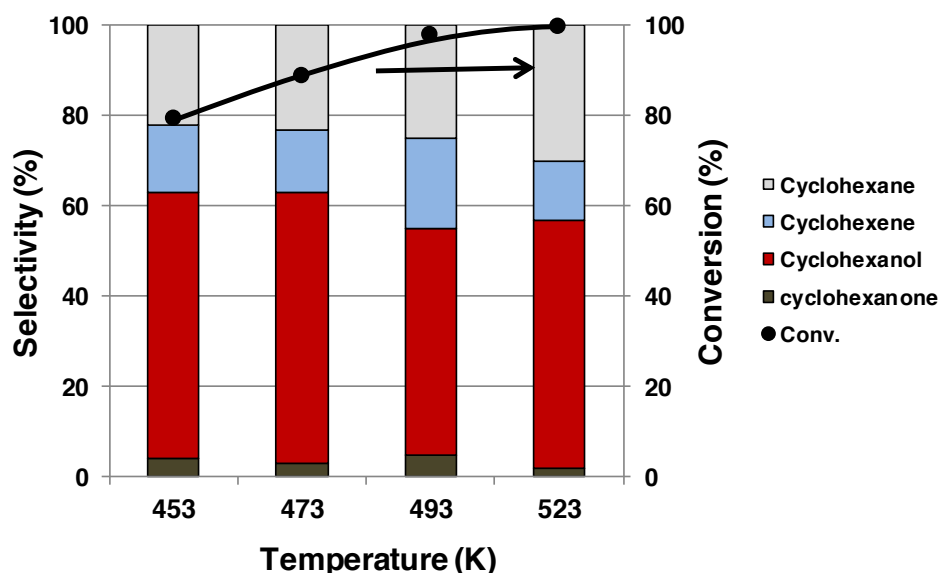


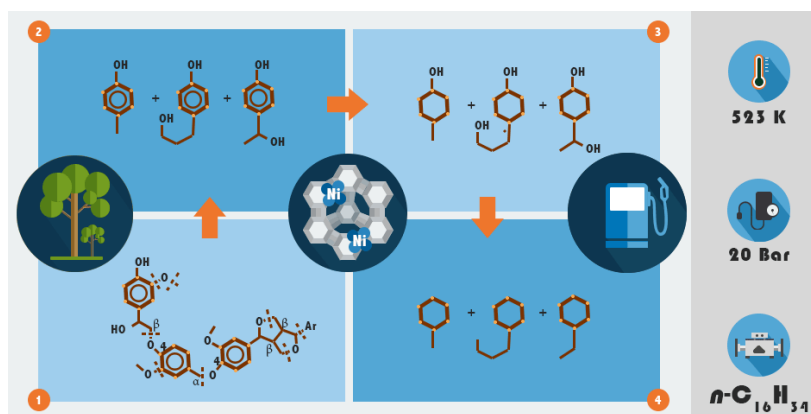
Figure A-3. Product distributions for phenol HDO over Ni/CZn-GI-SO₃H as a function of temperature. Reaction conditions: phenol (0.6 g), Ni/CZn-GI-SO₃H (0.12 g), hexadecane (60 ml), 4 MPa H_2 , stirring at 700 rpm, 2 h.

Chapter IV

Reductive deconstruction of organosolv lignin catalyzed by zeolite supported nickel nanoparticles

Abstract

Mechanistic aspects of deconstruction and hydrodeoxygenation of organosolv lignin using zeolite (HZSM-5 and HBEA) and SiO₂ supported Ni catalysts are reported. Lignin was deconstructed and converted to substituted



alicyclic and aromatic hydrocarbons with 5 to 14 carbon atoms. Full conversion with total yield of 70 ± 5 wt. % hydrocarbons was achieved at 593 K and 20 bar H₂. The organosolv lignin used consists of seven to eight monolignols subunits and has an average molecular weight of ca. 1200 g mol⁻¹. The monolignols were mainly guaiacyl, syringyl and phenylcoumaran, randomly interconnected through β -O-4, 4-O-5, β -1, 5-5' and β - β ether bonds. In situ IR spectroscopy was used to follow the changes in lignin constituents during reaction. The reductive catalytic deconstruction of organosolv lignin starts with the hydrogenolysis of aryl alkyl ether bonds, followed by hydrogenation of the aromatic rings to cyclohexenols. Oxygen is removed from the alcohols via dehydration on Brønsted acid sites to cyclic alkenes that are further hydrogenated.

1. Introduction

Lignin is one of the major components of lignocellulosic biomass, which constitutes also the most reduced carbon fraction.^[1-3] Conceptually, this minimizes the use of H₂ to produce linear and cyclic alkanes. The methoxylated phenylpropane units of lignin form a three-dimensional structure incorporated in the so-called lignin-carbohydrate complex (LCC).^[4, 5] Loosening the arrangement of LCC enables the separation of lignin and carbohydrates. One approach of isolating lignin from LCC is the so-called *organosolv* process, which is a chemically mild extraction through solvolysis, e.g., in ethanol/water mixtures at 473 K.^[6] This method leads to a lignin free of sulfur-containing compounds and other contaminants.^[7] Organosolv lignin is typically less condensed than the Kraft and soda lignins.^[8]

Conventionally, lignin is converted to liquid products in a two-stage process. The first stage includes rapid pyrolysis above 800 K or base-catalyzed deconstruction to yield bio-oil.^[9-12] The second stage involves upgrading of the thermally unstable bio-oils, which contain a variety of reactive oxygenates, into transportation fuels *via* hydrodeoxygenation (HDO). The HDO of various monomeric, bio-oil model compounds have been studied intensively.^[13-21] More recently, the cleavage of aryl ethers (i.e., dimeric phenolic compounds), as a key step in lignin depolymerization, has been a topic of increasing interest with focus on the effects of ring substituents, solvent and catalyst properties on the reactivities and selectivities during conversion of model ethers and real lignins.^[22-27] The complex structure of lignin has raised doubts concerning whether the direct hydrogenation of ring compounds as well as the hydrogenolysis is possible directly on the integral lignin polymer. To mitigate this perceived drawback, Rinaldi et al. explored Raney Ni catalyzed transfer hydrogenation of phenols, aldehydes and ketones as well as hydrogenolysis in aqueous iso-propanol solutions at autogenous pressures.^[28] Iso-propanol not only showed excellent hydrogen transfer properties, it simultaneously dissolved wood chips as the starting material.^[29] This strategy enables one-stage lignin isolation from whole cell wood to non-pyrolytic bio-oils, which are further hydrotreated. Non-polar solvents (e.g., methylcyclohexane) were found to be advantageous in terms of the higher selectivity to saturated products, compared to protic (e.g., alcohols) and polar aprotic (e.g., THF, dioxane) solvents, during the reductive deconstruction of organosolv lignin.^[30]

Although partial catalytic deconstruction of lignin has been achieved with these and other attempts using solid catalysts,^[31-34] the heterogeneity and complexity of real lignins renders complete deconstruction and the mechanistic understanding on a molecular level challenging.^[35] To address this, physicochemical methods probing both the catalyst and

the reaction mixture under working conditions have been used in the present contribution to link the previous model studies to a one-stage liquid phase process for hydro-deconstructing organosolv beech lignin (< 600 K, 20 bar H₂). In particular, attenuated total reflectance infrared spectroscopy (ATR-IR) is used to interrogate interaction between molecules and the surface of solid catalysts at operating conditions.

2. Experimental section

2.1 Chemicals

All chemicals were purchased from commercial suppliers and used without further purification: organosolv beech lignin (Fraunhofer Institute, Leuna), Ni(II) nitrate hexahydrate (Merck, 99 %), *n*-heptane (Merck, 99 %), *n*-hexadecane (Sigma-Aldrich, 99 %), ethyl acetate (Fluka, 99.7 %), tetrahydrofuran (Sigma-Aldrich, 99 %), cyclohexane (Sigma-Aldrich, 99 %), methylcyclohexane (Sigma-Aldrich, 99 %), ethylcyclohexane (Sigma-Aldrich, 99 %), *n*-propylcyclohexane (Sigma-Aldrich, 99 %), dimethyl sulfoxide (DMSO, Fluka, 99.5 %), ammonium hydroxide (Sigma-Aldrich, 28.0-30.0 % aqueous solution), dimethyl glyoxime (Sigma-Aldrich, 99 %), DMSO-*d*₆ (Sigma-Aldrich, 99.9%), acetone (VWR, 95%), urea (Merck, 99.5 %), HZSM-5 (H-form, Si/Al 45, Clariant AG), HBEA (H-form, Si/Al 75, Clariant AG), SiO₂ (Aerosil 200, Evonik AG).

2.2 Preparation of Ni-based catalysts

Nickel deposition on oxide supports was performed following the deposition precipitation (DP) procedure described in the literature.^[36] In a typical synthesis, a 250 ml aqueous solution of 0.14 M Ni(NO₃)₂ was prepared. 2 g of zeolite were suspended in 210 ml of that solution. The remaining 40 ml of Ni(II) solution was used to dissolve 10.2 g of urea, which was added dropwise to the zeolite suspension at 343 K. This mixture was heated further to 363 K to start the DP process. After 3 h, the suspension was cooled to ambient temperature, vacuum filtered, and the solid was washed three times with ultra-pure water. The recovered solid was dried at 383 K in air overnight. The dry solid was calcined at 673 K for 4 h in synthetic air with a heating rate of 1 K min⁻¹ (flow rate: 100 ml min⁻¹), and then reduced in pure hydrogen at 733 K for four hours with a heating rate of 1 K min⁻¹ (hydrogen flow: 100 ml min⁻¹). The synthesis of Ni/SiO₂ catalyst followed the same procedure as described above, but with a DP time of 3.5 h.

2.3 Catalyst characterization

2.3.1 Ni loadings

The catalysts were dissolved in a mixture of hydrofluoric acid and *aqua regia*. The concentration of Ni in the resulting solution was analyzed by atomic absorption spectroscopy (AAS) on a UNICAM 939 AA-spectrometer.

2.3.2 Sorption measurements

The BET specific surface areas and pore volumes were determined from N₂ adsorption-desorption isotherms measured at 77 K on a Thermo Scientific Surfer Analyzer automatic sorptometer. Prior to the measurements, the samples were activated in vacuum at 473 K for 2 h.

2.3.3 IR-spectra of adsorbed pyridine

The infrared spectra of adsorbed pyridine (Py-IR) were recorded on a Thermo Nicolet 5700 spectrometer at a resolution of 4 cm⁻¹. The sample was pressed to a self-supporting wafer and activated in vacuum ($p = 10^{-6}$ mbar) at 723 K for one hour (heating rate = 10 K min⁻¹). After cooling to 423 K, the sample was equilibrated with 0.1 mbar of pyridine for half an hour, outgassed for one hour, and the IR spectra of chemisorbed pyridine were recorded. For quantification, the IR spectra were normalized to the integral of the overtone lattice band between 2105 and 1740 cm⁻¹ of the activated sample, and molar extinction coefficients of 0.73 cm μmol⁻¹ and 0.96 cm μmol⁻¹ were used for the characteristic vibration bands of pyridinium ions and pyridine bound to Lewis acid sites, respectively.

2.3.4 Transmission electron microscopy (TEM)

Transmission electron microscopy (TEM) pictures were acquired by a JEM-2010 Jeol transmission microscope operating at 120 kV. The catalyst sample was first sonicated in methanol and a single drop of the suspension was placed onto a carbon coated Cu grid. Around 300 particles were measured to determine the average particle size of Ni.

2.3.5 X-ray diffraction (XRD)

X-ray diffraction (XRD) was applied to elucidate the crystal structures of the catalyst powder by a Philips X'Pert Pro System with Cu-K α radiation operating at 45 kV and 40 mA. The catalysts were measured with a scanning rate of 0.017° s⁻¹ in the range of 5 to 70° (2 θ). The metal particle size was calculated from the diffraction of Ni(111) using the Scherrer equation.

2.3.6 H₂ chemisorption

Ni dispersion was determined by H₂ chemisorption measurements on a Thermo Scientific Surfer Analyzer. Prior to sorption, 0.15 g of catalyst was activated in H₂ atmosphere at 723 K for 1 h and then cooled to ambient temperature. H₂ adsorption isotherms measured in the H₂ pressure range of 0.01 – 0.4 bar include both chemisorption and physisorption. The system was evacuated for at least one hour to remove physisorbed hydrogen. The chemisorbed hydrogen on the metal was determined by extrapolating the isotherm to zero H₂ pressure. The dispersion was calculated on basis of the assumption of an average Ni to H ratio of 1.

2.4 Organosolv Lignin characterization

2.4.1 Elemental Analysis

The sample was balanced on a tin plate with an accuracy of $\pm 1 \mu\text{g}$. Carbon, hydrogen, nitrogen and sulfur contents (CHNS) were determined on a EURO EA CHNSO analyzer from HEKAtech GmbH.

2.4.2 Gel permeation chromatography

The organosolv lignin was dissolved in anhydrous THF at a concentration of 1 mg ml⁻¹. Gel permeation chromatography measurements were conducted on a Varian PL GPC 50 Plus with a PL-gel Mixed C column at 303 K and a flow of 1 ml min⁻¹. The external calibration was performed with the EasiVial® polystyrene (PS)-H standard for GPC containing narrow distributed (DP of 1.02 – 1.08) PS standard. The calculation of the M_n and M_w was performed with the Cirrus Software Package.

2.4.3 MALDI-TOF MS

For MALDI-TOF MS analyses, the samples were prepared according to procedures reported in the literature.^[37, 38] The α -cyclodextrin/ α -cyano-4-hydroxycinnamic acid (α -CD/CHCA) matrix was prepared by mixing 2.4 ml of a 10 mM aqueous α -CD solution with 75 mM CHCA in 0.4 ml acetonitrile/H₂O (7/3 v/v) containing 0.1 vol.% trifluoroacetic acid. The α -CD/CHCA complex was obtained after sonication at 323 K for one hour. The organosolv lignin was dissolved in tetrahydrofuran at a concentration of 1 mg ml⁻¹. Both solutions were deposited on a metal target and the solvents were evaporated. High resolution mass spectra were recorded on an Ultraflex MALDI time-of-flight mass spectrometer (Bruker Daltonic) operating in the reflector positive mode using pulsed nitrogen laser (λ 337 nm, pulse rate of 10 Hz) as the ionization pulse. The analyzer was used at an acceleration voltage of ± 20 kV. For the lignin sample, MALDI-TOF MS spectra

were recorded on 9 distinct sample deposit zones to verify the representativeness of the analyses.

2.4.4 ATR-IR spectroscopy

Attenuated total reflection infrared (ATR-IR) spectra were collected on a Thermo Fischer Nicolet 6700 spectrometer at a resolution of 4 cm^{-1} accumulating 32 scans on a home-built ATR cell with a trapezoid ZnSe crystal as internal reflection element. 20 mg of organosolv lignin were suspended in 2-propanol by ultrasonication for a couple of minutes and drop coated on the ZnSe crystal, where isopropanol was removed on a heating plate at 353 K. A background spectrum of ZnSe was collected prior to the sampling of organosolv lignin.

The *in situ* ATR-IR study of organosolv lignin hydro-deconstruction was performed in a lab-built ATR-IR cell, where the idea of a double chamber cell design.^[39, 40] The technical drawing and more detailed descriptions of the ATR-IR cell are provided in the Figure 4-1 and Figure 4-2.

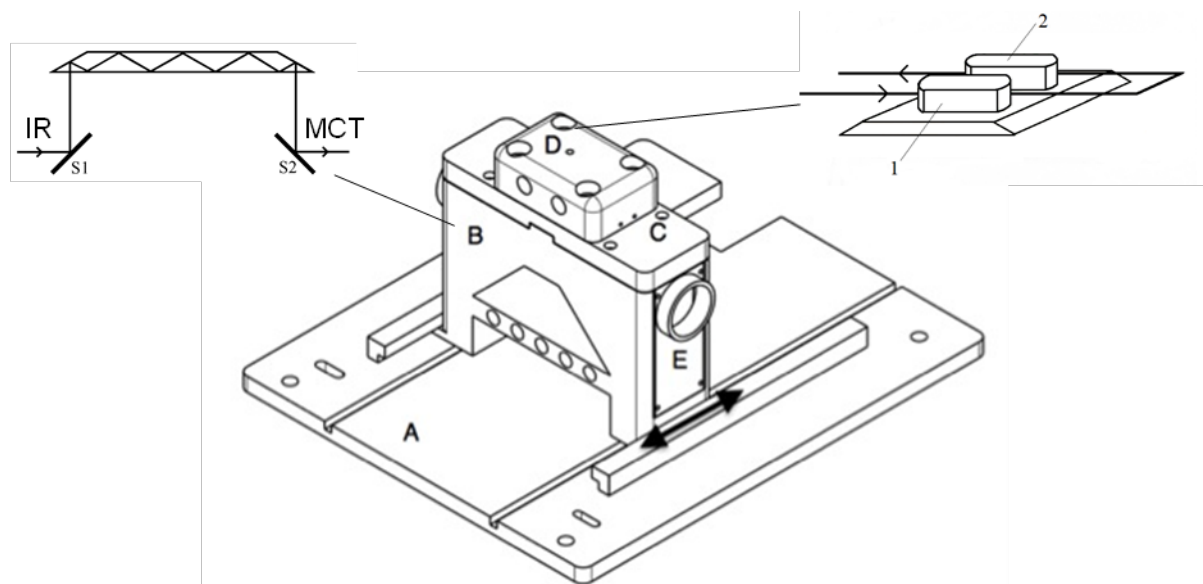


Figure 4-1. Schematic technical drawing of the home-made *in-situ* ATR-IR cell composed of the base unit (A) equipped with runners, reflector (B) with gold coated mirrors, ZnSe holder (C) with notch for IR beam, two chambers cell (D) with heating cartridges and thermocouple, connection to the N₂ purging lines (E).

The ATR-IR apparatus (see Figure 4-1) for the technical drawing and Figure 4-2 for a photograph) consists of five main parts. The base unit (A) enables a three-dimensional adjustment to align the cell within the spectrometer to the IR beam. Together with its runners, the ATR cell can be shifted forward and backward. The reflection unit (B) is connected to the base unit through complementary fittings to the runner lines. Within the reflection unit, two gold-coated mirrors reflect the IR beam to the top of the cell and back from the top to the detector. In the upper left corner of Figure 4-1 is an illustration of the IR beam path from the IR source to the reflecting mirror S1 to the ZnSe crystal with the

crystal geometry of $27 \times 20 \times 2 \text{ mm}^3$ and a phase of 30° resulting in a total of nine reflections inside the crystal and to the S2 mirror. The crystal holder (C) is attached to the reflection unit, where four 3-mm notches are left for the IR beam to penetrate the ZnSe crystal. Within the ZnSe crystal, the IR beam undergoes in total nine reflections where three are in contact with the measured sample. On top of the ZnSe crystal, the double-chamber ATR cell (D) is attached and tightened up to the crystal holder with graphene gaskets. It is equipped with the feeding lines for both cell compartments, which are connected through 1/16-inch lines and inlets for heating cartridges and a thermocouple. In the upper right corner of Figure S1 is a drawing of the cell design showing the two chambers and the flow of the liquid/gas feed, which goes first to chamber 1 and then passes through chamber 2. The volume of each chamber is around 0.3 ml, and the connecting line between chamber 1 and 2 has a volume of 0.02 ml.

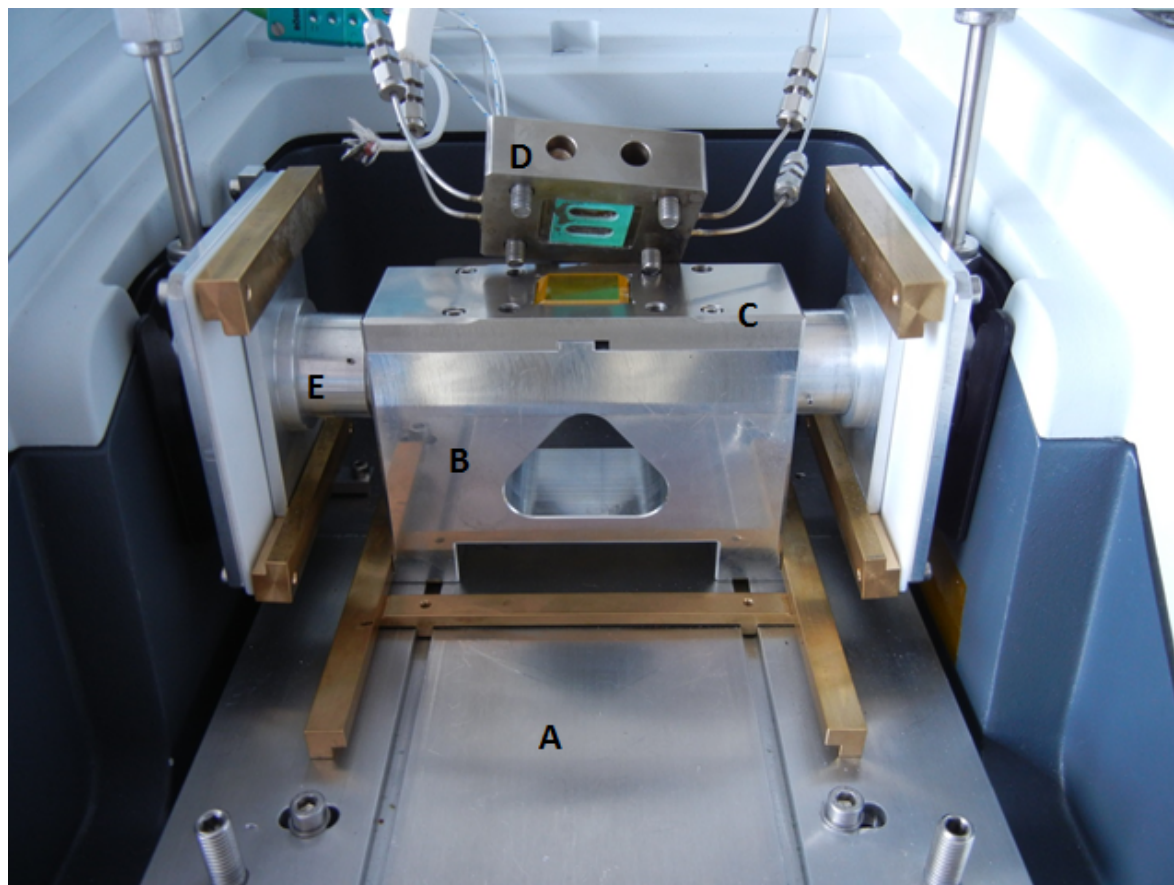


Figure 4-2. Photographed lab-built in-situ ATR-IR cell composed of the base unit (A) equipped with runners, reflector (B) with gold coated mirrors, ZnSe holder (C) with notch for IR beam, two chambers ATR cell (D) with temperature sensor and cartridge heaters, N_2 purging lines (E) adjustable to the forth and back movement of the cell.

In a typical *in situ* ATR-IR experiment, a mixture of organosolv lignin and Ni/HBEA catalyst at a weight ratio of 2:1 was mixed with isopropanol and sonicated for 5 min. The mixture

was then drop-coated on the surface of ZnSe and the solvent evaporated at 353 K. The drop-coated ZnSe crystal was placed on the holder and the cell was closed, pressurized with H₂ to 20 bar and heated to 523 K with a heating rate of 10 K min⁻¹. At this condition, a background spectrum of chamber 1 (catalyst/lignin mixture) and chamber 2 (empty cell) was collected at a resolution of 4 cm⁻¹ and 32 scans. After that, the reaction was initiated by pumping *n*-hexadecane through the cell at a rate of 0.05 ml min⁻¹. The single beam spectra were collected every 30 min, with an acquisition time of 40 s. The time difference of spectra collection between chamber 1 and chamber 2 was 2 min. The baseline correction of each single beam spectrum was derived by using a blank ZnSe crystal as background spectrum. The difference between spectra collected from Chamber 1 (sample cell) from Chamber 2 (reference cell). During each *in situ* ATR-IR experiment, a sample of the liquid phase was taken at a contact time of 90 min and analyzed through GC-MS as described in section 2.5. The schematic drawing of the periphery for H₂ and liquid phase supply, liquid phase sampling as well as the arrangement of the ATR-IR cell is shown in Figure 4-3.

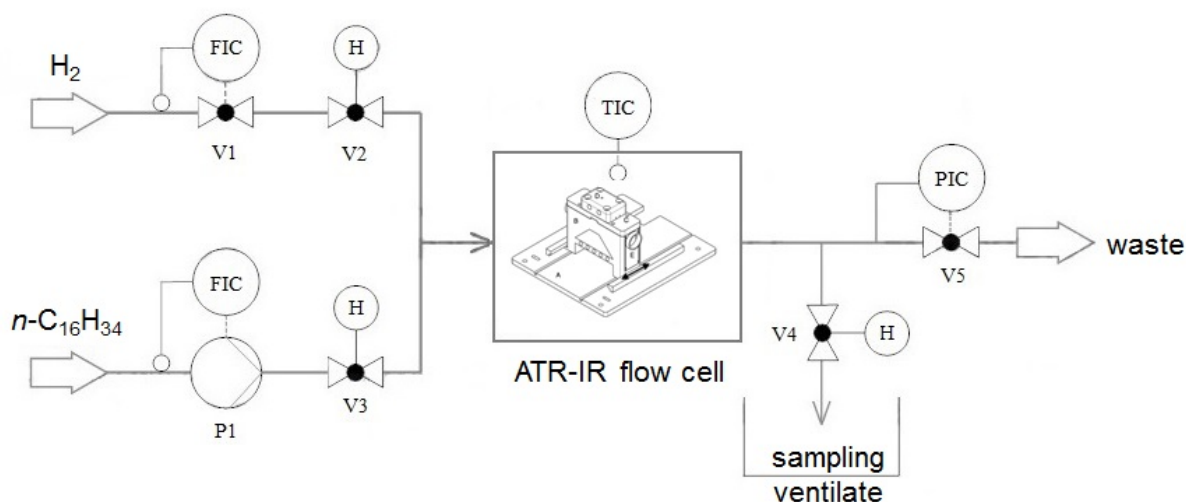


Figure 4-3. Schematic outline of the experimental set-up illustrating the peripheral arrangement of the ATR-IR apparatus.

2.4.5 Scanning electron microscopy (SEM) – energy dispersed X-ray analysis (EDX)

SEM was performed on a JEOL JSM 7500F, high-resolution scanning electron microscope with cold emission electron gun, operated at 1 kV. Sample preparation was similar to the drop coating procedure on ZnSe, but with a silicon wafer as sample carrier. EDX was performed during SEM measurements with a JEOL JED- 2300F energy dispersive X-ray analyzer with dry silicon drift detector.

2.4.6 Solution state NMR spectroscopy

HSQC NMR spectra were measured on Bruker AV500 (^1H NMR 500 MHz, ^{13}C NMR, 125 MHz) nuclear magnetic resonance spectrometer. The NMR spectra of the lignin sample were recorded in $\text{DMSO-}d_6$; the solvent peak was used as the internal reference.

2.5 Catalytic measurements

The catalytic reactions were carried out in a batch reactor (Parr Instruments, 300 ml). In a typical experiment, the reactor was loaded with 0.5 g Ni catalyst, 1 g organosolv lignin, 100 ml hexadecane and 1 ml of *n*-heptane as internal standard, sealed and purged with H_2 three times. The reactor was pressurized with 20 bar of H_2 at ambient temperature and heated up to either 523 K or 593 K while stirring at 700 rpm. The temperature was reached within 15 min, which was used as the zero reaction time. During the reaction, aliquots of 1.5 ml were sampled into GC vials. To end the reaction, stirring and heating was stopped, and the reactor was cooled down in air for the first 5 min, followed by quenching with an ice-water mixture to room temperature which lasted another 5 min.

2.6 Analysis of gas, solution and solid phases of reaction mixture

The gas phase was collected into a gas bag after the reaction and subsequently analyzed with an Agilent Technologies 7890B GC equipped with a HP-1 column (30 m x 0.4 μm) and thermal conductivity and flame ionization detectors (TCD and FID). Based on the external calibration with methane/ethane/propane standard mixture (1 vol.% for each) diluted in Argon from Westfalen, the integrated signals were quantified.

Subsequently, a liquid phase aliquot of the organic mixture was collected. This sample was analyzed on an Agilent Technologies 7890B GC equipped with a HP-5 column GC-FID (quantification) (30 m x 0.25 μm) connected to Agilent Technologies 5977A MSD GC-MS (identification of products). The yield in wt. % was calculated based on the internal standard *n*-heptane with the following equation:

$$\frac{\text{Peak area of products}}{\text{Peak area of } n\text{-heptane}} \times \frac{0.68 \text{ g}}{1 \text{ g}} \times 100\% = \text{Yield of hydrocarbons in wt. \% (1)}$$

The 0.68 g is the absolute weight of the added 1 ml of *n*-heptane and 1 g is the starting weight of the lignin sample. The selectivity in C% was calculated based on the following equation:

$$\frac{\text{Peak area of identified products}}{\text{Peak area of all products}} \times 100\% = \text{Selectivity in C\% (2)}$$

The fragmentation pattern in the MS has been compared using the NIST Mass Spectral Search Program for the NIST/EPA/NIH Mass Spectral Library Version 2.0 g, build Dec 4 2012 to match the identified products with probabilities higher than 73%. To further identify

the liquid product fraction, naphthenes as standard materials were mixed at defined concentrations (mimicking the concentrations of products in a real experiment) in the non-polar *n*-hexadecane. This standard series was used to calibrate the FID response factors of major products, such as methyl-, ethyl-, and *n*-propylcyclohexane. This quantification method produced almost identical quantification results as the one using *n*-heptane as the internal standard. Additionally as a cross-check, a mixture of branched saturated alkanes (2 mg/L) was identified with MS detector in order to evaluate the NIST database. The formed aqueous phase (mainly water containing traces of dissolved fractions, the exact concentrations of which were not determined) was not miscible with *n*-hexadecane, so it was readily separable and determined volumetrically. The solid residue was freeze-dried and weighed. The mass balance was 95 ± 5 % in this work.

2.7 Recycle runs

Catalyst recycling runs have been performed under the same conditions as described in section 2.5. The catalyst was recovered by filtration, freeze-dried and reactivated in hydrogen flow at 733 K. A small fraction of the recovered catalyst (0.1 g) has been stored for further analysis (TEM, BET, Pyridine-IR), the remaining 0.4 g of the catalyst has been mixed with 0.1 g of a fresh fraction of Ni catalyst to perform the recycling runs.

3. Results and Discussion

3.1 Physicochemical properties of Ni catalysts

Physicochemical characteristics of the Ni catalysts used in this work are summarized in Table 4-1. The textural properties of the catalysts and supports are compiled in Table 4-2. The Ni loadings are comparable at 21, 20, and 21 wt. % for HZSM-5, HBEA and SiO₂ supported catalysts, respectively. Catalysts with lower Ni loadings (10%, 15%) were less efficient for catalytic deconstruction of lignin, on a total Ni basis (i.e., normalized to the mass of Ni per gram of catalyst).

Table 4-1. Characterization of Ni catalysts: chemical composition, acid properties, and Ni particle size.

Catalyst	Ni (wt.%) ^a	Acidity ($\mu\text{mol}\cdot\text{g}^{-1}$) ^b		Ni particle size	
		BAS	LAS	d_{Ni} (nm) ^c	Ni dispersion (%) ^d
Ni/HZSM-5	21	36	91	4.8 ± 1.2	13
Ni/HBEA	20	19	71	5.1 ± 1.1	13
Ni/SiO ₂	21	-	39	4.5 ± 1.0	13

^a Determined by AAS.

^b Determined by IR spectra of adsorbed pyridine, BAS: Brønsted acid site, LAS: Lewis acid site.

^c Determined by TEM.

^d Determined by H₂ chemisorption.

Table 4-2. Physicochemical properties of bare supports and Ni catalysts.

Support/ Catalyst	BET surface area [$\text{m}^2 \text{g}^{-1}$]			Pore volume [$\text{cm}^3 \text{g}^{-1}$]		
	Micro	Meso	Total	Micro	Meso	Total
HZSM-5	369	55	424	0.17	0.12	0.29
Ni/HZSM-5	243	108	351	0.12	0.15	0.27
HBEA	289	180	469	0.19	0.34	0.53
Ni/HBEA	76	332	408	0.04	0.47	0.51
SiO ₂	27	160	187	0.04	0.26	0.30
Ni/SiO ₂	18	239	257	0.08	0.65	0.73

The physicochemical properties of parent supports as well as the Ni incorporated catalysts are summarized in Table 4-2. The zeolites showed higher specific surface areas, i.e., 469 $\text{m}^2 \text{g}^{-1}$ for HBEA and 424 $\text{m}^2 \text{g}^{-1}$ for HZSM-5, than silica with 187 $\text{m}^2 \text{g}^{-1}$. In comparison with HZSM-5, the Ni/HZSM-5 sample exhibited a smaller surface area of 351 $\text{m}^2 \text{g}^{-1}$; specifically, the mesoporous fraction increased by more than twice (55 $\text{m}^2 \text{g}^{-1}$ for parent HZSM-5 and 108 $\text{m}^2 \text{g}^{-1}$ for Ni/HZSM-5), whereas the micropore fraction decreased from 369 $\text{m}^2 \text{g}^{-1}$ (parent HZSM-5) to 243 $\text{m}^2 \text{g}^{-1}$ (Ni/HZSM-5). Similarly, for HBEA, the surface area reduced from 469 to 408 $\text{m}^2 \text{g}^{-1}$ upon Ni incorporation, where mesopores increased by almost twofold (180 $\text{m}^2 \text{g}^{-1}$ for HBEA and 332 $\text{m}^2 \text{g}^{-1}$ for Ni/HBEA, respectively) and micropores reduced by four times (289 vs 76 $\text{m}^2 \text{g}^{-1}$). These changes of the textural properties of support materials upon loading ca. 21% Ni are caused, in part, by the deposition precipitation procedure due to the acidic nature of aqueous suspension (pH ~ 2) during synthesis. Although urea decomposition generates *in situ* hydroxyl ions, which neutralizes the aqueous stirred suspension, the final mixture is still slightly acidic at pH ~ 5. The distribution of pore sizes changed as well after synthesis. The change of the textural properties can be explained by the hydrolytic degradation of the siliceous lattice during the acidic aqueous synthesis and the blockage of micropores by the deposited Ni particles. However, the change of the structural integrity of the support materials is beyond the scope of this work.

The concentrations of Brønsted (BAS) and Lewis acid sites (LAS) of the Ni catalysts as well as the parent support materials (Table 4-3) were determined from the IR spectra of adsorbed pyridine after outgassing at 423 K. The acid site concentrations of the catalysts differed substantially from those in the supports before deposition of Ni. The BAS concentrations in Ni/HZSM-5 (36 $\mu\text{mol g}^{-1}$) and Ni/HBEA (19 $\mu\text{mol g}^{-1}$) were reduced to 10% of the concentrations in the parent zeolites (360 and 190 $\mu\text{mol g}^{-1}$, respectively), caused by ion-exchange of Brønsted acid sites with Ni^{2+} .^[41] In contrast, the LAS concentrations (91 and 45 $\mu\text{mol g}^{-1}$ for Ni/HZSM-5 and Ni/HBEA, respectively) were slightly higher than in the parent zeolites (71 and 40 $\mu\text{mol g}^{-1}$, respectively). The Ni/SiO₂ catalyst showed 39 $\mu\text{mol g}^{-1}$ LAS without detectable BAS.

The Ni particle sizes have been determined through transmission electron microscopy (TEM pictures shown in Figure 4-4). According to the statistical analyses, the three catalysts contain Ni particles with 5-10 nm average diameter and very similar size distributions. The Ni dispersion measured by H₂ chemisorption was 13% for all three catalysts, in good agreement with TEM measurements.

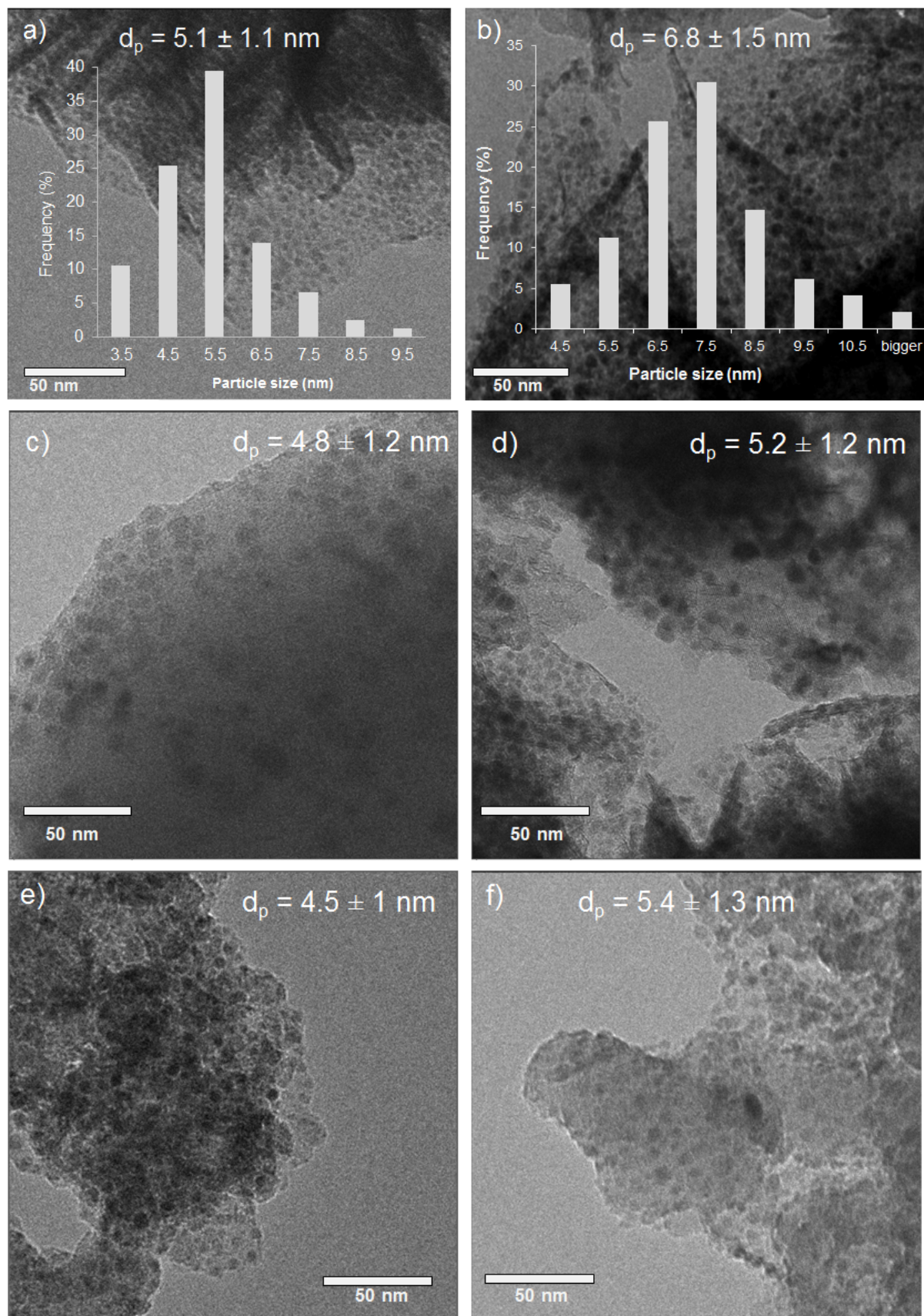


Figure 4-4. TEM of a) fresh Ni/HBEA catalyst, b) used Ni/HBEA, c) fresh Ni/HZSM-5 catalyst, d) used Ni/HZSM-5, e) fresh Ni/SiO₂ catalyst and f) used Ni/SiO₂

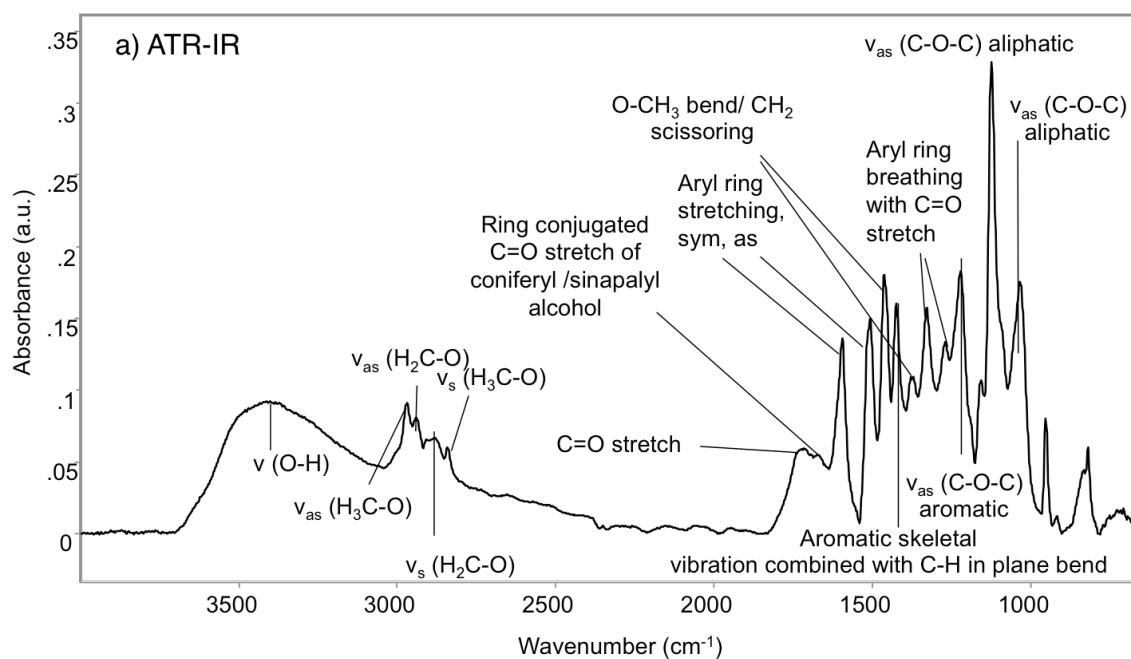
Table 4-3. Acid concentrations of parent support materials.

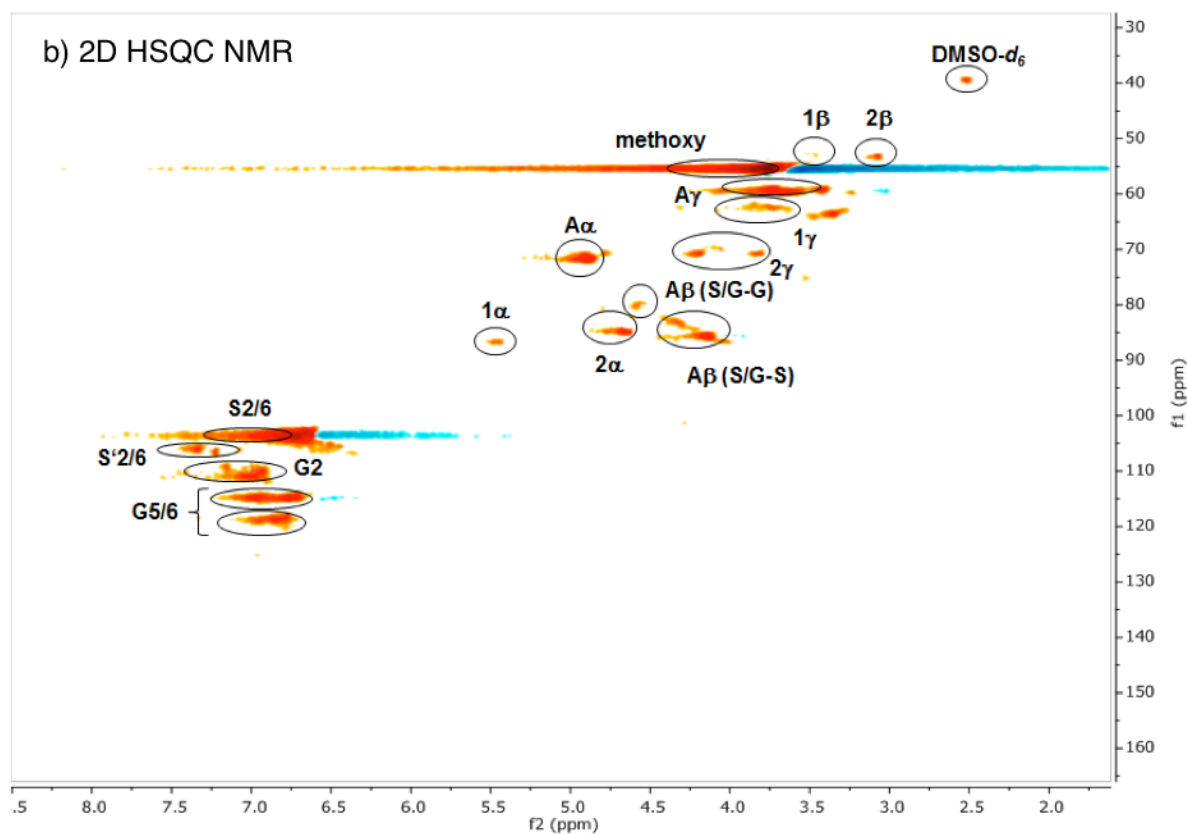
Support	Si/Al ratio	Acidity ($\mu\text{mol}\cdot\text{g}^{-1}$) ^a	
		BAS	LAS
HZSM-5	45	360	46
HBEA	75	190	41
SiO ₂	-	-	-

^a Determined by Pyridine-IR.

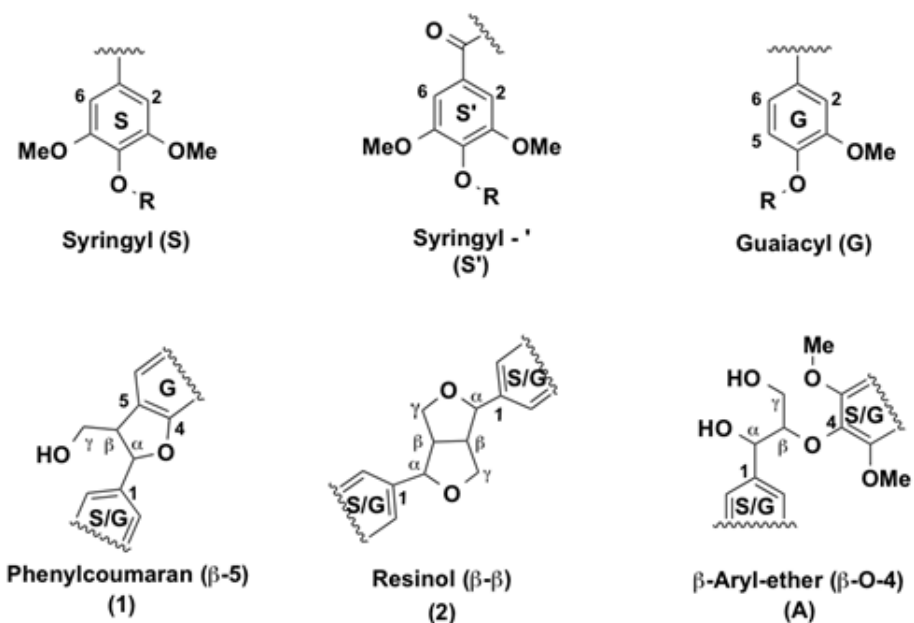
3.2 Analysis of organosolv lignin

Figure 4-5 compiles the main results obtained from different analytical approaches used to elucidate the structure of the starting organosolv lignin. The ATR-IR spectrum of the organosolv lignin (Figure 4-5a) shows a series of bands characteristic of aromatic structures, *i.e.*, ring C=C stretching vibrations (1593 for symmetric and 1504 cm^{-1} for asymmetric mode), aryl ring breathing combined with $\text{C}_{\text{aromatic}}\text{-O}$ vibration (1326 cm^{-1}) and C=O stretching vibration (1270 cm^{-1}) and aromatic skeletal vibrations combined with C-H in plane bending (1422 , 1156 cm^{-1}). Likewise, the oxy-functionalization is documented by bands of aromatic and aliphatic hydroxyl groups (3500 cm^{-1}), alkyl aldehyde and/or ketone groups (1722 cm^{-1}), aryl conjugated C=O (the shoulder peak at 1680 cm^{-1}), as well as methoxy groups (evidenced by a bending mode at 1369 cm^{-1}). The linkages between the aromatic structures of the lignin have bands characteristic of aliphatic C-O-H and ether C-O-C groups.⁴²⁻⁴⁴





c) Present monolignols and linkages



d) Representative structure of the lignin fragment

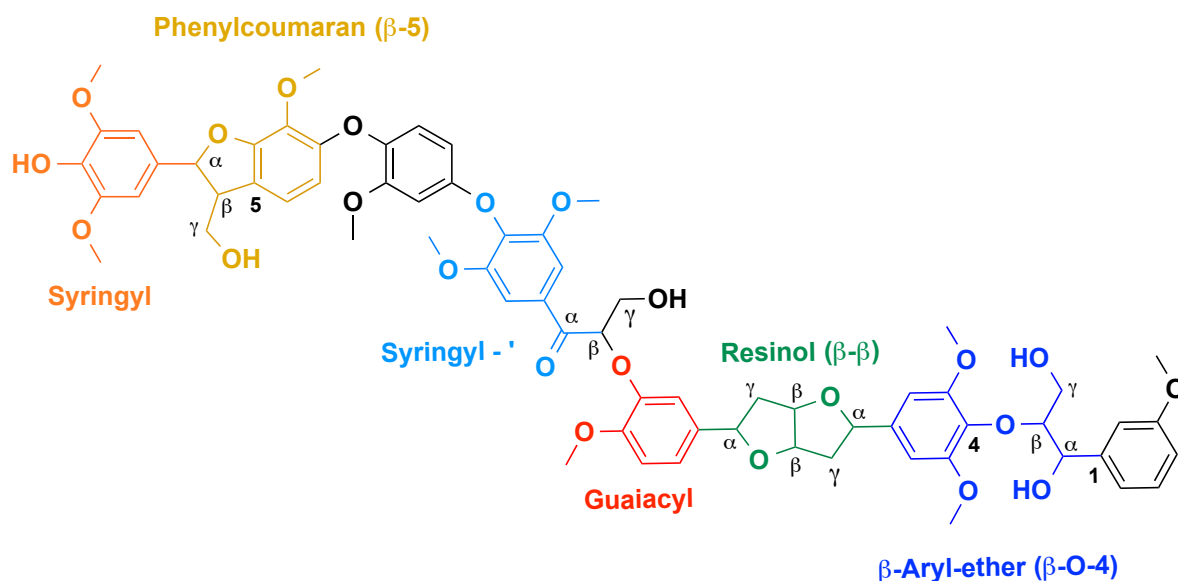


Figure 4-5. Elucidating the structure of beech extracted organosolv lignin. a) ATR-IR spectrum; b) 2D HSQC NMR ($\text{DMSO-}d_6$); c) Representation of monolignolic units (S, S' and G) and its lignol linkages (β -5, β -O-4, β - β); d) Schematic lignin fragment showing the seven monolignols identified.

The starting lignin material was further analyzed by liquid phase HSQC NMR in $\text{DMSO-}d_6$ (Figure 4-5b). The main monolignols are guaiacyl (G), syringyl (S) and carbonyl functionalized syringyl (S'), as indicated by the resonances in the aromatic region (100-130 ppm), characteristic of substituted benzene rings. Specifically, the signals correspond to the $-\text{CH}=\text{CH}-$ of guaiacyl (G5/6; G2), the syringyl and keto type syringyl $-\text{CH}=\text{CH}-$ linkages of the unsaturated ring.

In the aliphatic carbon region (60-90 ppm), peaks were detected for methoxy, CH- and HO-CH_2- groups associated with the β -O-4 (β -aryl ether) (A), β - β (resinol) (C) and β -5 (phenylcoumaran) linkages. Signals corresponding to the tetrahydrofuran ring were also observed: $-\text{CH-O}-$ (1α and 2α), OH-CH- ($A\alpha$), $-\text{CH-O}-$ ($A\beta$ syringyl and guaiacyl), and $-\text{CH}_2-\text{OH}$ ($A\gamma$, 1γ) and $-\text{CH}_2-\text{O}-$ (2γ). The ^{13}C signals detected at 53 ppm correspond to $-\text{CH-CH-O}-$ (1β , 2β) carbons in the saturated furan ring. The $-\text{CH}_3$ carbons of the methoxy group appeared at 55 ppm. The assignment is based on published attributions in the literature.^[45-47] From the 2D HSQC NMR analysis, we conclude that this organosolv lignin contains mainly guaiacyl and (C=O conjugated) syringyl units (Figure 4-5c), which are randomly connected through β -5, β -O-4 and β - β ether linkages.

According to the MALDI-TOF MS spectrum shown in Figure 4-6, the average molecular weight of the Beech extracted organosolv lignin was ca. 1200. Therefore, we conclude that this organosolv lignin is an oligomer comprised of approximately seven interconnected monolignols. GPC analysis (Figure 4-7) showed a number-averaged molecular weight of 1107 g mol^{-1} and a weight-averaged molecular weight of 2281 g mol^{-1} ,

corresponding to a dispersity of 2.1. MALDI-TOF MS is comparable to the GPC result (1200 vs. 1107 g mol⁻¹), where the molecular weight was slightly underestimated because of the difference of hydrodynamic volume of the external linear unbranched polystyrene and the branched or irregularly connected lignin sample. From the above analysis, we propose the structure shown in the Figure 4-5d as a model, including all structural characteristics of the starting organosolv lignin. This structure has a chemical formula of C₆₈H₇₄O₂₃ and a molecular weight of 1258 g mol⁻¹, which is consistent with the elemental analysis (C₇₀H₈₀O₂₄), GPC (1108 g mol⁻¹) and MALDI-TOF MS measurements (1239 g mol⁻¹). Note, however, that this proposed structure does not specifically take into account the abundance of each type of linkage, and is not meant to represent the only possible sequence, as lignin structures are intrinsically irregular.

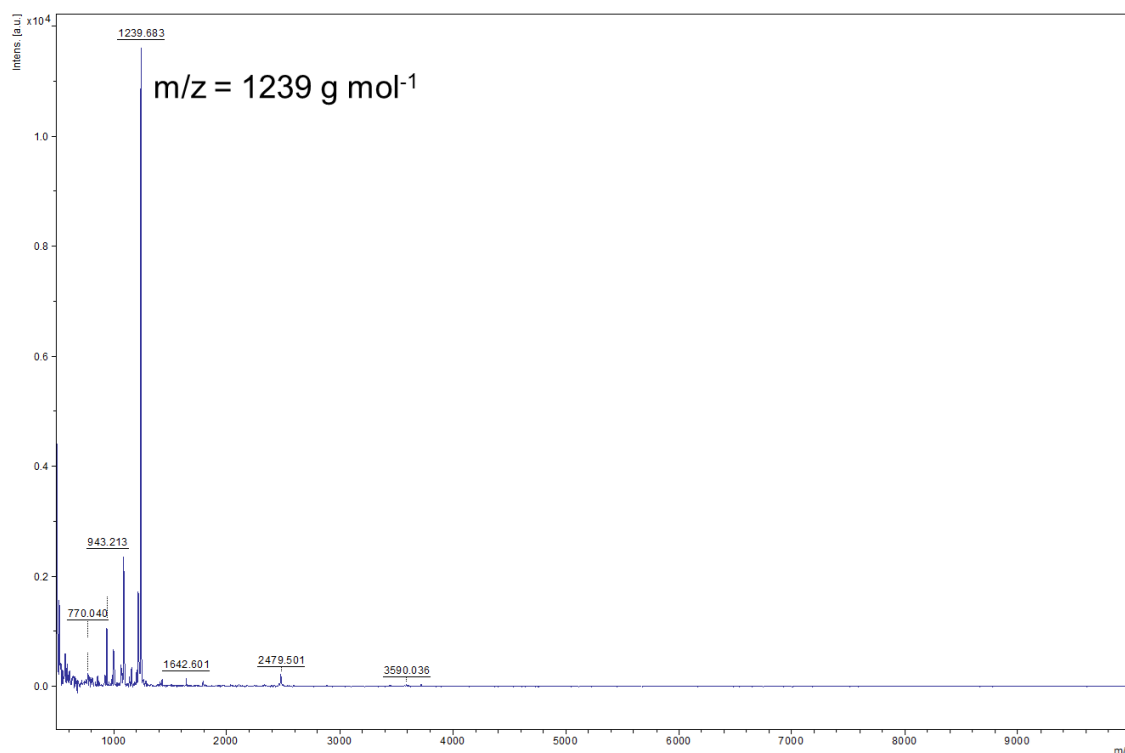
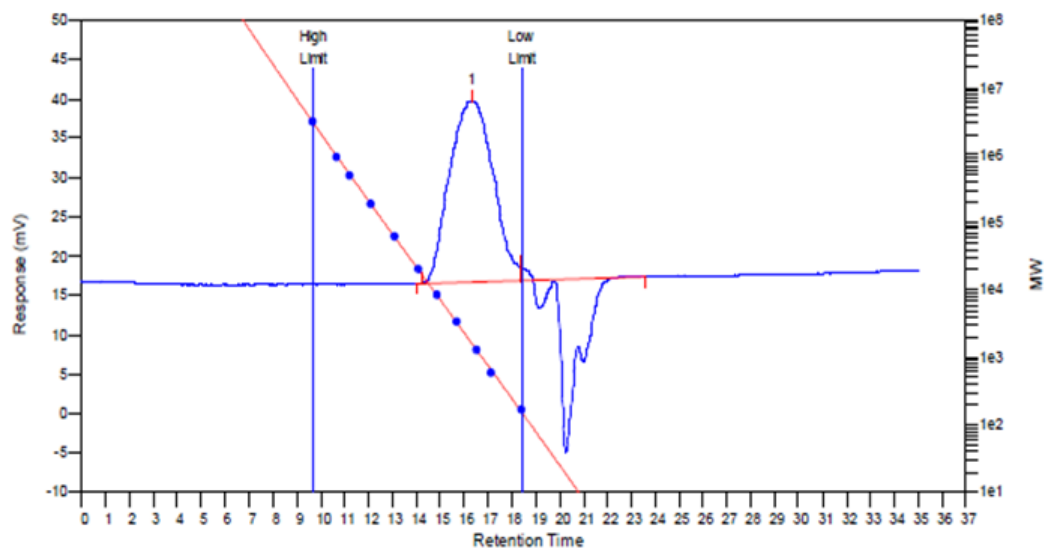


Figure 4-6. Matrix-assisted Laser Desorption/Ionization Time-Of-Flight Mass Spectrometry (MALDI-TOF MS) of organosolv lignin.



MW Averages

Peak No	Mp	Mn	Mw	Mz	Mz+1	Mv	PD
1	1654	1107	2261	3982	5769	2049	2.04246

Figure 4-7. Gel permeation chromatography (GPC) analysis of organosolv lignin in anhydrous tetrahydrofuran (THF) with a concentration of 1 mg ml^{-1} .

3.3 Ni catalyzed lignin deconstruction and upgrading in the presence of H₂ and hexadecane

The deconstruction and upgrading of organosolv lignin to cyclic saturated hydrocarbons were performed using Ni based catalysts. In preliminary tests, reaction conditions were optimized by varying reaction temperatures (473 – 543 K), pressure (10 – 50 bar H₂) and the catalyst-to-lignin weight ratio of 0.2–0.5 (Table 4-4). Results obtained at an optimized (among these preliminary tests) set of conditions of 523 K, 20 bar H₂, and a catalyst/lignin weight ratio of 0.5 are summarized in Table 4-5. The products are divided into gas phase (methane, propane and methanol), liquid phase (C₅ – C₁₄ naphthenes, H₂O) and remaining solids (carefully excluding unconverted lignin). The unconverted organosolv lignin was separated from the solid mixture (including the catalyst) by dissolving it in tetrahydrofuran (THF), evaporating the THF fraction, and drying.

Table 4-4. Varying reaction conditions for optimizing organosolv lignin conversion. ^a

Entry	Organosolv Lignin (g)	Ni/HBEA (g)	Temperature (K)	Initial H ₂ pressure (bar)	Liquid phase HC yield (wt. %)
1	1	0.5	523	50	33
2	1	0.5	523	20	35
3	0.5	0.25	523	20	35
4	0.5	0.25	523	10	32
5	0.5	0.25	543	20	36
6	0.5	0.25	493	20	27
7	0.5	0.25	473	20	14
8	0.5	0.25	453	20	7
9	4	2	523	20	35
10	1	0.2	523	20	14

^a General reaction conditions: 100 ml *n*-C₁₆H₃₄, 700 RPM, reaction duration 4 hours.

In order to elucidate the impact of reaction conditions, we have carried out a series of reactions varying the pressure from 50 to 10 bar (entry 1 – 4, Table 4-4), the temperature from 453 to 543 K (entry 5 – 8) and catalyst to lignin ratio from 0.5 to 0.2 (entry 9 and 10) with the best performing catalyst, i.e., 21 wt. % Ni/HBEA prepared by deposition precipitation. The experiment in the first entry was performed at the standard set of reaction conditions, with a H₂ initial pressure of 50 bar as performed in our previous hydrodeoxygenation studies. Decreasing the hydrogen pressure to 20 bar (40 and 30 bar H₂, not shown here) slightly increased the liquid phase hydrocarbon yield by 2 wt. % (entry

3). A further decrease of the hydrogen pressure to 10 bar (entry 4) led to a comparable yield as the first entry with 32 wt. %. This finding is in accordance with the studies on aryl ether cleavage, where the variation of the initial hydrogen pressure caused a maximum in the rates of Ni catalyzed hydrogenolysis.^[8]

Increasing the temperature from 523 to 543 K led to a marginal improvement of hydrocarbon yield by merely 1 wt. % (entry 5), whereas lowering the temperatures from 523 to 453 K resulted in a substantial loss of desired products, 27 wt. % at 493 K (entry 6), 14 wt.% at 473 K and 7 wt. % at 453 K, respectively (entries 7 and 8).

The effects of catalyst-to-lignin ratios, as well as the absolute weight of lignin and catalyst in the batch reactor, can be evaluated by looking at the entries 3 – 10. Changing the weights of catalyst and lignin, while keeping the catalyst-to-lignin ratio identical, did not affect product yields (entry 2, 3 and 9). The catalyst-to-lignin weight ratio of 0.5 resulted in the best yields (compare entries 2, 3, 5 and 9). Reducing this ratio to 0.2 caused the liquid hydrocarbon yield to decrease by a factor of 2.5 (entry 10), proportional to the decrease in the catalyst-to-lignin weight ratio.

Table 4-5. Products formed with Ni catalyzed organosolv lignin hydroconversion in hexadecane ^{a,b}

Catalyst	Hydrocarbons [wt. %]	Water [wt. %] ^c	Solid residue [wt. %] ^d	Unconverted lignin [wt. %] ^e
Ni/SiO ₂	27 ± 2	10	31 ± 5	25
Ni/HZSM-5	34 ± 2	16	26 ± 5	18
Ni/HBEA	42 ± 4	18	22 ± 5	12

^a Reaction conditions: 1 g lignin, 0.5 g Ni catalyst, 100 mL (77g) hexadecane as solvent, 20 bar H₂ initially charged into reactor at RT, 6 h, 523 K, 700 RPM stirring.

^b ± : Standard deviations for multiple reaction tests.

^c Determined by volumetric analysis.

^d THF-insoluble solids.

^e THF-soluble solids.

Converting organosolv lignin on Ni/SiO₂ (1 g lignin, 0.5 g catalyst, 100 mL hexadecane, 20 bar H₂, 523 K for 6 h) led to a total yield of 27 wt. % for both gas and liquid phase products, mainly as hydrocarbons, while most of the oxygen was removed as water (10 wt. %). On this catalyst, solid byproducts accounted for 31 (± 5) wt. % yields. After 6 h, 25 wt. % of the lignin remained unreacted. Higher yields of gas and liquid phase hydrocarbons were achieved at the same conditions with Ni/HZSM-5 and Ni/HBEA (34 and 42 wt. %, respectively) pointing to the importance of acids and the available space in the pores. The higher yields of hydrocarbons are consistent with the larger concentrations of water and the smaller concentrations of solid residues with the two zeolite-supported Ni catalysts than with Ni/SiO₂.

As all three catalysts had similar concentrations of accessible Ni, the higher yields of hydrocarbons on Ni/HBEA and Ni/HZSM-5 are attributed to the presence of Brønsted acid sites, catalyzing the dehydration of the intermediately formed alcohols. The slightly higher yields in hydrocarbons are tentatively attributed to more stable Ni particles on the two zeolite supports.

Table 4-6. Yield and selectivity of liquid and gas phase hydrocarbons for beech lignin conversion catalyzed by Ni catalysts in *n*-hexadecane^{a, b}.

Catalysts	Gas phase products [wt. %] ^c	Liquid phase products [wt. %]	Selectivity within liquid mix [wt. %]		
			Monocyclic alcohols	Monocyclic alkanes ^d	Bicyclic alkanes ^e
Ni/SiO ₂	4.1	23 ± 2	20	80	0
Ni/HZSM-5	5.5	28 ± 2	0	90	10
Ni/HBEA	6.8	35 ± 4	0	83	17

^a Reaction conditions: 1 g lignin, 0.5 g Ni catalyst, 100 mL (77 g) hexadecane as solvent, 20 bar H₂ initially charged into reactor at RT, 6 h, 523 K, 700 RPM stirring.

^b ± : Standard deviations for multiple reaction tests.

^c Methane, propane and methanol are the main components in the gas phase.

^d Monocyclic products and its isomers ranging from C5 to C9.

^e Bicyclic products greater than C9.

A breakdown of the yields of gas and liquid phase products, as well as the selectivity within liquid phase products, is shown in Table 4-6. The distributions of liquid phase products on the three Ni catalysts are depicted schematically in Figure 4-8. For Ni/SiO₂ catalyzed reaction, 4 wt. % of the lignin was converted to methane, propane and methanol. Naphthenes were produced at a yield of 23 wt. %, the majority being cycloalkanes, primarily cyclohexane with methyl, ethyl and propyl side chains (80 C % selectivity). Cyclic saturated alcohols, namely, cyclohexanol and its methyl-, ethyl-, propyl derivatives, were also present (20 C %). A typical GC trace of the liquid reaction mixture catalyzed by Ni/SiO₂ is shown in Figure 4-9a. Variations of the reaction time between 1 and 24 h (Figure 4-10) showed the selectivity to cyclic saturated alcohols to be the highest after 2-h reaction time. Based on our studies of model compounds, we conclude that the cyclic alcohols are formed *via* hydrogenolysis and subsequent hydrogenation of the lignol on Ni^[25]. The deoxygenation of cyclic saturated alcohols on Ni/SiO₂ suggests that surface reactions of Ni²⁺ with SiO₂ or small concentrations of NiO have generated Lewis acid sites, able to catalyze dehydration of alcohols. At this point we would not fully exclude, however, that some direct hydrogenolysis of cyclic alcohols occurs on Ni/SiO₂.

With Ni/HZSM-5, gas phase products were formed at a combined yield of 5.5 wt. %. The product distribution in the liquid phase with Ni/HZSM-5 (Figure 4-9b) shows saturated

cyclic hydrocarbons in the range of C₅ – C₁₀ only, i.e., ranging from cyclopentanes (formed *via* acid catalyzed isomerization of cyclohexyl rings) to decalin. Performing the reaction for longer durations up to 24 h on Ni/HZSM-5 (Figure 4-11) resulted in naphthenes yields of 28 wt.% after 6 h and 36 wt.% after 24 h with mainly (> 90 %) monocyclic (isomerized) C₅ to C₉ and bicyclic C₉ to C₁₁ hydrocarbons (ca. 10 %).

In comparison, Ni/HBEA yielded 7 wt. % gas phase products and 35 wt. % of liquid hydrocarbons, with carbon numbers ranging from C₅ to C₁₄ (Figure 4-9c). The higher selectivities towards bicyclic products (18 %) contributed to the overall higher yield. Based on extensive studies about the alkylation during hydrodeoxygenation of phenol^[48], we conclude that the medium pore of HZSM-5 hinders the alkylation of aromatic monomers by alcohols or olefins formed during hydrogenation or hydrodeoxygenation, leading to the low selectivity to bicyclic products with Ni/HZSM5. Note that some bicyclic products may originate from C-C bonds present in the starting lignin.

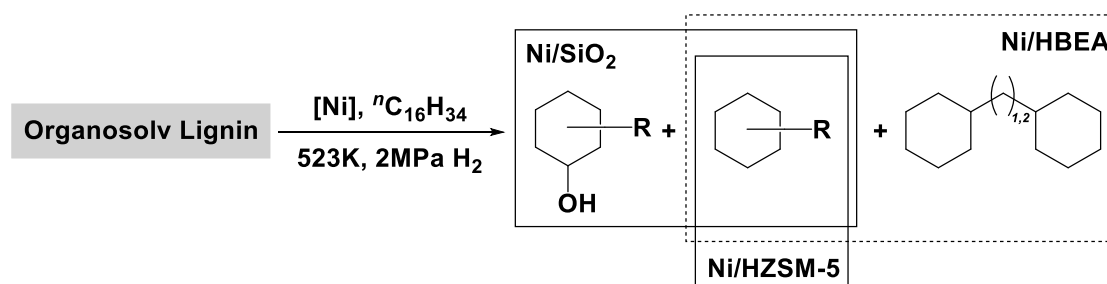
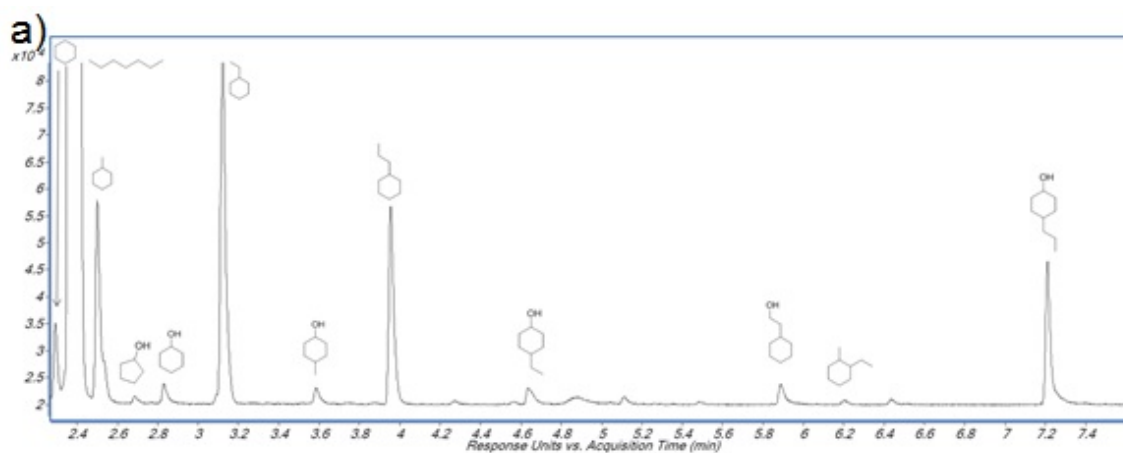


Figure 4-8. Schematic product distributions in the organosolv lignin deconstruction over Ni/SiO₂, Ni/HZSM-5 and Ni/HBEA catalysts.



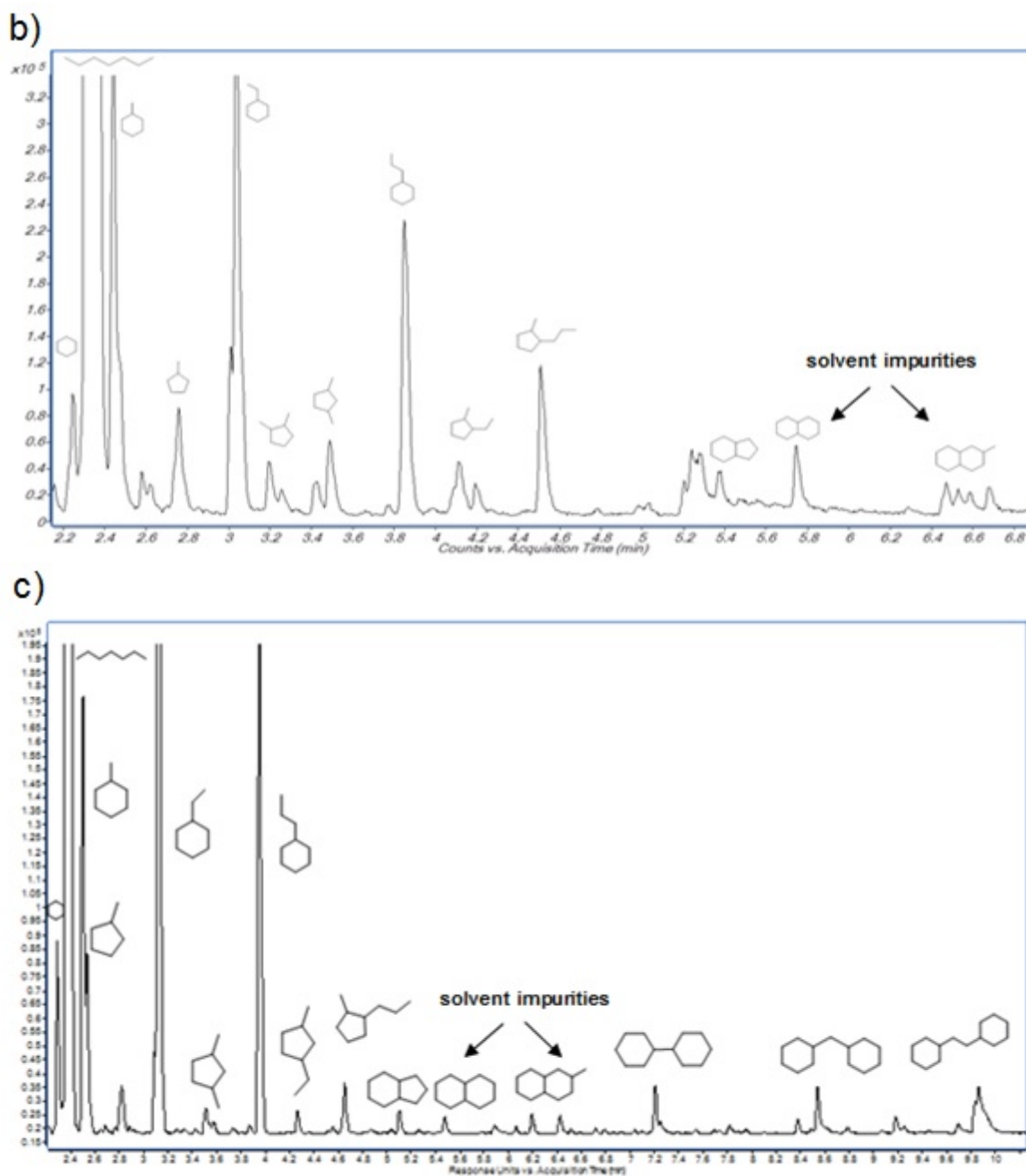


Figure 4-9. The representative gas chromatogram of reacted mixture liquid phase products after reaction of organosolv lignin (1 g) with a) 20 wt. % Ni/SiO₂ b) Ni/HZSM-5 and c) Ni/HBEA catalyst (each 0.5 g) and 100 ml hexadecane at 523 K, 20 bar H₂, 680 RPM, 6 h.

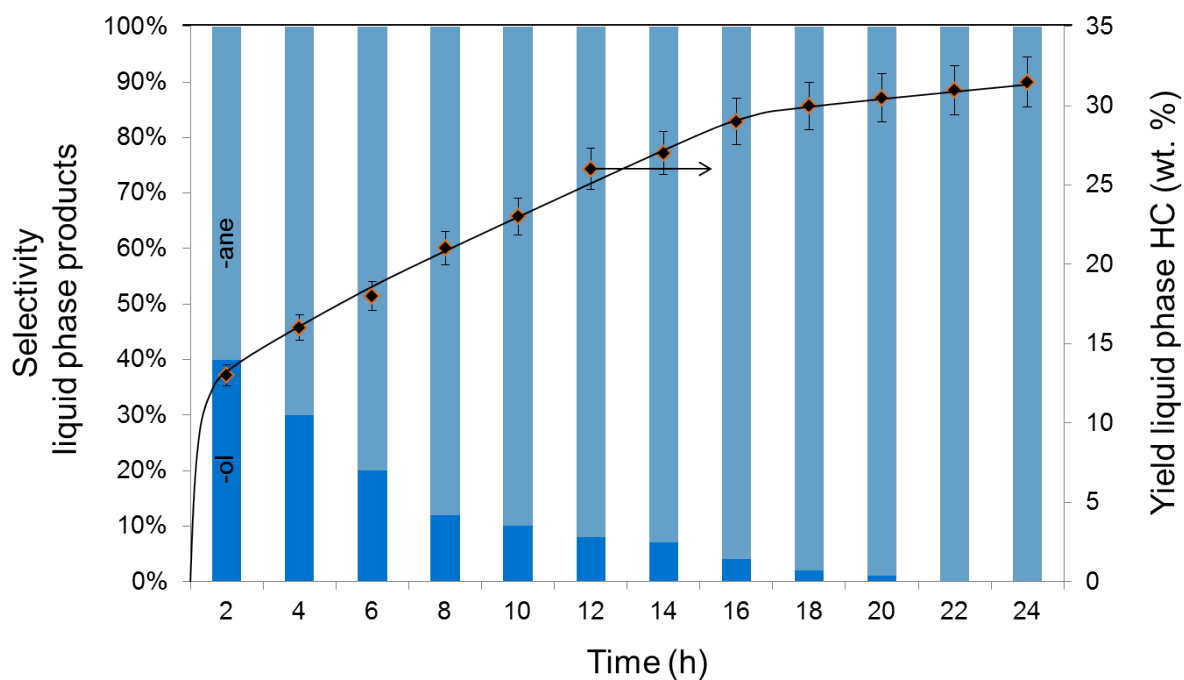


Figure 4-10. Hydro-deconstruction of organosolv lignin on Ni/SiO₂ catalysts as a function of contact time at the following conditions: organosolv lignin (1 g), 20 wt.% Ni/SiO₂ (0.5 g), 523 K, 2 MPa H₂ charged before reaction started, 700 RPM.

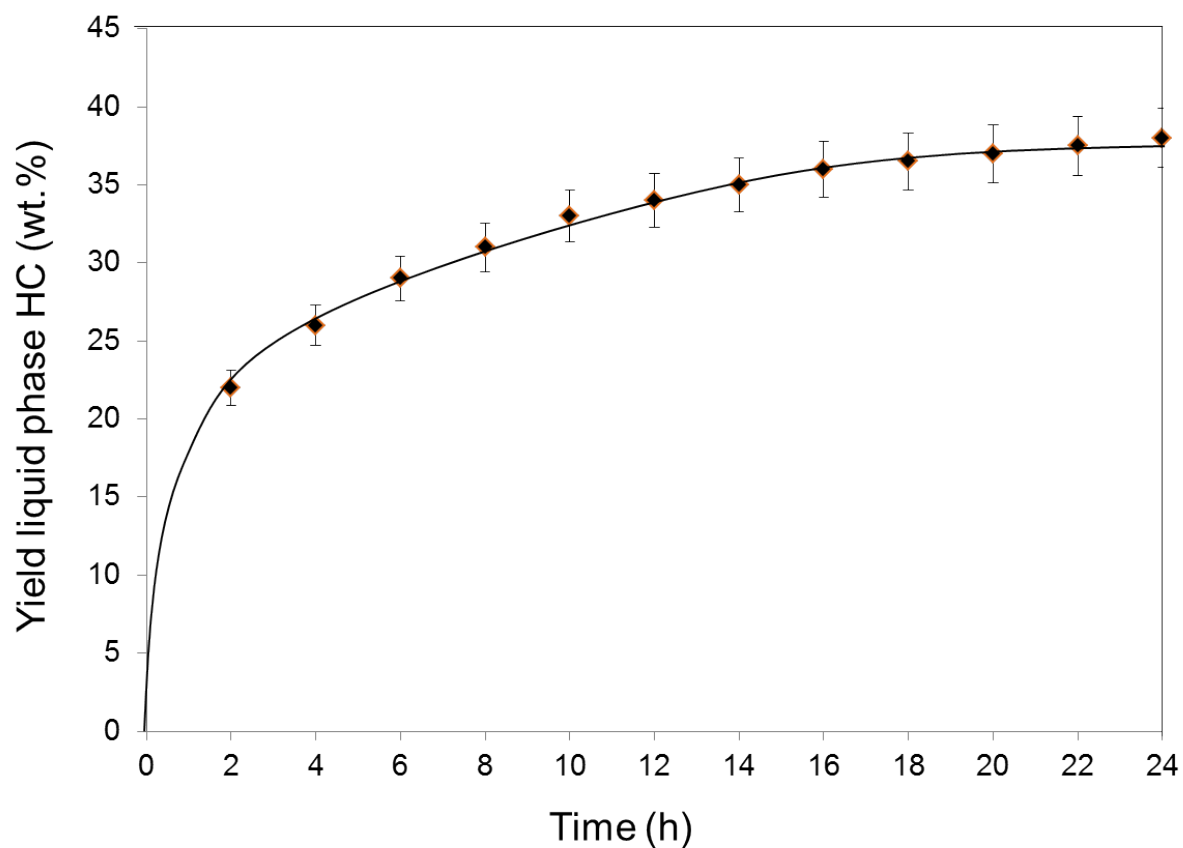


Figure 4-11. Conversion of organosolv lignin on Ni/HZSM-5 as a function of contact time at the following conditions: organosolv lignin (1 g), 21 wt. % Ni/HZSM-5 (0.5 g), 523 K, 2 MPa H₂ charged before reaction started, 700 RPM.

To show that the catalysts could be recycled, experiments were performed, in which the Ni catalyst was recovered and reused for total of three cycles. The yield of liquid phase naphthenes (Figure 4-12) decreased by approximately 5% with each reuse. Analysis of the TEM images of catalysts before and after reactions (Figure 4-4) showed that the average sizes of Ni particles were bigger in recovered catalysts. Therefore, the decline in activity with reuse is attributed to particle sintering.

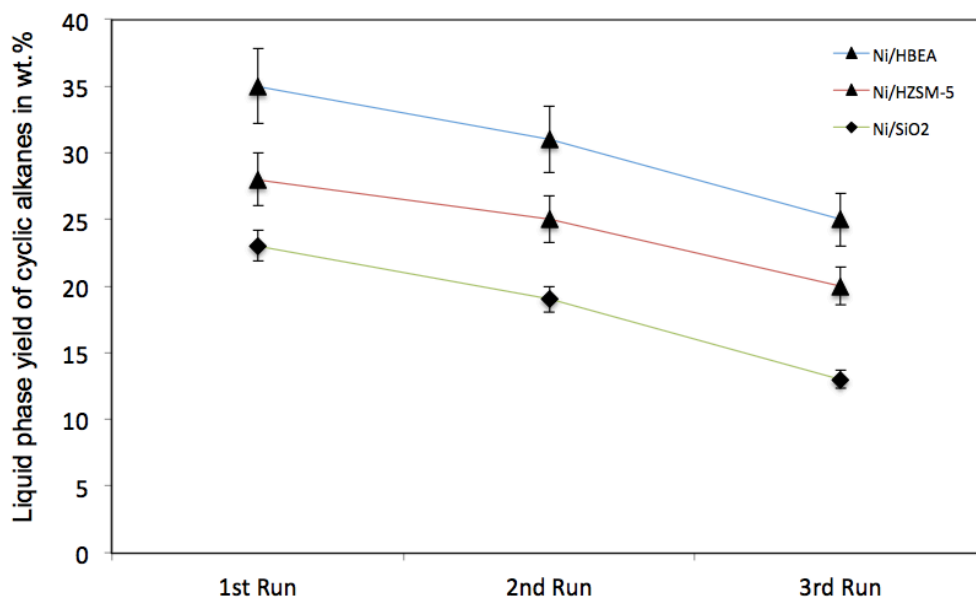


Figure 4-12. Recycling runs with Ni/HBEA (blue line), Ni/HZSM-5 (red line) and Ni/SiO₂ (green line) catalysts at reaction conditions: 523 K, 2 MPa H₂ at ambient conditions, 100 ml n-C₁₆H₃₄, 680 RPM, 6 h.

Recent reports on lignin depolymerization on carbon-supported Ru,^[49] Ni^[31, 32] and Pd/Zn catalysts^[34, 50] in aqueous and/or alcoholic liquid phases have reported yields of aromatic monolignols ranging from 12 to 54 wt.%, with little subsequent hydrogenation/deoxygenation even under high pressures of H₂. In the present work, the catalytic lignin conversion at 523 K, in the presence of H₂ and hexadecane solvent, produced saturated hydrocarbons with comparable liquid phase yields (23 – 35 wt.%) on Ni based catalysts. This is in agreement with Rinaldi and Wang suggesting that Lewis basic solvents (H₂O, methanol, THF, 1,4-dioxane) reduce the rate of catalytic hydrogenation on Ni catalysts, while the hydrogenolysis activity was not affected to the same extent during conversion of diphenyl ether or organosolv lignin.^[30] In the aprotic non-Lewis basic solvent, methylcyclohexane as an example, the main products derived upon organosolv lignin conversion on Raney Ni were saturated cyclic alcohols and hydrocarbons.

While the effects of reaction conditions, such as temperature, gas environment and its pressure, solvent and catalyst systems, have been widely explored for converting lignin,

these studies^[9, 24, 26, 32, 34, 51] have been addressing mechanistic aspects of the C-O bond cleavage of model compounds or on the comparison of *ex situ* analysis of lignins before and after catalyzed reactions. The kinetics of lignin deconstruction on a molecular level and the potential for a complete lignin conversion has not been explored.^[23, 35] To follow these conversions, we use attenuated total reflection infrared (ATR-IR) spectroscopy for monitoring changes in the structure of lignin under the same reaction conditions used throughout this study.

3.4 ATR-IR spectroscopy during reductive deconstruction of lignin on Ni/HBEA

We decided to use the most active catalysts Ni/HBEA for following the changes of the lignin structure during its conversion under hydrogenation conditions using ATR-IR spectroscopy *in situ* during conversion (Figure 4-5a). For this purpose a physical mixture of Ni/HBEA and organosolv lignin was deposited onto the ZnSe crystal (Figures 4-1, 4-2 and 4-3). *n*-Hexadecane saturated with 2 MPa H₂ was pumped through the cell at 523 K to initiate the deconstruction of lignin; no spectroscopic changes occurred in the absence of this solvent. The surface of the ZnSe crystal was also probed with HR-SEM (Figure 4-13) showing that the deposited (porous) catalyst/lignin layer (10–20 μm) was approximately an order of magnitude thicker than the penetration depth of the evanescent wave (1–2 μm).

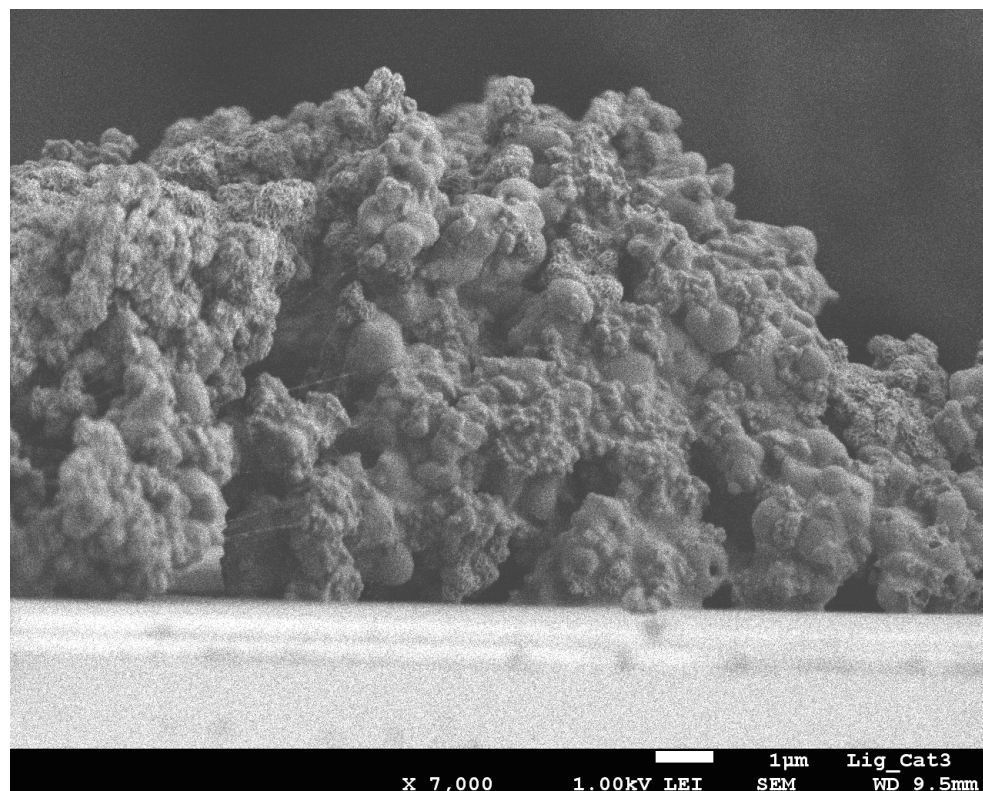


Figure 4-13. HR-SEM cross section of the lignin-catalyst physical mixture being deposited as a layer on the silicon crystal through drop coating.

EDX element mapping in that film showed the distribution of Ni particles to be uniform across the coated film (Figure 4-14), thus, ensuring that the ATR-IR technique probes a region of the sample in which both lignin and Ni-catalyst are in contact. Figure 4-15 shows a series of stacked background-corrected ATR-IR difference spectra of organosolv lignin reacting on Ni/HBEA catalyst as a function of contact time.

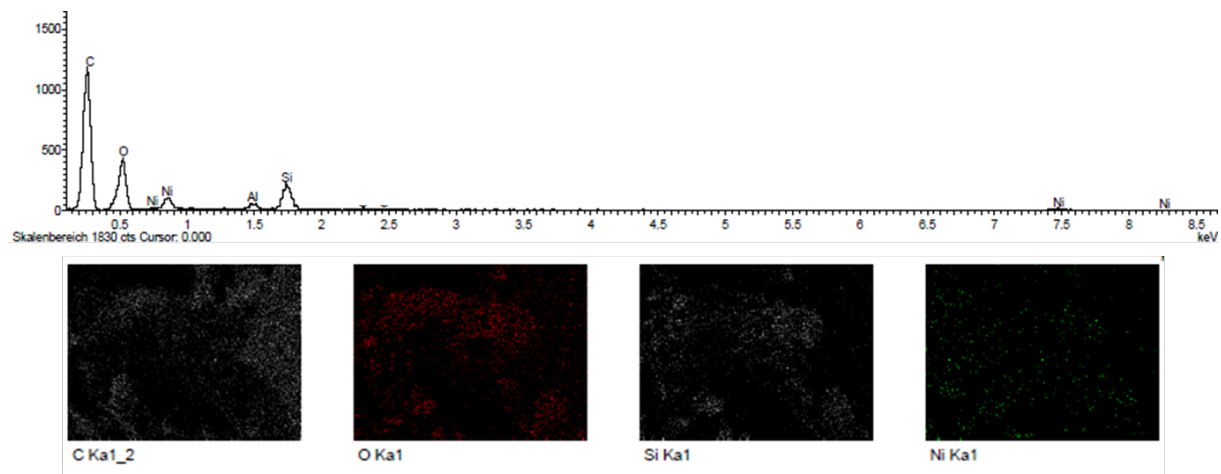


Figure 4-14. EDX spectra during the HR-SEM measurements mapping the elemental distribution (C, O, Si and Ni) across the coated film containing lignin and Ni/HBEA catalyst.

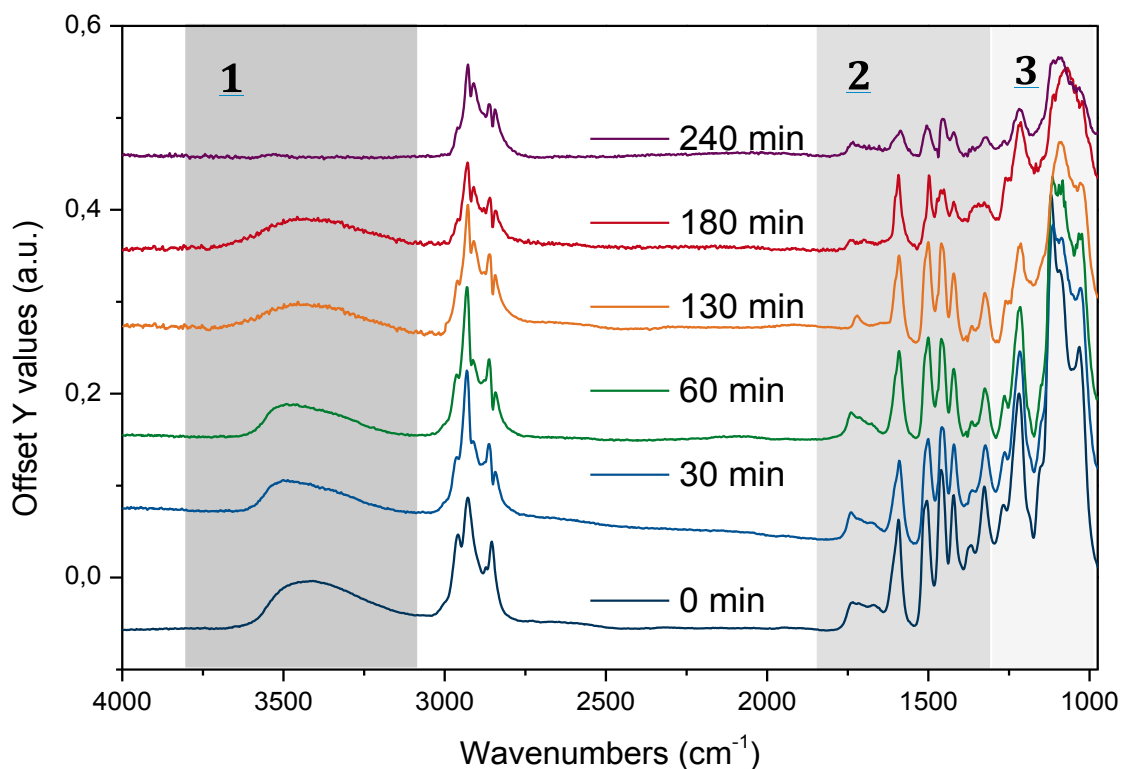


Figure 4-15. Time-resolved *in situ* ATR-IR difference spectra of organosolv lignin reacting over Ni/HBEA catalysts in *n*-hexadecane at 523 K and 20 bar H_2 .

The time-resolved ATR-IR spectra clearly indicate a systematic change of the lignin structure with bands characteristic of individual functionalities in the lignin and intermediate products evolving at different reaction times. We have identified three characteristic regions, which are discussed in the sequence of decreasing wavenumbers, i.e., (i) O-H and C-H stretching, 3800 – 2500 cm^{-1} , (ii) aryl C=C, C=O and C-OMe stretching, 1800 – 1400 cm^{-1} , and (iii) lignol C-O-C linkages 1400 – 950 cm^{-1} .

In the region of the O-H stretching vibration between 3640 and 3150 cm^{-1} (Figure 4-16a), the broad band with a maximum at 3500 cm^{-1} is attributed to hydrogen bonded OH groups attached to alkyl or aryl groups. The bands between 2990 and 2816 cm^{-1} are assigned to the asymmetric and symmetric CH_3 and CH_2 stretching vibrations, which overlap with the signals of asymmetric and symmetric C-H stretching vibrations in $\text{CH}_2\text{-O}$ groups, see Table 4-7.^[44] The presence of *n*-hexadecane as solvent, however, makes the assignment and further deconvolution of the C-H stretching vibrations unfeasible at present. With increasing reaction time (Figure 4-16b), the integrated peak areas of the O-H stretching vibration decrease quite rapidly (black trace), indicating gradual removal of the hydroxy groups.

Table 4-7. The stretching vibrational frequencies of aliphatic C-H and aliphatic C-H with carbon attached to oxygen (all numbers in cm^{-1})⁴⁴.

Group	Asymmetric	Symmetric
CH_3	2962 ± 10	2872 ± 10
CH_2	2926 ± 10	2855 ± 10
$\text{CH}_3\text{-O}$	2970 - 2920	2830 ± 10
$\text{CH}_2\text{-O}$	2955 - 2920	2878 - 2835

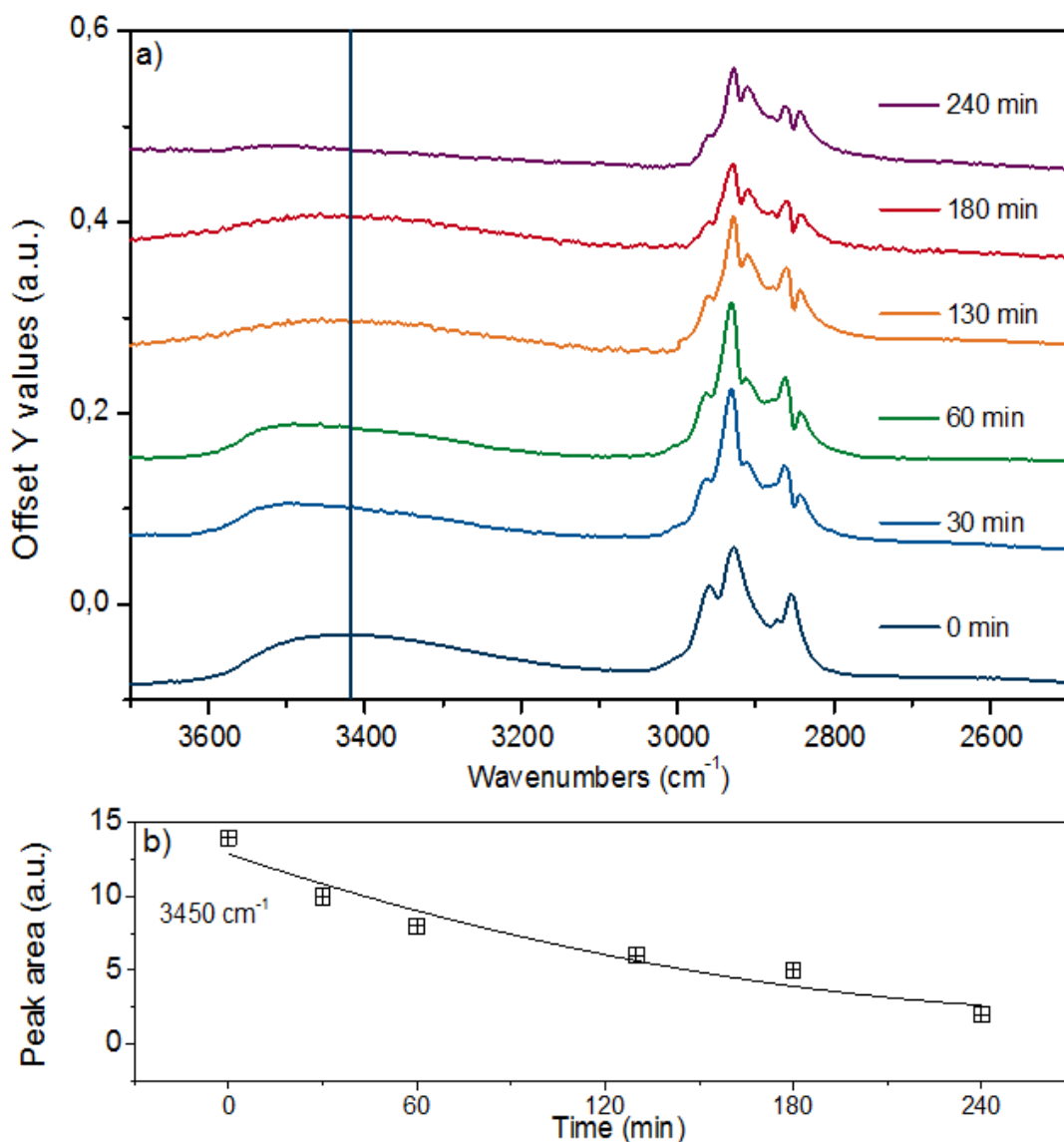


Figure 4-16. ATR-IR spectra in the spectral region of 3800 – 2500 cm⁻¹ (O–H and C–H stretching vibrations) for organosolv lignin reacting over Ni/HBEA in n-hexadecane at 523 K and 20 bar H₂. b) The evolution of integrated peak area at 3430 cm⁻¹, representing the O–H stretching vibration, as a function of reaction time.

While qualitative changes have been very reproducible, we caution against the quantitative interpretation of these observed changes, as during continuous reaction in the ATR cell the catalyst/lignin layer may change composition at the interface with of the ZnSe element, i.e., more or less material may be present in the zone probed by ATR spectroscopy. Considering the sum of all C–H stretching bands on a semi-quantitative basis, it is concluded that the increase of the total band area within the first 60 min is associated with the partial hydrogenation of the aromatic rings (in products in the layer), while the decreasing intensity points to a depletion of organic matter close to the probed ZnSe surface.

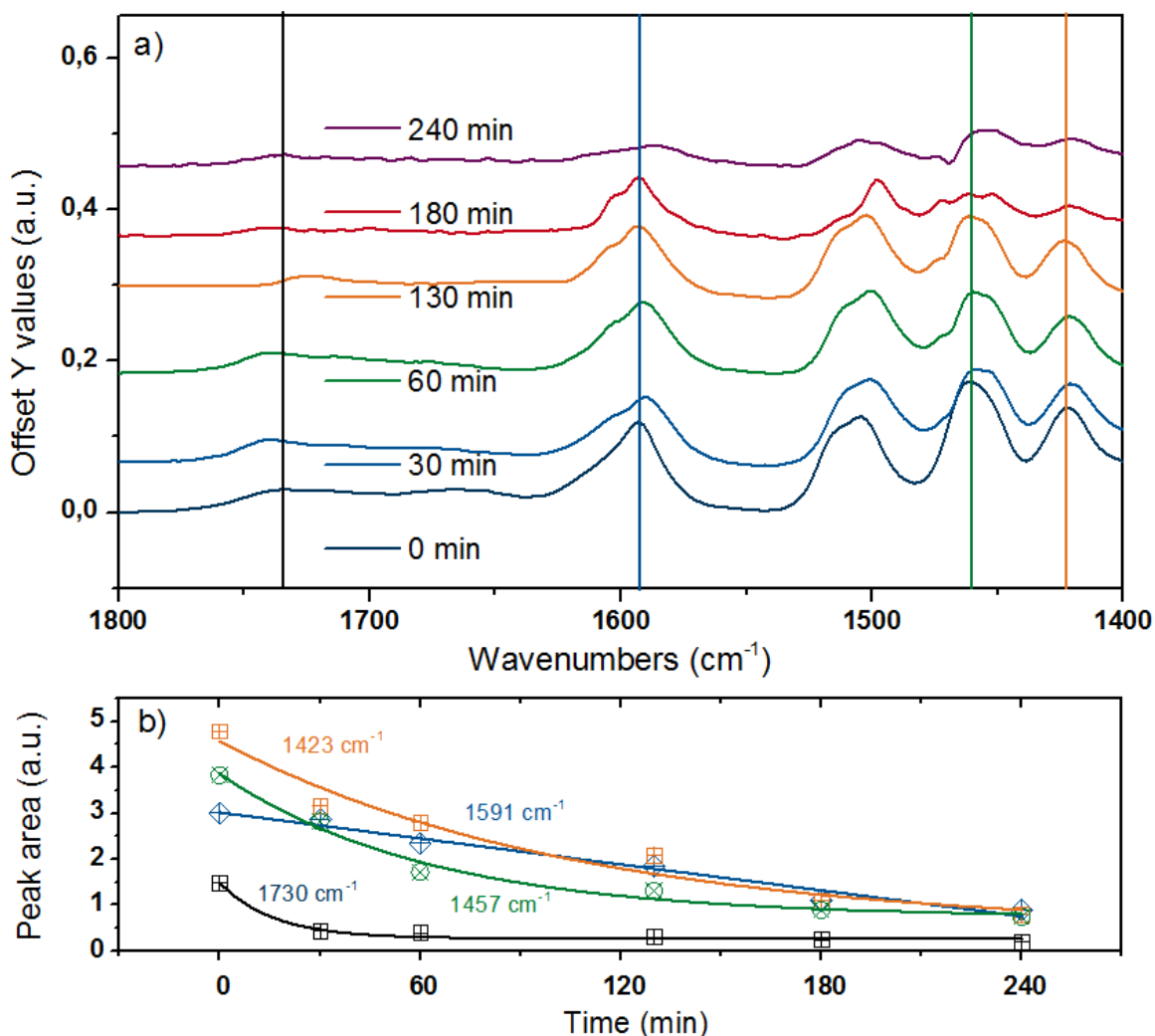


Figure 4-17. ATR-IR spectra in the spectral region of 1800 – 1300 cm⁻¹ for organosolv lignin reacting over Ni/HBEA in n-hexadecane at 523 K and 20 bar H₂. b) Qualitative trend for peak areas at 1730 cm⁻¹ for C=O stretching vibration, 1591 cm⁻¹ for symmetric aryl ring stretch, 1457 cm⁻¹ for CH₃-O bend and 1423 cm⁻¹ for aromatic skeletal vibration. ^{43, 44, 52}

The bands in the region between 1800 and 1400 cm⁻¹ (Figure 4-17) are attributed to C=O stretching vibrations (1738 cm⁻¹ and 1674 cm⁻¹), aryl ring stretching vibrations (1591 cm⁻¹, symmetric and 1503 cm⁻¹ asymmetric), O-C-H (methoxy) bending vibrations (1457 cm⁻¹), aromatic skeletal vibrations combined with C-H in-plane bending (1423 cm⁻¹), and aryl ring breathing with C=O stretch (1324 cm⁻¹). ^[43, 44, 52] These bands were deconvoluted to determine the changes of individual vibrational bands, which are plotted in Figure 4-17b as a function of reaction time.

By monitoring the temporal evolution of two vibrational modes, the symmetric aryl ring stretching at 1591 cm⁻¹ and aromatic skeletal vibration 1423 cm⁻¹, we follow systematically the loss of aromaticity as lignin is being deconstructed and the fragments are being hydrogenated. The band intensity of the carbonyl group associated with the syringyl-' (S') unit at 1740 cm⁻¹ ^[43, 44] also dropped significantly, pointing again to the reduction of the

C=O groups and/or the deconstruction of lignin. Note that the bending mode of C-H attached to oxygen is linked to the peak at 1457 cm^{-1} , whose integrated area declines as a function of time. [43, 44] This suggests that lignin was demethoxylated also via hydrogenolysis.

Figure 4-18a displays the third spectroscopic region, comprising vibrational modes in $1400 - 1000\text{ cm}^{-1}$. The abundant ether linkages connecting the monolignols lead to a group of pronounced bands. Due to the variety of ether linkages in lignin, it is impossible to resolve individual vibrational modes. To facilitate further analyses, we deconvoluted the broad IR peaks into components (denoted with vertical lines), assigning the IR bands at 1219 cm^{-1} to phenolic C-C-O asymmetric stretching and both of the bands at 1122 cm^{-1} and 1080 cm^{-1} to aliphatic C-C-O asymmetric stretching vibration. [43, 44, 52] The time-resolved evolution of these peaks is presented in Figure 4-18b.

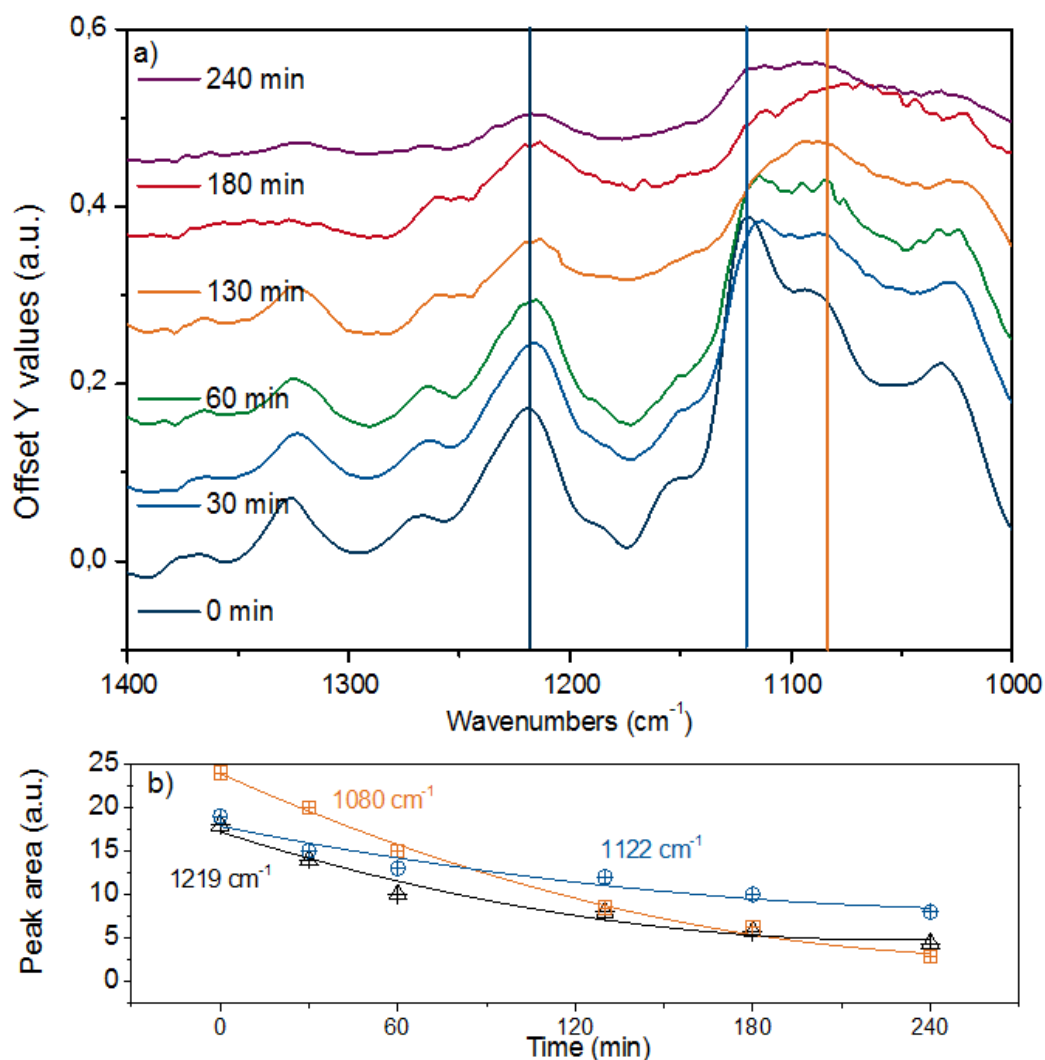
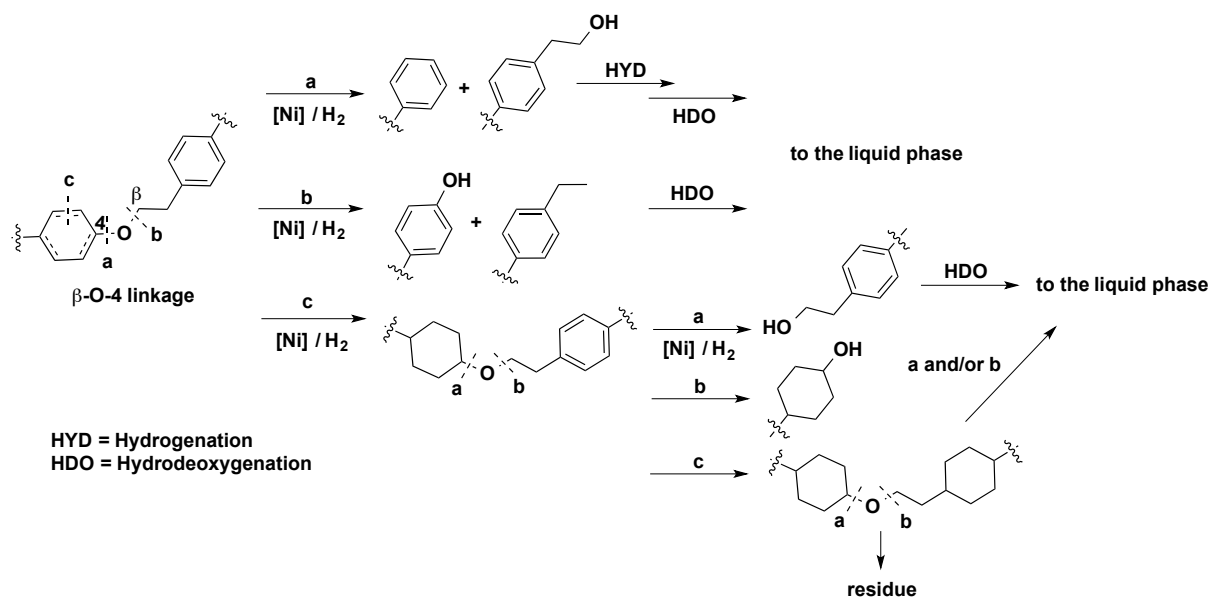


Figure 4-18. a) ATR-IR spectra in the spectral region of $1400 - 1000\text{ cm}^{-1}$ for organosolv lignin reacting over Ni/HBEA in *n*-hexadecane at 523 K and 20 bar H_2 . b) Deconvoluted and integrated peak areas at 1219 cm^{-1} , 1122 cm^{-1} and 1080 cm^{-1} representing the aromatic C-C-O stretching vibration, the aliphatic secondary and primary C-C-O stretching vibrations, respectively.

The monotonous decrease in intensity and the observation of primarily mononuclear products allow us to conclude that the changes observed are associated with C-O-C ether bond cleavage, i.e., that the cleavage of aryl alkyl ether bonds like in β -O-4 and α -O-4 linkages result in the parallel disappearance of IR bands at 1219 cm^{-1} , 1122 cm^{-1} and 1080 cm^{-1} . If we assume that the phenolic and aliphatic C-C-O stretching vibrations have comparable molar extinction coefficients, the higher initial disappearance rate of the 1080 cm^{-1} together with the 1122 cm^{-1} peaks compared to the 1219 cm^{-1} mode suggests that the ether bonds connecting lignols are preferably cleaved at the $C_{\text{aliphatic}}\text{-O}$ site, in line with observations for diphenyl ethers in aqueous and non-polar liquid phase.^[22, 25]

3.5 A proposed mechanism for Ni catalyzed reductive deconstruction of lignin

The analyses presented above and the product analyses by GC-MS (Figure 4-19) allow us to propose a sequential mechanistic pathway for lignin deconstruction, reduction and hydrodeoxygenation. Taking as an example the β -O-4 linkage, the predominant ether bond linkage, we have drawn three possible reaction pathways in Scheme 4-2, including a) $C_{\text{aromatic}}\text{-O}$ bond scission b) $C_{\text{aliphatic}}\text{-O}$ bond scission and c) aryl ring hydrogenation.



Scheme 4-1. Proposed reaction pathways for Ni catalyzed C-O bond cleavage in a representative β -O-4 bond interconnecting monolignols.

The direct C-O bond hydrogenolysis at the aromatic carbon through pathway a is a minor route, as evidenced by the less marked decrease in the phenolic C-O stretching band at 1219 cm^{-1} than the aliphatic C-O bands at 1122 and 1080 cm^{-1} . This is consistent with the higher bond dissociation energies of $C_{\text{aromatic}}\text{-O}$ bonds than those of the $C_{\text{aliphatic}}\text{-O}$ bonds in aryl ethers, e.g., 322 vs. $289\text{ kJ}\cdot\text{mol}^{-1}$ for phenethyl phenyl ether.^[53] Hydrogenolysis of $C_{\text{aliphatic}}\text{-O}$ bonds (Route b) and arene hydrogenation (Route c) are major pathways. Dimer

model compound studies on Ni catalysts in aqueous phase showed that the hydrogenolysis rate is one order of magnitude faster than arene ring hydrogenation.^[20, 25] Our ATR IR results indicate that C_{aliphatic}-O bond hydrogenolysis is faster than ring hydrogenation also in hexadecane. Once one of the ether bonded aryl rings is hydrogenated (Route c), the rate of C-O bond cleavage becomes very slow.^[25] Thus, hydrogenation of the aromatic rings would lead to large ethers. Table 4-8 shows that increasing reaction temperatures selectively enhances dehydration, hydrogenolysis and hydrogenation, retarding on the other hand retrograde reactions. By this, it is possible to nearly quantitatively deconstruct lignin to substituted cycloalkanes and some light products. While increasing the temperature from 523 to 543 K led to marginal increases in hydrocarbon yield and lignin conversion, temperatures at 573 K and above helped overcome the bottlenecks for full lignin conversion.

Table 4-8. Analysis of products formed by Ni catalyzed organosolv lignin conversion in *n*-hexadecane at different temperatures^{a,b}

Temperature (K)	Hydrocarbons [wt. %]	Selectivity [C %]	Water [wt. %] ^c	Solid residue [wt. %] ^d	Unconv. lignin [wt. %] ^e
493	29 ± 2	40	10	31 ± 5	26
523	42 ± 4	57	18	22 ± 5	12
543	44 ± 4	60	18	23 ± 5	11
573	60 ± 5	82	19	11 ± 5	4
593	70 ± 5	96	21	4 ± 5	0.1

^a Reaction conditions: 1 g lignin, 0.5 g Ni/HBEA catalyst, 100 mL (77 g) hexadecane as solvent, 20 bar H₂ initially charged into reactor at RT, 6 h, temperature range from 493 to 593 K, 700 RPM stirring.

^b ± : Standard deviations for multiple reaction tests.

^c Determined by volumetric analysis.

^d THF-soluble solids.

^e THF-insoluble solids.

Combining these findings, the mechanism for catalytic reductive deconstruction of organosolv lignin on Ni catalysts is proposed (Scheme 4-2). Lignin is schematically represented by a pentameric lignol fragment, containing methoxylated phenylpropanoid moieties connected through β -O-4, α -O-4 and β - β ether bonds as prevailing in lignin^[1, 29] and in the proposed structure (Figure 4-5d). The first step is the hydrogenolysis of the ether bonds (pathway A). Under conditions used in this work, all types of ether linkages (β -O-4, α -O-4 and 4-O-5), while being intrinsically different in reactivities, were cleaved on Ni surfaces. In this step, phenolic intermediates are formed, which subsequently follow the hydrodeoxygenation pathways B, C and D on the Ni and zeolite catalyst components as described previously.^[16, 19, 21, 54] As cyclic alcohols were also deoxygenated on Ni/SiO₂ it is

concluded that acid sites are formed with fractions of oxidized Ni (Ni-phyllsilicates) [55], while we do not rigorously exclude Ni-catalyzed hydrogenolysis of C-O bonds under the experimental conditions. Especially at lower temperatures, the phenolic molecules recombine (pathway F) to form undesired higher molecular weight oligomers.[25, 29] We propose that retrograde reactions occur in competition with pathway B, especially at lower temperatures ($T < 543$ K), where the phenolic molecules recombine (pathway F) to form refractory compounds[25, 29] probably of high molecular weight since the solid material after reaction (Table 4-8) is insoluble in THF or acetone. The increased conversion of lignin at higher temperatures (≥ 573 K, Table 4-8) is a consequence of the rates of hydrogenation of phenolics (pathway B) increasing more with temperature than the retrograde reactions (pathway F). Thus, an almost complete conversion of lignin was achieved (96% at 593 K, Table 4-8). The modest effects of temperature on both hydrocarbon yields and lignin conversion, however, suggest that the mobility of lignin on the Ni surface, rather than chemical reactions such as hydrogenolysis of bonds (with barriers typically > 100 kJ mol⁻¹), limits the conversion of the solid lignin material. It should be noted in passing that in the presence of water hydrolysis may occur, the extent of which is dictated by the free energy barrier for this pathway and the availability of water at the surface active sites.[25]

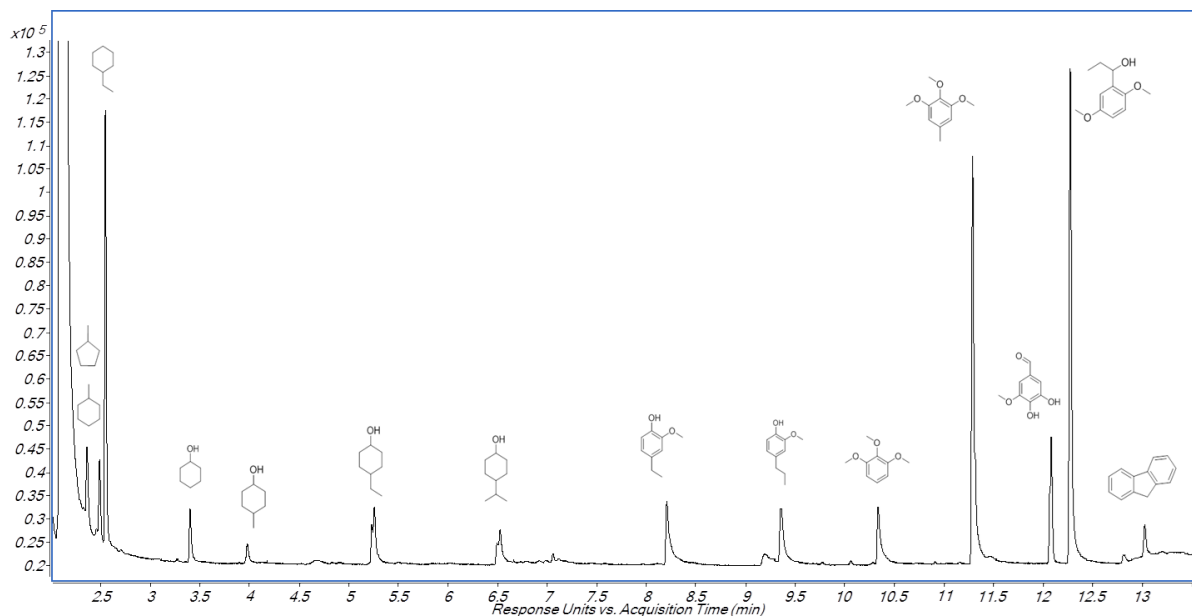
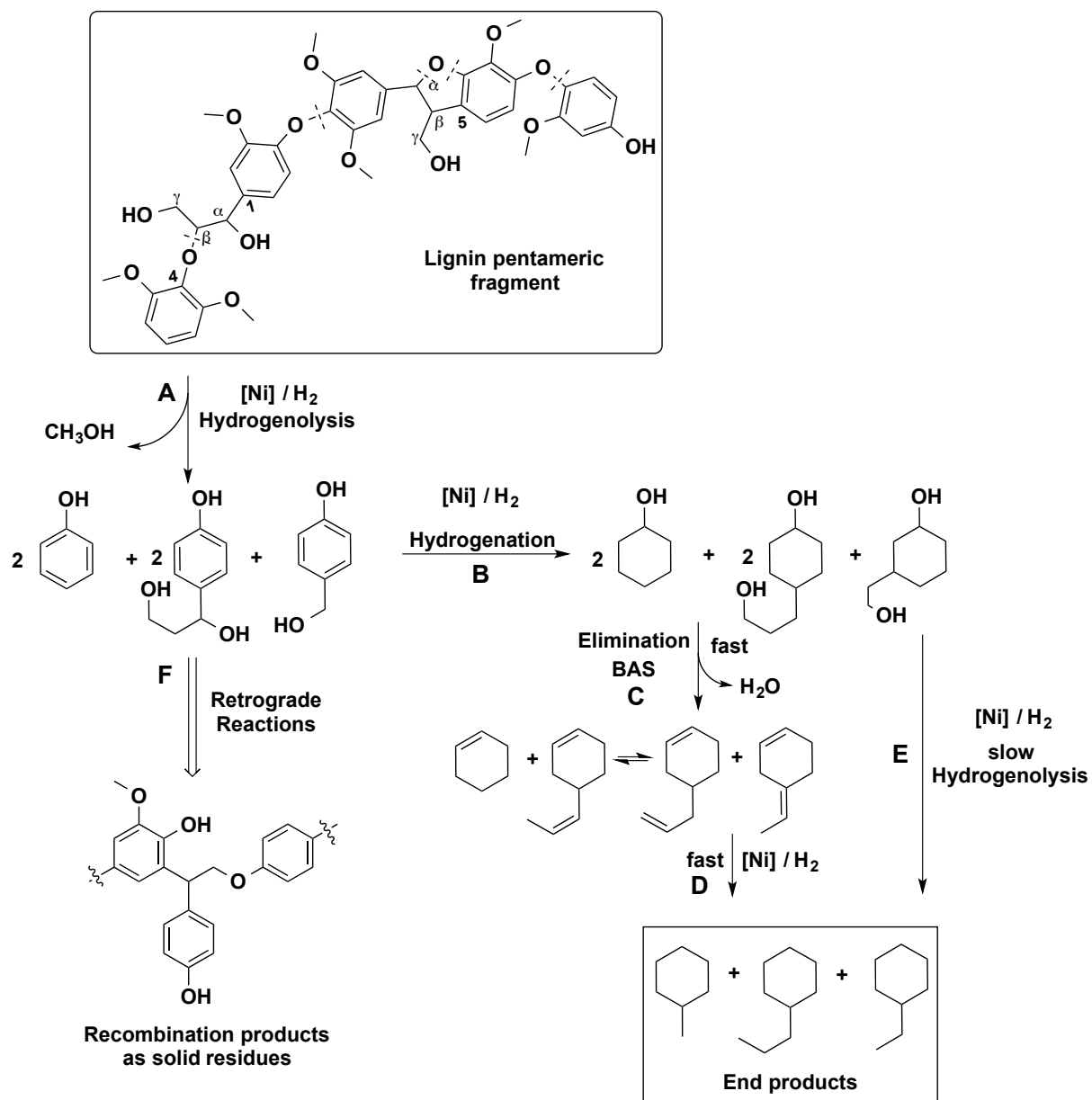


Figure 4-19. Gas chromatogram of liquid phase aliquot taken during in situ ATR-IR studies at a contact time of 90 minutes. Catalyst: Ni/HBEA.



Scheme 4-2. Proposed pathways for organosolv lignin deconstruction and hydrodeoxygenation on Ni based catalysts.

4. Conclusion

We have shown that a one stage process for complete reductive deconstruction of organosolv lignin is possible using Ni catalysts supported on zeolites under relatively mild conditions (500–600 K, 20 bar H₂) in a non-polar liquid phase such as *n*-hexadecane. The organosolv lignin used for the successful demonstration in the current study was a lignol oligomer with an average molecular weight of ca. 1200 Da and with 7–8 monolignols interconnected through a variety of aryl alkyl ether bonds. Full selective (to saturated hydrocarbons) conversion was achieved with Ni/H-BEA catalysts nearly avoiding retrograde reactions to high molecular weight compounds by increasing the temperature to 593 K. The HBEA zeolite catalyzed, however, some alkylation, leading to bicyclic products with up to 14 carbon atoms.

The kinetics of the reduction and transformation of the aromatic structures and individual oxy-functional groups to reduced species were explored using ATR IR spectroscopy. It is shown that the reductive deconstruction of lignin proceeds *via* stepwise hydrogenolysis of the ether bonds followed by hydrogenation of the aromatic rings, and alkylation between partially reduced lignin monomers and substituted phenols. The results show that small lignin oligomers can be reductively deconstructed, opening a pathway to a full utilization of a wider range of lignin polymers.

5. References

1. J. Zakzeski, P. C. A. Bruijninx, A. L. Jongerius and B. M. Weckhuysen, *Chemical Reviews*, 2010, 110, 3552-3599.
2. J. Holladay, J. Bozell, J. White and D. Johnson, *DOE Report PNNL*, 2007, 16983.
3. T. Wiesenthal and A. Mourelatou, How much bioenergy can Europe produce without harming the environment?, 2006.
4. M. Lawoko, R. Berggren, F. Berthold, G. Henriksson and G. Gellerstedt, *Holzforschung*, 2004, 58, 603.
5. R. P. Overend and K. G. Johnson, in *Enzymes in Biomass Conversion*, American Chemical Society, 1991, vol. 460, ch. 21, pp. 270-287.
6. A. Johansson, O. Aaltonen and P. Ylinoen, *Biomass*, 1987, 13, 45-65.
7. N.-E. E. Mansouri and J. Salvadó, *Industrial Crops and Products*, 2006, 24, 8-16.
8. M. H. Hussin, A. A. Rahim, M. N. Mohamad Ibrahim and N. Brosse, *Industrial Crops and Products*, 2013, 49, 23-32.
9. M. P. Pandey and C. S. Kim, *Chemical Engineering & Technology*, 2011, 34, 29-41.
10. B. A.V, *Applied Catalysis A: General*, 1994, 116, 5-47.
11. C. J. Zhang Qi, Wang Tiejun, Xu Ying, *Energy Conversion and Management*, 2007, 48, 87 - 92.
12. A. A. Boateng, C. A. Mullen, N. Goldberg, K. B. Hicks, H.-J. G. Jung and J. F. S. Lamb, *Industrial & Engineering Chemistry Research*, 2008, 47, 4115-4122.
13. C. Zhao and J. A. Lercher, *ChemCatChem*, 2012, 4, 64-68.
14. K. Li, R. Wang and J. Chen, *Energy & Fuels*, 2011, 25, 854-863.
15. C. Zhao, Y. Kou, A. A. Lemonidou, X. Li and J. A. Lercher, *Angewandte Chemie International Edition*, 2009, 48, 3987-3990.
16. C. Zhao, Y. Kou, A. A. Lemonidou, X. Li and J. A. Lercher, *Chemical Communications*, 2010, 46, 412-414.
17. R. K. K. M. L. H. A. Gutierrez, R. Slioor, A.O.I. Krause, *Catalysis Today*, 2009, 147, 239 - 246.
18. E. Furimsky, *Catalysis Reviews*, 1983, 25, 421-458.
19. S. Kasakov, C. Zhao, E. Baráth, Z. A. Chase, J. L. Fulton, D. M. Camaioni, A. Vjunov, H. Shi and J. A. Lercher, *Chemistry – A European Journal*, 2015, 21, 1567-1577.
20. C. Zhao, J. He, A. A. Lemonidou, X. Li and J. A. Lercher, *Journal of Catalysis*, 2011, 280, 8-16.
21. C. Zhao, S. Kasakov, J. He and J. A. Lercher, *Journal of Catalysis*, 2012, 296, 12-23.

22. J. He, C. Zhao and J. A. Lercher, *Journal of the American Chemical Society*, 2012, 134, 20768-20775.
23. M. Zaheer and R. Kempe, *ACS Catalysis*, 2015, 5, 1675-1684.
24. A. G. Sergeev and J. F. Hartwig, *Science*, 2011, 332, 439-443.
25. J. He, L. Lu, C. Zhao, D. Mei and J. A. Lercher, *Journal of Catalysis*, 2014, 311, 41-51.
26. A. G. Sergeev, J. D. Webb and J. F. Hartwig, *Journal of the American Chemical Society*, 2012, 134, 20226-20229.
27. W. Schutyser, S. Van den Bosch, J. Dijkmans, S. Turner, M. Meledina, G. Van Tendeloo, D. P. Debecker and B. F. Sels, *ChemSusChem*, 2015, 8, 1805-1818.
28. X. Wang and R. Rinaldi, *Energy & Environmental Science*, 2012, 5, 8244-8260.
29. P. Ferrini and R. Rinaldi, *Angewandte Chemie International Edition*, 2014, 53, 8634-8639.
30. X. Wang and R. Rinaldi, *ChemSusChem*, 2012, 5, 1455-1466.
31. I. Klein, B. Saha and M. M. Abu-Omar, *Catalysis Science & Technology*, 2015, 5, 3242-3245.
32. Q. Song, F. Wang, J. Cai, Y. Wang, J. Zhang, W. Yu and J. Xu, *Energy & Environmental Science*, 2013, 6, 994-1007.
33. A. K. Deepa and P. L. Dhepe, *ACS Catalysis*, 2015, 5, 365-379.
34. T. H. Parsell, B. C. Owen, I. Klein, T. M. Jarrell, C. L. Marcum, L. J. Haupert, L. M. Amundson, H. I. Kenttamaa, F. Ribeiro, J. T. Miller and M. M. Abu-Omar, *Chemical Science*, 2013, 4, 806-813.
35. C. Xu, R. A. D. Arancon, J. Labidi and R. Luque, *Chemical Society Reviews*, 2014, 43, 7485-7500.
36. R. Nares, J. Ramírez, A. Gutiérrez-Alejandre, C. Louis and T. Klimova, *The Journal of Physical Chemistry B*, 2002, 106, 13287-13293.
37. A. Richel, C. Vanderghem, M. Simon, B. Wathélet and M. Paquot, *Analytical Chemistry Insights*, 2012, 7, 79-89.
38. D. S. Kosyakov, N. V. Ul'yanovskii, E. A. Sorokina and N. S. Gorbova, *J Anal Chem*, 2014, 69, 1344-1350.
39. F. Meemken, P. Müller, K. Hungerbühler and A. Baiker, *Review of Scientific Instruments*, 2014, 85, 084101.
40. J.-M. Andanson and A. Baiker, *Chemical Society Reviews*, 2010, 39, 4571-4584.
41. P. Burattin, M. Che and C. Louis, *The Journal of Physical Chemistry B*, 1998, 102, 2722-2732.
42. O. Faix, *Holzforschung - International Journal of the Biology, Chemistry, Physics and Technology of Wood*, 1991, 45, 21.

43. S. Y. Lin and C. W. Dence, *Methods in lignin chemistry*, Springer, 1992.
44. B. C. Smith, *Infrared spectral interpretation: a systematic approach*, CRC press, 1998.
45. H. Kim and J. Ralph, *Organic & Biomolecular Chemistry*, 2010, 8, 576-591.
46. S. Dabral, J. Mottweiler, T. Rinesch and C. Bolm, *Green Chemistry*, 2015, DOI: 10.1039/C5GC00186B.
47. A. Rahimi, A. Azarpira, H. Kim, J. Ralph and S. S. Stahl, *Journal of the American Chemical Society*, 2013, 135, 6415-6418.
48. C. Zhao, D. M. Camaioni and J. A. Lercher, *Journal of Catalysis*, 2012, 288, 92-103.
49. D. D. Laskar, M. P. Tucker, X. Chen, G. L. Helms and B. Yang, *Green Chemistry*, 2014, 16, 897-910.
50. T. Parsell, S. Yohe, J. Degenstein, T. Jarrell, I. Klein, E. Gencer, B. Hewetson, M. Hurt, J. I. Kim, H. Choudhari, B. Saha, R. Meilan, N. Mosier, F. Ribeiro, W. N. Delgass, C. Chapple, H. I. Kenttamaa, R. Agrawal and M. M. Abu-Omar, *Green Chemistry*, 2015, 17, 1492-1499.
51. A. Rahimi, A. Ulbrich, J. J. Coon and S. S. Stahl, *Nature*, 2014, 515, 249-252.
52. O. Derkacheva and D. Sukhov, *Macromolecular Symposia*, 2008, 265, 61-68.
53. Y.-R. Luo, *Comprehensive handbook of chemical bond energies*, CRC press, 2007.
54. W. Song, Y. Liu, E. Barath, C. Zhao and J. A. Lercher, *Green Chemistry*, 2015, 17, 1204-1218.
55. Z. A. Chase, S. Kasakov, H. Shi, A. Vjunov, J. L. Fulton, D. M. Camaioni, M. Balasubramanian, C. Zhao, Y. Wang and J. A. Lercher, *Chemistry – A European Journal*, 2015, DOI: 10.1002/chem.201502723.

6. Associated Content

Peer-Reviewed Publication

The chapter IV is based on the following article: Stanislav Kasakov, Hui Shi, Donald M. Camaioni, Chen Zhao, Eszter Baráth, Andreas Jentys, Johannes A. Lercher, Reductive deconstruction of organosolv lignin catalyzed by zeolite supported nickel nanoparticles, accepted by Green Chemistry for the invited themed issue “Lignin chemistry and valorization” published by the RSC Royal Chemistry, *Green Chem.*, 2015, **17**, 5079 - 5090

Contributions

Stanislav Kasakov performed the experiments and contributed with design of experiments. Hui Shi, Donald M. Camaioni and Andreas Jentys were involved in the development of the lab-built ATR-IR instrument and with the interpretation of IR spectra. Chen Zhao and Eszter Barath supervised the work and were involved in the data analysis. Eszter Barath was responsible for 2D HSQC NMR interpretation. Stanislav Kasakov, Hui Shi, Donald M. Camaioni and Johannes A. Lercher were responsible for manuscript preparation. Johannes A. Lercher is the principal investigator of this work.

Acknowledgment

The financial support from TUM-PNNL cooperation project “Development of new methods for in situ characterization in liquid phase reactions” (CN-177939) is highly appreciated. The work by S.K., H.S., and J.A.L. was partially supported by the U.S. Department of Energy (DOE), Office of Science, Office of Basic Energy Sciences (BES), Division of Chemical Sciences, Geosciences & Biosciences. Pacific Northwest National Laboratory is a multi-program national laboratory operated for DOE by Battelle through Contract DE-AC05-76RL01830. Dr. Sergei Vagin is acknowledged for conducting GPC measurements. Moreover, we want to thank Dr. Jürgen Behr and Prof. Dr. Rudi F. Vogel for conducting the MALDI-TOF MS analysis. Further, we want to thank M.Sc. Moritz Schreiber for the help on the gas phase analysis. Dipl. Min. Katia Rodewald is acknowledged for HR-SEM EDX measurements. We thank Stas Vaisman for the help on the graphical abstract. Lastly, we want to acknowledge M.Sc. Nikita Popov for his assistance in the lab.

Clearance by the Publisher

RSC Royal Chemistry provided the rights for the approval to non-commercially reproduce the accepted article both in print and online.

Chapter V.

Monitoring catalysis by *in situ* IR spectroscopy

Abstract



The mechanism of the catalytic reduction of palmitic acid to *n*-pentadecane at 260 °C in the presence of hydrogen over catalysts combining multiple functions has been explored. The reaction involves rate-determining reduction of the carboxylic group of palmitic acid to give hexadecanal, which is catalyzed either solely by Ni or synergistically by Ni and the ZrO₂ support. The latter route involves adsorption of the carboxylic acid group at an oxygen vacancy of ZrO₂ and abstraction of the α-H with elimination of O to

produce the ketene, which is in turn hydrogenated to the aldehyde over Ni sites. The aldehyde is subsequently decarbonylated to *n*-pentadecane on Ni. The rate of deoxygenation of palmitic acid is higher on Ni/ZrO₂ than that on Ni/SiO₂ or Ni/Al₂O₃, but is slower than that on H-zeolite-supported Ni. As the partial pressure of H₂ is decreased, the overall deoxygenation rate decreases. In the absence of H₂, ketonization catalyzed by ZrO₂ is the dominant reaction. *In situ* IR spectroscopy unequivocally shows the presence of adsorbed ketene (C=C=O) on the surface of ZrO₂ during the reaction with palmitic acid at 260 °C in the presence or absence of H₂.

1. Introduction

Fatty acid alkyl esters are components of micro algae, regarded as the third generation biofuels. The algae as biomass resources are attractive renewable liquid biodiesel fuels, but the high oxygen content in the ester component limits their application. It would clearly be advantageous if oxygen-free hydrocarbons could be catalytically produced from animal, vegetable, or algal oils.^[1,2] Long carbon chain (C₁₆-C₂₂) fatty acids are usually selected as model compounds for investigating the upgrading of triglycerides. Currently, three methods can be utilized for the deoxygenation of fatty acids to alkanes. The first relies on a supported noble metal catalyst, such as Pd/C or Pt/C, for the decarboxylation and decarbonylation of fatty acids to alkanes in the absence of H₂, giving selectivities higher than 98 % at 573 – 603 K.^[3-5] The second employs conventional hydrotreating catalysts, such as NiMo and CoMo sulfides, for the deoxygenation of fatty acids to C₁₅-C₁₈ alkanes at 573 – 723 K in the presence of H₂.^[6-8] However, sulfide catalysts contaminate products and become deactivated due to sulfur leaching, especially in the presence of trace quantities of water.^[9-11] The third utilizes zeolite-supported metal catalysts, such as Ni/HBEA or Pt-Re/HZSM-5, for the hydrodeoxygenation (HDO) of fatty acids to alkanes at 523 – 573 K.^[12,13] It has been reported that the transformation of triglycerides to alkanes on Ni/HBEA catalysts involves initial hydrogenation and hydrogenolysis of these substrates to fatty acids (primary products), followed by deoxygenation of these intermediates to hydrocarbons by sequential hydrogenation-dehydration-hydrogenation.^[6,12]

Since the H₂ consumption for the deoxygenation of fatty acids follows the order decarboxylation < decarbonylation < hydrodeoxygenation, the decarbonylation and decarboxylation routes may be more economical than the hydrodeoxygenation pathway. In the vapor phase, methanation and water-gas shift are the reactions that occur between CO, CO₂, and H₂ over Ni.^[12]

To develop a next-generation hydrodeoxygenation catalyst, the deoxygenation of C₁₆ palmitic acid has been studied with a variety of sulfur-free supported metal catalysts at 533 K in the presence and absence of H₂. Specifically, *in situ* IR spectroscopy has been used to monitor the concentrations of reactants and intermediates during the reactions, as well as of the adsorbed species on the surface of the catalysts (ZrO₂ and Ni/ZrO₂) in the presence and absence of H₂.

2. Experimental section

2.1 Chemicals

All chemicals were purchased and used as received: palmitic acid (Sigma, $\geq 99\%$ Reagent Plus), 1-hexadecanol (Aldrich, $\geq 99\%$), palmityl palmitate (Sigma, $\geq 99\%$), dodecane (Sigma-Aldrich, $\geq 99\%$ Reagent Plus), eicosane (Aldrich, $\geq 99\%$ GC assay), *n*-pentadecane (Fluka, $\geq 99.8\%$ analytical standard), *n*-hexadecane (Fluka, $\geq 99.8\%$ analytical standard), palmitone (TCI, $>90\%$ GC assay), nickel(II) nitrate hexahydrate (Sigma-Aldrich, $\geq 98.5\%$), tetraammineplatinum(II) nitrate (Strem Chemicals, 99%), and tetraamminepalladium(II) nitrate (Aldrich, 10 wt.% aqueous solution). The supports employed, namely γ -Al₂O₃ (Aeroxide Alu C-Degussa), SiO₂ (Aeroxide Alu C-Degussa), ZrO₂ derived from zirconium hydroxide (MEL Chemicals), HZSM-5 (Süd-Chemie AG, Si/Al=200), and HBEA (Zeolyst, Si/Al=180), were obtained from commercial sources as indicated.

2.2 Catalyst preparation

The catalysts consisting of Ni supported on γ -Al₂O₃, SiO₂, ZrO₂, HZSM-5, and HBEA, were synthesized by the incipient wetness impregnation method. The ZrO₂ support was prepared by calcination of zirconium hydroxide in static air at 673 K for 4 h. In a representative procedure, 5 wt.% Ni/ZrO₂ was prepared by first dissolving Ni(NO₃)₂·6H₂O (2.92 g) in water (5 g) and then slowly dropping this solution onto ZrO₂ (10 g) with continuous stirring. After allowing the metal to incorporate into the support over 4 h at ambient temperature, the catalyst was first dried overnight at ambient temperature and then dried at 383 K for 12 h. Thereafter, it was calcined in dry synthetic air at 673 K for 4 h (flow rate: 100 mL min⁻¹) and reduced at 773 K for 4 h (ramp: 2 K min⁻¹) in hydrogen (flow rate: 100 mL min⁻¹).

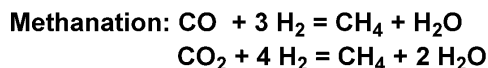
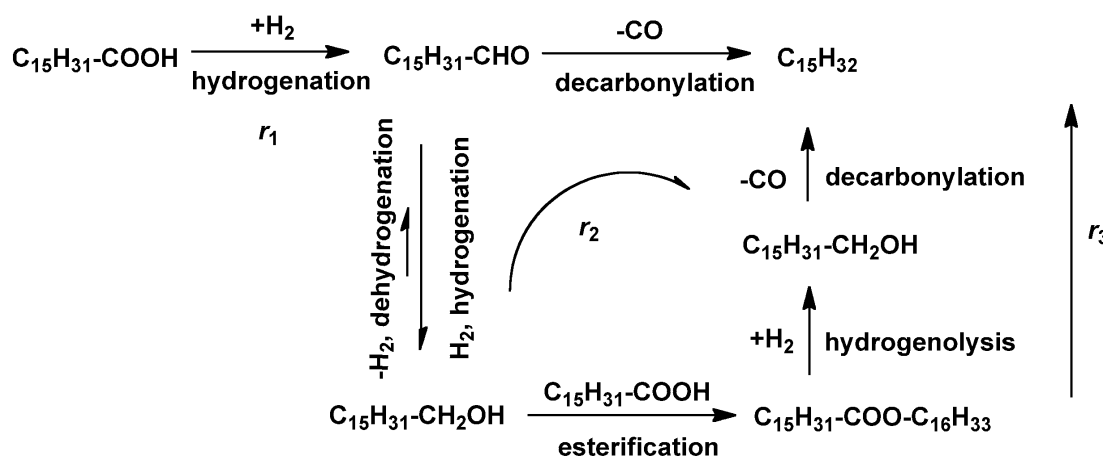
2.3 *In situ* IR measurements

The *in situ* IR spectroscopic study used a React IR device (Mettler Toledo, React IR 1000) coupled to a Parr reactor (100 mL), and a diamond placed in the bottom of the autoclave was used as a probe to collect *in situ* IR spectra in the liquid phase. In the first step, a background spectrum was collected under the reaction conditions (523 K, 40 bar H₂) with catalyst (0.25 g) dispersed in dodecane (50 mL). The autoclave reactor was then loaded with the reactant palmitic acid (5.0 g), and H₂ (40 bar) was introduced into the system once the reaction temperature (523 K) had been reached. Spectra were collected at intervals of 10 min over 480 min. The schematic view of the *in situ* IR setup is similar to that shown in Figure 3-1.

3. Results and Discussions

3.1 Proposed reaction pathways for palmitic acid conversion

Combining the reaction rates of palmitic acid, 1-hexadecanol, and palmityl palmitate allows us to formulate the overall reaction pathways for the conversion of palmitic acid on the Ni/ZrO₂ catalyst in the presence of H₂ (see Scheme 5-1). The process involves initial hydrogenation of the carboxylate group of palmitic acid to produce hexadecanal (major route). This major route benefits from the hydrogenation/dehydrogenation equilibrium of 1-hexadecanol, and hexadecanal is subsequently decarbonylated to *n*-pentadecane and carbon monoxide. In parallel, the equilibrium amount of the intermediate 1-hexadecanol also forms an ester with palmitic acid (palmityl palmitate), a process that is catalyzed by the acid sites of ZrO₂. As the reaction proceeds, this ester can be cleaved by metal-catalyzed hydrogenolysis, leading to 1-hexadecanol and hexadecanal, which are decarbonylated to form *n*-pentadecane. The weakly acidic sites of ZrO₂ cause slight cracking and isomerization of the straight-chain alkanes. The produced CO₂/CO may further react with H₂ to produce methane and water.



Scheme 5-1. Proposed main reaction pathways for palmitic acid conversion over Ni/ZrO₂ in the presence of H₂

To delineate the rate-determining step, the individual kinetics for the conversions of palmitic acid, 1-hexadecanol, and palmityl palmitate are compared in Table 5-1. As 1-hexadecanol and hexadecanal are in equilibrium during conversion of the former, the rate of decarbonylation of hexadecanal (13.1 mmol g⁻¹ h⁻¹) was estimated to be approximately an order of magnitude higher than that of the hydrogenation of palmitic acid (1.3 mmol g⁻¹ h⁻¹) on 5 wt.% Ni/ZrO₂ under the present reaction conditions. Additionally, the rate of hydrogenolysis-deoxygenation of palmityl palmitate (2.4 mmol g⁻¹ h⁻¹) was

around twice that of hydrogenation of the fatty acid. Therefore, we conclude that the hydrogenation of palmitic acid to hexadecanal is the rate-determining step in the overall reaction. On increasing the reaction temperature from 503 to 543 K, the initial hydrogenation rate increased from 0.3 to 2.8 mmol g⁻¹ h⁻¹ and the conversion increased from 38 to 100%. Concomitantly, the yield of *n*-pentadecane increased from 1.7 to 85% C% after a reaction time of 6 h. The yield of *n*-pentadecane after 6 h decreased sharply from 58 to 4.6% C% when the temperature was lowered from 523 to 513 K, with the major product shifting from *n*-pentadecane (selectivity: 82%) at 523 K to 1-hexadecanol (selectivity: 90%) at 513 K after attaining conversion levels of 60-70%. Thus, the rate of the decarbonylation step for 1-hexadecanol showed a marked temperature dependence. A high apparent activation energy ($E_a = 156$ kJ mol⁻¹) for palmitic acid conversion was obtained over Ni/ZrO₂, which is in line with the low forward reaction rate constant for this hydrogenation step.

Table 5-1. Kinetic data of elementary steps in the overall deoxygenation of palmitic acid with 5 wt.% Ni/ZrO₂ at 533 K in the presence of H₂

Elementary step	Initial rate [mmol g ⁻¹ h ⁻¹]
hydrogenation of palmitic acid (rate-determining step)	$r_1 = 1.3$ ($E_a = 156$ kJ mol ⁻¹)
decarbonylation of 1-hexadecanol	$r_2 = 13.1$
hydrogenolysis of palmityl palmitate	$r_3 = 2.4$

3.2 Monitoring the conversion of palmitic acid over ZrO₂ and Ni/ZrO₂ catalysts by *in situ* IR spectroscopy

To elucidate the proposed reaction pathway, palmitic acid conversion in dodecane was monitored by means of time-resolved *in situ* IR spectroscopy. A probe diamond connecting the reactor interior with the IR spectrometer was incorporated in the bottom of an autoclave. This allowed the collection of the signals of the liquid compounds and of the surface species adsorbed on the catalyst, which was deposited on the diamond. The time-resolved IR spectra measured during the deoxygenation of palmitic acid over ZrO₂ (in the presence or absence of H₂) and Ni/ZrO₂ catalysts with H₂ at 523 K are shown in Figure 5-1 a-c. The spectra shown are after subtracting the background of the catalyst, solvent, and gas atmosphere under the working conditions, as shown in the Figure A-1 in the Appendix. The reference IR spectra of the reactant, intermediates, products, and solvent are compiled in Figure A-2, in the Appendix. Preliminary experiments showed that signals of alkenes and alkanes were not discernible due to their high similarity to those of the solvent, whereas signals of aldehyde and alcohol intermediates were, as expected, very weak because of overlapping fatty acid bands.

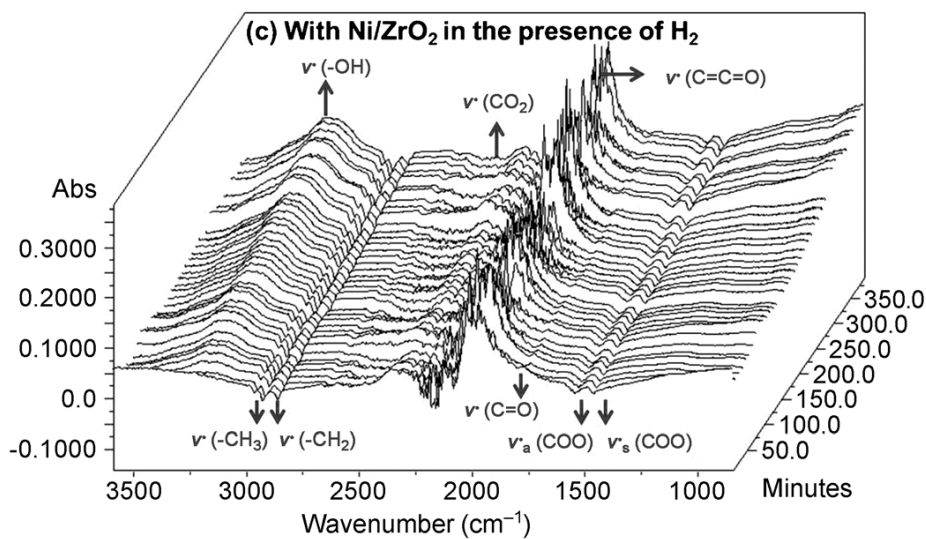
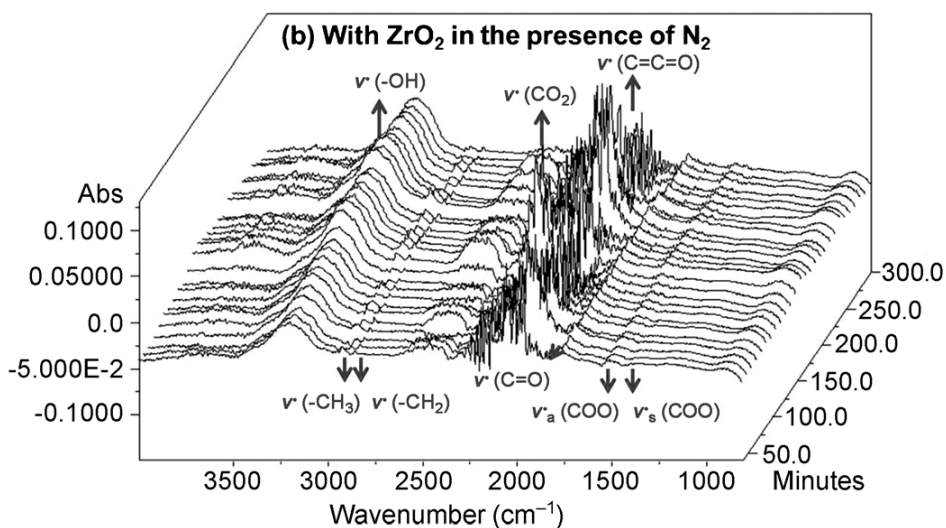
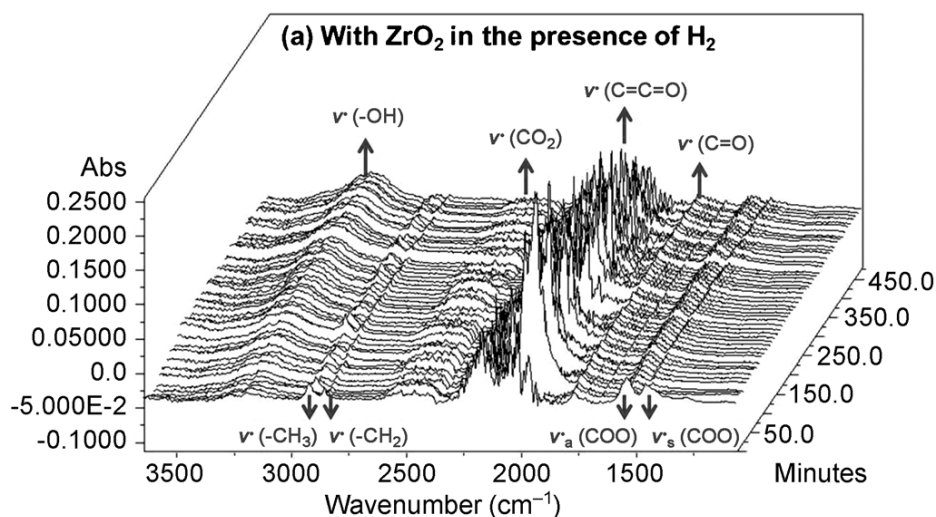
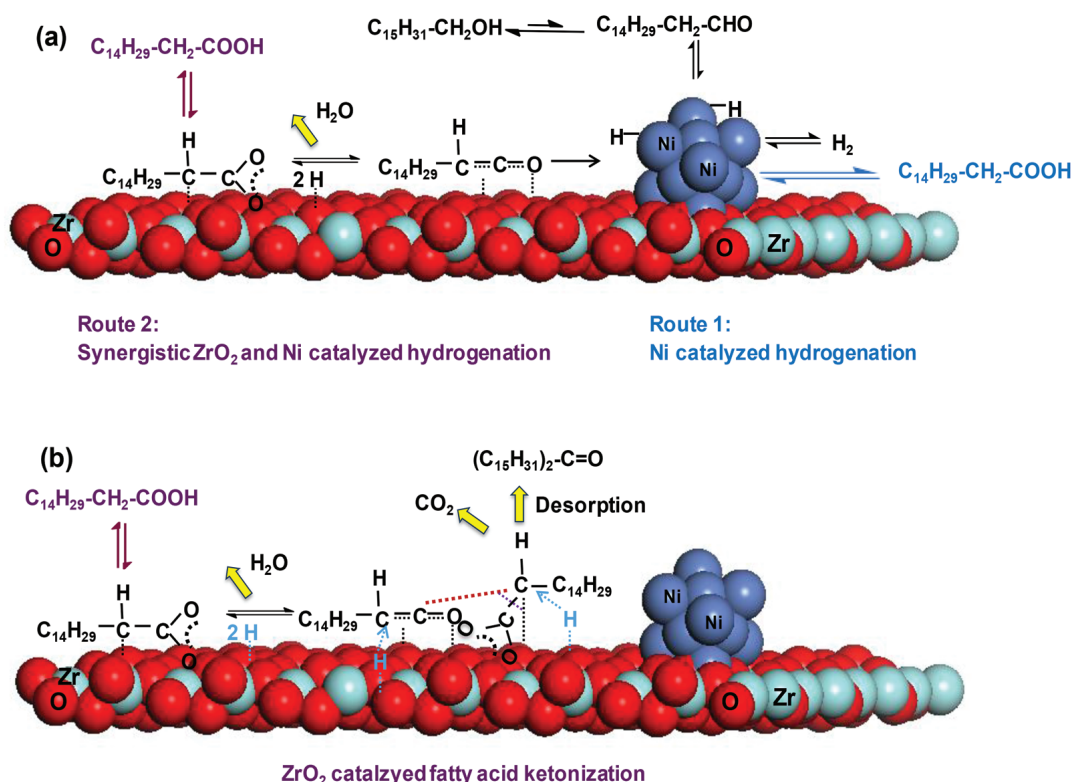


Figure 5-1. *In situ* IR spectra of palmitic acid conversion at 523 K. Experimental conditions: palmitic acid (2 g), dodecane (50 mL), a) ZrO₂ (0.25 g), 40 bar H₂, b) ZrO₂ (0.25 g) 1 bar N₂, and c) Ni/ZrO₂ (0.25 g), 40 bar H₂.

During the reaction of palmitic acid on ZrO_2 in the presence of either H_2 or N_2 (Figure 5-1 a,b), strong $\nu(\text{C}=\text{C}=\text{O})$ stretching bands were observed at 2050–2150 cm^{-1} (compare with the reference IR spectrum of the ketene in Figure A-2). The signal of the ketene adsorbed on ZrO_2 was quite intense, because the diamond window was largely covered with ZrO_2 . This allowed operation of the reactor like an in situ attenuated total reflection (ATR) cell for probing surface-adsorbed species. The observation of ketene strongly supports the mechanism proposed in Scheme 5-2. Moreover, decarboxylation producing CO_2 (the $\nu(\text{CO}_2)$ band appeared at 2450–2550 cm^{-1}) occurred in both cases under selected conditions. Decarbonylation (leading to CO production) could not be excluded, as the wavenumber of the $\nu(\text{CO})$ band overlaps with the region of light absorption of diamond. Lastly, the intensity of the $\nu(\text{OH})$ band increased and shifted in the presence of H_2 due to the gradual formation of $\text{C}_{16}\text{H}_{33}\text{OH}$ from $\text{C}_{15}\text{H}_{31}\text{COOH}$. The hydrogenation rate was slow in the presence of the ZrO_2 support alone. No ketonization product was observed in the presence of N_2 , probably because its rate of formation was too slow at 523 K.



Scheme 5-2. Proposed reaction mechanism for a) the hydrogenation of palmitic acid to hexadecanal by synergistic catalysis over Ni/ZrO_2 in the presence of H_2 , and b) for the ketonization of palmitic acid to palmitone over ZrO_2 in the absence of H_2 .

In comparison, the product distribution from palmitic acid conversion was significantly altered on going from ZrO_2 to Ni/ZrO_2 (Figure 5-1c). Firstly, the $\nu(\text{CO}_2)$ band was not observed, but the intensity of the $\nu(\text{OH})$ band increased rapidly, suggesting a switch in the

major pathway of palmitic acid conversion from decarboxylation--decarbonylation with ZrO_2 to hydrogenation with Ni/ZrO_2 . Furthermore, the intensity of the $\nu(\text{OH})$ band increased more rapidly with Ni/ZrO_2 than with ZrO_2 in the presence of H_2 , implying that the hydrogenation rate was much faster with Ni/ZrO_2 under otherwise identical conditions. Secondly, the $\nu(\text{C}=\text{C}=\text{O})$ band appeared over Ni/ZrO_2 , indicating that the ketene was also an important intermediate with this catalyst because of the strong adsorption of the fatty acid at the oxygen vacancy sites of ZrO_2 . This created another synergistic route, thereby accelerating the hydrogenation (Scheme 5-2). It should be emphasized that the results of the *in situ* IR spectroscopic study were fully consistent with the aforementioned results and thus support the hypothesized mechanism over ZrO_2 and Ni/ZrO_2 in the presence or absence of H_2 .

4. Conclusion

The reaction pathways for the conversion of palmitic acid have been explored over various catalysts, and a route for the quantitative formation of *n*-pentadecane has been developed with Ni/ZrO₂ at 533 K in the presence of H₂. The deoxygenation mechanism proceeds through an initial hydrogenation of palmitic acid to hexadecanal (rate-determining step), which is in equilibrium with 1-hexadecanol at high H₂ pressure. The aldehyde may then undergo decarbonylation to produce the target *n*-pentadecane and carbon monoxide (major route). The direct decarboxylation--decarbonylation and hydrogenation--dehydration reactions are minor routes.

In the presence of H₂, ZrO₂-supported metal catalysts show an enhanced rate of hydrogenation of palmitic acid compared to C-, Al₂O₃-, and SiO₂-supported metal catalysts. This is because hydrogenation of the fatty acid to the aldehyde is catalyzed by parallel aldehyde formation on metallic Ni or through adsorption of the carboxylate at the oxygen vacancies of ZrO₂, followed by abstraction of α -H to produce the ketene.

The reaction mechanism for the conversion of palmitic acid on ZrO₂-supported metal catalysts involved initial adsorption of the substrate at oxygen vacancies of ZrO₂ to form palmitate, which was then transformed to the adsorbed ketene through α -H abstraction and H₂O elimination. The adsorbed ketene follows different reaction routes dictated by the reactive gas environment. In H₂, the ketene is hydrogenated to hexadecanal at the metal site. In the absence of H₂, the ketene combines with a neighboring palmitate molecule on the ZrO₂ surface to form palmitone.

In situ IR spectroscopy strongly supports the proposed mechanism through capturing the ketene intermediates on ZrO₂ and Ni/ZrO₂ in the presence or absence of H₂. The spectra demonstrate that hydrogenation is the major initial route for palmitic acid conversion with Ni/ZrO₂, whereas decarboxylation--decarbonylation is more pronounced with ZrO₂. ZrO₂-catalyzed hydrogenation of palmitic acid occurs at a much slower rate than the Ni/ZrO₂-catalyzed process in the presence of H₂.

5. References

- [1] D. Kubicka, J. Horúček, *Appl. Catal. A* 2011, 394, 9–17.
- [2] L. X. Li, E. Coppola, J. Rine, J. L. Miller, D. Walker, *Energy Fuels* 2010, 24, 1305 – 1315.
- [3] M. Snåre, I. Kubickov, P. Mäki-Arvela, K. Eränen, D. Y. Murzin, *Ind. Eng. Chem. Res.* 2006, 45, 5708 – 5715.
- [4] M. Snåre, I. Kubickov, P. Mäki-Arvela, D. Chichova, K. Eränen, D. Y. Murzin, *Fuel* 2008, 87, 933 – 945.
- [5] J. G. Immer, M. J. Kelly, H. H. Lamb, *Appl. Catal. A* 2010, 375, 134 – 139.
- [6] G. W. Huber, P. O. Connor, A. Corma, *Appl. Catal. A* 2007, 329, 120 – 129.
- [7] R. Kumar, B. S. Rana, R. Wiwari, E. Verma, R. Kumar, R. K. Joshi, M. O. Garg, A. K. Sinha, *Green Chem.* 2010, 12, 2232 – 2239.
- [8] R. Sotelo-Bojús, Y. Y. Liu, T. Minowa, *Ind. Eng. Chem. Res.* 2011, 50, 2791–2799.
- [9] E. Laurent, B. Delmon, *J. Catal.* 1994, 146, 281 – 291.
- [10] A. Centeno, E. Laurent, D. Delmon, *J. Catal.* 1995, 154, 288 – 298.
- [11] T. R. Viljava, R. S. Komulanien, A. O. I. Krause, *Catal. Today* 2000, 60, 83–92.
- [12] B. Peng, Y. Yao, C. Zhao, J. A. Lercher, *Angew. Chem.* 2012, 124, 2114 – 2117; *Angew. Chem. Int. Ed.* 2012, 51, 2072 – 2075.

6. Associated Content

Peer-Reviewed Publication

This chapter is based on the full article: Baoxiang Peng, Chen Zhao, Stanislav Kasakov, Sebastian Foraita and Johannes A. Lercher, Manipulating Catalytic Pathways: Deoxygenation of Palmitic Acid on Multifunctional Catalysts, *Chemistry – A European Journal*, 2013, Vol 19, p. 4732 – 4741.

Contributions

Baoxiang Peng performed the experiments. Sebastian Foraita synthesized the catalysts and performed additional batch experiments. Stanislav Kasakov performed the in situ IR experiments and contributed with experimental design. Baoxiang Peng, Chen Zhao, Stanislav Kasakov, Sebastian Foraita and Johannes A. Lercher were responsible for manuscript preparation. Chen Zhao and Johannes A. Lercher are the principal investigators of this work.

Acknowledgments

We appreciate financial support from EADS Deutschland GmbH. This work was also partially supported by the Technische Universität München in the framework of the European Graduate School on Sustainable Energy. The authors would like to thank X. Hecht for performing the BET measurements and M. Neukamm for performing the AAS measurements.

Clearance by the Publisher

Wiley VCH gave approval to non-commercially reproduce the accepted article both in print and online.

7. Appendix

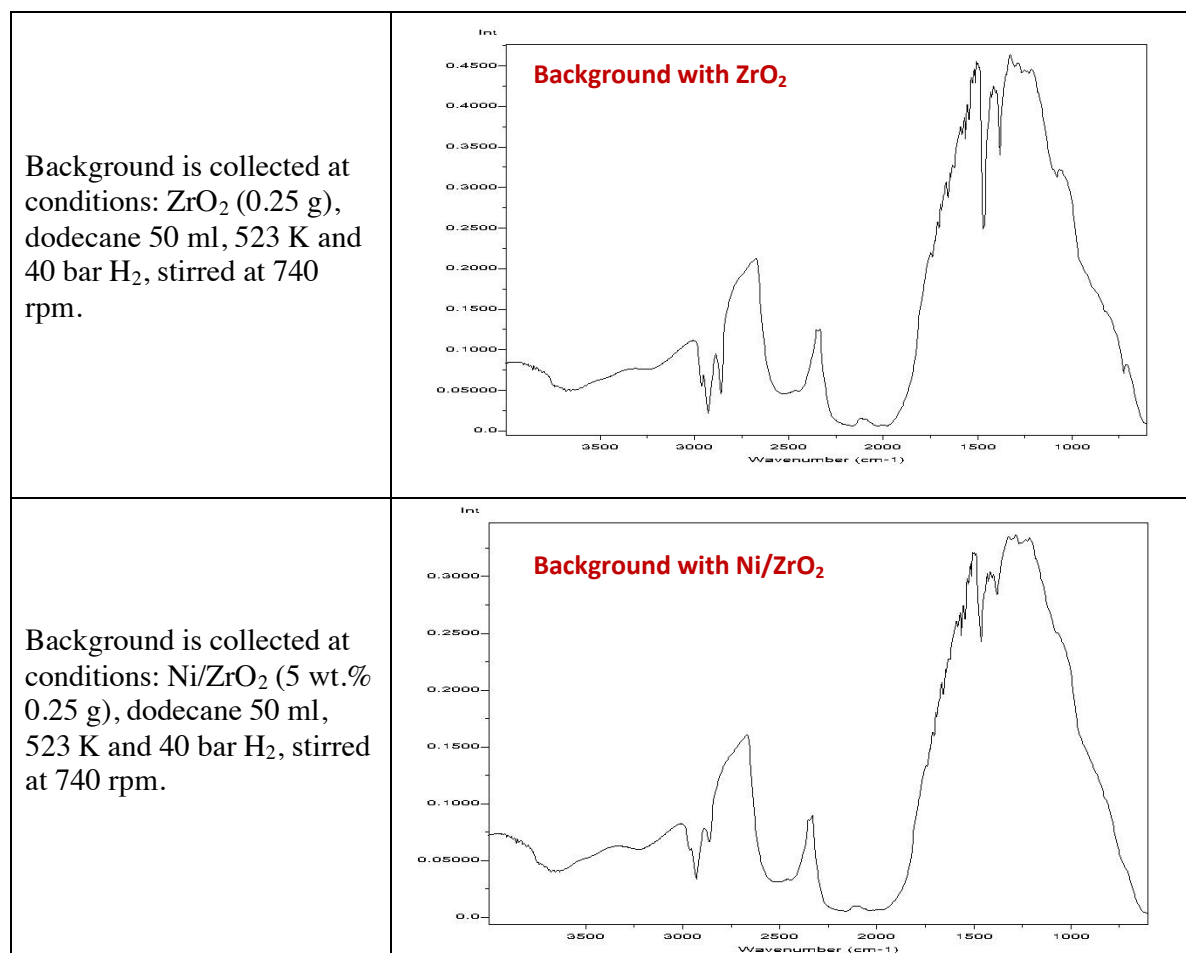


Figure A-1. The IR backgrounds used for the in situ React IR sequence

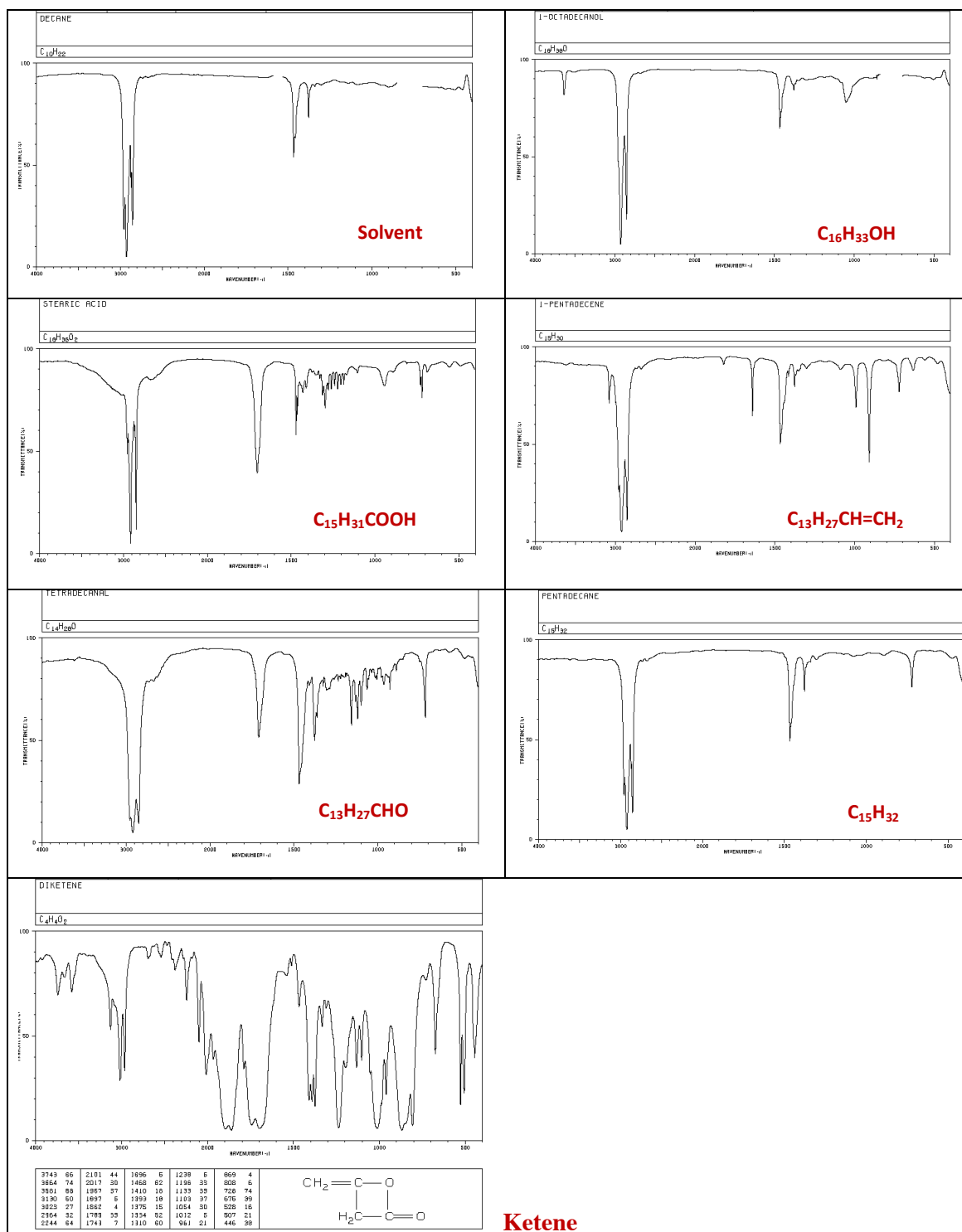


Figure A-2. The standard IR reference spectra (solvent, reactant, intermediate, and products) used for analyzing in situ IR.

The spectra shown in Figure A-2 are based on the AIST:Spectral Database for Organic Compounds, SDBS, available at http://sdb.sdb.aist.go.jp/sdb/cgi-bin/cre_list.cgi.

Chapter VI.

Summary and Conclusions

This dissertation concerns the development of Ni based catalysts for the liquid phase catalyzed lignin-derived biomass conversion. The dual functional catalysts comprised Ni as base metal supported on a material bearing acid-base sites in various concentrations, such as zeolites (HBEA, HZSM-5), sulfonated low surface and high surface carbon, and ZrO_2 . Presented data provides insight into the mechanism of the hydrodeoxygenation of phenol through kinetic and *in situ* IR studies with the Ni based catalysts. While the Ni metal shows a great ability to hydrogenate aromatic compounds, the deoxygenation process catalyzed with a Brønsted acid site (BAS) via elimination reaction. The sequence of the hydrodeoxygenation reaction can be separated into four subsequent reaction steps, described as follows: i) hydrogenation of phenol to cyclohexanone, ii) keto-enol hydroisomerization of cyclohexanone to cyclohexanol, iii) dehydration of cyclohexanol to cyclohexene and subsequent cyclohexene hydrogenation to cyclohexane, the final product. The *in situ* IR study provided insight towards a better understanding of the reaction mechanism in condensed phases. The rate determining step for HZSM-5 supported Ni catalysts was shown to be the first step, the phenol hydrogenation. Further, the activity and stability of two catalysts (HZSM-5 and Al_2O_3 bounded HZSM-5) has been explored in this work. The growth of the Ni sites and the change of the acid sites on the fresh and used catalysts lead to a slight deactivation of the catalysts.

To further improve the HDO catalysis, Ni nanoparticles has been synthesized and incorporated on sulfonated carbon supports derived from glucose or cellulose. The Ni/C-SO₃H catalysts have been investigated to hydrodeoxygenate phenol in liquid phases (water and hexadecane). The state of 3 – 5 nm Ni particles was further analysed by *in situ* X-ray absorption spectroscopy. The results show that the metallic Ni was rapidly formed *in situ* without detectable leaching to the aqueous phase. Bare C-SO₃H carbon catalysts are prone to deoxygenate cyclohexanol in both phases, water and hexadecane, but the *in situ* IR study revealed that cyclohexanol dehydration is the rate limiting step for the Ni/C-SO₃H catalysts. Thus, phenol HDO catalysis was further improved by physically admixing C-SO₃H with Ni/C-SO₃H catalyst to balance the two catalytic functions. The addition of C-SO₃H to the most active of the Ni/C-SO₃H catalyst indirectly shows that the proximity of the Ni site limits the acid properties of the support.

In addition, this dissertation describes a new process for one-pot converting lignin to hydrocarbons with almost quantitative yields (94 C% of the theoretical maximum yield) at relatively mild reaction conditions (523 - 573 K, 2 MPa H₂). The developed nanosized Ni/HZSM-5 and Ni/HBEA catalysts possess the ability to reductively deconstruct lignin through scission of C_{aromatic}-O and C_{aliphatic}-O bonds in the lignin polymer, subsequently forming the phenolic oligomers to further cleave the C-O bond towards phenolic dimers and monomers. These phenolic building blocks undergo subsequent hydrodeoxygenation to form the desired products in the gasoline (and kerosene) range of C₅ - C₁₄. Further, a self-developed *in situ* ATR-IR - attenuated total reflection infrared - cell was used to track the Ni catalyzed ether bond cleavage of lignin. While the rates of the hydrodeoxygenation of phenol were elucidated to be dependent on rather the hydrogenation (Ni/HZSM-5) of phenol or the dehydration step of cyclohexanol (Ni/C-SO₃H), the rate limiting step for the lignin deconstruction was the hydrogenolysis of the ether bonds in the lignin poly- and oligomer.

The results show that the relatively small lignin oligomers can be reductively deconstructed, opening a pathway to a full utilization of a wider range of lignin and lignocellulosic materials. Further, the flow through *in situ* ATR-IR cell enables to understand catalyzed biomass conversions in liquid phases for various known and recently studied systems.

Lastly in this thesis, the batch *in situ* IR spectroscopy has been applied to elucidate the reaction mechanism for the liquid phase conversion of palmitic acid with Ni/ZrO₂ catalysts. The mechanism proceeds with concerted adsorption of the acid at oxygen vacancies to form carboxylates and H₂ activation *via* dissociative adsorption on oxygen defect sites of the ZrO₂ surface. The α -H atoms of the carboxylate are subsequently abstracted forming the ketene intermediate, which is then hydrogenated to octadecanal on Ni particles. The presence of the ketene intermediate has been confirmed by *in situ* IR spectroscopy. Without H₂ the ketene intermediate forms palmitone *via* interaction with the adjacent palmitate over the ZrO₂ support by eliminating CO₂. Therefore the H coverage on the active sites favors either hydrogenation-decarbonylation or self-condensation (ketonization) pathways.

This dissertation has shown that IR spectroscopy is a valuable and indispensable tool to elucidate the reaction pathways and mechanistic aspects of catalyzed biomass conversion processes enabling to track the intermediates and consequently improve the overall efficiency of catalysts.

Curriculum Vitae

Stanislav Kasakov was born on November, the 13th 1985 in Chisinau, Republica Moldova. In the year 1997 he migrated with his family to Germany, where he completed the high school education at Schiller-Gymnasium Hof/Saale in 2006. In the same year he enrolled as a student into the Department of Chemistry at the Technische Universität München in Garching. After receiving his B.Sc. and M.Sc. in Chemistry, he continued his research studies in March 2012 as a PhD student at the Lehrstuhl für Technische Chemie 2 under the supervision of Prof. Dr. Johannes A. Lercher. The PhD thesis was in close collaboration with the Institute of Integrated Catalysis at the Pacific Northwest National Laboratory in Richland, Washington, USA.

List of publications

1. Comparison of kinetics, activity and stability of Ni/HZSM-5 and Ni/Al₂O₃-HZSM-5 for phenol hydrodeoxygenation, Chen Zhao, [Stanislav Kasakov](#), Jiayue He, Johannes A. Lercher, *Journal of Catalysis*, 296, 2012: p. 12-23
2. Manipulating Catalytic Pathways: Deoxygenation of Palmitic Acid on Multifunctional Catalysts, Baoxiang Peng, Chen Zhao, [Stanislav Kasakov](#), Sebastian Foraita, Johannes A. Lercher, *Chemistry: A European Journal*, 19 (15) 2013: p. 4732–4741
3. Glucose and Cellulose derived Ni/C-SO₃H catalysts for liquid phase phenol hydrodeoxygenation, [Stanislav Kasakov](#), Chen Zhao, Eszter Baráth, Zizwe A. Chase, John L. Fulton, Donald M. Camaioni, Aleksei Vjunov, Hui Shi, Johannes A. Lercher, *Chemistry: A European Journal*, 21, 2015, p. 1567 - 1577
4. State of Supported Ni Nanoparticles during Catalysis in Aqueous Media, Zizwe A. Chase, [Stanislav Kasakov](#), M. Balasubramanian, John Fulton, Aleksei Vjunov, Donald M. Camaioni, Chen Zhao and Johannes A. Lercher, *Chemistry: A European Journal*, 2015, doi:10.1002/chem.201502723.
5. Reductive deconstruction of organosolv lignin on zeolite supported Ni catalysts, [Stanislav Kasakov](#), Hui Shi, Chen Zhao, Eszter Baráth, Donald M. Camaioni, Andreas Jentys and Johannes A. Lercher, *Green Chemistry*, 2015, DOI: 10.1039/C5GC02160J